

INFORMATION TO USERS

This manuscript has been reproduced from the microfilm master. UMI films the text directly from the original or copy submitted. Thus, some thesis and dissertation copies are in typewriter face, while others may be from any type of computer printer.

The quality of this reproduction is dependent upon the quality of the copy submitted. Broken or indistinct print, colored or poor quality illustrations and photographs, print bleedthrough, substandard margins, and improper alignment can adversely affect reproduction.

In the unlikely event that the author did not send UMI a complete manuscript and there are missing pages, these will be noted. Also, if unauthorized copyright material had to be removed, a note will indicate the deletion.

Oversize materials (e.g., maps, drawings, charts) are reproduced by sectioning the original, beginning at the upper left-hand corner and continuing from left to right in equal sections with small overlaps.

Photographs included in the original manuscript have been reproduced xerographically in this copy. Higher quality 6" x 9" black and white photographic prints are available for any photographs or illustrations appearing in this copy for an additional charge. Contact UMI directly to order.

ProQuest Information and Learning
300 North Zeeb Road, Ann Arbor, MI 48106-1346 USA
800-521-0600

UMI[®]

SPIN RELAXATION IN GEOMETRICALLY FRUSTRATED
PYROCHLORES

By

Sarah Ruth Dunsiger

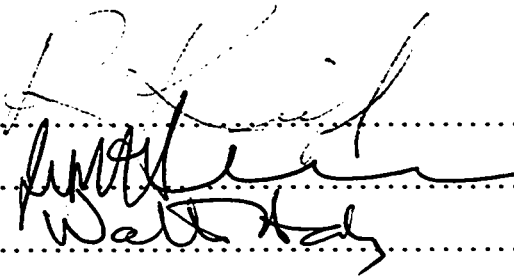
B. Sc. (Physics) University of Manchester, 1991

A THESIS SUBMITTED IN PARTIAL FULFILLMENT OF
THE REQUIREMENTS FOR THE DEGREE OF
DOCTOR OF PHILOSOPHY

in

THE FACULTY OF GRADUATE STUDIES
PHYSICS AND ASTRONOMY

We accept this thesis as conforming
to the required standard



.....
.....
.....
.....
.....

THE UNIVERSITY OF BRITISH COLUMBIA

2000

© Sarah Ruth Dunsiger, 2000



**National Library
of Canada**

**Acquisitions and
Bibliographic Services**

**395 Wellington Street
Ottawa ON K1A 0N4
Canada**

**Bibliothèque nationale
du Canada**

**Acquisitions et
services bibliographiques**

**395, rue Wellington
Ottawa ON K1A 0N4
Canada**

Your file Votre référence

Our file Notre référence

The author has granted a non-exclusive licence allowing the National Library of Canada to reproduce, loan, distribute or sell copies of this thesis in microform, paper or electronic formats.

The author retains ownership of the copyright in this thesis. Neither the thesis nor substantial extracts from it may be printed or otherwise reproduced without the author's permission.

L'auteur a accordé une licence non exclusive permettant à la Bibliothèque nationale du Canada de reproduire, prêter, distribuer ou vendre des copies de cette thèse sous la forme de microfiche/film, de reproduction sur papier ou sur format électronique.

L'auteur conserve la propriété du droit d'auteur qui protège cette thèse. Ni la thèse ni des extraits substantiels de celle-ci ne doivent être imprimés ou autrement reproduits sans son autorisation.

0-612-61084-5

Canada

In presenting this thesis in partial fulfilment of the requirements for an advanced degree at the University of British Columbia, I agree that the Library shall make it freely available for reference and study. I further agree that permission for extensive copying of this thesis for scholarly purposes may be granted by the head of my department or by his or her representatives. It is understood that copying or publication of this thesis for financial gain shall not be allowed without my written permission.

(Signature) Swati Durriger

Department of PHYSICS AND ASTRONOMY

The University of British Columbia
Vancouver, Canada

Date 11th December 2000

Abstract

This thesis describes μ SR experiments which focus on systems where the magnetic ions occupy the vertices of edge or corner sharing triangular units, in particular the pyrochlores $A_2B_2O_7$. The scientific interest in pyrochlores is based on the fact that they display novel magnetic behaviour at low temperatures due to geometrical frustration. The ground state of these systems is sensitively dependent on such factors as the range of the spin-spin interactions, disorder, anisotropy, thermal and quantum fluctuations.

For example, $Y_2Mo_2O_7$ shows many features reminiscent of a conventional spin glass, even though this material has nominally zero chemical disorder. It is found that the muon spin polarisation obeys a time-field scaling relation which indicates that the spin-spin autocorrelation function has a power law form in time, in stark contrast with the exponential form often assumed for conventional magnets above their transition temperature.

$Gd_2Ti_2O_7$ shows long range order, but only at a temperature much lower than its Curie-Weiss temperature, a signature of a frustrated system. In the paramagnetic regime, it is well described by an isotropic Heisenberg Hamiltonian with nearest neighbour couplings in the presence of a Zeeman interaction, from which the spin-spin autocorrelation function may be calculated as a power series in time. The muon spin relaxation rate decreases with magnetic field as the Zeeman energy becomes comparable with the exchange coupling between Gd spins. Thus, an independent measure of the exchange coupling or equivalently the Gd spin fluctuation rate is extracted.

By contrast, $Tb_2Ti_2O_7$ has been identified as a type of cooperative paramagnet. Short range correlations develop below 50 K. However, there is no long range ordering down to very low temperatures (0.075 K). The Tb^{3+} ion is subject to strong crystal electric field

effects: point charge calculations indicate that this system is Ising like at low temperatures. Thus this system may be analogous to water ice, a system theoretically predicted to have finite entropy at zero temperature. It is possible to qualitatively explain the unusual changes in T_1^{-1} as a function of applied magnetic field which are also observed using μ SR.

Table of Contents

Abstract	ii
Table of Contents	iv
List of Tables	vi
List of Figures	viii
Acknowledgements	xvi
1 Introduction	1
2 Theory of Geometric Frustration on the Pyrochlore Lattice	11
2.1 Classical Heisenberg pyrochlore antiferromagnet	14
2.2 Quantum spin 1/2 Heisenberg pyrochlore antiferromagnet	23
2.3 Spin 1/2 Ising pyrochlore: “spin ice”	24
3 The Pyrochlore Environment	29
3.1 Sample Preparation and Characterisation	29
3.2 Crystal electric field effects	34
3.3 Muon sites	47
4 Description of the Experiments	52
4.1 Production of Spin Polarised Muons	52
4.2 μ SR Experimental Setup	54
5 Muon Spin Relaxation	67
5.1 Static Internal fields	67

5.2	Fluctuating Internal Fields	71
6	$Y_2Mo_{2-x}Ti_xO_7$: a comparison with <u>AuFe</u>	80
6.1	<u>AuFe</u> : an archetypal spin glass	82
6.2	$Y_2Mo_2O_7$	94
6.2.1	Spin glass autocorrelation functions	104
6.3	Titanium substituted Yttrium compounds	109
6.3.1	$Y_2Ti_2O_7$	119
7	$Gd_2Ti_2O_7$: the paramagnetic phase	125
8	$Tb_2Ti_2O_7$: an intriguing puzzle	134
8.1	Calculations of T_1^{-1}	143
8.2	Evidence for <i>partial</i> spin ordering	152
9	Conclusions	160
	Bibliography	163
A	Crystal electric field and spin-orbit hamiltonians for $Y_2Mo_2O_7$	174
B	Magnetic field map of HELIOS solenoid	183
C	Cooling polycrystalline samples in a dilution refrigerator	184

List of Tables

2.1	Eigenstates of Heisenberg Hamiltonian as linear combinations of initial single spin up-down states of four spin 1/2 particles.	12
2.2	Eigenvalues and associated total spin of a system of 4 antiferromagnetically coupled spin 1/2 particles.	13
3.3	Pyrochlore ($A_2B_2O_6O'$) Structure Data (Origin at B Site).	30
3.4	Lattice constants and 48f oxygen parameter x of selected $A_2^{3+}B_2^{4+}O_6O'$ pyrochlores. Values from Ref. [74].	32
3.5	Eigenvalues and corresponding eigenvectors of the CEF Hamiltonian of the Mo^{4+} ion in its pyrochlore environment.	39
3.6	Eigenvalues and corresponding eigenvectors of the combined CEF and spin-orbit interaction Hamiltonians applied to the Mo^{4+} ion in its pyrochlore environment.	40
3.7	Eigenvalues and corresponding eigenvectors of the CEF Hamiltonian of the Tb^{3+} ion in its pyrochlore environment.	41
3.8	Electron configurations of selected Iron group and Lathanide ions.	46
3.9	Stevens' multiplicative factors and radial expectation values for selected ions. The latter quantities are in units of Bohr radii. (*) Only values for Mo^{3+} are available.	46
4.10	Selected properties of μ^+ and other particles.	53
4.11	Various geometries for a μ SR experiment. The \hat{x} axis points upwards, the \hat{y} axis from left to right, and the \hat{z} axis in the direction of the muon momentum.	59

C.12 Characteristic resistances on cooling a powder sample in a dilution refrigerator. 188

List of Figures

1.1	a) Unfrustrated and b) frustrated plaquettes due to random interactions. c) Geometrically frustrated plaquette of spins.	2
1.2	Pyrochlore lattice of corner sharing tetrahedra. The magnetic moments occupy the corners of the tetrahedra.	10
2.3	a) $q = 0$ and b) $\sqrt{3} \times \sqrt{3}$ Néel like ground states of the kagomé lattice. .	18
2.4	The effect of a non-magnetic impurity I in a tetragonal spinel. Three planes of spins are shown, the \hat{z} axis lying perpendicular to the planes. The interactions are restored between the spins at a, c and c' , which would cancel in the pure material. In an indiluted system the coupling between spins <i>along</i> infinite chains AA', BB' and CC' is given by \mathcal{J} , that <i>between</i> chains by \mathcal{J}' . After Villain [2].	20
2.5	Ground state configuration of spins on a single tetrahedron given ferromagnetic interactions and strong easy axis anisotropy along the dashed lines.	25
3.6	Description of the pyrochlore structure from Pannetier and Lucas [76]. a) B tetrahedra with 48f oxygen outside. b) Corner shared B tetrahedra indicating the octahedral oxygen coordination around each B ion. c) A ion tetrahedron showing central O' ion with near perfect tetrahedral angles.	30
3.7	Change in shape of coordination polyhedra of A and B ions with 48f oxygen parameter x . After Faucher and Caro [77].	31
3.8	The static susceptibility of <u>Au</u> Fe (0.5% at.) versus temperature in a magnetic field of 0.001 T, a) before and b) after annealing at 900° C for 24 hours and quenching.	33

3.9	<u>Au</u> Fe (0.5% at.) foil sealed under vacuum in a quartz tube. (S. R. Dunsiger)	35
3.10	The effect of varying terbium ion charge on its CEF energy level splittings. The lower box shows the 3 lowest doublets on an expanded scale.	43
3.11	The effect of varying the charge of the surrounding oxygen ions on the CEF energy level splittings of the Tb ³⁺ ion. The lower box shows the 3 lowest doublets on an expanded scale.	44
3.12	The effect of varying oxygen parameter x on the CEF energy level splittings of the Tb ³⁺ ion. The lower box shows the 3 lowest doublets on an expanded scale.	45
3.13	Map of electrostatic potential energy on several (100) planes for Y ₂ Mo ₂ O ₇ . The horizontal and vertical axes are parallel to the [010] and [001] directions respectively. Contour lines are in units of hartrees (27.2 eV).	50
4.14	A polar coordinate plot of the rate of positron emission from muon decay as a function of angle from the muon spin, at various energies ε . The distribution has axial symmetry about the muon spin polarisation direction, which points towards the right in this plot.	53
4.15	Signal timing for a typical time differential μ SR experiment using a Lecroy 4204 TDC.	55
4.16	General counter arrangement for a ${}^z\text{TF}_x$ μ SR experiment. In the ${}^z\text{TF}_x$ geometry shown, the muon spin precesses about the vertical axis at an angular frequency of $\omega_\mu = \gamma_\mu H$. (From Ref. [114]).	58
4.17	Sketch of the apparatus used for high LF and high ${}^z\text{TF}_z$ measurements. The superconducting solenoid is 24" in length and has a warm bore 6" in diameter.	60
4.18	Cross sectional view of the apparatus for measuring two μ SR spectra simultaneously. The apparatus has cylindrical symmetry and the sample is held in place on a stage (not shown) which has 2 thin vanes slotting into the Al cylinder.	61

4.19 Schematic logic diagram of the fast electronics for time differential μ SR experiments using the “Separate spectra” apparatus and a Lecroy 4204 TDC.	62
4.20 Fourier transform of the muon precession signal in a transverse magnetic field of 1.45 T with a) Al_2O_3 and b) Ag samples.	64
4.21 d.c. susceptibilities of a) lucite and b) Bicron BC412 scintillator in an applied magnetic field of 1.5 T.	65
4.22 Relative precession frequency shift as a function of temperature in an applied magnetic field of 1.45 T with silver in both the sample and reference positions.	66
5.23 LF spin relaxation functions for isotropic static internal magnetic fields with a) Gaussian and b) Lorentzian distributions.	68
5.24 Zero field dynamic Gaussian Kubo-Toyabe functions for different field fluctuation rates. The curves are calculated using the strong collision model.	71
5.25 Spectral density plot for three values of fluctuation rate, illustrating the variation of T_1^{-1} with ν_I in Eq. (5.59).	78
6.26 Muon spin relaxation rate T_1^{-1} above the spin glass transition temperature in <u>AuFe</u> (0.5%) measured in a longitudinal field of 0.005 T. The low temperature behaviour is shown on an expanded scale in the lower panel.	83
6.27 Parameter β above the spin glass transition temperature in <u>AuFe</u> (0.5%) measured in a longitudinal field of 0.005 T. Above 50 K the data is fit to an exponential function $\exp(-t/T_1)$, while below the transition temperature Eq. (6.68) is used.	84
6.28 Typical μ SR spectra in <u>AuFe</u> (0.5%) in 0.005 T longitudinal field. The solid lines are fits to Eq. (6.68).	86
6.29 a) Fluctuation rate and b) spin glass order parameter in <u>AuFe</u> (0.5%) measured in a longitudinal field of 0.005 T.	87

6.30	Muon spin depolarisation functions appropriate for dilute spin glasses in a) zero applied field [Eq. (6.67)] and b) longitudinal field $\omega_\mu = \Delta$ [Eq. (6.68)].	90
6.31	Typical μ SR spectra in <u>Au</u> Fe (0.5%) in 0.005 T longitudinal field.	91
6.32	Typical μ SR spectra in <u>Au</u> Fe (0.5%) at 0.025 K in various longitudinally applied magnetic fields.	92
6.33	Typical longitudinal field μ SR spectra in $Y_2Mo_2O_7$ at 27.5 K.	95
6.34	a) Muon spin relaxation rate and b) β as a function of temperature in $Y_2Mo_2O_7$ measured in a longitudinal field of 0.02 T. Below 2 K β is held constant at a value of 0.47.	96
6.35	Fluctuation rate as a function of temperature in $Y_2Mo_2O_7$. The triangles indicate values from inelastic neutron scattering measurements by Gardner <i>et al.</i> (Ref. [154]). The values obtained by μ SR (square symbols) are extracted using Eq. (5.59) from measurements in a longitudinal field of 0.02 T. The area to the left of the dot-dashed line indicates where the concept of a single fluctuation rate is likely no longer appropriate.	98
6.36	a) Short time behaviour of the muon polarisation in $Y_2Mo_2O_7$ at 2.32 K and b) the depolarisation of the 1/3 component. The solid, dashed and dot-dashed lines are fits which are described in the text.	99
6.37	Simulation of the magnetic field at the muon site (0.16, 0.16, -0.17) as- suming randomly oriented spins of magnitude $2.8 \mu_B$. For comparison, the solid and dashed lines indicate internal fields distributions with Gaus- sian and Lorentzian $\hat{x}, \hat{y}, \hat{z}$ components respectively.	100
6.38	Resultant muon spin depolarisation function given the static internal field distribution shown in Fig. 6.37 (dot-dashed line). The solid and dashed lines are Eqs. 5.40 and 5.42 respectively using the values of Δ, a shown in Fig. 6.37.	101

6.39	Characteristic spectra in $Y_2Mo_2O_7$ in various longitudinal magnetic fields at ~ 40 mK. The increase in the amplitude of the long time tail with field is evidence of a static internal field distribution.	103
6.40	Static internal field as a function of temperature in $Y_2Mo_2O_7$ assuming Gaussian (dashed line) and Lorentzian (solid line) internal field distributions. The quoted values are from fits to Eq. (6.69).	104
6.41	Asymmetry in $Y_2Mo_2O_7$ at 22.5 K in various longitudinal magnetic fields.	107
6.42	Asymmetry in $Y_2Mo_2O_7$ at 22.5 K in various longitudinal magnetic fields H , plotted as a function of t/H^γ	108
6.43	a) Muon spin relaxation rate and b) β as a function of temperature in $Y_2Mo_{1.6}Ti_{0.4}O_7$ measured in a longitudinal field of 0.02 T. The parameter β is defined by Eq. (6.70).	110
6.44	a) Muon spin relaxation rate and b) β as a function of temperature in $Y_2Mo_{1.2}Ti_{0.8}O_7$ measured in a longitudinal field of 0.02 T. The parameter β is defined by Eq. (6.70).	111
6.45	a) Muon spin relaxation rate and b) β as a function of temperature in Y_2MoTiO_7 measured in a longitudinal field of 0.02 T.	112
6.46	a) Transition temperature and b) residual relaxation rate as a function of Ti substitution in $Y_2Mo_{2-x}Ti_xO_7$	115
6.47	Behaviour at early times of the muon spin depolarisation in $Y_2Mo_{2-x}Ti_xO_7$: a) $x=0$; b) $x=0.4$; c) $x=0.8$; and d) $x=1$	116
6.48	Muon polarisation decay asymmetries of silver and $Y_2Ti_2O_7$ measured in a tranverse field of 0.005 T at $T=295$ K.	120
6.49	Typical μ SR spectra in $Y_2Ti_2O_7$ in a longitudinally applied field of 0.02 T. Note that the vertical scale starts at a muon spin polarisation of 0.75, <i>i.e.</i> the relaxing signal is small. This small effect is attributed to residual magnetic impurities (see text).	121

6.50 a) Asymmetry and b) T_1^{-1} of the fast relaxing component in $Y_2Ti_2O_7$ in a longitudinally applied field of 0.02 T.	122
6.51 dc magnetisation measurements in $Y_2Ti_2O_7$ in a magnetic field of 0.02 T.	123
7.52 Typical μ SR spectra in $Gd_2Ti_2O_7$ in a longitudinally applied field of 0.005 T.	130
7.53 Spin relaxation rates T_1^{-1} in $Gd_2Ti_2O_7$ as a function of temperature in various applied longitudinal fields.	131
7.54 Spin relaxation rates T_1^{-1} in $Gd_2Ti_2O_7$ as a function of longitudinal magnetic field at 7.5 and 100 K. The fitted curve is described in the text [Eq. (7.91)].	132
7.55 Corrected asymmetry in $Gd_2Ti_2O_7$ as a function of longitudinal magnetic field at T=100 K.	133
8.56 Muon spin depolarisation rate versus temperature for $Tb_2Ti_2O_7$ in a longitudinal field of 0.005 T. The squares indicate data taken on a powder sample, the circles a [111] single crystal.	135
8.57 A neutron diffraction pattern in $Tb_2Ti_2O_7$ at 2.5 K is shown in the top panel. The difference between diffraction patterns taken at 2.5 K (filled circles) and 50 K (open circles) and that taken at 100 K is shown in the bottom panel. The solid lines are fits to Eq. (8.94).	137
8.58 Inelastic neutron scattering data obtained at a temperature of 12 K and $Q=2.2 \text{ \AA}^{-1}$ in $Tb_2Ti_2O_7$	139
8.59 Top panel: constant $ Q $ scans at 12 K in $Tb_2Ti_2O_7$. Lower panel: Dispersion of the magnetic excitation spectrum at 12 and 30 K.	140
8.60 Muon spin depolarisation rate versus temperature for a powder sample of $Tb_2Ti_2O_7$ in a various longitudinally applied magnetic fields. The spectra at 0.005, 0.1 and 0.5 T were analysed using a single exponential function, those at 1 and 2 T with a stretched exponential.	144

8.61	The parameter β versus temperature for $\text{Tb}_2\text{Ti}_2\text{O}_7$ in an applied field of 1 T. The spectra were fitted to a stretched exponential function $G_{zz}(t) = \exp[-(t/T_1)^\beta]$	145
8.62	Muon spin depolarisation rate versus magnetic field for a powder sample of $\text{Tb}_2\text{Ti}_2\text{O}_7$ at various temperatures. All the spectra were fitted to a single exponential function $G_{zz}(t) = \exp(-t/T_1)$	147
8.63	Calculation of the muon spin relaxation rate using Eqs. (8.96) and (8.101).	150
8.64	Plot of the Brillouin function describing the magnetisation of a set of identical free Tb^{3+} ions in their ${}^7\text{F}_6$ ground state.	152
8.65	Temperature times fractional frequency shift versus applied magnetic field for $\text{Tb}_2\text{Ti}_2\text{O}_7$ at 285 and 3 K. The fractional frequency shift, a measure of the local susceptibility χ' , is proportional to χ''/ω and through the fluctuation dissipation theorem to T_1^{-1} [Eq. (6.79)].	153
8.66	Corrected asymmetry versus temperature for $\text{Tb}_2\text{Ti}_2\text{O}_7$ [111] single crystals in a longitudinal field of 0.005 T.	154
8.67	Muon precession signals observed in a) Ag and b) $\text{Tb}_2\text{Ti}_2\text{O}_7$ in a transverse field of 0.092 T at 3 K. The data were recorded using the separate spectra apparatus described in Chapter 4.	157
8.68	Inverse fractional shift in the muon precession frequency relative to a silver reference versus temperature for $\text{Tb}_2\text{Ti}_2\text{O}_7$ in a transverse field of 0.09 T. The squares indicate data taken on a powder sample, the circles and triangles a [111] single crystal.	158
B.69	Magnetic field map of HELIOS solenoid in the a) axial and b) radial directions.	183
C.70	Sample holder for a top loading dilution refrigerator with the sample of $\text{Y}_2\text{Mo}_2\text{O}_7$. The electrical connections for the thermometer are imbedded in teflon, shown at the bottom of the photograph. (S. R. Dunsiger) . . .	185

C.71 $\text{Y}_2\text{Mo}_2\text{O}_7$ prepared for a temperature calibration. The two pellets are wrapped with the copper wire leads attached to a RuO_2 thermometer. The silver plate behind is ~ 2.5 cm long. (S. R. Dunsiger) 186

Acknowledgements

This work has been done as a collaboration between Professors R. F. Kiefl (UBC), Y. J. Uemura (Columbia) and B. D. Gaulin (McMaster) and was funded by an NSERC collaborative grant “Geometrically Frustrated Magnetic Materials”. I would particularly like to thank my research supervisor, Rob Kiefl, for his support, patience and encouragement. Through his generosity I have had the opportunity to work with a number of other groups and to travel to experiments and conferences.

The μ SR experiments would not have been possible without the help of W. A. MacFarlane, K. M. Kojima, J. E. Sonier, K. H. Chow, R. I. Miller, G. D. Morris, J. A. Chakhalian, A. N. Price, W. D. Wu and A. Keren, who set up equipment and took shifts. B. D. Gaulin, J. S. Gardner, and Z. Tun gave me the chance to participate in a number of neutron scattering experiments.

I would also like to thank A. J. Berlinsky, J. H. Brewer, W. J. L. Buyers, M. J. P. Gingras, G. M. Luke and Y. J. Uemura for useful conversations. For synthesising and providing the pyrochlore samples I acknowledge N. P. Raju and J. E. Greedan. J. L. Tholence supplied a sample of AuFe at very short notice, which R. Liang then annealed and quenched under vacuum.

Finally, I have learned that the technical support of the facility is essential to successfully complete μ SR experiments. For their dedication I would like to thank the μ SR facility manager S. Kreitzman and facility personnel M. Good, C. Ballard, B. Hitti, D. Arseneau and K. Hoyle, as well as the machine and scintillator shops at TRIUMF.

Zoë, thank you for your moral support and long distance telephone calls!

Chapter 1

Introduction

Recently there has been a great deal of scientific interest in systems where the magnetic ions occupy the vertices of edge or corner sharing triangular units [1]. In these cases the natural magnetic coupling between ions is *geometrically* frustrated, while the translational symmetry of the lattice is preserved. The curiosity about these systems stems from the possibility that if conventional magnetic order is highly frustrated then one may find novel forms of magnetism. There is now considerable evidence that the low temperature state is “fragile”, *i.e.* it depends sensitively on a variety of factors such as anisotropy [2], the range of the spin-spin interactions [3, 4], thermal [5] and quantum [6, 7, 8] fluctuations and residual disorder.

It is important to distinguish between frustration arising from disorder and that due to the geometry or topology of the crystal structure. To illustrate this difference consider a plaquette of four Ising spins with random interactions favouring either parallel (+) or antiparallel (−) alignment, as shown in figures 1.1a and 1.1b. Note that for a plaquette with an even number of (−) interactions (1.1a) there exists a spin configuration which satisfies all the antiferromagnetic couplings between ions. On the other hand, when there happens to be an odd number of (−) couplings on the plaquette (see 1.1b) no spin configuration satisfies all four couplings and the plaquette is said to be frustrated. Similarly, a square lattice of spins with random nearest neighbour interactions is frustrated by disorder. Generally, frustration from random disorder is thought to be responsible for the observed magnetic behaviour in conventional spin glasses, which is characterised by finite local spontaneous magnetisation but with an average or staggered magnetisation which is zero. An example of a conventional spin glass would be a metal in which a dilute concentration of magnetic ions are distributed randomly: e.g. AuFe, CuMn or AgMn, although

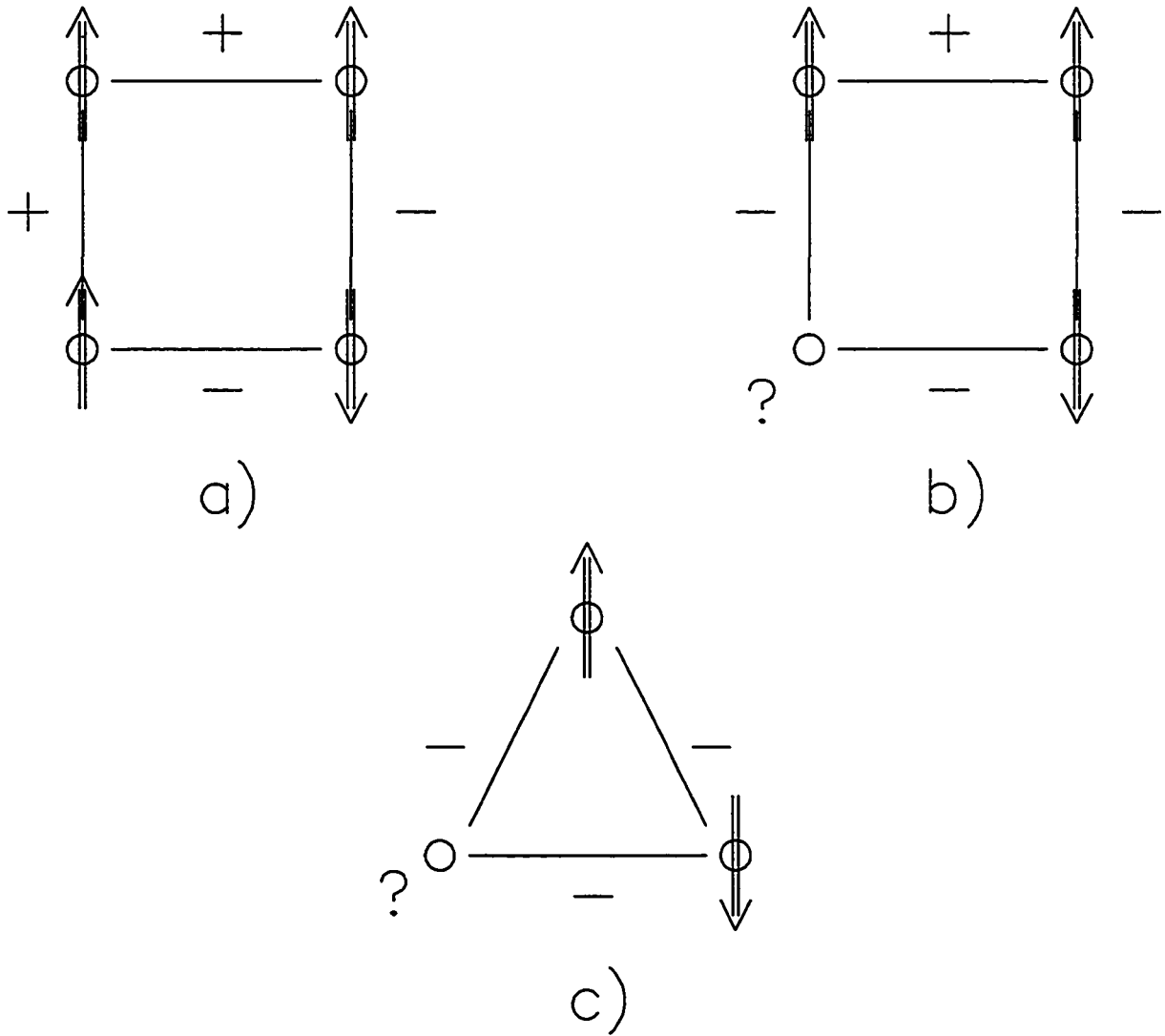


Figure 1.1: a) Unfrustrated and b) frustrated plaquettes due to random interactions. c) Geometrically frustrated plaquette of spins.

insulating spin glasses have also been observed. The ions in the metallic systems interact primarily through the Ruderman-Kittel-Kasuya-Yosida (RKKY) interaction arising from polarisation of the host conduction electrons. Since the RKKY interaction is oscillatory in nature and the distance between ions is somewhat variable, the magnetic coupling between ions is random both in magnitude and *sign*. It is observed that the spins freeze below a critical temperature T_F , leading to random but static order of the spin orientations, *i.e.* a spin glass state as $T \rightarrow 0$. A complete discussion of random spin glasses is beyond the scope of this thesis. More details can be found in the review article by Binder and Young [9] and a recent book by Fischer and Hertz [10]. While this thesis concentrates on frustrated systems with nominally *zero* chemical disorder, many of them nevertheless show features reminiscent of conventional spin glasses. Some of the ideas developed for spin glass materials are relevant for geometrically frustrated systems.

Now consider the plaquette shown in 1.1c, where all the interactions between spins favour antiparallel alignment. In this case there is no bond disorder and yet it is still frustrated, since there is no spin configuration which simultaneously satisfies all three of the antiferromagnetic couplings. In systems where the magnetic ions occupy the vertices of edge or corner sharing triangular units, the natural antiferromagnetic coupling between ions is said to be *geometrically* frustrated. The key point here is that there is a high degree of magnetic frustration while preserving the translational symmetry of the lattice.

Edge sharing triangles and tetrahedra form the well known stacked triangular [11] and face centred cubic lattices in two and three dimensions respectively. In two dimensions, a network of corner sharing triangles forms the kagomé lattice, while in three dimensions a lattice of corner sharing triangles gives rise to the garnets. There are a variety of systems which are based on a three dimensional arrangement of corner sharing tetrahedra. For instance, the intermetallic Laves phase compounds have a general formula AB_2 [12, 13], where A is a rare earth and B is a transition ion. Spinel of general formula AB_2O_4 or $A_2B_2O_4$ [14, 15, 16, 17, 18, 19] constitute a second family. A third one is comprised of fluoride pyrochlores with general formula $AB^{2+}C^{3+}F_6$ [20, 21] (A is an alkali metal, B and

C are transition metals). Finally, there is the family of oxide pyrochlores with the general formula $A_2B_2O_7$ (A is a rare earth and B is a transition ion). Strictly speaking, the only candidates which can be described by a localised uniform Heisenberg model are the oxide pyrochlores. These systems are well ordered with a uniform distribution of magnetically localised ions. By contrast, the second and third sets often possess positional or chemical disorder, while the first is better described within an itinerant model. Hence the oxide pyrochlores are perhaps the most promising systems in which to isolate the effects of geometric frustration on the low temperature behaviour of magnets. These compounds are the subject of the majority of the experiments described in this thesis. Chapter 3 includes details of their structure and synthesis, as well as the effect of the surrounding ligands on the energy levels of the magnetic ions. There is also a discussion of possible muon sites within this family of compounds.

Whenever a muon stops in an insulator there are always free carriers (and the accompanying positive ions) produced. The possible effect of these radiolysis products is discussed in Chapter 6. Muon spin relaxation measurements on a non-magnetic insulating pyrochlore $Y_2Ti_2O_7$ are presented with the intention of quantifying any influence of muonium formation in the magnetic pyrochlores. The possibility of "muon induced" effects by the interstitial μ^+ charge or spin are also discussed. The muon itself is usually assumed to be an innocuous probe. This premise is demonstrated by comparisons with the results other techniques. In particular, the Tb^{3+} spin fluctuation rates in the pyrochlore $Tb_2Mo_2O_7$ extracted from neutron scattering and μ SR measurements are in good agreement [22]. The same is true for $Y_2Mo_2O_7$, as illustrated in Chapter 6.

In conventional magnets spontaneous symmetry breaking at a phase transition leads to a uniquely defined ground state (*e.g.* the Néel state in the case of an antiferromagnet). Typically, in heavily frustrated systems one can expect a large macroscopic ground state degeneracy [23]. Theoretical predictions of the ground state of geometrically frustrated pyrochlores are discussed in Chapter 2 of this thesis. As mentioned above, the ground state of these systems depends on *all* the interactions in an extremely sensitive way.

Omitting terms which might be considered negligible in conventional magnets from theoretical models of frustrated systems may explain the discrepancies which arise between theory and experiment. The dominant experimental feature which characterises frustration is that if there is a phase transition, it is at a temperature well below that predicted for unfrustrated systems with the same exchange coupling, \mathcal{J} . Note however that this behaviour is distinct from truly one dimensional systems, where no ordering is predicted. A variety of experimental methods have been used to characterise the magnetic properties of frustrated spin systems. Muon Spin Relaxation/Rotation/Resonance (μ SR) has been shown to be particularly effective at elucidating spin dynamics which occur over a broad range of frequencies between $10^4 - 10^{11} \text{ s}^{-1}$, too low for neutron scattering but too high for ac susceptibility. Chapter 4 describes this technique, as well as some developments in the equipment used over the course the experiments. The formalism necessary to understand muon spin depolarisation or relaxation is introduced in Chapter 5.

The methods being used to investigate geometrically frustrated magnets with muons have also been used to investigate conventional spin glasses. The first μ SR experiments on dilute metallic spin glasses were performed in the mid seventies. The earliest were transverse field (TF) μ SR measurements [24] where the damping or linewidth parameter (T_2^{-1}) was observed to increase as one approaches T_F from above, due to the critical slowing down of spin fluctuations. Subsequently, zero field (ZF) μ SR and longitudinal field (LF) μ SR techniques, which allow one to distinguish the static and fluctuating components of the internal field more easily, have been particularly useful in random spin systems where it is often very difficult to carry out NMR measurements under similar conditions.

One of the most significant contributions which μ SR has made to the understanding of spin glasses has to do with the nature of the spin fluctuations. ZF and LF μ SR measurements on AuFe and CuMn [25] show the simultaneous presence of static random field components and rapidly fluctuating components. This provides strong confirmation of the Edwards-Anderson model of spin glasses, where each impurity spin has its

own preferred direction and undergoes restricted fluctuations about this direction. This technique also played an important role in understanding the spin-spin autocorrelation function in spin glasses. It had previously been thought that the spin dynamics could be characterised by a single correlation time. Neutron spin echo [26] and later μ SR measurements [27, 28, 29] suggested exotic dynamics both above and below the spin freezing transition T_F , implying dynamics on many timescales. Even more surprisingly, as the spin freezing temperature is approached from above, it is found that the muon spin polarisation obeys a time-field scaling relation which indicates that the spin-spin autocorrelation function has a power law form in time [30]. This is in stark contrast with the exponential form often assumed for conventional paramagnets.

As a comparison, consider the autocorrelation functions in a two sublattice antiferromagnet. Below the Néel temperature there are collective spin excitations, or magnons, which may be scattered by the muon spins, emitted or absorbed by them or converted into phonons, all leading to fluctuating magnetic fields and hence relaxation processes. The fluctuations of the electronic spins may be expressed using the Holstein-Primakoff representation of spin operators in terms of Bose creation and annihilation operators of spin waves. Linear terms with respect to these operators give rise to muon spin transitions accompanied by the absorption or emission of one spin wave. This is called a direct process; only those spin waves of an energy which corresponds exactly to the muon Larmor frequency can take part in these processes. The dominant effect therefore comes from Raman processes, which are related to bilinear terms with respect to the creation and annihilation operators. In a Raman process a muon spin flip is accompanied by a simultaneous emission of one spin wave and absorption of another, while the total energy is conserved.

The spin fluctuations δS_l^\pm at site l are linear in the spin wave creation and annihilation operators and therefore contribute to direct processes, to lowest order. However, δS_{lz} is bilinear and can induce Raman processes, provided that the direction of antiferromagnetic alignment $\pm z$ is not parallel with the initial direction of muon spin, remembering that

only components of the fluctuating local field transverse to the muon spin quantisation are effective in causing relaxation. The autocorrelation functions in the non-interacting spin-wave approximation are discussed by Lovesey [31] and by Moriya [32, 33]. In zero applied magnetic field:

$$\langle S^+ S^-(t) \rangle \propto \sum_{\mathbf{q}} \{ \langle n_{\mathbf{q}} + 1 \rangle \exp(i\omega_{\mathbf{q}} t) + \langle n_{\mathbf{q}} \rangle \exp(-i\omega_{\mathbf{q}} t) \} \quad (1.1)$$

and

$$\begin{aligned} \langle S_z S_z(t) \rangle \propto & \sum_{\mathbf{q}} \sum_{\mathbf{q}'} \{ \langle n_{\alpha\mathbf{q}} \rangle \langle n_{\alpha\mathbf{q}'} + 1 \rangle \exp[i(\omega_{\mathbf{q}} - \omega_{\mathbf{q}'})t] + \\ & \langle n_{\beta\mathbf{q}} + 1 \rangle \langle n_{\beta\mathbf{q}'} \rangle \exp[-i(\omega_{\mathbf{q}} - \omega_{\mathbf{q}'})t] \} \end{aligned} \quad (1.2)$$

where $\langle n_{\alpha\mathbf{q}} \rangle$ and $\langle n_{\beta\mathbf{q}'} \rangle$ are the thermal averages of the number operators of magnons of wave-vector \mathbf{q} and \mathbf{q}' on each sublattice. The magnons are governed by Bose-Einstein statistics and hence

$$\langle n_{\mathbf{q}} \rangle = \{ \exp(\hbar\omega_{\mathbf{q}}/k_B T) - 1 \}^{-1}. \quad (1.3)$$

Finally, the autocorrelation functions are a superposition of oscillatory functions at frequencies $\omega_{\mathbf{q}}$, given by the spin wave dispersion relations, such that, overall, the oscillation becomes damped.

$\text{SrCr}_x\text{Ga}_{12-x}\text{O}_{19}$ (SCGO) is the most well studied example of a Heisenberg antiferromagnet on a kagomé lattice. A spin glass-like cusp is observed at $T_F \sim 2-5$ K as well as history dependence of the susceptibility, similar to that seen in random spin glasses. This material has recently been studied by Uemura *et al.* [34] using μSR . Surprisingly, dynamic spin fluctuations are observed without any evidence for static internal fields even at 100 mK. Neutron scattering measurements by Lee *et al.* [35], which imply an ordered moment only one third of the full value for $S=3/2$ Cr^{3+} ions, support the idea of only a partial ordering with significant residual spin dynamics. However, possible complications arise in investigating this material, as there are alternating kagomé lattice and triangular lattice planes and $(9-x)/9$ of the Cr sites are randomly substituted by nonmagnetic Ga atoms. So far it has not been possible to synthesise SCGO without appreciable chemical

disorder. Jarosites $\text{AFe}_3(\text{OH})_6(\text{SO}_4)_2$ [36] are more perfect realisations of an antiferromagnetic kagomé lattice. However, these materials have been less extensively studied, mainly due to difficulties in synthesis [37]. Typically the occupation of Fe^{3+} sites is in the range of 83-94%, once again introducing some randomness.

A remarkable feature of many geometrically frustrated systems is the suppression of long range magnetic ordering and in some cases a high sensitivity to the presence of an external magnetic field. Gadolinium gallium garnet has perhaps the best known example of a field induced phase transition. Specific heat and magnetic susceptibility in zero field indicate there is no long-range magnetic ordering down to at least $T = 0.14$ K, which is more than an order of magnitude below the Curie Weiss temperature of $\Theta_{CW} \sim -2$ K (Ref. [38]), though a spin glass transition, controlled by the amount of site disorder from Gd on Ga sites, has been reported. Similar measurements on a [100] needlelike single crystal have shown that the application of an external field between 0.6 and 1.4 T can induce long range AF order [39]. Recently, neutron diffraction measurements [40] have found that short range magnetic ordering can occur at temperatures as high as 5 K and that spatial correlations of up to ~ 100 Å can exist below 140 mK. The low temperature spin dynamics have been investigated using muon spin relaxation [41]. Surprisingly, no evidence for static order is seen down to a temperature of 25 mK or a few percent of the Curie Weiss temperature. Instead there is a linear decrease in the Gd spin fluctuation rate below 1 K which extrapolates to a small but finite value of 2 GHz at zero temperature. In terms of the spin fluctuations the system appears essentially to remain dynamic at low temperatures ($T > 0.02$ K) and in magnetic fields up to 1.8 T.

A wide variety of low temperature behaviour has been observed in the geometrically frustrated pyrochlores of general formula $\text{A}_2\text{B}_2\text{O}_7$. As described in Chapter 6, the pyrochlore $\text{Y}_2\text{Mo}_2\text{O}_7$ exhibits a type of spin freezing at a temperature T_F which is similar to that seen in conventional spin glasses. Experiments on a conventional spin glass AuFe are included in this chapter to allow direct comparison. The magnetic Mo ions were also intentionally diluted with non-magnetic Ti^{4+} ions to study the effect of random disorder

in a controlled manner.

Muon spin relaxation measurements on $\text{Gd}_2\text{Ti}_2\text{O}_7$ are described in Chapter 7. While specific heat and susceptibility measurements by others indicate that this compound *does* show long range order, albeit at a temperature much less than its Curie Weiss temperature, our experiments have concentrated on the behaviour of T_1^{-1} at higher temperatures and fields. The Gd^{3+} ion has a $^8\text{S}_{7/2}$ ground state and hence to first order is not subject to crystal field effects, which depend on the orbital contribution to the angular momentum of the ion in question. This system is therefore perhaps the closest real example of a geometrically frustrated system with Heisenberg spins. Short range spin-spin correlations develop as the temperature is reduced and their effect on the muon spin relaxation rate is observed.

Chapter 8 involves a discussion of $\text{Tb}_2\text{Ti}_2\text{O}_7$ which includes both μSR and neutron scattering measurements. A rich variety of behaviour is observed as a function of temperature and magnetic field. To fully understand this material is more difficult, as crystal electric field effects, exchange and dipolar interactions are all significant. This material perhaps best highlights the need to develop more sophisticated theoretical models describing the dynamics of systems of electronic moments specifically relevant to muon spin relaxation functions.

As outlined above, a wide variety of magnetic ground states are possible in geometrically frustrated spin systems. Pyrochlores are particularly interesting since they are three dimensional structures and can be made with little disorder. Perhaps the most unexpected feature in pyrochlores discovered so far is the persistent spin relaxation at the lowest temperatures, indicating a large density of magnetic excitations near zero energy. Most other geometrically frustrated spin systems also show evidence for these persistent spin fluctuations.

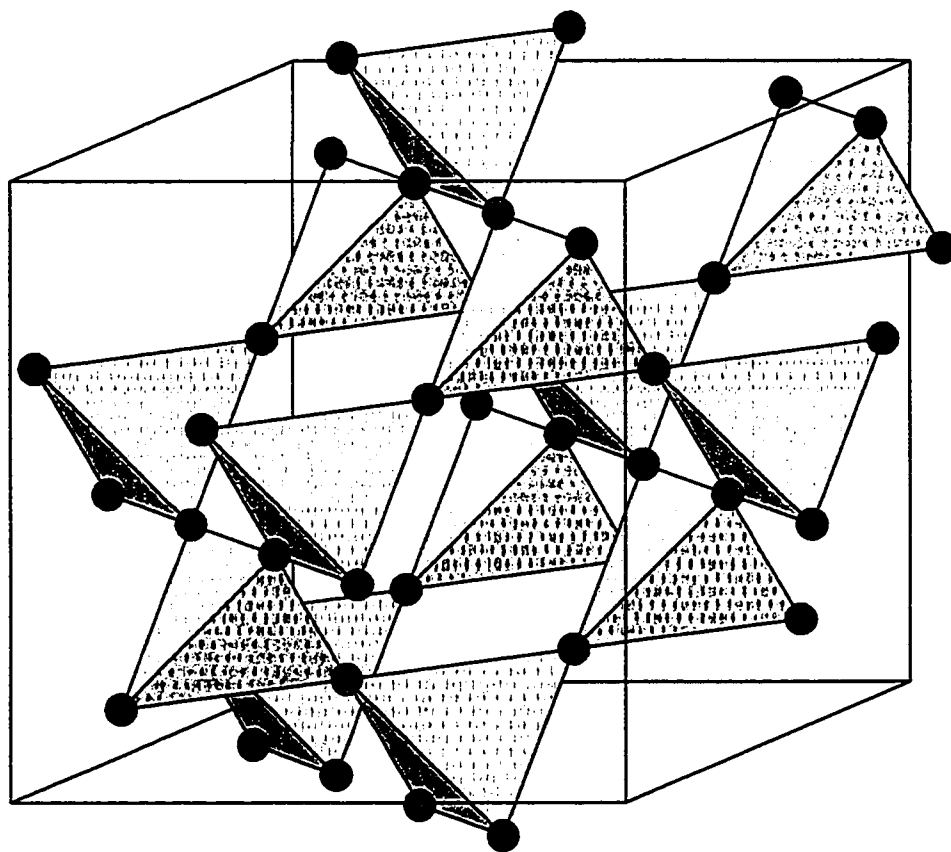


Figure 1.2: Pyrochlore lattice of corner sharing tetrahedra. The magnetic moments occupy the corners of the tetrahedra.

Chapter 2

Theory of Geometric Frustration on the Pyrochlore Lattice

The Heisenberg Hamiltonian is the starting point of many investigations of magnetic systems. It is written as

$$\mathcal{H} = -\frac{1}{2} \sum_{j \neq k} \mathcal{J}_{jk} \mathbf{S}_j \cdot \mathbf{S}_k, \quad (2.4)$$

where \mathcal{J}_{jk} is known as the coupling constant: the vector spin operators \mathbf{S}_j and \mathbf{S}_k favour antiparallel alignment if the coupling is negative. This section includes a brief description of various theoretical calculations and numerical simulations of spins on a lattice of corner sharing tetrahedra.

For example, consider the Heisenberg Hamiltonian applied to 4 antiferromagnetically coupled spin 1/2 ions on the corners of a tetrahedron. Diagonalising \mathcal{H} , the eigenstates of this system can be written as linear combinations of products of single spin states, as shown in Table 2.1, where the basis states are the projection of \mathbf{S} along the [001] axis. The corresponding energy eigenvalues are given in Table 2.2. In the state $|\uparrow\uparrow\uparrow\downarrow\rangle$, for example, the component along the \hat{z} or [001] axis of the spin of particles 1 through 4 are respectively $+\hbar/2$, $+\hbar/2$, $+\hbar/2$ and $-\hbar/2$. However, in some instances single ion anisotropy means the spins are constrained to lie along the four *local* $\langle 111 \rangle$ axes, such that the spins point either into or out of the tetrahedron. In this case all sixteen 4-spin states are mixed together.

As can be seen from Table 2.2, the ground state is determined by the condition

$$\sum_{j=1}^4 \mathbf{S}_j = 0. \quad (2.5)$$

More generally, given a small finite cluster of p spins all coupled equally to each other with a coupling \mathcal{J} , the reduced energy per spin or $E/p|\mathcal{J}|$ for $\mathcal{J} < 0$ can be found by

$\uparrow\uparrow\uparrow\uparrow$	$\frac{1}{2}$	(0
$\uparrow\uparrow\uparrow\downarrow$	$\frac{1}{2}$	(0
$\uparrow\uparrow\downarrow\uparrow$	$\frac{1}{\sqrt{2}}$	(0
$\uparrow\uparrow\downarrow\downarrow$	$\frac{1}{\sqrt{2}}$	(0
$\uparrow\downarrow\uparrow\uparrow$	$\frac{1}{\sqrt{2}}$	(0
$\uparrow\downarrow\uparrow\downarrow$	$\frac{1}{\sqrt{2}}$	(0
$\uparrow\downarrow\downarrow\uparrow$	$\frac{1}{\sqrt{2}}$	(0
$\uparrow\downarrow\downarrow\downarrow$	$\frac{1}{\sqrt{2}}$	(0
$\downarrow\uparrow\uparrow\uparrow$	0	(0
$\downarrow\uparrow\uparrow\downarrow$	0	(0
$\downarrow\uparrow\downarrow\uparrow$	0	(0
$\downarrow\uparrow\downarrow\downarrow$	0	(0
$\downarrow\downarrow\uparrow\uparrow$	0	(0
$\downarrow\downarrow\uparrow\downarrow$	0	(0
$\downarrow\downarrow\downarrow\uparrow$	0	(0
$\downarrow\downarrow\downarrow\downarrow$	0	(0
$\uparrow\uparrow\uparrow\uparrow$	0	(1)
$\uparrow\uparrow\uparrow\downarrow$	$\frac{1}{2}$	(0
$\uparrow\uparrow\downarrow\uparrow$	$\frac{1}{\sqrt{6}}$	(0
$\uparrow\uparrow\downarrow\downarrow$	$\frac{1}{2}$	(0
$\uparrow\downarrow\uparrow\uparrow$	(1	(0
$\uparrow\downarrow\uparrow\downarrow$	0	(0
$\uparrow\downarrow\downarrow\uparrow$	0	(0
$\uparrow\downarrow\downarrow\downarrow$	0	(0
$\downarrow\uparrow\uparrow\uparrow$	0	(0
$\downarrow\uparrow\uparrow\downarrow$	0	(0
$\downarrow\uparrow\downarrow\uparrow$	0	(0
$\downarrow\uparrow\downarrow\downarrow$	0	(0
$\downarrow\downarrow\uparrow\uparrow$	0	(0
$\downarrow\downarrow\uparrow\downarrow$	0	(0
$\downarrow\downarrow\downarrow\uparrow$	0	(0
$\downarrow\downarrow\downarrow\downarrow$	0	(0
$\uparrow\uparrow\uparrow\uparrow$	0	(0
$\uparrow\uparrow\uparrow\downarrow$	0	(0
$\uparrow\uparrow\downarrow\uparrow$	0	(0
$\uparrow\uparrow\downarrow\downarrow$	0	(0
$\uparrow\downarrow\uparrow\uparrow$	0	(0
$\uparrow\downarrow\uparrow\downarrow$	0	(0
$\uparrow\downarrow\downarrow\uparrow$	0	(0
$\uparrow\downarrow\downarrow\downarrow$	0	(0
$\downarrow\uparrow\uparrow\uparrow$	0	(0
$\downarrow\uparrow\uparrow\downarrow$	0	(0
$\downarrow\uparrow\downarrow\uparrow$	0	(0
$\downarrow\uparrow\downarrow\downarrow$	0	(0
$\downarrow\downarrow\uparrow\uparrow$	0	(0
$\downarrow\downarrow\uparrow\downarrow$	0	(0
$\downarrow\downarrow\downarrow\uparrow$	0	(0
$\downarrow\downarrow\downarrow\downarrow$	0	(0

Table 2.1: Eigenstates of Heisenberg Hamiltonian as linear combinations of initial single spin up-down states of four spin 1/2 particles.

Energy Eigenvalues ($ \mathcal{J} $)	S	S_z
-3/2	0	0
-3/2	0	0
-1/2	1	-1
-1/2	1	-1
-1/2	1	-1
-1/2	1	0
-1/2	1	0
-1/2	1	0
-1/2	1	1
-1/2	1	1
-1/2	1	1
3/2	2	-2
3/2	2	-1
3/2	2	0
3/2	2	1
3/2	2	2

Table 2.2: Eigenvalues and associated total spin of a system of 4 antiferromagnetically coupled spin 1/2 particles.

rewriting Eq. (2.4) as

$$\frac{\mathcal{H}}{p|\mathcal{J}|} = \frac{1}{2p} \left(\sum_{j=1}^p \mathbf{S}_j \right)^2 - \frac{1}{2p} \sum_{j=1}^p \mathbf{S}_j^2 \quad (2.6)$$

$$= \frac{1}{2p} S_T(S_T + 1) - \frac{1}{2} S_j(S_j + 1), \quad (2.7)$$

where S_j is the spin quantum number at each site and S_T the total spin over the cluster. If p is even, S_T may take integer values between 0 and pS_j . Similarly, for odd values of p , S_T ranges from S_j to pS_j . Again, the lowest energy or ground state arises when the total spin over the cluster is minimised, *i.e.* zero for a pyrochlore. Using the rules for the addition of angular momenta, the ground state degeneracy of the cluster may be found by counting the number of states with minimum S_T out of a possible number

of $(2S_i + 1)^p$. A highly degenerate ground state is a feature of frustrated magnetic systems. As demonstrated above, it is straightforward to find the eigenstates of a single cluster. However, it is more complicated to find the ground state of an entire system with a macroscopic number of interacting spins. While any state in which all the clusters have their energy separately minimised is a ground state of the entire system by periodic repetition, other ground states are also possible, once the interactions between tetrahedra are included.

2.1 Classical Heisenberg pyrochlore antiferromagnet

The problem of antiferromagnetic ordering on the pyrochlore lattice was first considered by Anderson [42] in 1956. Calculating the ground state configurational entropy, which is finite, he predicted that no long range order (LRO) would exist at any temperature for Ising spins. Later Villain [2] used qualitative arguments to show that the same is true for a system of Heisenberg spins with nearest neighbour antiferromagnetic interactions. He coined the expression “cooperative paramagnet” to describe a state with only short range spin-spin correlations for all $T > 0$. Both this and the term “classical spin liquid”, which also appears in the literature, are intended to emphasise that the spins are strongly interacting but fluctuating as $T \rightarrow 0$, rather than frozen into a static configuration. Anderson [43] discusses an insulating resonating valence bond (rvb) state, appropriate for some spin 1/2 Heisenberg systems, where the real ground state is a fluid of mobile valence bonds, *i.e.* pairs of spins correlated together into singlets. There is an energy gap to any excited state, by analogy with a Mott insulator. Such a system is referred to as a “quantum spin liquid”.

Extensive mean field calculations have been performed by Reimers, Berlinsky and Shi [3] for n -component classical vector spins on the pyrochlore lattice given a Heisenberg plus Zeeman Hamiltonian. They consider the spin-spin interaction matrix $\mathcal{J}(\mathbf{q})$ in terms

of its Fourier components:

$$\mathcal{J}^{ab}(|\mathbf{r}_{jk}|) = \frac{1}{N} \sum_{\mathbf{q}} \mathcal{J}^{ab}(\mathbf{q}) \exp(-i\mathbf{q} \cdot \mathbf{r}_{jk}), \quad (2.8)$$

where N is the number of unit cells and a and b are sublattice indices. Expressing the free energy in terms of a Landau expansion of the order parameter $\mathbf{B}(\mathbf{r}_j)$, the quadratic term is given by

$$\frac{1}{2} \sum_{\mathbf{q}} \sum_j \Phi_j(\mathbf{q}) \cdot \Phi_j(-\mathbf{q}) (nT - \lambda_j(\mathbf{q})). \quad (2.9)$$

Equation (2.9) has been written in terms of the normal modes of the system

$$\mathbf{B}^a(\mathbf{q}) = \sum_j U_j^a(\mathbf{q}) \Phi_j(\mathbf{q}), \quad (2.10)$$

where $U(\mathbf{q})$ is a unitary matrix which diagonalises $\mathcal{J}(\mathbf{q})$ with eigenvalues $\lambda(\mathbf{q})$:

$$\sum_b \mathcal{J}^{ab}(\mathbf{q}) U_j^b(\mathbf{q}) = \lambda_j(\mathbf{q}) U_j^a(\mathbf{q}). \quad (2.11)$$

By diagonalising the spin-spin interaction matrix using standard numerical packages the eigenvalues $\lambda(\mathbf{q})$ are obtained. A continuous phase transition occurs at the temperature where the coefficient of the quadratic term goes to zero. Thus the first ordered state of the system is associated with the critical modes which have the largest eigenvalue, selecting out the ordering wave vector. The possible spin structures are expressed in terms of combinations of normal modes. For the simplest model with only nearest neighbour antiferromagnetic interactions and only the B site (see Figs. 3.6 and 3.7) magnetic, three of the four possible modes are degenerate at the Brillouin zone centre, while two are degenerate and dispersionless right across the zone. Since no point in reciprocal space is favoured, the conclusion is that long range order cannot exist at any temperature. In some cases further neighbour interactions will break the degeneracy, stabilising $\mathbf{q} = 0$ or incommensurate structures. More recently Raju *et al.* [44] have extended Reimers' calculations to include the effect of dipolar interactions as well. Surprisingly, the long range and anisotropic nature of the dipolar interaction alone is not sufficient to lift all macroscopic ground state degeneracies.

Experimentally, the most extensively studied example of a pyrochlore which does show evidence of LRO with a $\mathbf{q} = 0$ structure is FeF_3 [45, 46]. The low temperature phase consists of four sublattices oriented along the four $\langle 111 \rangle$ directions, as indicated by the systematic absence of magnetic contributions to the $[hhh]$ reflections in neutron scattering measurements. Any two sublattices are at an angle of 109° from each other and the spins point alternately in and out of the tetrahedra. No additional neutron diffraction peaks appear below $T_N = 20(2)$ K, indicating that the magnetic and nuclear cells are identical. However, the contribution from the $[220]$ and $[311]$ peaks increases below T_N .

Monte Carlo simulations [4] using a classical model with nearest neighbour antiferromagnetic interactions confirm that there is no spin freezing at non-zero temperature. This is evidence that thermal fluctuations beyond the mean field approximation do not stabilise LRO. The simulations were carried out using the standard Metropolis spin-flipping algorithm [47] over a temperature range of $0.05 \leq T/\mathcal{J} \leq 20$. A number of thermodynamic quantities including the internal energy and heat capacity of the system were calculated. No maxima or finite size effects in the heat capacity were observed. Hence the spin-spin correlations do not extend beyond a distance of two unit cells. The Edwards Anderson spin glass order parameter (see Chapter 6) was also calculated and approaches zero at all temperatures, eliminating the possibility of some kind of disordered but static spin configuration. Nor were any sharp peaks or finite size effects observed in the powder neutron scattering function calculated from the low temperature spin configurations. These would have indicated ordering at incommensurate wave vectors.

Similar classical Monte Carlo calculations at 0 K of have been performed for antiferromagnetic Heisenberg interactions between nearest neighbours, to study the distinctive neutron scattering function for a single crystal [48, 20]. There is a very large degree of anisotropy in the scattering, revealing an anisotropy in the length scales of the magnetic correlations. Along the $\langle 001 \rangle$ and $\langle 111 \rangle$ directions the scattering is relatively sharp, signifying correlations which extend over tens of nearest neighbour distances, whereas

correlations along the $\langle 110 \rangle$ directions extend no further than nearest neighbours. Using Moessner's arguments [49], it follows from the ground state condition $\sum_{j=1}^4 \mathbf{S}_j = 0$ that the sum of all spin vectors in two adjacent planes is zero. Therefore, these planes are antiferromagnetically correlated and since these correlations are long ranged, *sharp* peaks are expected in the $\langle 200 \rangle$ directions. However, these features differ from Bragg peaks in that they are sharp only in one direction in reciprocal space and scale differently with sample size. This is similar to the type of order seen in liquid crystalline materials.

Possibly the most interesting feature of the classical ground state of pyrochlore and kagomé [51, 52] lattice antiferromagnets is the prediction of a dispersionless zero frequency spin-wave branch ("zero modes"). These local zero modes are degrees of freedom (unhindered rotation at zero frequency) in the ground state which involve only spins in a finite region in the bulk of the system. They differ from Goldstone modes [50], spin wave excitations in which the sublattice magnetisation oscillates slowly as a function of position and which have zero frequency only at the ordering wave-vector, rather than all \mathbf{q} .

Consider the kagomé lattice, where the zero modes are more easily visualised. Through the mechanism of "order-by-disorder" described later, nematic order is stabilised [52, 53], where the spins select a single plane but may orient themselves randomly within the plane. There are still an infinite number of coplanar ground states satisfying the condition that all spins point along one of three directions mutually oriented at 120° or $\sum_{j=1}^3 \mathbf{S}_j = 0$. However, among these the $\mathbf{q} = 0$ and $\sqrt{3} \times \sqrt{3}$ structures shown in Fig. 2.3 are special in that they are characterised by a single wave-vector each. For the $\mathbf{q} = 0$ Néel state, zero modes correspond to tilting spins around a hexagon alternately into and out of the plane. In the case of the $\sqrt{3} \times \sqrt{3}$ structure, all neighbouring spins for each hexagon are collinear; hence those spins on the hexagon may rotate without energy cost around this common axis. Using these zero modes to rotate spins, any ground state may be constructed from any other. Zero modes manifestly affect the thermodynamics of these

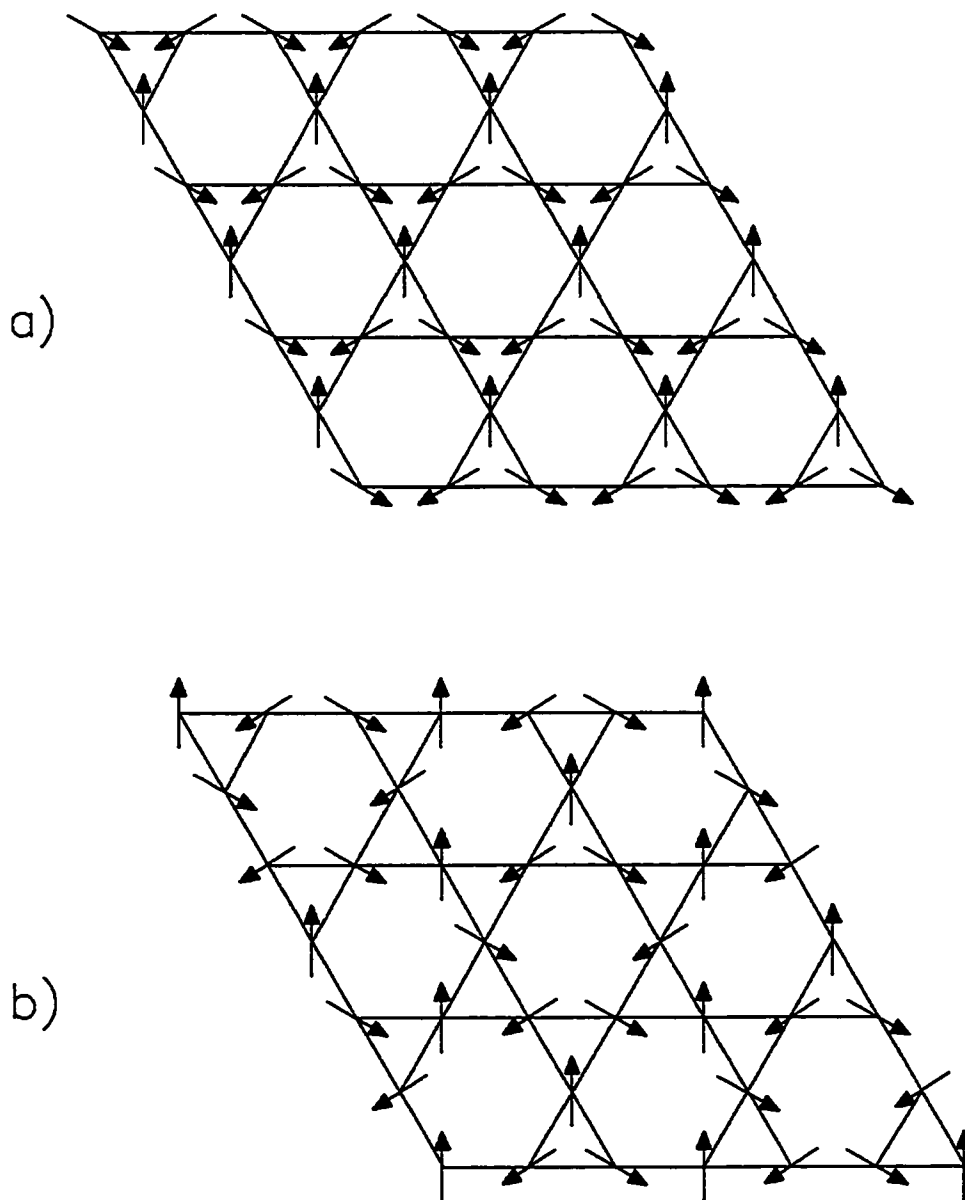


Figure 2.3: a) $q = 0$ and b) $\sqrt{3} \times \sqrt{3}$ Néel like ground states of the kagomé lattice.

classical systems, as demonstrated by Monte Carlo simulations, where the low temperature specific heat, C_v , falls below the classical value k_B expected from equipartition of energy [3, 4]. However, while zero modes do not contribute to the specific heat of the theoretical model, in a real material they would likely be stabilised by quartic energy terms and appear as diffusive or overdamped excitations [54]. Also, again because of these zero modes, the kagomé and pyrochlore antiferromagnets should display large spin fluctuations down to $T = 0^+$, at least theoretically.

Moessner *et al.* [49, 55] have considered a classical n component vector spin model with nearest neighbour interactions to study the precessional dynamics. Using qualitative arguments they describe how to construct all the ground states of the systems and show that the ground state manifold is “connected”, or not separated by energy barriers. Thus any ground state may be continuously deformed into any other without cost in energy. This is in contrast with the highly disordered regime of traditional spin glasses. In this latter case the various ground states are thought to be separated by energy barriers, explaining the wide variety of time dependent effects observed. The dynamics of the system were studied with both analytical techniques and by numerical integration of the equations of motion of the system,

$$\begin{aligned}\frac{d\mathbf{S}_j}{dt} &= \mathbf{S}_j \wedge \mathbf{H}_j(t) \\ &= -\mathcal{J}\mathbf{S}_j \wedge (\mathbf{L}_\alpha + \mathbf{L}_\beta),\end{aligned}$$

using a fourth order Runge-Kutta algorithm, where $\mathbf{H}_j(t)$ is the exchange field acting at site j and $\mathbf{L}_\alpha, \mathbf{L}_\beta$ are the total spins of the 2 tetrahedra to which each spin belongs. No freezing is observed even at $T = 5 \times 10^{-4}\mathcal{J}$. As the temperature is lowered towards approximately $T < 0.1\mathcal{J}$, the form of the autocorrelation function changes. Rather than decaying initially as $\langle \mathbf{S}_j(0) \cdot \mathbf{S}_j(t) \rangle \propto 1 - ct^2$, the autocorrelation function becomes exponential in time and *independent* of exchange energy with a characteristic relaxation time of $\hbar/k_B T$. The correlations are also very small beyond second neighbour distances. The density of states is finite at $\omega = 0$, neither diverging with a delta function contribution

nor vanishing as $\omega \rightarrow 0$. Note that this differs from the frequency dependence (proportional to ω^2) expected for Néel ordered antiferromagnets, including ordered states of the pyrochlore antiferromagnet [56].

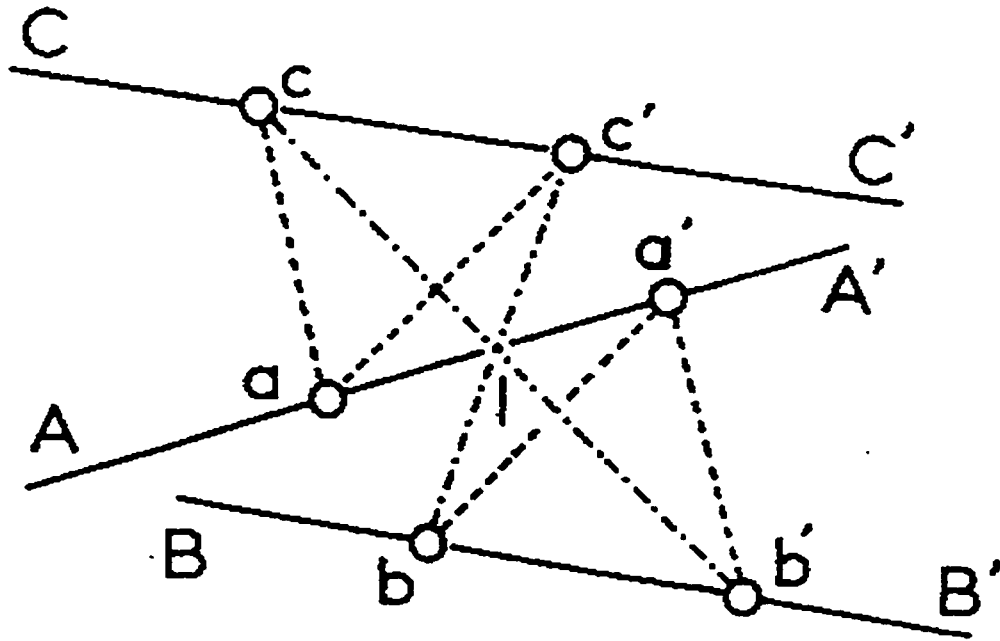


Figure 2.4: The effect of a non-magnetic impurity I in a tetragonal spinel. Three planes of spins are shown, the \hat{z} axis lying perpendicular to the planes. The interactions are restored between the spins at a, c and c', which would cancel in the pure material. In an indiluted system the coupling between spins *along* infinite chains AA', BB' and CC' is given by \mathcal{J} , that *between* chains by \mathcal{J}' . After Villain [2].

In his classic paper, Villain considers the effects of anisotropy and non-magnetic impurities on the ground states of classical spins otherwise described by a Heisenberg Hamiltonian. For a cubic spinel, the ground states of each tetrahedron (not all ground states) can be obtained by associating the four spins with two antiparallel pairs. An infinite number of ground states can be obtained by forming closed loops so that each bond is involved with only one loop and different loops are independent. Correlations are thus only short range and so the system behaves as a cooperative paramagnet. For a tetragonal spinel, pairs of nearest neighbour spins perpendicular to the tetragonal axis

\hat{z} form chains parallel to two orthogonal directions \hat{x} and \hat{y} , as shown in Fig. 2.4. There are two cases depending on the ratio of the coupling constants \mathcal{J} and \mathcal{J}' perpendicular and parallel to the \hat{z} axis: if $(\mathcal{J}/\mathcal{J}') < 1$, the chains are ferromagnetic and chains of two successive planes perpendicular to \hat{z} couple antiferromagnetically. In this case the ground state is non-degenerate, except under identical rotation of all spins. Alternatively, if $(\mathcal{J}/\mathcal{J}') > 1$, the chains are antiferromagnetic and interactions between chains cancel out; the ground state remains degenerate, but much less so than for the cubic system. Villain claims that a vanishingly small concentration of *non-magnetic* impurities suppresses the ground state degeneracy and transforms the system into a spin glass. The qualitative argument can be understood by considering Fig. 2.4. With no impurity present, infinite chains AA', BB' and CC' are decoupled. When an impurity is present, the chain AA' is broken. However, half chains A,C,C' are now coupled together, as well as A', B, B', since the interactions between chains no longer cancel. Therefore a small but finite number of impurities is sufficient to couple all the spins. The difference between cubic and tetragonal systems arises from the number of impurities necessary, believed to be approximately equal to the ground state entropy. The latter is proportional to N for a cubic spinel and to $N^{2/3}$ for a tetragonal spinel, where N is the number of spins, of the order of Avogadro's constant.

The theoretical arguments are similar for impurities alone. For a small concentration of non-magnetic impurities the system is expected to remain a cooperative paramagnet with degeneracy. However, if the system is sufficiently diluted such that no tetrahedra have 4 magnetic ions, only tetrahedra with 2 or 3 magnetic sites need to be considered. For one isolated tetrahedron with one non-magnetic impurity, a 120° structure is formed with no degeneracy, except under identical rotation of all spins. Then a spin glass is predicted, *i.e.* there are infinite range correlations between pairs of ions but the sample average does vanish at zero temperature when r goes to infinity. The above considerations are believed to be correct for Heisenberg or XY models. In Ising models the system is expected to remain a cooperative paramagnet for all impurity concentrations, because

tetrahedra with 3 magnetic ions still have a degenerate ground state.

Experimentally, the normal spinel ZnCr_2O_4 undergoes a transition to an antiferromagnetic state with a tetragonal distortion below $T_N=13$ K (Ref. [18]). However, the addition of defects like non-magnetic impurities stabilises a spin glass phase, as observed in $\text{ZnCr}_{1.6}\text{Ga}_{0.4}\text{O}_4$ [19]. The magnetic phase diagram of the $\text{ZnCr}_{2-x}\text{Ga}_{2-2x}\text{O}_4$ system has been mapped out using dc and ac-susceptibility, neutron diffraction and Mössbauer effect measurements [57], which show a *decrease* in the spin glass transition temperature with increasing non-magnetic Ga ion concentration. The normal spinel ZnFe_2O_4 has also recently been studied using neutron diffraction, ^{57}Fe and ^{67}Zn Mössbauer spectroscopy and μSR [17]. Short range correlations develop below ~ 100 K, which then coexist with the onset of long range anti-ferromagnetic order at 10.5 K. Partial inversion, where A atoms occupy a fraction of the B sites, introduces disorder which broadens the magnetic transition, but does not suppress the long range order. By contrast, an *increasing* spin glass ordering temperature occurs on dilution of $\text{SrCr}_{8-x}\text{Ga}_{4+x}\text{O}_{19}$ (Ref. [58]) with non-magnetic Ga ions.

More recently, Bramwell *et al.* [5] have also examined a classical Heisenberg pyrochlore lattice antiferromagnet with local planar single ion anisotropy:

$$\mathcal{H} = -\frac{1}{2}\mathcal{J}\sum_{j,k}\mathbf{S}_j\cdot\mathbf{S}_k - \mathcal{D}\sum_j(\mathbf{S}_j\cdot\mathbf{n}_j)^2. \quad (2.12)$$

The exchange coupling $\mathcal{J} < 0$ and $\mathcal{D} < 0$ is an anisotropy constant. The \mathbf{n}_j axes for each spin are parallel to the four threefold axes of the tetrahedra, *i.e.* the four $\langle 111 \rangle$ directions. The *zero temperature* ground state is predicted to be macroscopically degenerate and without long range order, as in the case $\mathcal{D} = 0$. The alternate case of $\mathcal{D} > 0$ gives rise to a non-degenerate four-sublattice ground state, as observed experimentally in FeF_3 . However, Monte Carlo simulations used to investigate the properties of the system for $\mathcal{D} < 0$ at *finite temperature* show that thermal fluctuations select a subset of the ground state manifold and induce a first order phase transition to a conventional Néel ground state. This behaviour is referred to as “order-by-disorder” [59]. At a small but finite temperature T^+ the system can explore various ground state configurations and their

corresponding low lying excitations. There are usually a greater number of softer and more easily excitable states associated with the ordered ground states than with the disordered ones. Therefore, the ordered states are preferentially selected by entropy considerations, the greater number of accessible states resulting in increased entropy or Boltzmann weights. In a quantum system zero point fluctuations can achieve the same effect. Villain's argument about impurities in Heisenberg spinels with tetragonal distortions could also apply to a system with local easy plane anisotropy.

2.2 Quantum spin 1/2 Heisenberg pyrochlore antiferromagnet

There are only a limited number of papers which discuss geometric frustration on the pyrochlore lattice from a quantum mechanical point of view. Harris *et al.* [6] used field theory techniques to examine a quantum spin 1/2 Heisenberg antiferromagnet with nearest neighbour interactions. It was found that quantum fluctuations lead to a state with static correlations not in $\langle \mathbf{S} \rangle$ but in $\langle \mathbf{S}(\mathbf{r}) \cdot \mathbf{S}(\mathbf{r} + \boldsymbol{\delta}) \rangle$, where $\boldsymbol{\delta}$ is the nearest neighbour vector. Correlations propagating around a hexagon of bonds spanning six corner sharing tetrahedra lead to critical fluctuations. There are symmetry breaking and long range static correlations which extend throughout the whole crystal. The pyrochlore lattice may be thought of as face centred cubic (fcc) with one "up" and one "down" tetrahedron per fcc unit cell, or in terms of one independent tetrahedron per unit cell, coupled by intertetrahedral bonds which are equal in strength to the intratetrahedral bonds. The ordered state is one in which, say, the "down" tetrahedra are disordered and the "up" tetrahedra are ordered. However these up-tetrahedra are not all ordered identically. Rather, 4 equivalent interpenetrating cubic sublattices are formed. On 3 of the sublattices dimers are formed according to the 3 ways of forming four spins into pairs. Sublattice 4 is disordered or randomly dimerised.

The field theory results are consistent with results using degenerate perturbation theory to analyse the ground state manifold. The unperturbed Hamiltonian is the highly degenerate manifold which results when the intertetrahedral bonds are neglected. The

perturbing Hamiltonian splits the ground state degeneracy. Quantum fluctuations are thus shown to play an essential role in the ordering.

Recent work by Canals *et al.* [7, 8] would at first glance seem to contradict that of Harris. The former papers claim that the ground state is a spin liquid with low energy excitations which are singlet to singlet transitions. To make the two results consistent, the static, long range dimer ordering would have to melt, presumably because the dimers become delocalised. Whether or not there were a gap in the excitation spectrum would distinguish the two states. Canals *et al.* calculated the density operator to third order in \mathcal{J}'/\mathcal{J} but were mainly interested in the spin-spin correlation functions, which were calculated up to the 16th neighbour. In fact, in this calculation it was assumed that there was no ordering of any kind; this is consistent with their results, which indicate very short range correlations. Dimer-type ordering cannot be excluded, but to study dimer ordering it would be necessary to calculate other types of correlation functions. Order parameters involving three or four spins cannot be tested with their method.

2.3 Spin 1/2 Ising pyrochlore: “spin ice”

In water ice the oxygen atoms form a hexagonal lattice (wurtzite structure). Of the 4 hydrogen atoms arranged tetrahedrally around each oxygen atom, two form strong covalent O–H bonds and are close to it to form a water molecule; the remaining two are hydrogen bonded and further removed. The arrangement of protons obeys the Bernal-Fowler ice rules [60], but need not be the same in each unit cell. In a crystal of $2N$ bonds there are 2^{2N} possible ways of arranging the protons, not all of which satisfy the ice rules. Out of $2^4=16$ ways of arranging the bonds around a single oxygen, only 6 satisfy this condition. The total number of allowed configurations is therefore of the order of $(6/16)^N 2^{2N} = (3/2)^N$. Experimentally, the associated residual entropy is found to be close to the theoretical value $S_0 = Nk \ln(3/2)$. Although the H disorder can be represented as configurational entropy, there is no clear violation of the third law of thermodynamics. This is because energy barriers of the order of 1 eV would have to be

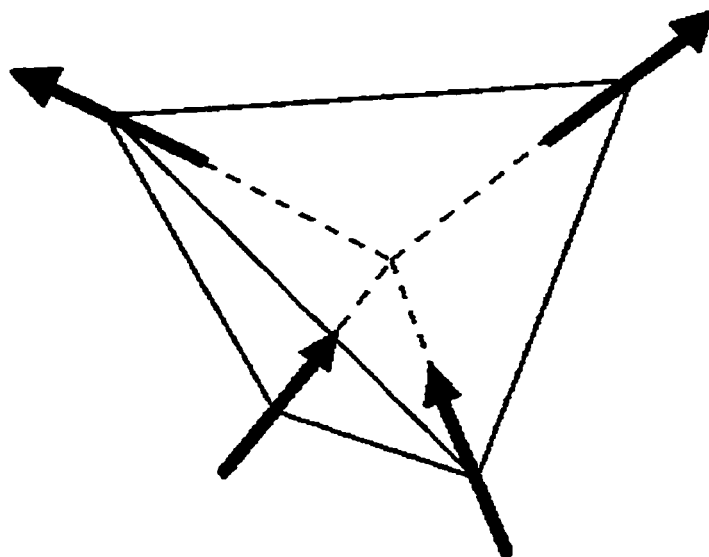


Figure 2.5: Ground state configuration of spins on a single tetrahedron given ferromagnetic interactions and strong easy axis anisotropy along the dashed lines.

surmounted to establish long range order in hydrogen ion position. As a result, relaxation through tunnelling into a lower entropy state is an extremely slow process below ice's freezing temperature and the system is therefore not in thermal equilibrium.

The only exact solutions of three-dimensional ice-type models are for very special "frozen" states [61]. Baxter considers only ice type models on a square lattice [62], but they exhibit similar behaviour. The hydrogen ion bonds between atoms form electric dipoles, so they can conveniently be represented by arrows placed on the bonds pointing towards the end occupied by the ion. The ice rule is then equivalent to saying that at each site there are two arrows in and two out, as shown in Fig. 2.5. Spin orientation thus plays a similar role to that of hydrogen position in ice and magnetic analogues of water ice, so called "spin ice" are currently of extreme interest. Moessner [63] shows that a strongly anisotropic classical Heisenberg model on the pyrochlore lattice can be

mapped onto an Ising pseudospin model with an exchange constant opposite in sign. To understand how this arises consider the case of strong anisotropy ($|\mathcal{J}/\mathcal{D}| \ll 1$): the second term in Eq. (2.12) dominates, constraining the spins to lie along the $\langle 111 \rangle$ axes. The first term defines the direction in which they point, such that the enclosing angle between any pair may only take on values of 70.5° or 109.5° with corresponding energies of $\pm \mathcal{J} \cos 70.5^\circ \approx \pm \mathcal{J}/3$. Now Ising pseudospin variables T_j may be assigned to the spins \mathbf{S}_j . If a given spin points out of the tetrahedron T_j is chosen to be $+1$ and conversely $T_j = -1$ for a spin pointing inwards. Equation (2.12) can now be rewritten as

$$\mathcal{H} = \frac{\mathcal{J}}{6} \sum_{j,k} T_j T_k - \mathcal{D}N, \quad (2.13)$$

where N is the total number of spins in the system. The second term becomes a constant, but more importantly, the sign of the exchange interaction has been reversed and in addition, an anisotropic Heisenberg model has been converted into an Ising model.

The ground states of the anisotropic frustrated *ferromagnet* are separated by large energy barriers. The energy of a single tetrahedron can be minimised with two spins in and two spins out. There are 6 ways of arranging 4 spins satisfying such a constraint — the whole system thus has finite entropy per spin down to $T = 0$. By contrast, strong anisotropy in a pyrochlore Heisenberg *antiferromagnet* may be described by a ferromagnetic Ising model, which appears unfrustrated. The frustration cannot actually be removed, but the anisotropy lifts the ground state degeneracy completely. Such a relieved antiferromagnet should be simply described by a unique long range ordered state at low temperatures and the dynamics by spin wave excitations. However, this is not the case for large values of $|\mathcal{D}/\mathcal{J}|$. If the system is cooled down quickly or in an applied magnetic field, it will be trapped in a metastable state at $T \sim |\mathcal{D}|$, which is separated from the ground state by large energy barriers. This occurs before the magnetic ordering temperature may be reached, at temperatures of the order of \mathcal{J} . By contrast, for small $|\mathcal{D}/\mathcal{J}|$, freezing does not occur because the system is then well approximated by an isotropic Heisenberg antiferromagnet. Long range correlations are thus absent, as described in Section 2.1 and there are neither internal nor free energy barriers to

overcome as the temperature is lowered through \mathcal{J} down to the ordering temperature below $|\mathcal{D}|$.

Bramwell and Harris [64] present Monte Carlo simulations of the susceptibility for a number of models. The unfrustrated models, namely the “up-down” Ising spin model with ferromagnetic interactions, and the antiferromagnetically coupled “in-out” model where there are four local $\langle 111 \rangle$ anisotropy axes, show evidence of the expected phase transition at $T/|\mathcal{J}| = 4$. The $\langle 111 \rangle$ Ising ferromagnet shows deviations from Curie like behaviour below $T/|\mathcal{J}| = 10$, but the susceptibility diverges only at $T = 0$, as expected for a paramagnet. This reflects the presence of a significant number of magnetised states in the degenerate ground state manifold. The up-down Ising antiferromagnet does however show evidence of a peak in susceptibility, as the spins settle into their local ground states.

Experimentally, the magnetic ions in a number of pyrochlores have recently been found to be subject to significant single ion anisotropies, whose local easy axis is along the $\langle 111 \rangle$ directions and which are thus candidates for spin ice behaviour. Heat capacity measurements on $\text{Dy}_2\text{Ti}_2\text{O}_7$ [65] are in good agreement with Pauling’s prediction [66]: there is missing entropy between 0.2 and 12 K compared to the value of $R \ln 2$ expected for the ground state doublet. Instead, a value close to $R(\ln 2 - 1/2 \ln 3/2)$ is observed, consistent with the prediction of Pauling for ice. Susceptibility measurements [67] do not show the sharp cusp expected for a spin glass, but rather a broad feature peaked at $T = 0.7$ K. Sharp peaks in the specific heat do however develop on application of a magnetic field.

To date, the most extensively studied spin ice material is $\text{Ho}_2\text{Ti}_2\text{O}_7$ [68, 69]. The Ho^{3+} ion is Ising like due to crystal field splittings which result in a ground state doublet with $J_z = \pm 8$. Neutron scattering measurements indicate that no long range order develops down to temperatures of at least 0.35 K in zero magnetic field, but instead, short range ferromagnetic correlations are observed. The idea which seems to be emerging is that there is no phase transition to a spin glass state, for example, but rather a continuous slowing down of spin fluctuations as the temperature is reduced, due to the development

of energy barriers. A number of ordered phases have also been observed on application of a magnetic field, as well as history dependent behaviour. Monte Carlo simulations by Harris *et al.* [70] show that the degree of degeneracy breaking depends on the direction of the applied field relative to the crystal axes.

The typically large magnetic moments associated with the rare earth oxide pyrochlores raise another issue. Given local Ising axes along the $\langle 111 \rangle$ directions, the magnitude of the dipole-dipole interaction between nearest neighbours is given by $D_{nn} = (5/3)$ times the usual estimate of the dipole energy, $(\mu_0/4\pi)g^2\mu^2/r_{nn}^3$, comparable with the exchange interaction. Competing dipolar and superexchange interactions were first studied within a spin-ice type model by Siddharthan *et al.* [71] using Monte Carlo simulations. The dipole-dipole interaction was truncated beyond the fifth nearest neighbour in this work. In subsequent studies [72] den Hertog and Gingras argue that due to the long range nature of this interaction the truncation can lead to misleading results. They therefore use Ewald summation techniques to consider the effect of infinite range dipolar interactions. They present Monte Carlo simulations and mean field analysis which shows that spin ice behaviour persists in the presence of AF exchange up to $\mathcal{J}_{nn}/\mathcal{D}_{nn} \sim -0.91$. For smaller values there is a second order phase transition to the doubly degenerate $\mathbf{q} = 0$ phase of the nearest neighbour AF exchange only model, where all spins either point in or out of a tetrahedron.

Chapter 3

The Pyrochlore Environment

3.1 Sample Preparation and Characterisation

Pyrochlores are face centred cubic in structure with space group $Fd\bar{3}m$ (no. 227). The compounds studied in this thesis have a general formula $A_2^{3+}B_2^{4+}O_6^{2-}O'$, though other oxidation states of the A and B site ions are possible. A is generally a rare earth ion; B a transition metal. The symbol O' indicates an O^{2-} ion in a crystallographically different site. There are 8 formula units per conventional unit cell; the coordinates of the various ions are listed in Table 3.3. The ions on the 16d site form a network of corner sharing tetrahedra; the 16c sites constitute an identical sublattice, displaced by $(\frac{1}{2}, \frac{1}{2}, \frac{1}{2})$. B^{4+} ions occupy the 16c site, A^{3+} ions the 16d site. The structure is built up of slightly distorted BO_6 octahedra and AO_8 distorted cubes, as shown in Figure 3.6. It will be convenient to redefine the four $\langle 111 \rangle$ axes as the \hat{z} axis in the crystal field calculations described in the next section. Using this natural axis of symmetry, the B ion is then surrounded by 3 oxygen ions forming a triangle in a plane above it and three below, all equidistant. The A ion is surrounded by 6 equidistant oxygens which form a puckered hexagon in the $\hat{x} - \hat{y}$ plane, as well as 2 more which lie on the $\pm \hat{z}$ axis, at slightly greater distances. However, the precise positions of the oxygen anions depend on the parameter x , as can be seen in Fig. 3.7. At two extremes in the value of x of 0.3125 (5/16) and 0.375 (3/8), there is respectively perfect octahedral symmetry about B or regular cubic coordination around A. $Y_2Mo_2O_7$ is a semiconductor with a small band gap of 0.013 eV [73], while the titanate pyrochlores are highly insulating.

Ion	Location	Site symmetry	Coordinates
16A	16d	$\bar{3}m(D_{3d})$	$(0,0,0; 0, \frac{1}{2}, \frac{1}{2}; \frac{1}{2}, 0, \frac{1}{2}; \frac{1}{2}, \frac{1}{2}, 0) +$ $\frac{1}{2}, \frac{1}{2}, \frac{1}{2}; \frac{1}{2}, \frac{1}{4}, \frac{1}{4}; \frac{1}{4}, \frac{1}{2}, \frac{1}{4}; \frac{1}{4}, \frac{1}{4}, \frac{1}{2};$
16B	16c	$\bar{3}m(D_{3d})$	$0,0,0; 0, \frac{1}{4}, \frac{1}{4}; \frac{1}{4}, 0, \frac{1}{4}; \frac{1}{4}, \frac{1}{4}, 0;$
48O	48f	$mm(C_{2v})$	$x, \frac{1}{8}, \frac{1}{8}; \bar{x}, \frac{7}{8}, \frac{7}{8}; \frac{1}{4} - x, \frac{1}{8}, \frac{1}{8}; \frac{3}{4} + x, \frac{7}{8}, \frac{7}{8};$ $\frac{1}{8}, x, \frac{1}{8}; \frac{7}{8}, \bar{x}, \frac{7}{8}; \frac{1}{8}, \frac{1}{4} - x, \frac{1}{8}; \frac{3}{4} + x, \frac{7}{8};$ $\frac{1}{8}, \frac{1}{8}, x; \frac{7}{8}, \frac{7}{8}, \bar{x}; \frac{1}{8}, \frac{1}{8}, \frac{1}{4} - x; \frac{7}{8}, \frac{7}{8}, \frac{3}{4} + x;$
8O'	8b	$\bar{4}3m(T_d)$	$\frac{3}{8}, \frac{3}{8}, \frac{3}{8}; \frac{5}{8}, \frac{5}{8}, \frac{5}{8}$

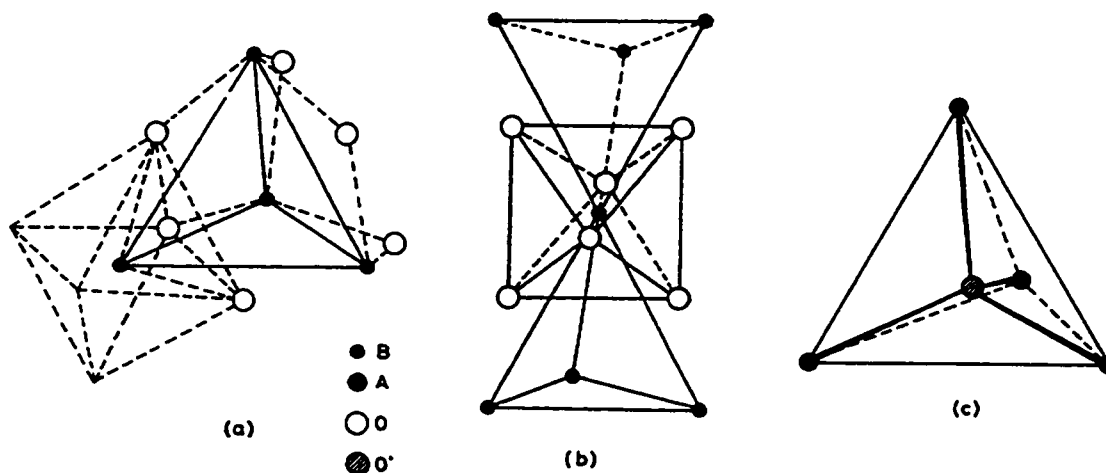
Table 3.3: Pyrochlore ($A_2B_2O_6O'$) Structure Data (Origin at B Site).

Figure 3.6: Description of the pyrochlore structure from Pannetier and Lucas [76]. a) B tetrahedra with 48f oxygen outside. b) Corner shared B tetrahedra indicating the octahedral oxygen coordination around each B ion. c) A ion tetrahedron showing central O' ion with near perfect tetrahedral angles.

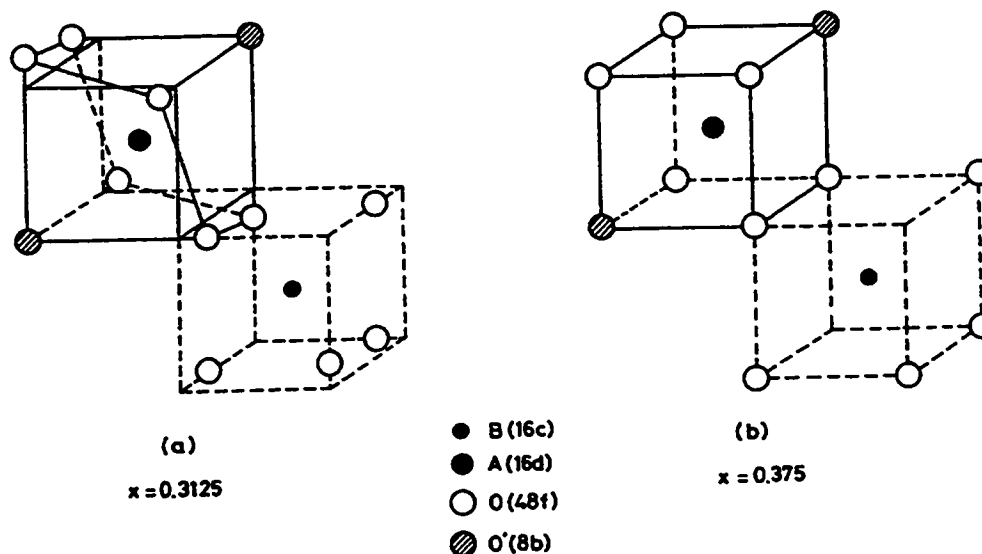


Figure 3.7: Change in shape of coordination polyhedra of A and B ions with 48f oxygen parameter x . After Faucher and Caro [77].

All the polycrystalline pyrochlore samples studied were made by N. P. Raju at McMaster University, using a solid state reaction. To ensure all water had been removed, high purity R_2O_3 powders (99.99%) were pre-fired at 1000°C for 5 hours and cooled down to room temperature before weighing them. R_2O_3 and MoO_2 powders were taken in stoichiometric proportion, mixed thoroughly and pressed into pellets. These pellets were then heated in an alumina crucible at 1400°C for 24 hours in an argon atmosphere before cooling to room temperature. This procedure was repeated until X-ray diffraction patterns revealed only a single phase.

X-ray [78] and powder neutron scattering measurements [79] on $Y_2Mo_2O_7$ indicate the crystal structure is consistent with a fully ordered pyrochlore model. From Rietveld profile refinements of neutron diffraction measurements [80], one can say the concentration of oxygen vacancies, likely the main source of crystalline disorder in these materials, is below the detectable limit of 1%. Hubert [81] has suggested that the O' atoms may be disordered over the 32e sites. Including this did not significantly improve Rietveld profile refinements. A distribution of O' over the 8b and normally vacate 8a sites [82] also gives

Material	Cubic Lattice Parameter (Å)	Oxygen parameter x
$\text{Y}_2\text{Mo}_2\text{O}_7$	10.232	0.338
$\text{Y}_2\text{Ti}_2\text{O}_7$	10.095	0.328
$\text{Gd}_2\text{Ti}_2\text{O}_7$	10.185	0.322
$\text{Tb}_2\text{Ti}_2\text{O}_7$	10.152	
$\text{Tm}_2\text{Ti}_2\text{O}_7$	10.054	

Table 3.4: Lattice constants and 48f oxygen parameter x of selected $\text{A}_2^{3+}\text{B}_2^{4+}\text{O}_6\text{O}'$ pyrochlores. Values from Ref. [74].

no significant improvement. Direct evidence for positional disorder between Y and Mo is difficult to obtain because of the similarity in their neutron scattering cross sections. However, there is indirect evidence in that the bond angles and lengths are comparable to similar materials. Significant disorder would imply intermediate bond lengths to those observed. Since the ionic radii of Y^{3+} and Mo^{4+} are very different, there should be no admixing between the 16c and 16d cations. This is confirmed by analysis of X-ray data. It should be pointed out that the Mo ion has a substantially enhanced thermal or Debye-Waller factor, which could be due to an unusually low Debye temperature or to static positional displacements not well analysed by standard Rietveld profile refinement. Recent x-ray absorption fine structure (XAFS) measurements by Booth *et al.* [83] suggest that it is due to disorder on the level of $\sim 5\%$ in the Mo-Mo *pair distances* at approximately right angles to the Y-Mo pairs.

The sample of AuFe (0.5% at.) described in this thesis (see Chapter 6) was provided by J. L. Tholence (LEPES-CNRS, France). This material is usually made by induction or arc melting [84, 85, 86]. This particular specimen had been stored at room temperature for several years. It is well known that the spatial distribution of the magnetic impurities in archetypal spin glass alloys is of crucial importance in determining the number and type of magnetic interactions or bonds. Morgownik and Mydosh [87] have shown that the distribution of Fe or Mn impurities in Cu, Pt and Au metallic hosts is non-random

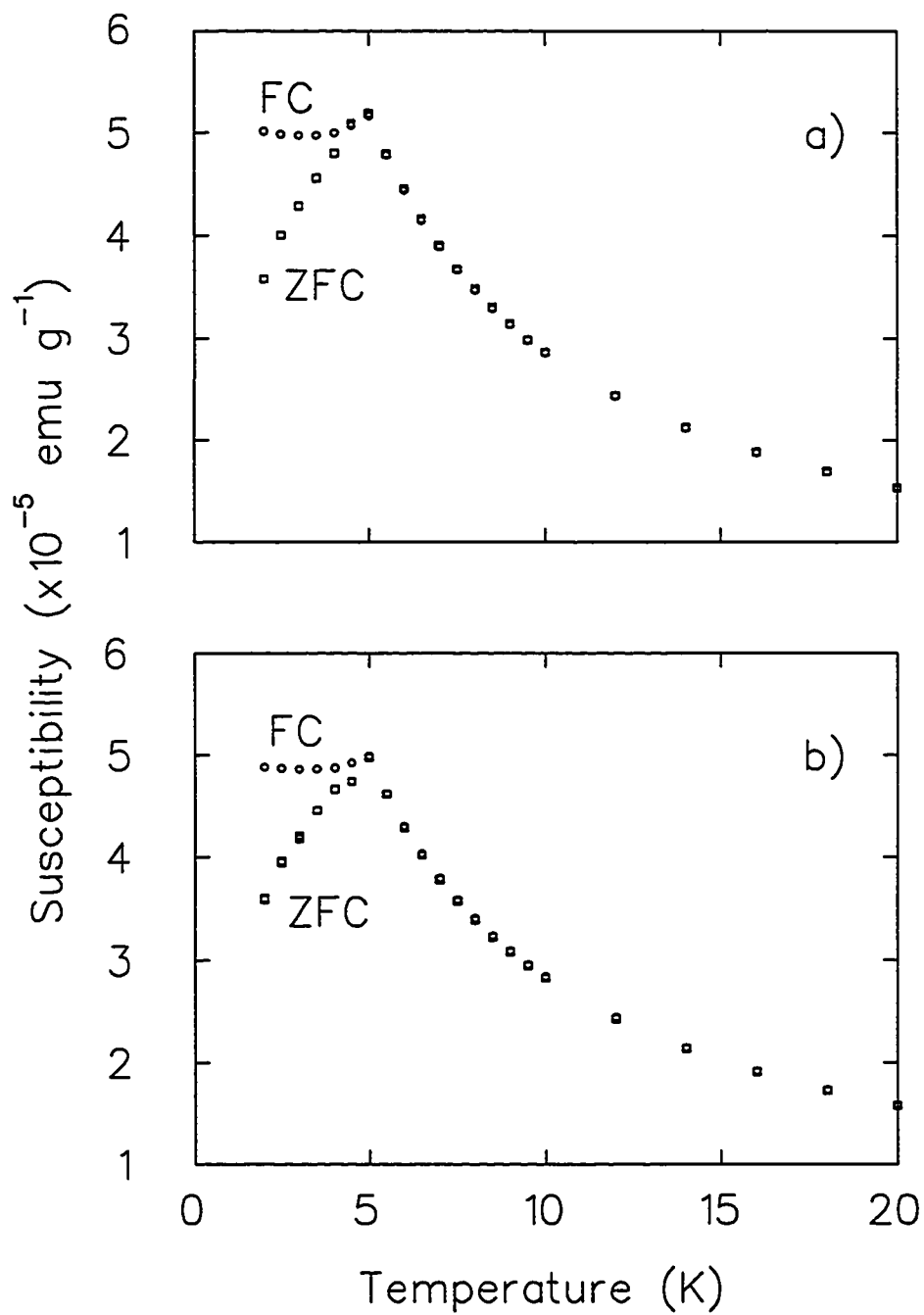


Figure 3.8: The static susceptibility of $AuFe$ (0.5% at.) versus temperature in a magnetic field of 0.001 T, a) before and b) after annealing at 900° C for 24 hours and quenching.

and further that the atomic short range order influences the magnetic phase diagram. In addition, ageing, or the dependence of measured properties on the temperature and magnetic field history of the sample is an unavoidable phenomenon in spin glasses. This is due to the non-equilibrium behaviour of these materials. With these ideas in mind, a series of susceptibility measurements were carried out. Initially the sample was zero field cooled (ZFC) from 30 K before applying a magnetic field of 0.001 T. The measurements were then taken on warming. Subsequently it was field cooled from 200 K and the susceptibility again recorded on warming. As can be seen in Fig. 3.8a, the characteristic ZFC cusp in the dc susceptibility and the difference between FC and ZFC measurements are apparent, despite having been stored at ~ 300 K for such an extended period. One might have anticipated that diffusion of Fe atoms to form clusters would affect its macroscopic behaviour. The alloy was then sealed under vacuum in a quartz tube (see Fig. 3.9) and annealed at 900° C for 24 hours, before being quenched in ice water and repeating the SQUID measurements, shown in Fig. 3.8b. There are only very subtle differences compared to Fig. 3.8a. Nevertheless, after rolling the sample into a ~ 0.25 mm foil more suitable for μ SR measurements, the annealing and quenching process was repeated and the sample stored in liquid nitrogen until the experiments took place.

3.2 Crystal electric field effects

The energy scale for the cooperative phenomena observed in a magnetic system is usually a function of the strength of the spin-spin coupling. However, in general there are a number of other stronger interactions which set the energy levels of a multi-electron atom. The Coulomb interaction of an electron with its nucleus and with the other electrons, suitably averaged such that it has central symmetry, gives rise to electronic shells *e.g.* $3d^3$. Single electron spin-orbit coupling is most simply described by a Hamiltonian of the form

$$\mathcal{H}_{ls} = \xi(\mathbf{l} \cdot \mathbf{s}). \quad (3.14)$$

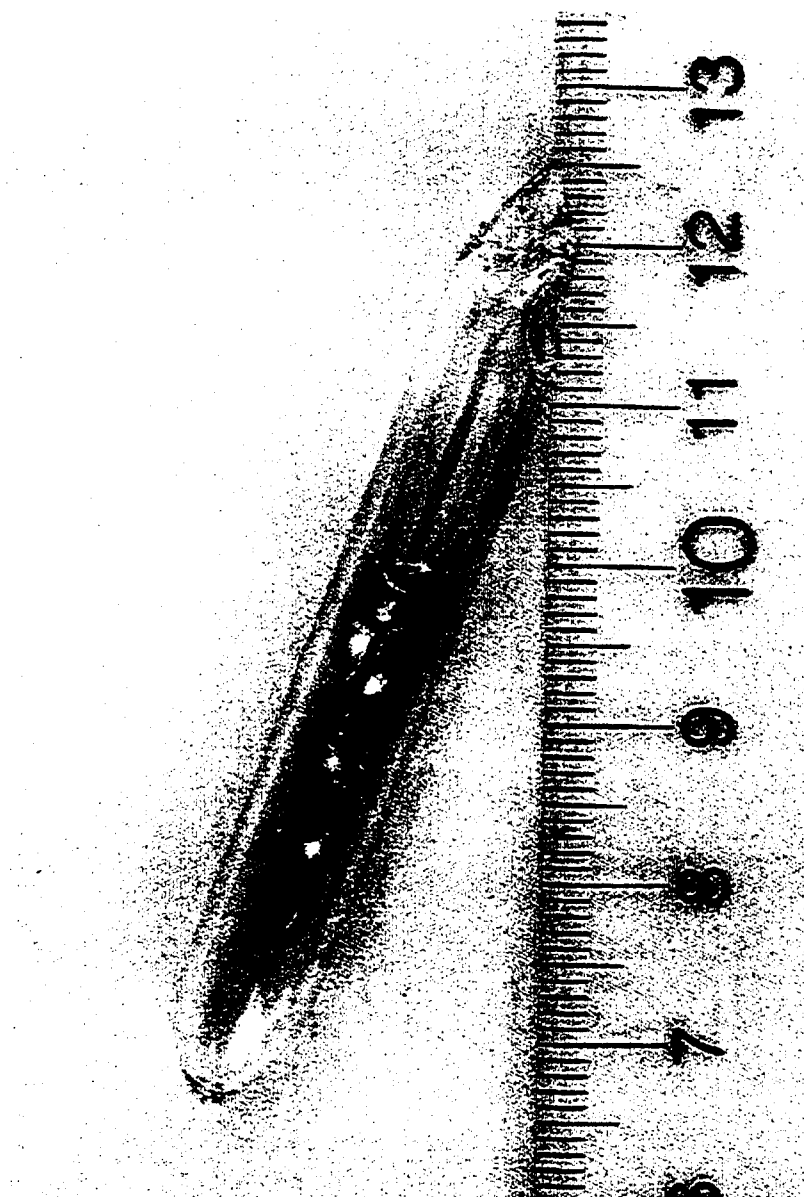


Figure 3.9: AuFe (0.5% at.) foil sealed under vacuum in a quartz tube. (S. R. Dunsiger)

Assuming the electron spin-orbit coupling is negligible compared with intra-atomic electron-electron Coulomb interactions, a reasonable approximation for light atoms, the ground state is described by Hund's rules. In this case, to a good approximation the Hamiltonian of the atom or ion obeys Russel-Saunders or LS coupling, where J , L and S are all good quantum numbers. For multi-electron atoms in their ground state and where Hund's rules are applicable, LS coupling is described by an equation of the form

$$\lambda \mathbf{L} \cdot \mathbf{S} \equiv \pm \frac{\xi}{2S} \mathbf{L} \cdot \mathbf{S} \quad (3.15)$$

where the $+$ and $-$ signs are appropriate for electron shells which are respectively less than or more than half full. Typically, λ is 10 - 100 meV for transition group ions and 100 - 1000 meV for rare earths.

Crystalline electric field effects, due to the interaction of an ion with surrounding ligands, can be treated as a perturbation on the free single ion wave functions and energy levels. To estimate the energy levels and eigenfunctions of the ion in the crystalline field the matrix elements of the perturbing Hamiltonian between free ion states are evaluated. The free ion wave functions used will depend on the relative size of the crystal field Hamiltonian and the intra-ionic interaction energies. The crystal electric field affects closed shells of electrons and S state ions only in a high order of perturbation theory. At the other extreme, crystal electric field effects are large compared to the spin-orbit coupling in $3d$ transition metals and thus interact with the orbital angular momentum only, lifting the $2L + 1$ degeneracy of the eigenstates $|L, S, L_z, S_z\rangle$ which characterise the isolated ion. In $4d$ and $5d$ ions, the ligand fields are larger still, Hund's rules are no longer appropriate and single electron states must be used. In this case the ions are all in the so called "strong ligand field" regime. By contrast, in the "weak ligand field regime", the $4f$ electrons in rare earths are subject to spin-orbit couplings much larger than the crystal electric fields. The free ion is thus characterised by eigenfunctions $|L, S, J, J_z\rangle$.

The crystal electric field calculations described in this section are based on the point charge ionic model discussed by Hutchings [88]. Given a magnetic ion at the origin, the

potential V due to k surrounding point charges q_j at \mathbf{R}_j is given by a Coulomb potential

$$V(r, \theta, \phi) = \sum_{j=1}^k \frac{q_j}{|\mathbf{R}_j - \mathbf{r}|}. \quad (3.16)$$

It is convenient to write the crystalline electric potential in terms of spherical harmonics as it is easier to calculate the matrix elements of the the potential energy in this form.

$$V(r, \theta, \phi) = \sum_{n=0}^{\infty} \sum_{\alpha} \sum_{j=1}^k r^n \frac{4\pi}{2n+1} q_j \frac{Z_{n\alpha}(\theta_j, \phi_j)}{R_j^{(n+1)}} Z_{n\alpha}(\theta, \phi) \quad (3.17)$$

$$= \sum_{n=0}^{\infty} \sum_{\alpha} \gamma_{n\alpha} r^n Z_{n\alpha}(\theta, \phi) \quad (3.18)$$

where $Z_{n\alpha}$ are tesseral harmonics, or linear combinations of spherical harmonics. Using the Stevens' "operator equivalents" method, the crystalline electric field Hamiltonian is given by

$$\begin{aligned} \mathcal{H} &= \sum_i q_i V(x_i, y_i, z_i) \\ &= \sum_n \sum_m [-Q \gamma_n^m Z_{coeff}(r^n) \Theta_n] O_n^m, \end{aligned}$$

where the sum i is over the magnetic electrons; Q is the charge of the magnetic ion. The Stevens' operator equivalents, matrices which transform under rotation in the same way as the potential, are denoted by O_n^m . These matrices are tabulated in the article by Hutchings, as are the coefficients Z_{coeff} of the tesseral harmonics. The quantities in the square brackets are known as the "crystal field parameters" and the operator equivalent Hamiltonian is often written as

$$\mathcal{H} = \sum_n \sum_m B_n^m O_n^m, \quad (3.19)$$

which is usually fitted to experimental data, allowing the coefficients B_n^m to vary.

The potential reflects the point symmetry of the lattice site in question. All terms of order $n > 2l$, where l is the orbital quantum number of the single magnetic electrons, vanish. The "operator equivalent" method is really an application of the Wigner-Eckart theorem, where functions of \hat{x} , \hat{y} and \hat{z} are replaced by operators J_x , J_y and J_z , allowing for their commutation rules.

Point charge calculations were performed for the Mo^{4+} ion on the B site of the pyrochlore and the Tb^{3+} ion on the A site, using the appropriate Stevens' operator equivalents given the spin and orbital angular momentum of each ion, as listed in Table 3.8. As noted above, the $\langle 111 \rangle$ directions are natural axes of symmetry for both A and B ions in their distorted cubic crystalline environments. For the Mo^{4+} ion the crystal field Hamiltonian has terms

$$\mathcal{H} = B_2^0 O_2^0 + B_4^0 O_4^0 + B_4^3 O_4^3, \quad (3.20)$$

while for Tb^{3+} it is of the form

$$\mathcal{H} = B_2^0 O_2^0 + B_4^0 O_4^0 + B_4^3 O_4^3 + B_6^0 O_6^0 + B_6^3 O_6^3 + B_6^6 O_6^6. \quad (3.21)$$

The Y^{3+} ion has the electronic configuration of krypton, *i.e.* a closed shell structure and is therefore diamagnetic. On the other hand, the Mo^{4+} ion has an electronic configuration resulting in a spin $S = 1$ and an orbital angular momentum $L = 3$ by Hund's first and second rules. The palladium ($4d$) group has been less thoroughly studied than the $3d$ group of transition metals, mainly because their compounds are more involved to prepare. The wave functions for $4d$ electrons have the same angular dependence as $3d$ electrons but are more extended radially. However, near the nucleus the radial part of the wavefunction increases rapidly with atomic number. Since the coupling parameter ξ for spin-orbit interactions depends on the amplitude of the wavefunction, this effect becomes more important. Blume *et al.* [89] have calculated ξ to be 950 cm^{-1} for the Mo^{4+} ion. Unfortunately, radial expectation values for the $4+$ oxidation state of this ion are not available. Values for Mo^{3+} [90] are listed in Table 3.9. It is these values which have been used in the calculation described.

The strong ligand field approach appropriate to the $4d^2$ ion in an octahedral field is discussed by Abragam and Bleaney [91]. For this particular ion both strong and weak field approaches predict an orbital triplet. The 3F_2 ground state constructed from Hund's rules for the isolated ion become mixed with a 3P excited state. Adding in the effect of the trigonal distortion to the cubic crystal electric field (CEF) Hamiltonian leads

Eigenvalues (THz)	L_z	3	2	1	0	-1	-2	-3
1783.84		-0.541476	0	0	-0.643123	0	0	0.541476
-1119.87		-0.454757	0	0	0.765763	0	0	0.454757
-809.784		0	0.80313	0	0	-0.595803	0	0
-809.784		0	0	-0.595803	0	0	-0.80313	0
582.842		-0.707107	0	0	0	0	0	-0.707107
186.38		0	0.595803	0	0	0.80313	0	0
186.38		0	0	0.80313	0	0	-0.595803	0

Table 3.5: Eigenvalues and corresponding eigenvectors of the CEF Hamiltonian of the Mo^{4+} ion in its pyrochlore environment.

Eigenvalues (THz)	\tilde{L}_z		S_z		0	0	0	-1	-1	-1	-1	-1
	1	1	0	-1								
327.214	0.703	0	0	0	-0.107	0	0	0	0	0	0	0
323.412	0.707	0	0	0	0	0	0	0	0	0	0	-0.707
312.080	0	0	0	0.080	0	0	0	0	0	0	-0.997	0
312.080	0	-0.997	0	0	0	0.080	0	0	0	0	0	0
296.762	0	0	0	0	0	0	0	0	0	0	0	0
296.762	0	0	0	0	0	0	0	1.	0	0	0	0
-3.802	-0.076	0	0	0	-0.994	0	0	0	0	0	0	-0.076
-1.993	0	0	0	-0.997	0	0	0	0	0	0	-0.080	0
-1.993	0	-0.080	0	0	0	-0.997	0	0	0	0	0	0

Table 3.6: Eigenvalues and corresponding eigenvectors of the combined CEF and spin-orbit interaction Hamiltonians applied to the Mo⁴⁺ ion in its pyrochlore environment.

Eigenvalues (THz)	J_z	6	5	4	3	2	1	0	-1	-2	-3	-4	-5	-6
4.891	0.018	0	0	-0.134	0	0	0.981	0	0	0.136	0	0	0.033	0
4.107	0	0.153	0	0	-0.975	0	0	-0.156	0	0	-0.031	0	0	0
4.080	0	0.009	0	0	-0.113	0	0.982	0	0	0.151	0	0	0	0
-3.733	0	-0.968	0	0	-0.223	0	-0.034	0	0	0.113	0	0	0	0
-3.727	0	0	0.046	0	0	0.002	0	0.222	0	0	-0.974	0	0	0
-3.377	0	0	0.987	0	0	0.154	0	-0.002	0	0	0.047	0	0	0
-3.375	0	0.120	0	0	0.002	0	-0.151	0	0	0.981	0	0	0	0
1.990	0	-0.222	0	0	0.968	0	0.107	0	0	0.041	0	0	0	0
1.959	0	0	-0.016	0	0	0.158	0	-0.963	0	0	-0.219	0	0	0
-1.772	-0.461	0	0	-0.692	0	0	-0.032	0	0	-0.462	0	0	0.308	0
-1.750	0.308	0	0	0.451	0	0	0.136	0	0	-0.686	0	0	0.460	0
0.364	-0.737	0	0	0.490	0	0	0.032	0	0	0.257	0	0	0.387	0
0.342	-0.386	0	0	0.244	0	0	0.132	0	0	-0.481	0	0	-0.737	0

Table 3.7: Eigenvalues and corresponding eigenvectors of the CEF Hamiltonian of the Tb^{3+} ion in its pyrochlore environment.

to an orbital singlet. Starting from a 3F_2 state, essentially assuming an intermediate ligand field, the eigenvalues and eigenfunctions of the CEF Hamiltonian are presented in Table 3.5. The effect of spin-orbit coupling on the three lowest CEF energy levels is incorporated using Eq. (3.15) with an effective orbital angular momentum operator \tilde{L} . Its matrix elements are written in terms of the 3 CEF eigenvectors lowest in energy. As shown in Table 3.6, diagonalising the transformed spin-orbit interaction Hamiltonian, the degeneracy of the spin triplet is broken into a doublet and singlet with the singlet lowest. Details of the calculation, implemented with a MATHEMATICA [92] code, are given in Appendix A.

There is little experimental information available on the $3d^2$ ion in an octahedral field to allow comparison. However, the vanadium ammonium alum $V(NH_4)(SO_4)_2$ is also thought to have a local octahedral structure with a small trigonal distortion [93]. Susceptibility measurements are consistent with the author's calculations, indicating an orbital singlet ground state. The three fold spin degeneracy is similarly split by second order effects like spin-orbit coupling.

The results of point charge CEF calculations on the Tb^{3+} ion in its pyrochlore environment are summarised in Table 3.7. While group theory arguments predict either a singlet or non-magnetic doublet for this ion in an cubic field [94], the author's calculation, which includes the trigonal distortion, indicates the ground state doublet is predominantly made up of $J_Z = \pm 5$, whereas the first excited doublet is mostly $J_Z = \pm 4$. The oxygen and terbium charge, as well as the oxygen parameter x have been adjusted to reproduce the results of inelastic neutron scattering measurements on this material, described in Chapter 8. Figures. 3.10, 3.11 and 3.12 illustrate the effect of varying each of these parameters. A more sophisticated *ab initio* calculation of the crystal field parameters has been carried out by Gingras *et al.* [95]. The lowest energy and first excited state doublets are found to have large ($\sim 90\%$) $J_Z = \pm 4$ and $J_Z = \pm 5$ components respectively. Note the order is reversed from the simpler calculation above. The point charge model has several weaknesses: it neglects the finite extent of the charges on the ions; the overlap of the

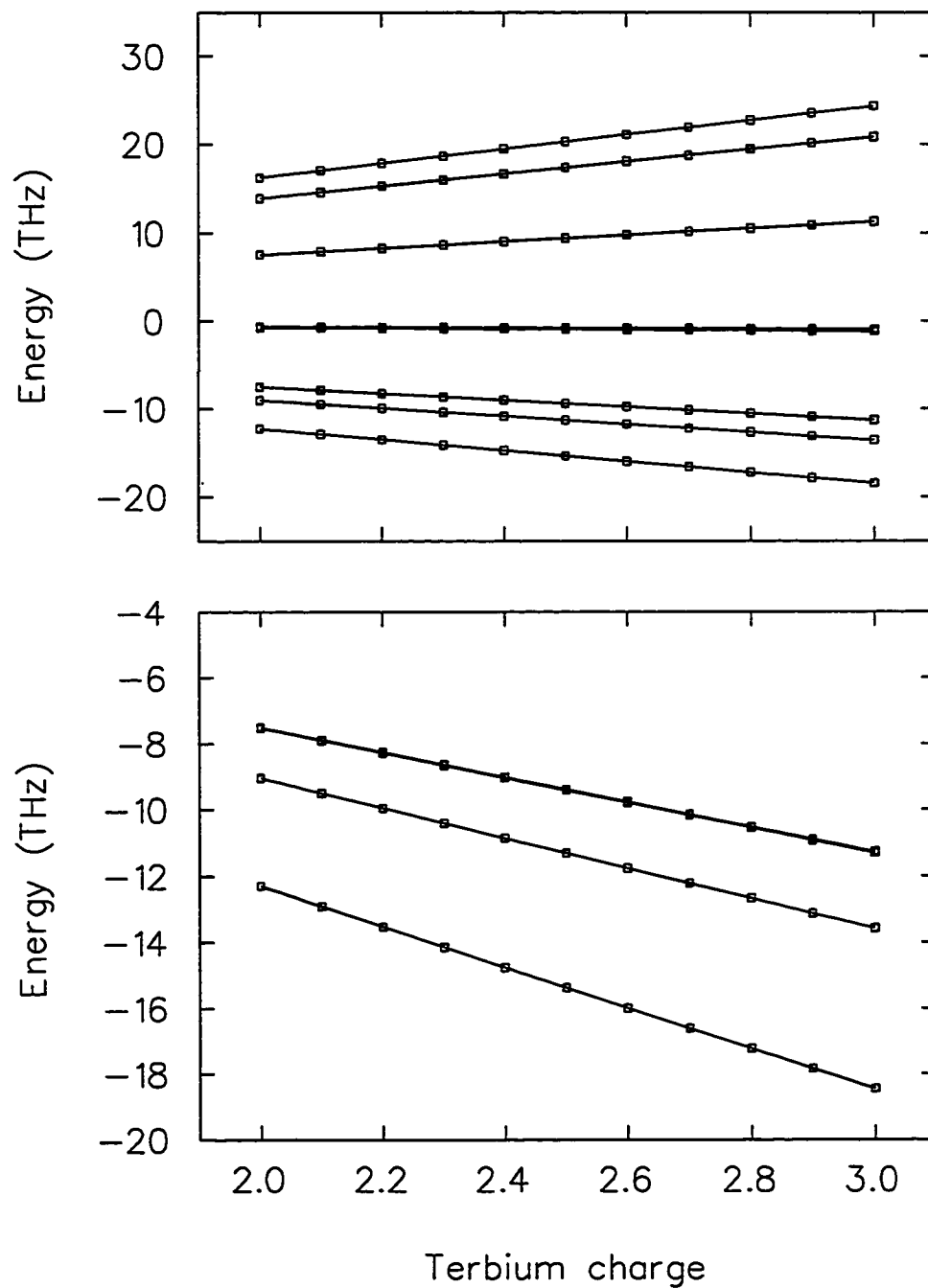


Figure 3.10: The effect of varying terbium ion charge on its CEF energy level splittings. The lower box shows the 3 lowest doublets on an expanded scale.

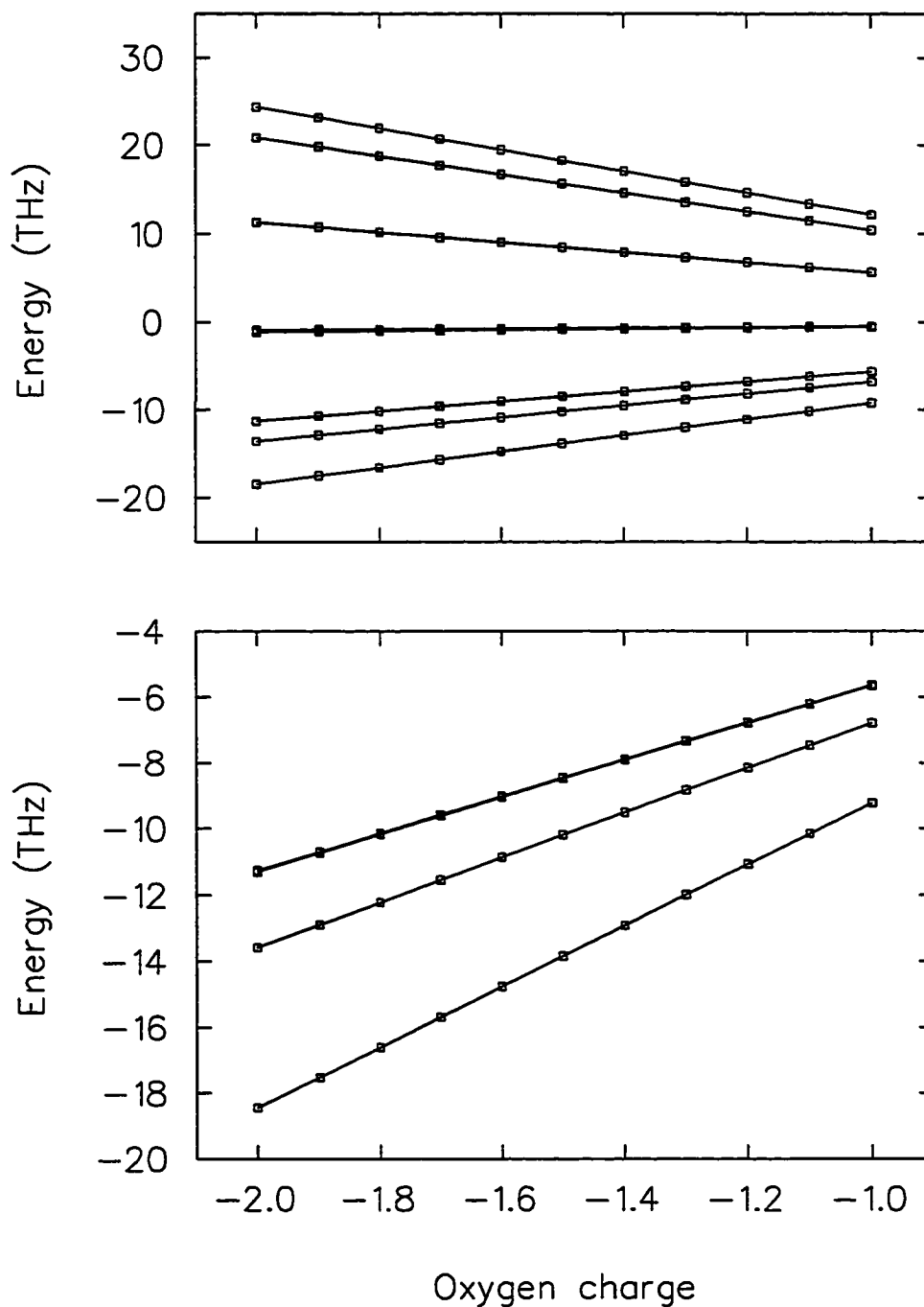


Figure 3.11: The effect of varying the charge of the surrounding oxygen ions on the CEF energy level splittings of the Tb^{3+} ion. The lower box shows the 3 lowest doublets on an expanded scale.

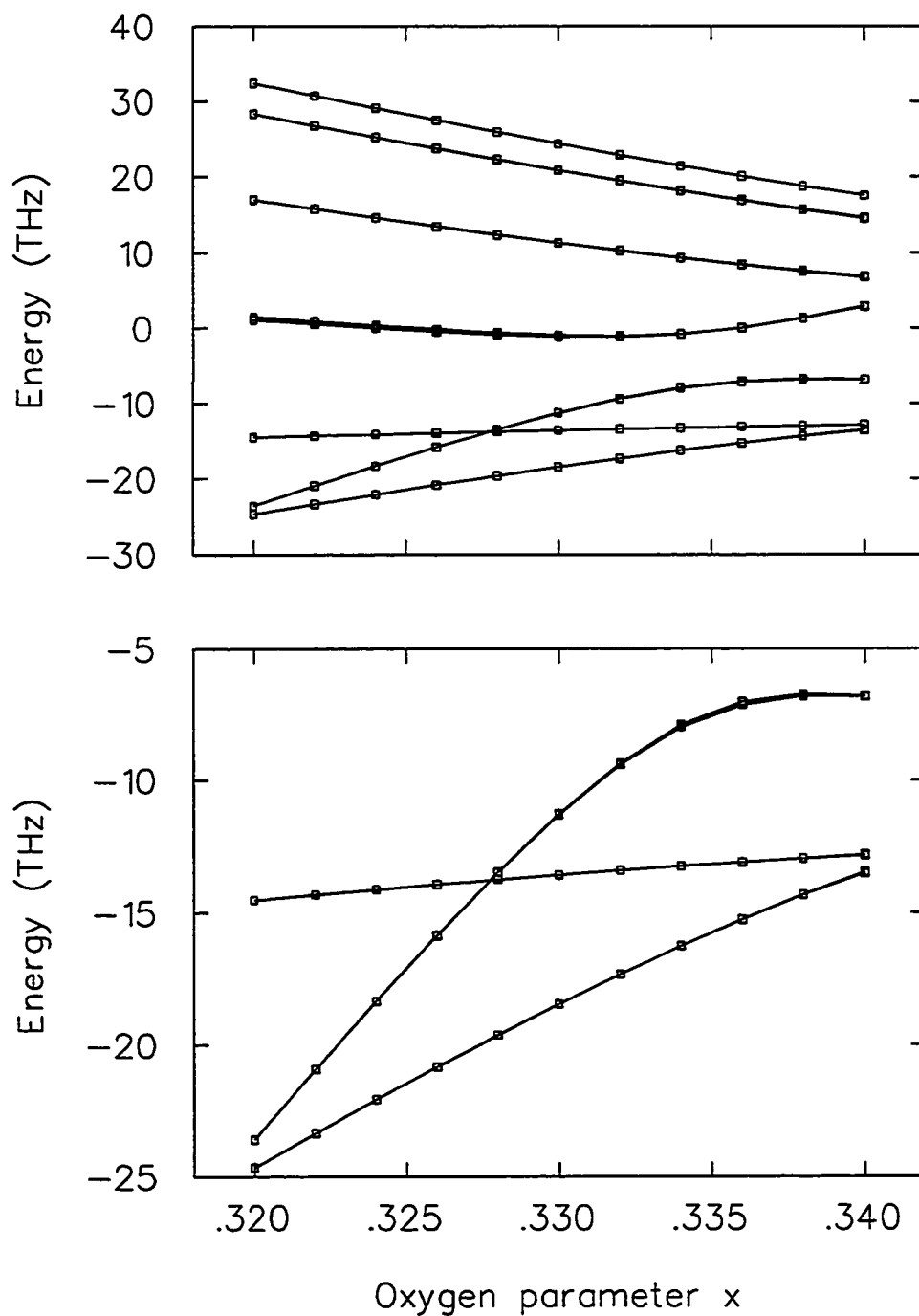


Figure 3.12: The effect of varying oxygen parameter x on the CEF energy level splittings of the Tb^{3+} ion. The lower box shows the 3 lowest doublets on an expanded scale.

Ion	Basic Electron Configuration	Ground State Term
Mo ⁴⁺	[Kr]4d ²	³ F ₂
Gd ³⁺	[Xe]4f ⁷	⁸ S _{7/2}
Tb ³⁺	[Xe]4f ⁸	⁷ F ₆
Tm ³⁺	[Xe]4f ¹²	³ H ₆

Table 3.8: Electron configurations of selected Iron group and Lathanide ions.

	Θ_2	Θ_4	Θ_6	$\langle r^2 \rangle$	$\langle r^4 \rangle$	$\langle r^6 \rangle$
Mo ⁴⁺	$\frac{-2}{105}$	$\frac{-2}{315}$	-	2.9052*	14.3861*	
Tb ³⁺	$\frac{-1}{3^2 \cdot 11}$	$\frac{2}{3^3 \cdot 5 \cdot 11^2}$	$\frac{-1}{3^4 \cdot 7 \cdot 11^2 \cdot 13}$	0.755	1.419	5.688
Tm ³⁺	$\frac{1}{3^2 \cdot 11}$	$\frac{2^3}{3^4 \cdot 5 \cdot 11^2}$	$\frac{5}{3^4 \cdot 7 \cdot 11^2 \cdot 13}$	0.646	1.067	3.647

Table 3.9: Stevens' multiplicative factors and radial expectation values for selected ions. The latter quantities are in units of Bohr radii. (*) Only values for Mo³⁺ are available.

magnetic ions' wave functions with those of neighbouring ions and the complex effects of "screening" of the magnetic electrons by the outer electrons of the magnetic ion. However, this method serves as a first approximation to illustrate the principles involved and calculate the ratio of terms of the same degree in the Hamiltonian for lattice sites of high symmetry, since these ratios are independent of the model used and depend solely on the symmetry. A calculation for Tm³⁺ on the A site was also performed to gauge the reliability of the technique as Tm₂Ti₂O₇ is known to have a singlet ground state [96]. Below ~ 40 K measurements of the a.c. susceptibility are temperature independent in this material, due to van Vleck contributions. Inelastic neutron scattering measurements show evidence of a single peak at an energy transfer of 10.64 meV (123 K). Point charge calculations correctly predict the singlet ground state with a splitting of 81 K to the first excited state.

3.3 Muon sites

Knowledge of the muon site(s) is often necessary for a complete understanding of the μ SR signals observed, yet is difficult to determine reliably. The muon may even be mobile at elevated temperatures approaching room temperature. When single crystal samples are available, the point symmetry of the muon site may be deduced from the dependence of the μ SR signal on the orientation of the initial muon polarisation with respect to the principal crystal axes. The bare μ^+ is quite likely bonded to the most electronegative species present. For example, in oxide and fluoride insulators there is considerable evidence that the muon bonds to fluorine or oxygen. In fluorides this often results in the formation of a hydrogen bonded $(F\mu F)^-$ ion, generating a characteristic oscillating ZF- μ SR signal [97, 98, 99]. In oxide materials it is believed that the μ^+ sits 1 Å away from an oxygen ion, as in the high T_c superconductors like rare earth orthoferrites [100, 101] and $YBa_2Cu_3O_{6+\delta}$ [102] for example.

There are a variety of numerical packages involving quantum chemical calculations on molecular or crystal systems which find minimum energy locations for protons or muons. They range from purely empirical (the so-called molecular modelling programs) through semi-empirical (MNDO, for example) to *ab initio* or first principles density functional approaches. They all work on the variational principle, in that the lower the overall energy of the system, the closer one must be to the “true” structure. The study of defects in various semiconductors is perhaps the most well established. A recent review article on hydrogen related defects in crystalline semiconductors [103] focuses mostly on the theoretical developments in this field. It provides an introduction to Hartree-Fock, density-functional and molecular dynamics techniques, their strengths and limitations—a discussion which is beyond the scope of this thesis.

As a simplified approach to the problem, the author has instead used Ewald’s method [104] to find the the electrostatic potential throughout the pyrochlore lattice. A detailed description of this method is given by Slater [105] and the calculation described below

follows his notation. The electrostatic potential energy of a set of charges q_j is given by

$$E_{el} = \frac{1}{2} \sum_{j \neq k} \frac{q_j q_k}{r_{jk}} \quad (3.22)$$

using Gaussian units. It is impractical to solve the problem by direct summation, as this involves an oscillating series where the terms decrease extremely slowly. In fact, even though the potential energy decreases as $1/r$, the number of neighbour ions k in a shell a distance r removed from ion j increases as r^2 and hence the series may not converge at all. It is more convenient to solve this problem of calculating the potential ϕ using Poisson's equation:

$$\nabla^2 \phi = -4\pi\rho, \quad (3.23)$$

again in Gaussian units and where ρ is the charge density, *i.e.* charge per volume of the conventional unit cell A_0^3 . That the two techniques are equivalent may be verified using Green's theorem.

Expressing ϕ and ρ as a three dimensional Fourier series to take advantage of the periodicity of the lattice,

$$\rho = \sum \mathbf{K}_m P(\mathbf{K}_m) \exp(i\mathbf{K}_m \cdot \mathbf{r}), \quad (3.24)$$

where the \mathbf{K}_m 's are the wave vectors of the reciprocal lattice and the P 's Fourier coefficients. Ewald assumes a unit positive charge at the lattice points of a Bravais lattice, plus a uniform negative charge distribution such that the crystal is electrically neutral. The uniform negative and positive charge distributions cancel out. The solution of Poisson's equation is then

$$\phi = 4\pi \sum_{\mathbf{K}_m} P(\mathbf{K}_m) \frac{\exp(i\mathbf{K}_m \cdot \mathbf{r})}{|\mathbf{K}_m|^2}. \quad (3.25)$$

However, it can be shown that this summation does not converge either, given point charges. Therefore each point charge is replaced by a Gaussian distribution

$$\frac{\epsilon^3}{\pi^{3/2}} \exp(-\epsilon^2 r^2) \quad (3.26)$$

where ϵ describes the width of the distribution. Quoting the solution without proof (see Ref. [105]), we arrive at the potential for a unit positive charge:

$$\phi = \frac{4\pi}{\Omega} \sum_{\mathbf{K}_m \neq 0} \frac{\exp(-|\mathbf{K}_m|^2/4\epsilon^2) \exp(i\mathbf{K}_m \cdot \mathbf{r})}{|\mathbf{K}_m|^2} + \sum_{r_j} \frac{1 - \text{erf}(\epsilon r_j)}{r_j} - \frac{\pi}{\Omega\epsilon^2}. \quad (3.27)$$

This result is independent of the value of ϵ in Eq. (3.26) (chosen to be 18 in this calculation); Ω is the volume of the Wigner-Seitz unit cell for the fcc lattice. The potentials due to all the ions in the basis are shifted so that their singularities come at the appropriate lattice site. For instance, to calculate the solution for NaCl, two Ewald solutions are superposed: one for unit positive charge at the origin, the other for unit negative charges at points such as $x = A_0/2, y = z = 0$.

Finally, Born and Mayer [106] suggested a term in the potential of the form

$$\frac{1}{A_0} \sum_{r_j} \exp\left(\frac{(R - r_j)}{R_0}\right) \quad (3.28)$$

which acts as a hard core repulsion. The parameter R_0 describes the hardness and was the only quantity adjusted in this calculation, so that the potential energy minima occurred 1 Å away from the oxygen ions.

The potential energy in two (100) planes, chosen because they intersect minima, are illustrated in Fig 3.13. All the minima shown in black are equivalent, related by symmetry operations and occur at the position $A_0(0.16, 0.16, -0.17)$. The calculation was carried out using the values of unit cell cell, ionic charge and size appropriate to $Y_2Mo_2O_7$. As can be seen, the potential energy minima occur closest to oxygen ions. This is true for different values of the hardness parameter: only the oxygen - muon/proton separation changes. While their position is reassuring, their depth is probably an overestimate. This may be due in part to the fact that positional relaxation of the neighbouring ions was neglected in this calculation. As a comparison, maps of H^+ potential energy in the anhydrous pyrochlore $HTaWO_6$ [107] show that proton hopping occurs between adjacent 48f sites along edges of $(Ta,W)O_6$ coordination octahedra. The calculated activation energy of 0.6 eV, optimised by using fractional ionic charges, is in good agreement with

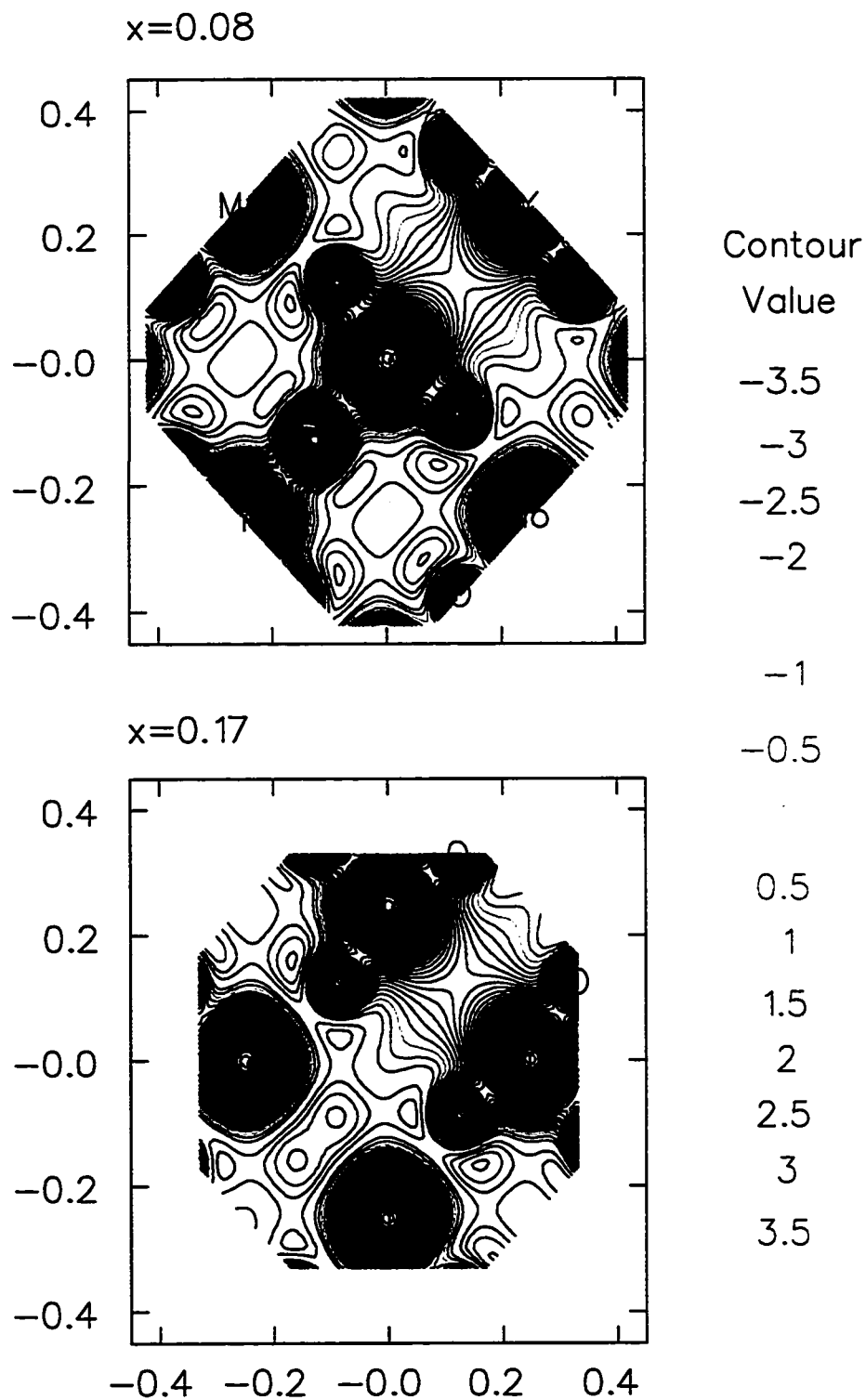


Figure 3.13: Map of electrostatic potential energy on several (100) planes for $Y_2Mo_2O_7$. The horizontal and vertical axes are parallel to the [010] and [001] directions respectively. Contour lines are in units of hartrees (27.2 eV).

the experimental value of 0.66 eV. The small value of $-0.70e$ obtained for the oxygen charge indicates the substantially covalent nature of the Ta-O and W-O bonds.

Since the implanted muon is a charged point impurity we expect that it will modify its local electronic environment. It is also possible that a hydrogen-like neutral species μ^+e^- or muonium (chemical symbol Mu) may form in any insulator or semiconductor, by capturing an electron from the stopping medium. See Chapter 6 for a discussion on muonium formation.

In metals the conduction electrons are redistributed, contributing to the screening of the μ^+ charge. In transition metals and compounds the muon may alter the exchange coupling between the conduction electrons and the local moments and therefore also the RKKY interaction between moments. The crystal electric field splittings may be changed in f -electron compounds in the neighbourhood of the implanted muon due to additional electric field gradients. This could in principle affect the local spin susceptibility, although in most 3D compounds such effects tend to be small.

It is interesting to note that in contrast to NMR, μ SR probes the local field at an interstitial site.

Chapter 4

Description of the Experiments

4.1 Production of Spin Polarised Muons

At TRIUMF and other “meson factories”, muons are produced as follows: ≥ 500 MeV protons are incident on a target of typically carbon or beryllium and the resulting proton-proton and proton-neutron collisions result in the production of pions. Negatively charged pions are almost immediately captured by the target nuclei and hence their subsequent decay into muons and neutrinos is not observed, while the π^0 rapidly decays electromagnetically with a lifetime of $(0.82 \pm 0.04) \times 10^{-16}$ s. Henceforth only positive pions and their subsequent parity violating weak decay will be considered:

$$\pi^+ \rightarrow \mu^+ + \nu_\mu \quad (4.29)$$

with a lifetime of $\tau = 26.02(4)$ ns [109].

The experiments described in the following chapters were carried out using so called “surface muons”, a type of muon beam first developed by Pifer *et al.* [110], which makes use of very low energy pions decaying at rest near the surface of the primary production target. Because the decay of the pion is a two body process, the muon and neutrino are emitted in antiparallel directions by conservation of momentum. They must also have a combined spin of 0, since the pion is spinless. Since the neutrino has been shown experimentally to have negative helicity [111], *i.e.* its spin is antiparallel to its momentum, the muon beam is also fully spin polarised opposite to its momentum direction with a kinetic energy of 4.12 MeV in the rest frame of the pion. This gives the muons a mean stopping range which varies with the material in question: typically 140 mg cm^{-2} in water with a straggling range of 20 mg cm^{-2} .

	μ^+	e^-	p^+
Lifetime	$2.19703(4) \mu s$	$> 4.3 \times 10^{23}$ years	$> 1.6 \times 10^{25}$ years
Type	lepton	lepton	baryon
Mass [Mev/c ²]	105.65839(4)	0.5109991(2)	938.2723(3)
Magnetic moment [μ_B]	4.8419710×10^{-3}	1.001165923(8)	1.521×10^{-3}
Magnetic moment [μ_N]	9.021	1838	2.79284739(6)
Gyromagnetic ratio $\gamma/2\pi$ [MHz/T]	135.54	28020	42.5759

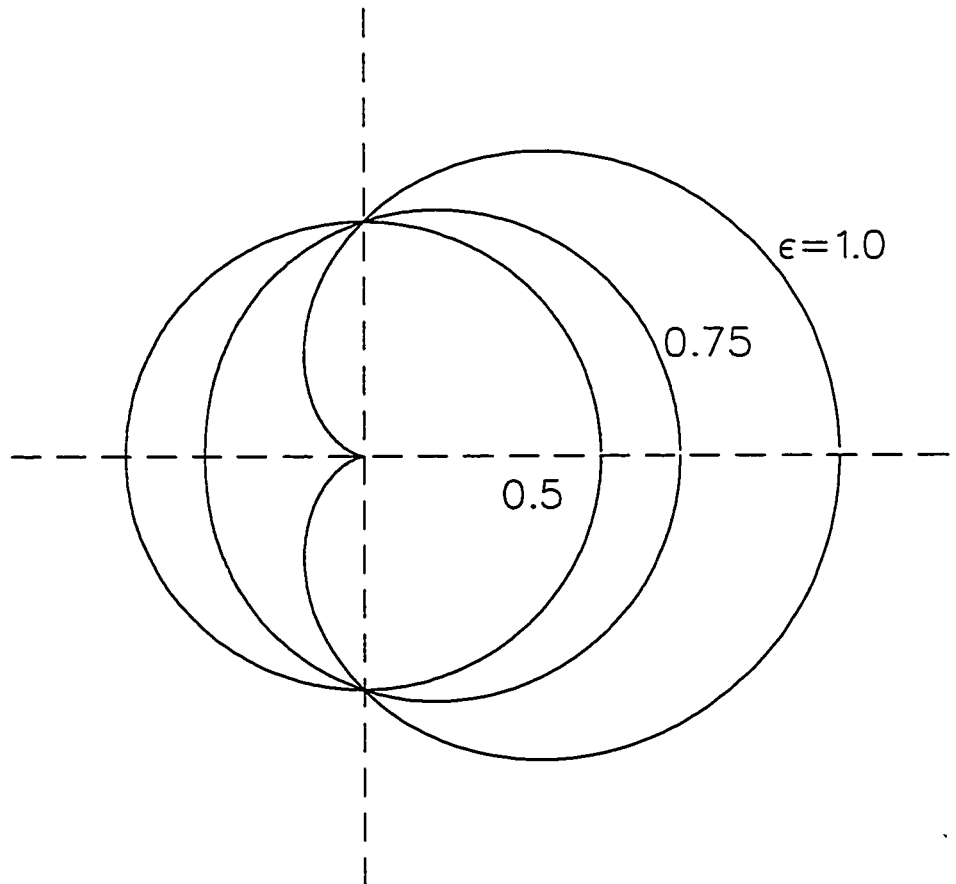
Table 4.10: Selected properties of μ^+ and other particles.

Figure 4.14: A polar coordinate plot of the rate of positron emission from muon decay as a function of angle from the muon spin, at various energies ϵ . The distribution has axial symmetry about the muon spin polarisation direction, which points towards the right in this plot.

Positive muons then decay via the interaction

$$\mu^+ \rightarrow e^+ + \bar{\nu}_\mu + \nu_e. \quad (4.30)$$

Because this involves a three body decay, the kinetic energy of the emerging positrons varies continuously from 0 to $E_{max} = 52.3$ MeV. The maximum positron energy corresponds to the situation where the neutrino and antineutrino travel together in a direction antiparallel to the positron. The direction in which a positron is emitted is correlated with the direction of the muon spin at the time of its decay because of the parity violating terms in the interaction Hamiltonian, first confirmed experimentally by Garwin, Lederman and Weinrich [112]. A quantitative description of muon decay involves writing the weak interaction in terms of the $V - A$ picture of a current-current interaction. Substituting this interaction Hamiltonian into Fermi's golden rule and integrating over the momenta of the neutrinos, which are not detected, the decay probability per unit time of the muon is given by

$$\frac{G^2 m_\mu^5}{192\pi^3} (3 - 2\varepsilon) \left[1 - \frac{(1 - 2\varepsilon)}{(3 - 2\varepsilon)} \cos\theta \right] d\varepsilon d\cos\theta. \quad (4.31)$$

The angle θ is that between the muon spin and the momentum of the emerging positron; $\varepsilon = E/E_{max}$. The asymmetry factor $(2\varepsilon - 1)/(3 - 2\varepsilon)$ depends on the positron energy (see Fig. 4.14). In a typical μ SR experiment there is no explicit energy resolution: the energy average of the asymmetry is nominally $1/3$. However, in practice the low energy positrons (whose asymmetry is actually negative) are unable to reach the detector, raising the effective asymmetry; the finite solid angle intercepted by the detector reduces the effective asymmetry, which is therefore treated as an empirical quantity.

4.2 μ SR Experimental Setup

Muons emitted in a particular direction pass down the beamline to a Wien velocity filter made up of crossed electric and magnetic fields. As well as preferentially selecting surface muons and by the same token removing beam positrons, the filter or "separator" can also

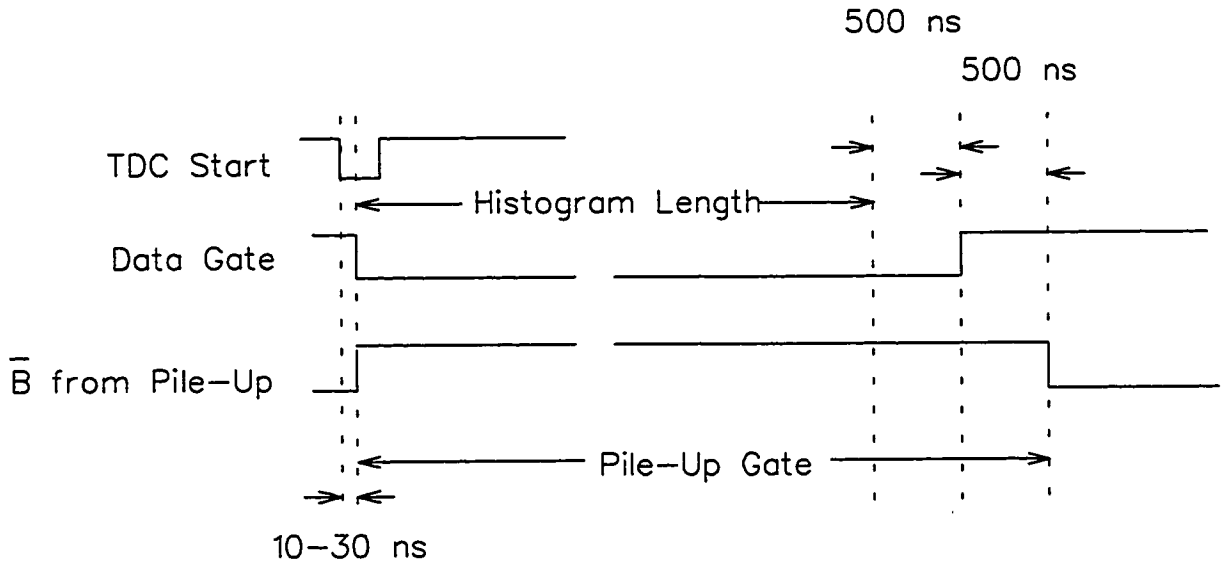


Figure 4.15: Signal timing for a typical time differential μ SR experiment using a Lecroy 4204 TDC.

be used at high fields to rotate the muon spin polarisation by 90° . Having optimised the beam using a series of bending and focusing (quadrupole) magnets the muon beam is typically collimated to about 1 cm diameter. In a conventional time differential μ SR experiment tailored for a continuous wave (cw) facility like TRIUMF, only those events where one and only one muon is in a sample at any one time are accepted. A thin muon counter (TM) made up of 0.01" plastic scintillator is placed between the end of the beam pipe and the μ SR spectrometer, detecting incoming muons and defining a time $t = 0$. A Lecroy 4204 time-to-digital-converter (TDC) is started in fast data acquisition electronics and a data gate of typically $10 \mu\text{s}$ or $\sim 5\tau_\mu$ is generated. The event is rejected if a second muon triggers the muon counter within a time set slightly longer than the data gate, resulting in "pile-up" (see Fig 4.15). The pile-up gate also rejects events with an incoming muon any time within the gate width *before* this incoming one. The optimal good event rate has been calculated by Garner [115] to be $1/(2 \text{ times the data gate width})$. This corresponds to an event acceptance rate of 37%. Thick ($1/4''$) scintillation counters register the muon decay positron and stop the TDC. The measured time then causes the corresponding channel in a histogramming memory to be incremented by one.

Further details are described elsewhere [113].

The probability that a decay positron will pass through a given counter depends on the asymmetric muon decay pattern, the shape and position of the counter and on the direction of the muon spin at the time of decay. The ensemble average of this last quantity is given by $\mathbf{P}(t)$, the polarisation function. For the n^{th} counter, the histogram of the time differences between muon implantation and decay positron detection is of the form

$$N_n(t) = N_n(0) \exp(-t/\tau_\mu)[1 + a_n \mathbf{P}(t) \cdot \hat{n}] + B_n, \quad (4.32)$$

where $N_n(0)$ is a normalisation constant; B_n a time independent random background due to cosmic rays, positron contamination of the muon beam or photomultiplier dark noise, for instance. It is assumed to be uncorrelated with the arrival time of the muon. The effective counter asymmetry is given by a_n , (on the order of 0.2 - 0.3) and \hat{n} is a unit vector along the direction joining the centre of the sample to the centre of the solid angle subtended by the counter. By recording the ratio of the number of positrons detected in scintillation counters 180° out of phase as a function of time, it is possible to reconstruct the muon spin depolarisation function from the experimental asymmetry A_{raw} :

$$A_{\text{raw}} \mathbf{P}(t) \cdot \hat{n} = \frac{[N_n(t) - B_n] - [N_{-n}(t) - B_{-n}]}{[N_n(t) - B_n] + [N_{-n}(t) - B_{-n}]} \quad (4.33)$$

The multiplicative factor associated with the exponential decay of the muon automatically cancels out. For N_n accumulated muons, the signal to noise ratio is proportional to $a_n \sqrt{N_n}$. However, Eq. (4.33) assumes the counters are identical. In reality, photomultiplier efficiencies, discrimination levels and counter positions will affect the random background and the normalisation. Counter solid angles and efficiencies will also affect the normalisation as well as the decay asymmetry a_n . The positron energy distributions are set by degrader thicknesses, from the cryostat walls for example. For a pair of counters, Eq. (4.32) becomes

$$\begin{aligned} N_n(t) &= N_n(0) \exp(-t/\tau_\mu)[1 + a_n \mathbf{P}(t) \cdot \hat{n}] + B_n \\ N_{-n}(t) &= \alpha N_n(0) \exp(-t/\tau_\mu)[1 - \beta a_n \mathbf{P}(t) \cdot \hat{n}] + B_{-i}, \end{aligned}$$

where $\alpha = N_{-n}(0)/N_n(0)$ and $\beta = |a_{-n}|/|a_n|$. A “corrected asymmetry” A_{corr} can then be extracted from the raw asymmetry as

$$A_{\text{corr}} \mathbf{P}(t) \cdot \hat{n} = \frac{[A_{\text{raw}} \mathbf{P}(t) \cdot \hat{n}](\alpha + 1) + (\alpha - 1)}{(\alpha\beta + 1) + [A_{\text{raw}} \mathbf{P}(t) \cdot \hat{n}](\alpha\beta - 1)}, \quad (4.34)$$

where β is often taken to be 1. A thorough discussion of statistical details and possible distortions in μSR spectra is given in Ref. [114], as well as in the theses of Garner [115] and Riseman [116].

The muon spin interacts with the internal nuclear and electronic spins of the material under analysis, probing the spatial and temporal variations in the local magnetic field. Consider the van Vleck or high transverse field limit. Then, in the case of a purely static field distribution, the muon spin depolarisation or relaxation $\mathbf{P}(t) \cdot \hat{n}$ occurs due to dephasing, since muons experience different magnetic fields and therefore precess at different frequencies. In the case of purely dynamic fluctuations, relaxation occurs due to the absorption of energy quanta resulting in a spin flip. The relaxation depends on the system’s spectral density at the muon Larmor frequency. However, these distinctions become much less clear as the applied field becomes comparable with the local fields or eventually goes to zero [125]. The technique of μSR is sensitive to spin fluctuation rates within a material from 10^{-4} to 10^{-11} seconds, a range set by the muon lifetime. The geometry used in a particular μSR experiment depends on the information to be extracted (see Fig. 4.16 and Table 4.11). In a transverse field (TF) experiment, an external magnetic field is applied perpendicular to the initial muon spin direction. The envelope of the resulting precession signal looks very much like a free induction decay signal in NMR, the damping rate or linewidth being identified with T_2^{-1} . Unfortunately, it is extremely difficult to distinguish between contributions to T_2^{-1} from static internal magnetic fields and those from fluctuations. A more effective method for studying spin dynamics in magnetic systems is to measure the component of the muon spin polarisation along the applied field (LF- μSR), using counters “backward” and “forward” of the sample position. Most of the experiments described in this thesis are of the latter type. The configuration used for the measurements in high applied magnetic field is shown in Fig. 4.17. In an applied

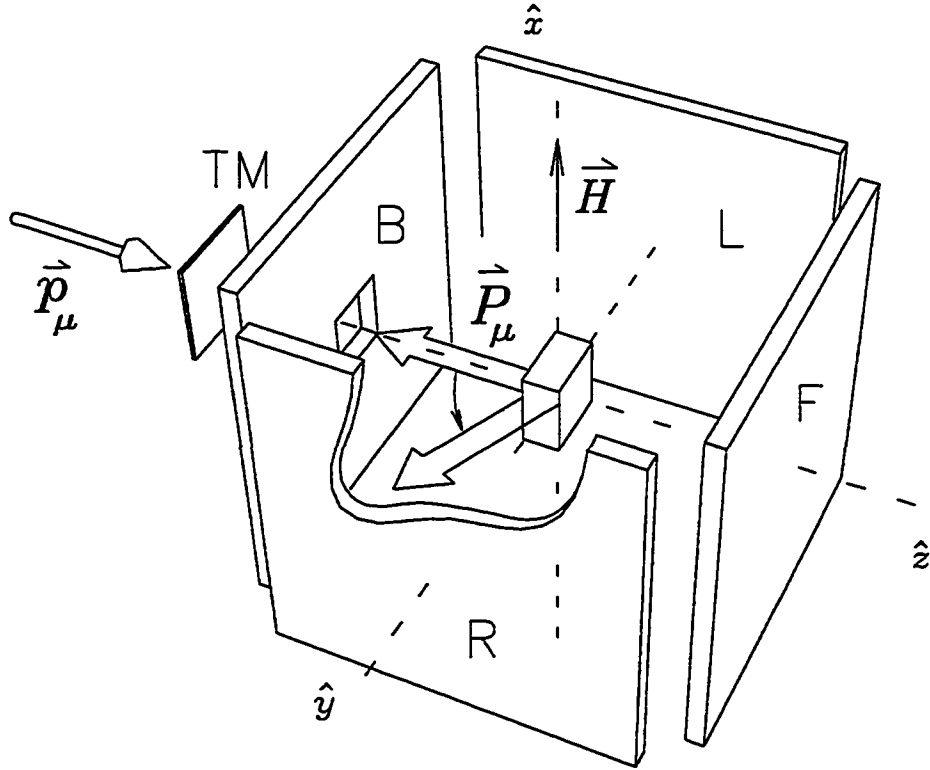


Figure 4.16: General counter arrangement for a ${}^2\text{TF}_x$ μSR experiment. In the ${}^2\text{TF}_x$ geometry shown, the muon spin precesses about the vertical axis at an angular frequency of $\omega_\mu = \gamma_\mu H$. (From Ref. [114]).

field, the positron paths follow spirals with axes parallel to the field. Thus the effective solid angles covered by the counters are altered and consequently the asymmetry as well. The Lorentz force $qv \wedge \mathbf{B}$ implies that a relativistic charged particle with momentum $p_\perp = \gamma m v_\perp$ perpendicular to the applied field \mathbf{B} will have a radius of curvature given by

$$\frac{\gamma m_{e^+} v_\perp}{eB}, \quad (4.35)$$

where

$$v = \left(\frac{e}{\gamma m_{e^+}}\right) \sqrt{\left(\frac{E_{e^+}}{ec}\right)^2 - \left(\frac{m_{e^+} c}{e}\right)^2} \quad (4.36)$$

and $\gamma = E_{e^+}/(m_{e^+} c^2)$. The maximum momentum for muon decay positrons is 52.83 MeV/c and thus in a 5 T field, a positron of this energy travelling perpendicular to the

P_μ	H	
$\pm\hat{x}$	$\pm\hat{z}$	TF - spin and field perpendicular
$-\hat{z}$	$\pm\hat{x}$ or $\pm\hat{y}$	wTF - spin and field perpendicular
$-\hat{z}$	\hat{z}	LF - spin and field parallel
$-\hat{x}$	$\pm\hat{x}$	wLF - spin and field parallel
$\pm x$ or $-\hat{z}$	0	ZF - no field

Table 4.11: Various geometries for a μ SR experiment. The \hat{x} axis points upwards, the \hat{y} axis from left to right, and the \hat{z} axis in the direction of the muon momentum.

field direction will have a radius of curvature of only 3.5 cm. The radius will be even smaller for all the slower or non-perpendicular positrons. It is interesting to note that, as can be seen in the LF measurements in Fig. 7.55, this phenomenon results in an initial decrease in A_{corr} as the magnetic field is increased due to increased solid angle, followed by an increase when lower energy positrons are no longer detected. They spiral back through the hole in the back counter, altering the positron energy distribution in favour of higher energies.

The cup shaped counter in Fig 4.17 serves two functions in a LF configuration:

- It allows one to reject events from muons which miss the sample by acting as a veto V. The “good” start is thus given by the condition $\overline{\text{TM}} \cdot \overline{\text{V}} \cdot \overline{\text{Busy}}$. In other words, there must be a coincidence of a pulse in the thin muon counter, but no pulses from both the veto and the pile-up gate generator indicating it is already busy.
- It also detects decay positrons from muons which land in the sample like an ordinary forward counter. Its small size close in behind the sample is advantageous in high fields, due to solid angle considerations. The alternative is to logically “OR” the 4 side positron counters in Fig. 4.17, each of which is in the shape of a 90° quadrant in cross section and move them 2” downstream of the magnet centre. While this configuration forms an adequate forward counter in low magnetic fields, the positron orbits become too small as the magnetic field increases and miss the detector.

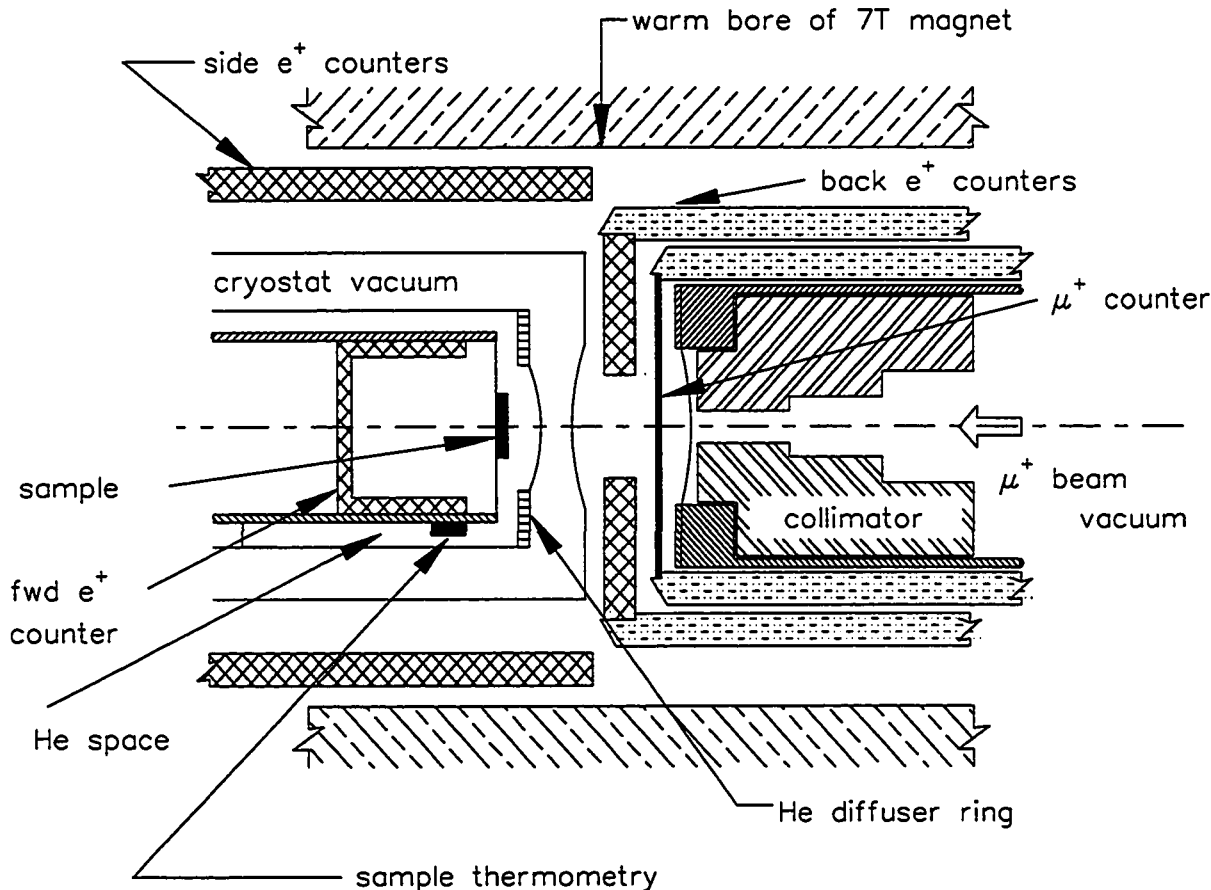


Figure 4.17: Sketch of the apparatus used for high LF and high $^2\text{TF}_z$ measurements. The superconducting solenoid is 24" in length and has a warm bore 6" in diameter.

It has also proved very useful to be able to collect μSR spectra on two different samples simultaneously with no appreciable "cross talk". To accomplish this, the apparatus sketched in Fig. 4.18 was designed and constructed. The crucial part of this arrangement is a second thin muon counter (TM_I), held in position by brass screws between the sample and a reference material, whose signal generates a second data gate. The geometry of the two materials is arranged such that the reference only partially covers the beam spot and those muons which miss stop in the sample. A valid muon stop in the sample is then defined as $F_n \cdot (\text{TM} + \text{TM}_I)$, where F_n is one of the positron counters (see Fig. 4.19)¹. The absence of a signal from the internal counter indicates that the muon stopped in

¹Since this apparatus was first built, the Lecroy 4204 TDCs have been replaced by BNC B980 TDCS. The data acquisition electronics have been correspondingly modified to suit.

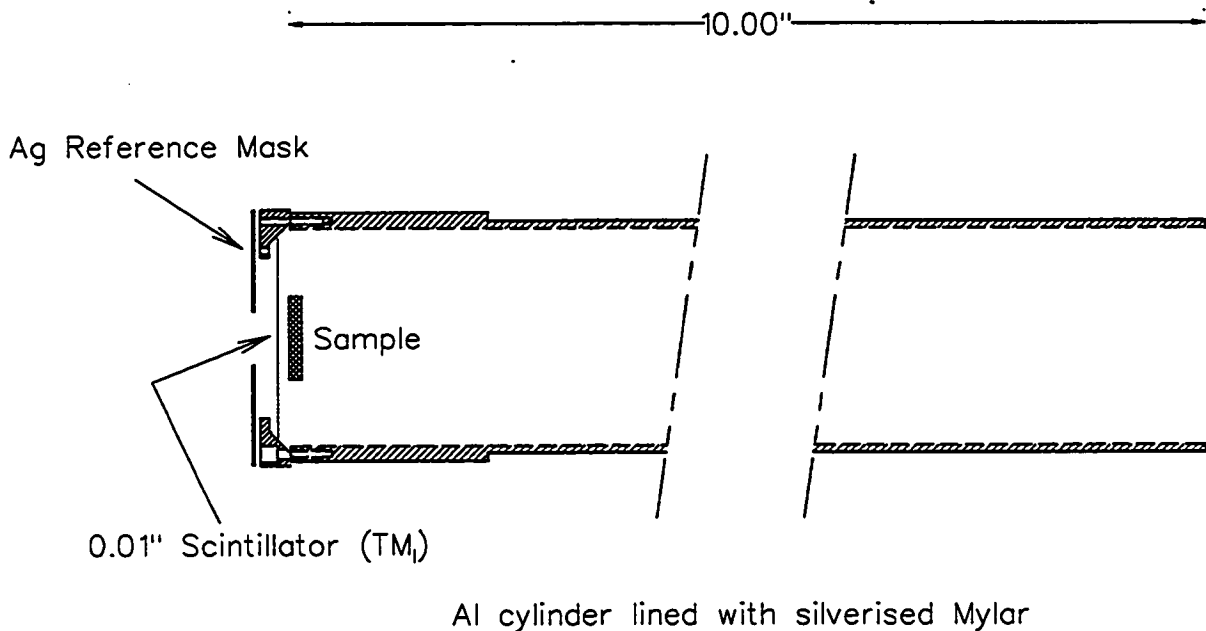


Figure 4.18: Cross sectional view of the apparatus for measuring two μ SR spectra simultaneously. The apparatus has cylindrical symmetry and the sample is held in place on a stage (not shown) which has 2 thin vanes slotting into the Al cylinder.

the reference. Light from the TM₁ scintillator is reflected 90° off a polished aluminium surface and guided out the back end of the cryostat to a photomultiplier (not shown). Using the technique described, time differential spectra are collected simultaneously for two different materials, but separated by the electronics. The main advantage of this technique is that, since the data on the reference and sample are taken under identical conditions, many systematic effects such as drifts in the magnetic field, thermal instabilities in the electronics, changes in the beam rate, or thermal contraction leading to changes in sample position will be the same for both. Field homogeneity over the volume of the sample is important, otherwise leading to increased linewidths in the μ SR spectra. The magnetic field variations in our experimental superconducting solenoid are shown in Appendix B for the axial and radial directions. Hence the Ag reference is positioned $\sim 1/16''$ upstream of the scintillator TM₁ and the sample in direct physical contact on the downstream side. The reference must be sufficiently thick to ensure that muons do not pass through to cause a pulse in the inner muon counter. By the same token, the second

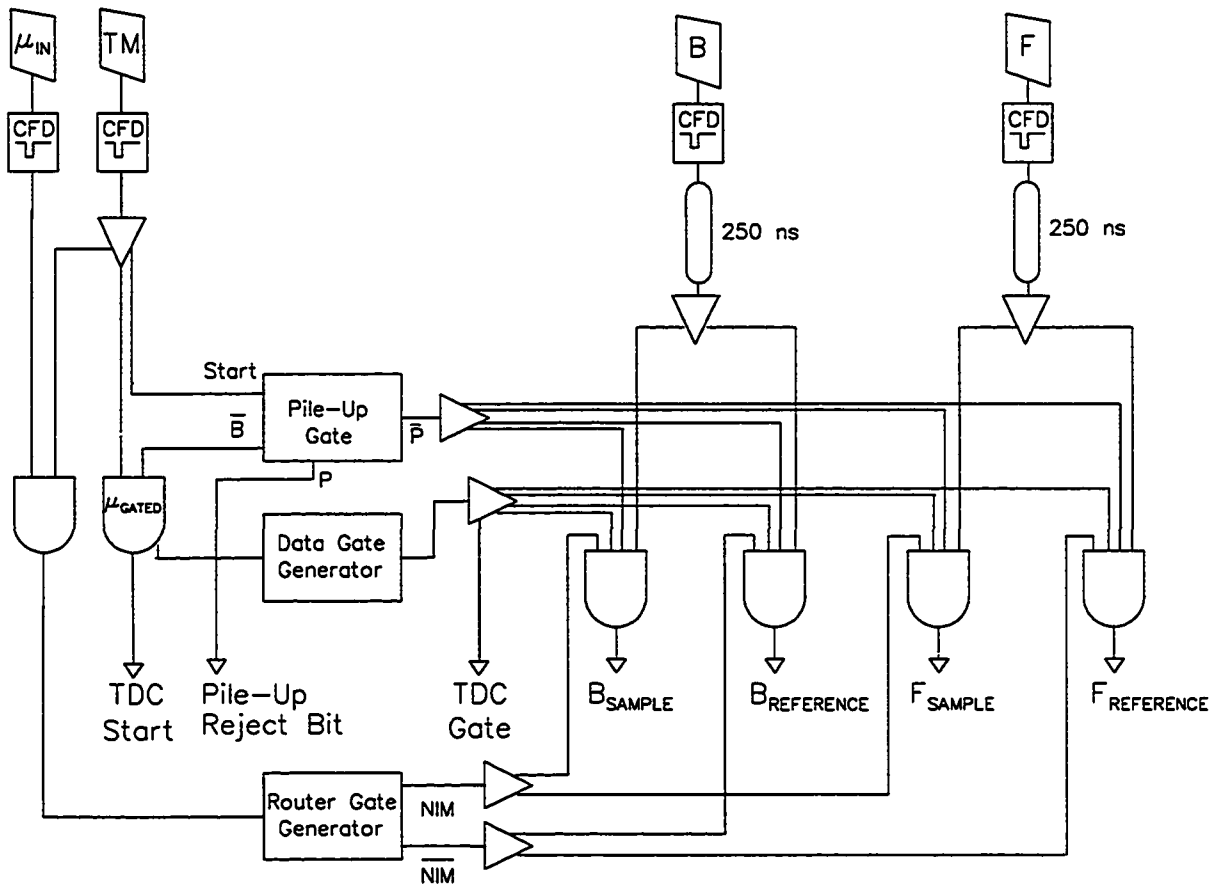


Figure 4.19: Schematic logic diagram of the fast electronics for time differential μ SR experiments using the “Separate Spectra” apparatus and a Lecroy 4204 TDC.

muon counter must be thin enough to avoid range straggling. If an initial momentum of 29 MeV/c (4.12 MeV) and zero initial momentum spread² is assumed, using the Bethe-Bloch formula, the muon kinetic energies range from $\sim 1.9 - 2.7$ MeV on reaching the sample in a typical setup with the separate spectra apparatus.

By ensuring that the shape of the reference material prevents any muons from hitting the sample stage, we ensure that the sample spectrum has essentially no detectable correlated background signal. This eliminates other sources of systematic error due to the fact that the ratio of background to foreground signal in a conventional setup may vary with time (due to instabilities in the beamline) or with magnetic field (due to focusing effects). High energy positrons and gamma rays are also detected by the muon

²The initial momentum spread is typically $\pm 5\%$.

counters, though with much less efficiency. The use of two muon counters is analogous to that of 2 positron counters in coincidence as a “telescope”. The “t0 peak” is thus suppressed, eliminating the associated distortion in the spectra at early times. Another benefit is the reduction in the uncorrelated background in the sample signal.

In order to test for “cross talk” between the two channels a spectrum was taken with Al_2O_3 at the sample position. Since Al_2O_3 produces almost no muon precession signal [117, 118] at 300 K, any observed signal can be attributed to false routing in the TM_I detector. Nor is any muonium precession observed [119], due to rapid depolarisation from large random local fields associated with the ^{27}Al nuclei. Figs. 4.20a and 4.20b show the Fourier transforms for the sample and reference respectively. The signal asymmetry of $A_{\text{corr}} = 0.006$ in Fig. 4.20a, due to false routing of the signal from the silver, demonstrates that there is at most a 3% background signal in the sample histograms. “Cross talk” in the other direction is also quite small as evidenced by the fact that the asymmetry in the reference spectrum ($A_{\text{corr}}=0.215$) is consistent with the maximum experimental value of 0.213 (obtained with Ag in both the sample and reference positions), indicating that there is little Al_2O_3 signal in the reference histograms. False routing in this direction is attributed to inefficiency in the TM_I counter.

In traditional muon and positron counters the scintillating material is optically coupled to a length of lucite, which acts as a light guide to a photomultiplier. Measurements of the dc susceptibility on the BC 412 scintillator and the lucite indicated the presence of a low temperature Curie-like contribution, as shown in Fig. 4.21. The present configuration ensured that as much magnetic material as possible was removed from the immediate sample surroundings. It is also vital to ensure that magnetic material is removed from around the cryostat as well. For instance, the beamline collimators must be made of lead or brass, not tungsten. Stainless steel also gives rise to an unacceptable magnetisation and alters the field at the sample.

In a transverse field geometry this method makes possible accurate frequency measurements in a sample relative to a known reference. The sample magnetisation is observed

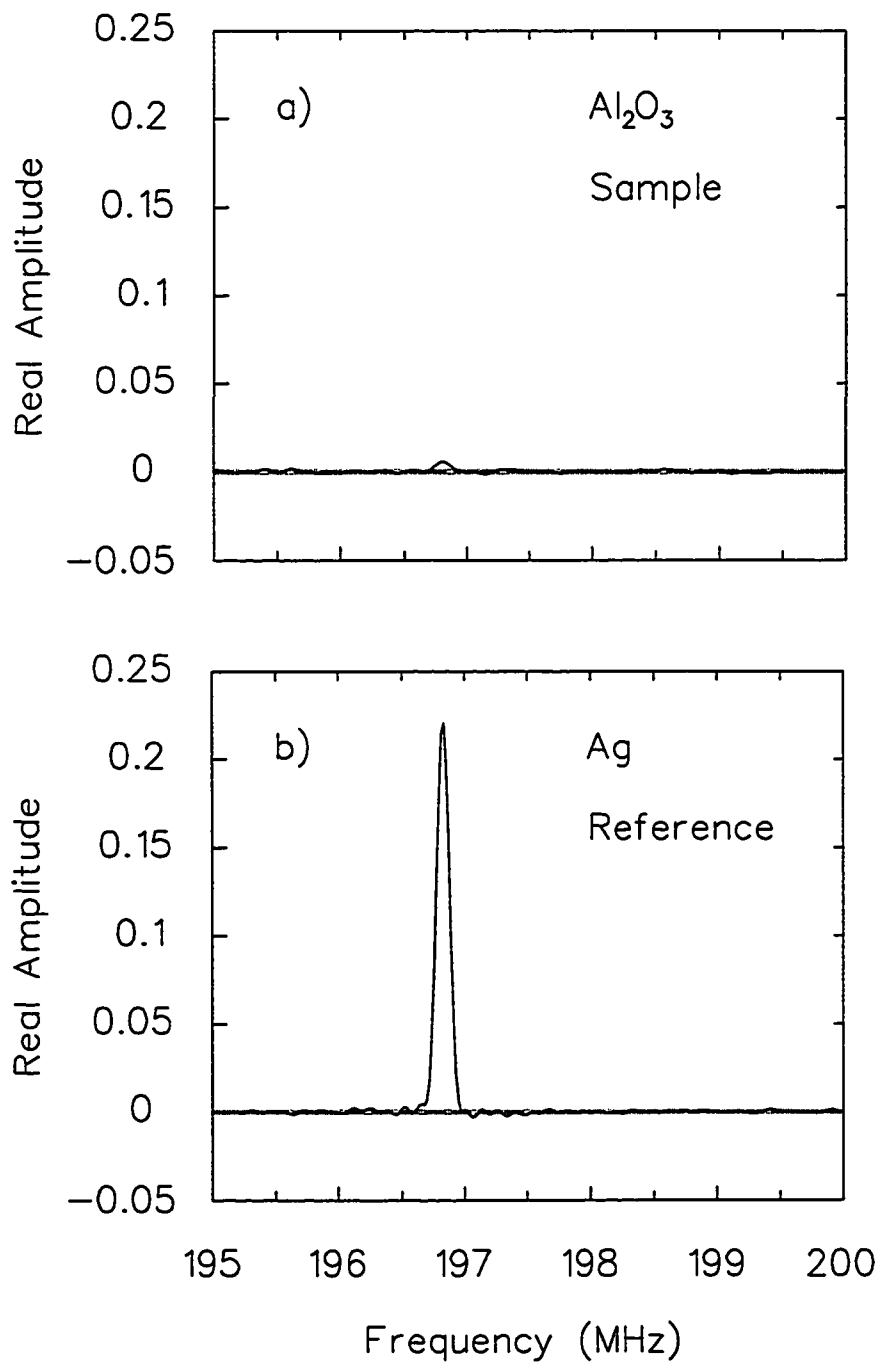


Figure 4.20: Fourier transform of the muon precession signal in a transverse magnetic field of 1.45 T with a) Al₂O₃ and b) Ag samples.

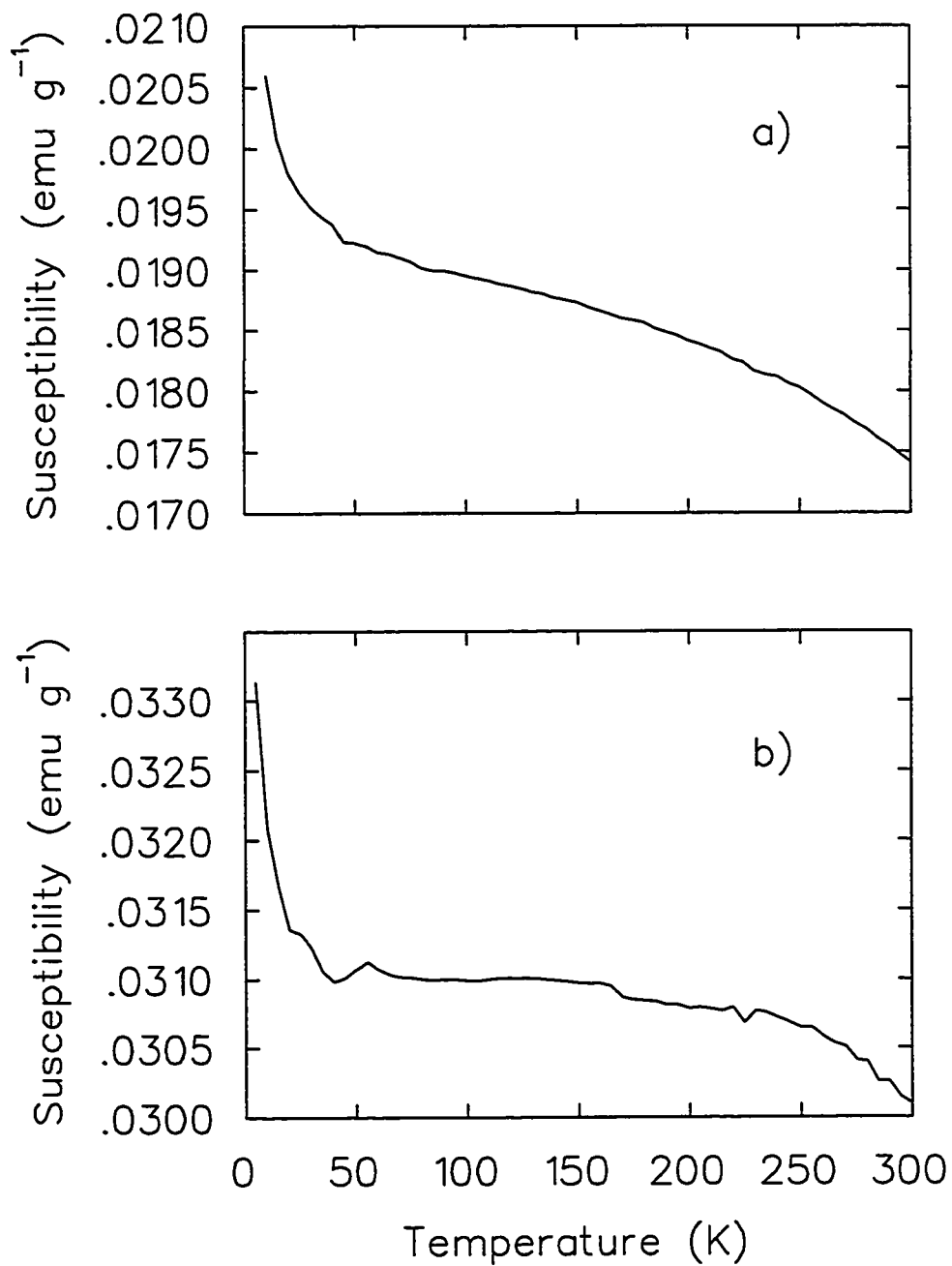


Figure 4.21: d.c. susceptibilities of a) lucite and b) Bicron BC412 scintillator in an applied magnetic field of 1.5 T.

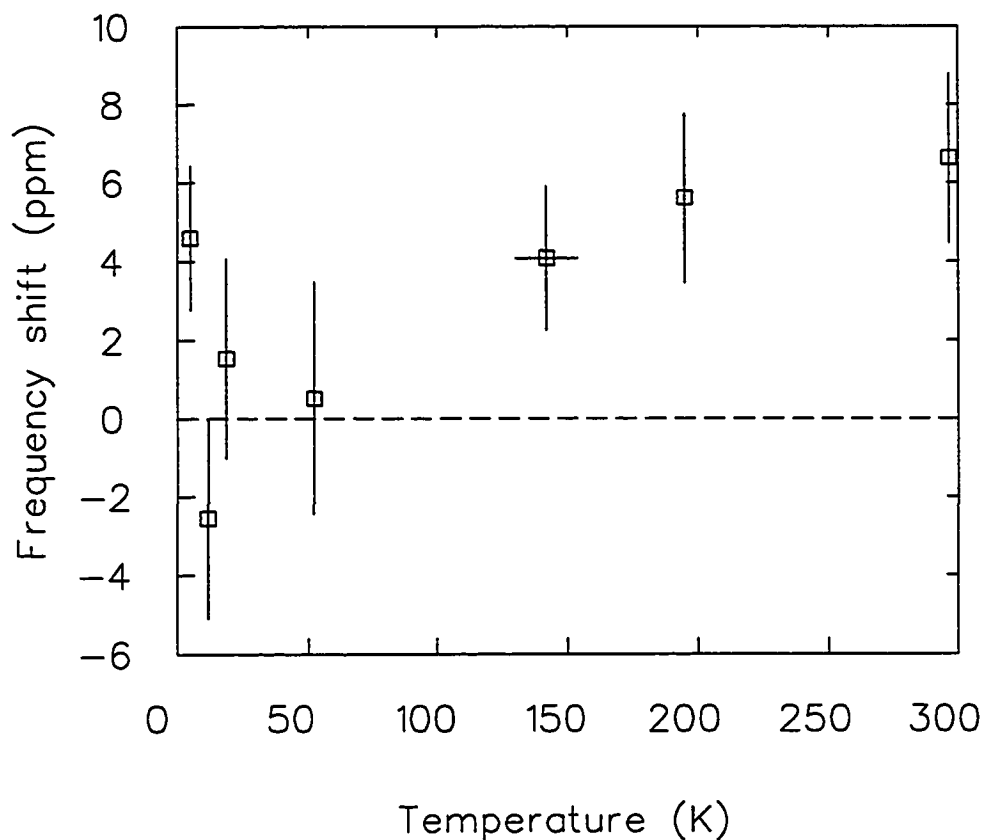


Figure 4.22: Relative precession frequency shift as a function of temperature in an applied magnetic field of 1.45 T with silver in both the sample and reference positions.

as a shift in the muon precession frequency, as shown for a series of calibration measurements on silver (Fig. 4.22). The reference material is typically a 0.25mm thick Ag foil (99.99+% purity). Silver is chosen for a number of reasons: in TF measurements the isotropic Knight shift at 300 K is well known (94.0 ± 3.5 ppm) [113]. In addition, there is nominally no muon spin depolarisation in LF measurements as muons diffuse rapidly in silver, which has negligibly small nuclear moments and Korringa relaxation occurs on a timescale too long for μ SR.

Chapter 5

Muon Spin Relaxation

The development of tools to describe muon spin relaxation has closely followed the more established theories applied to NMR data (see for example Refs. [120, 121]) and is thus geared to systems of nuclear spins. The extension to fluctuating electronic moments, the focus of this thesis, is not always straightforward.

The coupled motion of the muon and host spins, be they nuclear or electronic, are intrinsically quantum mechanical in nature. As such, the behaviour of the *combined* system should in principle be treated, as first illustrated by Celio and Meier [123]. However, in most situations, one exception being muonium, the local environment of the muon may be treated using a classical picture. The influence of the surrounding spins is approximated by a random local field. However, the classical picture is inappropriate if the muon spin couples mainly to only 1 or 2 paramagnetic moments with low values of spin (especially if $S_{ion} = 1/2$). There are marked differences in the long time behaviour, particularly for some symmetry directions [123]. The limitations of a classical treatment are beautifully illustrated by the simple spin system $^{19}\text{F}:\mu^+:^{19}\text{F}$ formed by the spin 1/2 muon and two fluorine nuclei in the metal fluorides [97].

5.1 Static Internal fields

Consider a situation where a muon is thermalised in a sample and experiences a completely static internal magnetic field $\mathbf{B} = (B_x, B_y, B_z)$ and zero applied field. Any given muon spin will precess around its local magnetic field, its \hat{c} component evolving in time as [122]:

$$\sigma_c(t) = \mathbf{P}(0) \cdot \mathbf{B} + \{ \mathbf{P}(0) \cdot \hat{c} - [\mathbf{P}(0) \cdot \mathbf{B}] (\mathbf{B} \cdot \hat{c}) \} \cos(\gamma_\mu B t) + [\mathbf{P}(0) \wedge \hat{c}] \cdot \mathbf{B} \sin(\gamma_\mu B t). \quad (5.37)$$

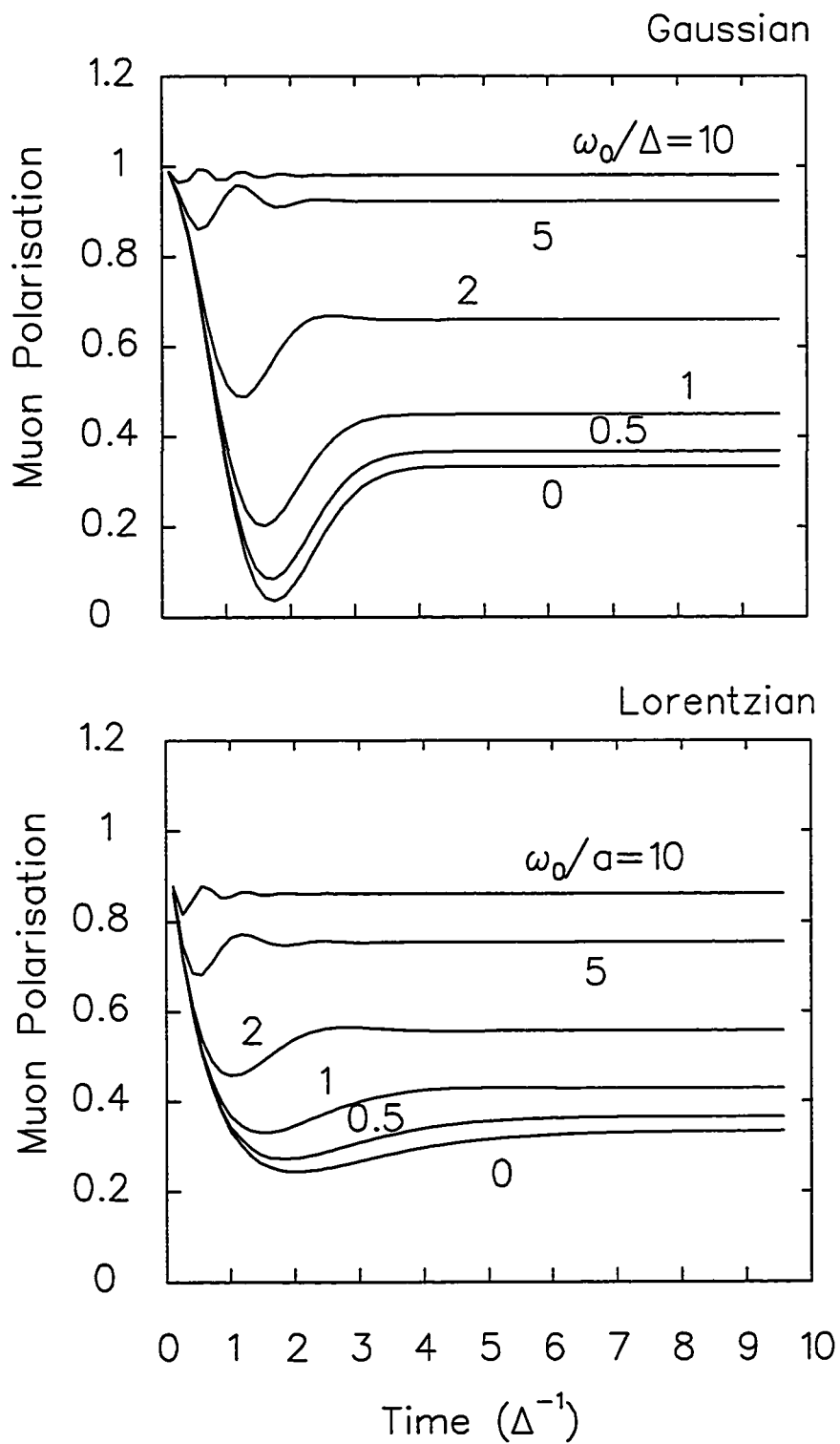


Figure 5.23: LF spin relaxation functions for isotropic static internal magnetic fields with a) Gaussian and b) Lorentzian distributions.

where $\mathbf{P}(0)$ is the initial muon spin polarisation and ϕ is the angle between \mathbf{B} and the \hat{c} axis. Taking the ensemble average of $\sigma_c(t)$ over a large number of muons (typically 10^7) which occupy magnetically inequivalent sites I with a probability f_I , one obtains the experimentally observable muon polarisation function:

$$P_c(t) = \sum_I f_I \iiint \sigma_c(t) \Phi_i(\mathbf{B}) dB_x dB_y dB_z. \quad (5.38)$$

In the case of a dense system of randomly ordered moments the field distribution $\Phi_i(\mathbf{B})$ for each component B_i of the internal field is often assumed to have an isotropic Gaussian shape:

$$\Phi_i(B_i) = \frac{\gamma_\mu}{\sqrt{(2\pi)\Delta}} \exp\left[-\frac{\gamma_\mu^2 B_i^2}{2\Delta^2}\right] \quad (5.39)$$

where Δ^2/γ_μ^2 is the second moment of the distribution. In this case and assuming only one muon site, Eq. (5.38) becomes

$$G_{zz}(t) = \frac{1}{3} + \frac{2}{3} (1 - \Delta^2 t^2) e^{-\frac{1}{2}\Delta^2 t^2}, \quad (5.40)$$

first derived by Kubo and Toyabe [125]. The relaxation in zero applied field initially shows a Gaussian like decay, but is followed by a recovery of the signal to 1/3. This recovery is unmistakable evidence for the static character of random fields. In a single crystal the long time asymptote will no longer necessarily be 1/3 but will depend on the dimensionality of the system, whether the spins are Ising, XY or Heisenberg like [126] and the orientation of the crystalline axes relative to the initial muon spin polarisation.

In dilute systems (if less than $\sim 10\%$ of the atoms have a moment [127]) then the field distribution is close to a Lorentzian [128, 129].

$$\Phi_i(B_i) = \frac{\gamma_\mu}{\pi} \frac{a}{a^2 + \gamma_\mu^2 B_i^2} \quad (5.41)$$

where a^2/γ_μ^2 is the FWHM of the Lorentzian distribution. This yields

$$G_{zz}(t) = \frac{1}{3} + \frac{2}{3} (1 - at) e^{-at}. \quad (5.42)$$

Of course a truly Lorentzian distribution is unphysical as the second and higher moments diverge. In addition, it leads to a depolarisation function with a non-zero slope as t approaches 0. In a real material the distribution is truncated at some maximum field.

ZF- μ SR is a very direct way to measure the static internal field distribution in the sample and the observed $G_{zz}(t)$ is quite sensitive to the type of magnetic order present. For example, in a system with long range order, where the muon always occupies the same magnetically equivalent site and there are no dynamics, the second term in Eq. (5.40) is replaced by an oscillatory signal $\cos(\gamma_{\mu}Bt)$, even in zero applied field. However, it should be noted that a distribution in the internal magnetic field acts to damp this “spontaneous precession” and in practice it may not be observed. One of the most useful aspects of ZF- μ SR is that it works equally well on both powders and single crystals. This is because the crystal orientation only affects the amplitude of precession and not the frequency.

Inclusion of an external magnetic field along the muon polarisation direction is also straightforward [130]. The most important effect is that the asymptotic value ($t \rightarrow \infty$) of $G_{zz}(t)$ rises from 1/3 towards 1 as the magnitude of the applied field approaches and then exceeds Δ/γ_{μ} (see Fig. 5.23).

The moments of the internal magnetic field distribution may be calculated, at least in high transverse field, without having to find the eigenstates of the total Hamiltonian, using van Vleck’s method of moments [131]. A knowledge of the n^{th} moment then gives information on the shape of the distribution and its associated resonance curve. Experimentally, important contributions come from the wings of the distribution, which may be difficult to observe. Thus only the secular terms of the dipolar Hamiltonian are included, not only for simplicity but more importantly so that signals at 0, $2\omega_0$ due to non-secular terms do not distort the calculation of the moments. The connection between ZF and high TF relaxation rates is discussed by Hayano *et al.* [130]. In the former case both the \hat{x} and \hat{y} components contribute, whereas in the latter the two directions perpendicular to the muon spin are inequivalent (since one is along the applied field). Hence, the ZF relaxation rate is a factor of $2^{1/2}$ larger than that in high transverse field. However, there is an additional effect: in zero field or the low longitudinal fields accessible with μ SR, the non-secular parts of the dipolar Hamiltonian may no longer be ignored. Therefore, the

two should differ such that in ZF $\Delta/\gamma_\mu = \sqrt{5/2}$ times the van Vleck linewidth in TF.

5.2 Fluctuating Internal Fields

To attain thermal equilibrium there must be some interaction between the spin system and the thermal fluctuations which define the temperature of the surrounding matrix or lattice in which it is embedded. In such dynamic depolarisation processes spin entropy is increased, by so called “spin-lattice relaxation”. In analysing μ SR data, the effects of magnetic fields which change on a timescale comparable with the muon lifetime, because of fluctuating moments and/or muon diffusional motion, need to be considered. Different

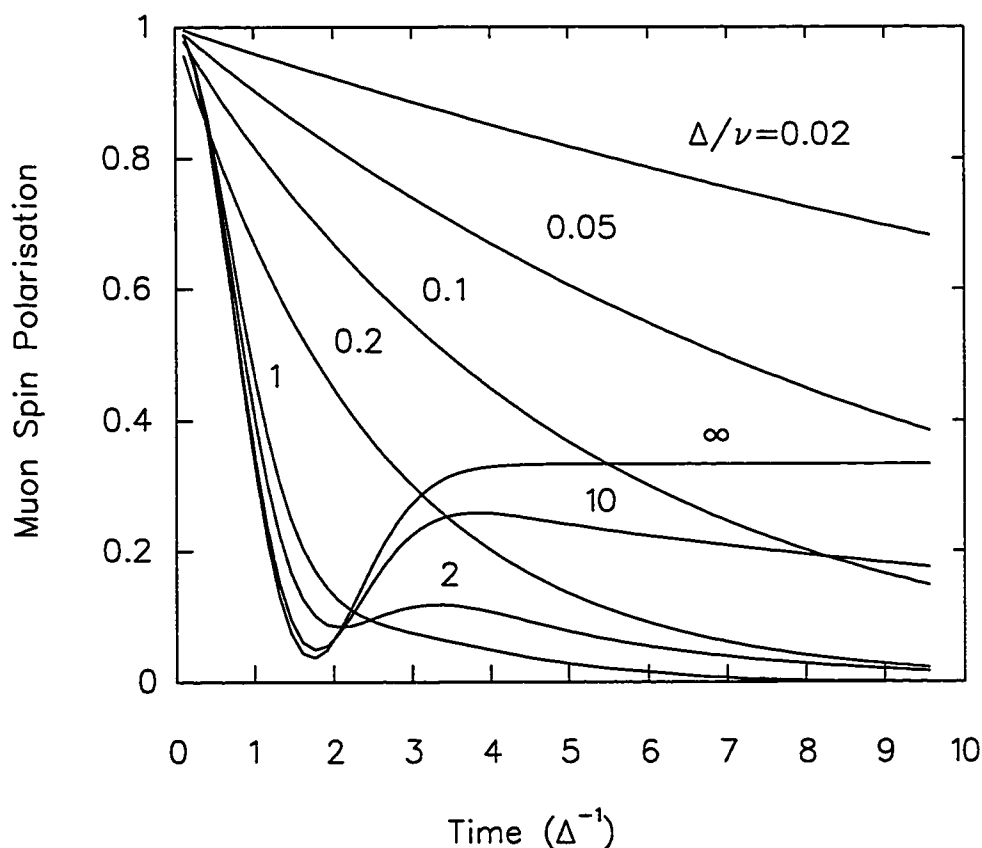


Figure 5.24: Zero field dynamic Gaussian Kubo-Toyabe functions for different field fluctuation rates. The curves are calculated using the strong collision model.

models have been assumed. For example, Gaussian-Markovian relaxation, which is perhaps the correct model for fluctuating moments, assumes a Gaussian internal field distribution with a width characterised by Δ and a field autocorrelation function which takes an exponential form $\exp(-t/\tau_c)$. The strong collision model retains the Markovian feature, *i.e.* there is no memory of the previous step, but the field now changes instantaneously to a new value. This model is usually applied to muon diffusion and is discussed by Hayano *et al.* [130]. The differences between the two models are small.

As a simple example, consider a harmonic oscillator, whose natural frequency $\omega(t)$ is modulated in some random way about ω_0 . Thus $\omega(t) = \omega_0 + \omega_1(t)$, where $\omega_1(t)$ represents the fluctuation in frequency, the average of which is zero. The resonance absorption spectrum is broadened around ω_0 by the random modulation, of amplitude Δ . Assuming that $\omega_1(t)$ is a Gaussian-Markovian stochastic process, Kubo has shown [132] that in the case of slow field modulations with correlation time τ_c , where $\Delta \cdot \tau_c \gg 1$, the relaxation function of the oscillator is well described by a Gaussian function $\exp(-\Delta^2 t^2/2)$. The resonant intensity distribution is given by its Fourier transform, also Gaussian. It turns out that in this regime the intensity distribution reflects directly the distribution of the modulation. In the limit of rapid modulation, the relaxation function has a form $\exp(-\Delta^2 \tau_c t + \text{constant})$. The resonance line becomes more Lorentzian in shape with a half width $\Delta^2 \tau_c$. However, it should be noted that for $|\omega - \omega_0| > \Delta$, the shape deviates from Lorentzian and approaches Gaussian. The problematic fact that a Lorentzian distribution has no finite second or higher moments is thus avoided. The second moment of the curve is not influenced by the modulation. However, the fourth moment increases with $1/\tau_c$. This narrowing of the lineshape may be understood by considering the following: in order for the modulation of frequency to be effective, a state should complete a cycle of 2π before the frequency changes. Hence the lifetime must be longer than $2\pi/\omega$. If this condition is not fulfilled, the modulation becomes averaged out. Bloembergen, Purcell and Pound observed that the thermal motion of atoms in liquids and some solids leads to such a narrowing of NMR lines, so called "motional narrowing" [133]. An analogous

effect in paramagnetic systems is discussed by Anderson [134], where the amplitude of the random frequency modulation is determined by the strength of the exchange interactions present.

McMullen and Zaremba [136] and subsequently Dalmas de Réotier and Yaouanc [137] developed a quantum mechanical description of the muon spin depolarisation in terms of the autocorrelation function of the local fields at the muon site(s). The interaction of the muon spin with the solid is treated perturbatively. In systems where the Hamiltonian is of the form of a steady part \mathcal{H}_0 plus a much smaller time-dependent term \mathcal{H}_1 , the equation of motion for the density matrix is given by

$$\frac{d\rho}{dt} = \frac{i}{\hbar}[\rho, \mathcal{H}_0 + \mathcal{H}_1]. \quad (5.43)$$

If \mathcal{H}_1 is 0 then

$$\rho(t) = e^{-i\mathcal{H}_0 t/\hbar} \rho(0) e^{i\mathcal{H}_0 t/\hbar}$$

so $\rho^*(t)$ is defined as $\rho(t) = e^{-i\mathcal{H}_0 t/\hbar} \rho^*(t) e^{i\mathcal{H}_0 t/\hbar}$. Hence, the Heisenberg equation describing the evolution of the system in the interaction representation is

$$\frac{d\rho^*(t)}{dt} = \frac{i}{\hbar}[\rho^*(t), \mathcal{H}_1^*(t)]. \quad (5.44)$$

Integrating,

$$\rho^*(t) = \frac{i}{\hbar} \int_0^t [\rho^*, \mathcal{H}_1^*(t')] dt' + \rho^*(0) \quad (5.45)$$

If $\mathcal{H}_1 = 0$, $\rho^*(t) = \rho(0)$, *i.e.* a constant in time, so for small \mathcal{H}_1 , $\rho^*(t)$ varies slowly. It may therefore be replaced by $\rho^*(0)$ in the integral:

$$\rho^*(t) = \rho^*(0) + \frac{i}{\hbar} \int_0^t [\rho^*(0), \mathcal{H}_1^*(t')] dt' + (i/\hbar)^2 \int_0^t \int_0^{t'} [[\rho^*(0), \mathcal{H}_1^*(t'')], \mathcal{H}_1^*(t')] dt'' dt'. \quad (5.46)$$

The complete Hamiltonian describing a single μ^+ in a solid consists of a number of terms, representing

- The solid in any externally applied magnetic field, independent of the coupling of the electrons with a probe muon. By far the most important contribution to magnetic phenomena is due to electron-electron interactions resulting in, for example,

direct or indirect dipolar and exchange interactions. The demagnetisation field, which depends on the shape of the sample, gives rise to a macroscopic term in the bulk magnetisation. The same is true of the Lorentz field arising in mean field theory, where the microscopic interactions within a material are studied within the “Lorentz sphere” only. Outside this fictitious sphere, their effect is modelled by an effective bulk magnetic field instead.

- The charge on the muon exerts an electrostatic influence over the electrons and ions; also if the surrounding nuclei have an electric quadrupole moment the electric field gradient from the muon will in general cause nuclear electric quadrupole splittings, discussed in more detail by Slichter [121].
- The μ^+ spin also interacts with the electronic and nuclear spins through magnetic hyperfine and/or dipolar couplings. The Fermi contact hyperfine interaction arises from a non-zero electron spin density at the site of the muon with an *s*-wave component in its wavefunction.
- Finally, the μ^+ spin interacts with the applied field H_{ext} .

The first term determines \mathcal{H}_s , the Hamiltonian operator of the host, while the third and fourth are given by $-\boldsymbol{\mu} \cdot \mathbf{B}(\mathbf{r})$. The operator $\mathbf{B}(\mathbf{r})$ represents the microscopic field at the position of the muon due to surrounding electrons and nuclei.

The hyperfine interaction between a nuclear spin and its own electronic shell is given by the Hamiltonian $\mathcal{H}_{HF} = \mathbf{I} \cdot \mathbf{A} \cdot \mathbf{J}$, where $\mathbf{J} = \mathbf{L} + \mathbf{S}$ is the total electronic spin of the atom and \mathbf{A} is in general a tensor. For non-magnetic ions the hyperfine interaction is due to the polarisation of filled shells and is proportional to the spin of the surrounding magnetic ions. In this case $\mathcal{H}_{HF} = \mathbf{I} \cdot \sum_j \mathbf{A}(\mathbf{R}_j) \mathbf{J}_j$, summing over the neighbouring magnetic ions. To give a net local field at the site of the muon or nucleus there must not only be a non-zero electron density $\rho(0) \equiv |\psi_s(0)|^2 \neq 0$, but also a non-zero spin density $|\psi_{s\uparrow}(0)|^2 - |\psi_{s\downarrow}(0)|^2 \neq 0$. Integrating over the electron coordinates, the calculation of the expectation value of the local field due to all the electrons requires a knowledge of the

distribution of electron and spin densities in the atom, given by ψ and also in general, in the whole crystal. Such calculations have been done using the Hartree-Fock method [138].

The coupling of the conduction electrons with the nuclear spins in metals is described by the same Hamiltonian as in non-metals, but there are special features: the conduction electrons are not localised and so have equal probability of being found in the neighbourhood of any nucleus. Thus each nuclear spin sees the magnetic fields produced by all the conduction electrons simultaneously, an ensemble average. The conduction electrons may also be polarised due to any dilute concentration of local moments present. For this so called RKKY interaction the coupling is long range and oscillatory in nature, where the coupling constant $\sim \cos(2k_F r)/r^3$, k_F being the Fermi wave vector ¹. In transition metal and rare earth elements the electrons of the inner *s*-shells may be spin polarised as a result of their exchange interaction with the electrons of the uncompensated *3d* or *4f* shell. Such *core polarisation* results in a contact hyperfine interaction. In addition, in metals and alloys the *4s* conduction electrons are also polarised.

In these systems interactions between electronic spins on different atoms or ions become extremely important and the overlap of electronic wave functions is described by an exchange integral. While the exchange interaction is a manifestation of the Pauli exclusion principle and electrostatic interactions, it can be written in terms of a scalar coupling between spins which depends only on their relative orientation, as given by Eq. (2.4). Note that the much weaker magnetic dipole-dipole interaction or an orbital contribution to the electronic spin may lead to anisotropy and a dependence of the Hamiltonian on the absolute spin orientation as well.

The local field affects the time dependent polarisation of the muon in two ways: by introducing changes in the energy levels of the muon spin and by coupling it with the lattice, which provides relaxation mechanisms. The field at the muon site $\mathbf{B}(\mathbf{r})$ may be

¹Bloembergen and Rowland [139] discuss the form of the RKKY interaction in *insulators*, which is of the form $\sim \exp[-\sqrt{(2m^*E_g)r/\hbar}] \cos(k_t r)/r^3$, where k_t is the wave vector associated with the top of the valence band and E_g the energy gap between the valence and conduction bands. The main difference arises from the exponential factor, which to a good approximation limits the interactions to nearest neighbours.

divided up into a static component with corresponding μ^+ precession frequency ω_μ and a fluctuating component $\delta\mathbf{B}$. The unperturbed part of the Hamiltonian \mathcal{H}_0 is defined as $\mathcal{H}_s - (1/2)\hbar\omega_\mu\sigma_z$, while $\mathcal{H}_1 = -(1/2)\gamma_\mu\boldsymbol{\sigma} \cdot \delta\mathbf{B}$.

Due to rapid thermalisation, the initial state of the system is taken to be a μ^+ in a spin state with polarisation \mathbf{P} but otherwise in thermal equilibrium with the solid. The corresponding density matrix of the combined muon plus crystal is

$$\rho = \rho_s \rho_\mu = \frac{e^{-\beta\mathcal{H}_s}}{\text{Tr} e^{-\beta\mathcal{H}_s}} \frac{(1 + \mathbf{P} \cdot \boldsymbol{\sigma})}{2} \quad (5.47)$$

where $\boldsymbol{\sigma}$ are the Pauli matrices. Since the residual polarisation of muons in thermal equilibrium with a Boltzmann distribution is generally very small at the fields usually applied, $\text{Tr}\{\rho_s\sigma_z(t)\} \approx 0$ and hence

$$G_{zz}(t) = \text{Tr}\{\rho_\mu\rho_s\sigma_z(t)\} \quad (5.48)$$

$$= \frac{1}{2}\text{Tr}\{\rho_s\sigma_z\sigma_z(t)\}. \quad (5.49)$$

The time evolution of σ_z can be approximated using Eq. (5.46) and the muon polarisation written as a perturbation expansion

$$G_{zz}(t) = G_{zz}^{(0)}(t) + G_{zz}^{(1)}(t) + G_{zz}^{(2)}(t) + \dots \quad (5.50)$$

The lowest order term is $G_{zz}^{(0)} = 1$; the term linear in \mathcal{H}_1 is proportional to the expectation value $\langle\delta\mathbf{B}\rangle$ and thus $G_{zz}^{(1)} = 0$ is zero by definition. Finally, using the relation for a well behaved function f

$$\int_0^t dt' \int_0^{t'} dt'' f(t' - t'') = \int_0^t d\tau (t - \tau) f(\tau) \quad (5.51)$$

where $\tau = t' - t''$, the third term is given by

$$P_z^{(2)}(t) = -\frac{\gamma_\mu^2}{2} \int_0^t d\tau (t - \tau) [\exp(i\omega_\mu\tau)\Phi_{+-}(\tau) + \exp(-i\omega_\mu\tau)\Phi_{-+}(\tau)]. \quad (5.52)$$

The previous equation is written in terms of the symmetrised local field autocorrelation function,

$$\begin{aligned} \Phi_{\alpha\beta}(\tau) &= \Phi_{\beta\alpha}(-\tau) \\ &= \frac{1}{2} [\langle\delta B_\alpha(\tau)\delta B_\beta + \delta B_\beta\delta B_\alpha(\tau)\rangle], \end{aligned} \quad (5.53)$$

where $\langle A \rangle$ indicates a thermal average

$$\frac{\text{Tr}[e^{-\beta\mathcal{H}_s} A]}{\text{Tr}[e^{-\beta\mathcal{H}_s}]} \quad (5.54)$$

of an operator A and

$$\delta\mathbf{B}(t) = e^{i\mathcal{H}_s t/\hbar} \delta\mathbf{B} e^{-i\mathcal{H}_s t/\hbar}. \quad (5.55)$$

In the fast fluctuation limit the muon spin depolarisation is often well described by an exponential function $G_{zz}(t) = G_{zz}(0) \exp[-\lambda(t)t]$, which may be expanded in powers of λ and compared with Eq. (5.50). Using this approach, it is thus possible to calculate the muon spin depolarisation function from $\Phi(\tau)$ directly². In the paramagnetic state it is often assumed that the autocorrelation function has an exponential form

$$\Phi_{+-}(\tau) = \Phi_{-+}(\tau) = 4 \frac{\Delta^2}{\gamma_\mu^2} \exp(-\nu\tau) \quad (5.56)$$

where Δ/γ_μ is the rms of the instantaneous magnetic field distribution and ν is the inverse correlation time. In this case the muon spin relaxation rate is described by [141]

$$\lambda(t)t = \frac{2\Delta^2}{(\omega_\mu^2 + \nu^2)^2} [(\omega_\mu^2 + \nu^2)\nu t + (\omega_\mu^2 - \nu^2)(1 - e^{-\nu t} \cos(\omega_\mu t)) - 2\nu\omega_\mu e^{-\nu t} \sin(\omega_\mu t)]. \quad (5.57)$$

When the fluctuation rate $\nu \gg \Delta$, the relaxation function for each magnetically equivalent muon site I can be described by a single exponential

$$e^{-\lambda_I t} \quad (5.58)$$

with a relaxation rate:

$$\lambda_I = \frac{2\Delta_I^2 \nu_I}{\nu_I^2 + \omega_\mu^2} \quad (5.59)$$

familiar from NMR. It is assumed that the field does not alter the fluctuation rate, nor the internal field distribution.

As may be seen from Eq. (5.52), the relaxation is determined by the spectral density of local field fluctuations at the muon Larmor frequency, illustrated schematically in

²The form of the correlation function is not in general trivial to calculate. If the interactions involve a great many spins, it may be well described by a diffusion process in a spin continuum. In this case, the correlation function must vary as $\tau^{-d/2}$, where d is the dimensionality of the system [140].

Fig. 5.25. The fluctuation rate of the system is characterised by the highest frequency with appreciable spectral weight and the area under the spectral density curve remains constant as ν_I varies. Hence, in the regime where $\nu_I \gg \omega_\mu$, an increase in ν_I results in a decrease in λ due to the decreased spectral weight at ω_μ . Note that λ_I is only weakly dependent on the applied field provided $\nu_I \gg \omega_\mu$. In other words, in zero field the muon spin relaxation rate is only determined by Δ^2/ν for a Gaussian distribution. For a Lorentzian field distribution in the fast fluctuation limit the muon spin relaxation is only dependent on $4a/3$ or equivalently does not show motional or exchange narrowing of the resonance line.

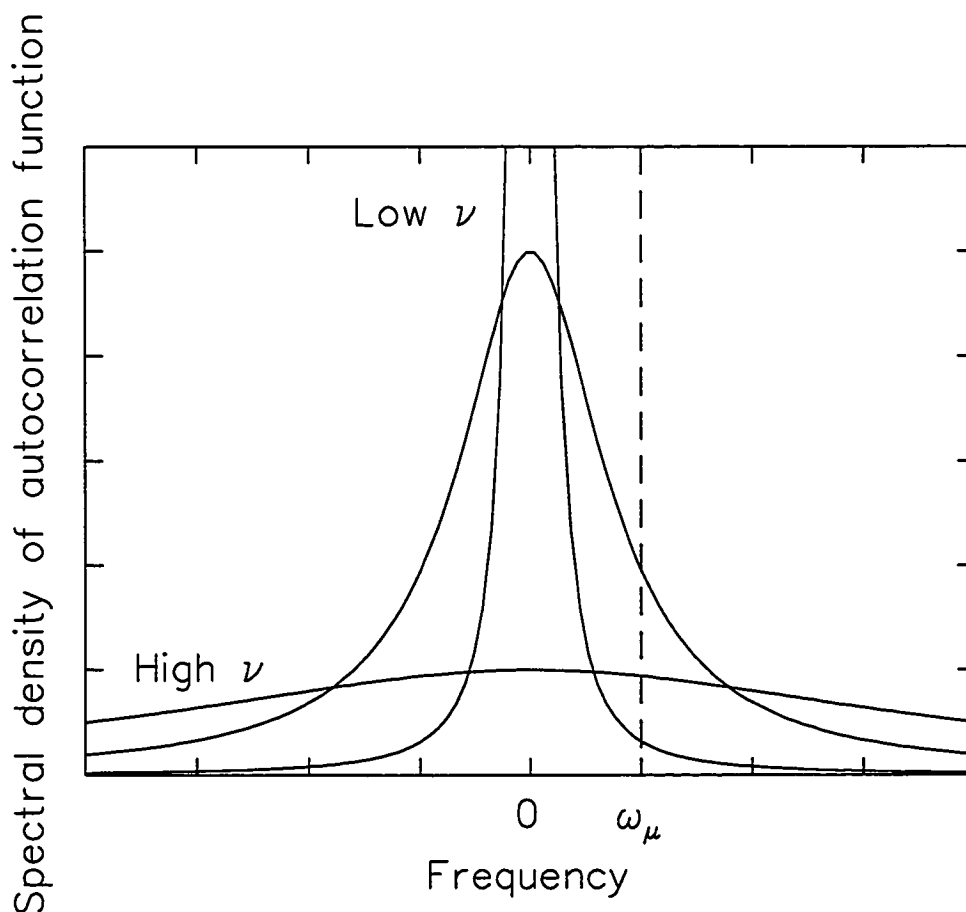


Figure 5.25: Spectral density plot for three values of fluctuation rate, illustrating the variation of T_1^{-1} with ν_I in Eq. (5.59).

As expected for a perturbation expansion, the iterative approach outlined above is

valid only for a limited range of parameters. It is an expansion in products of the internal field and time. The former is described by a field distribution which has a second moment on the scale of Δ/γ_μ , while the relevant scale for the latter is the inverse fluctuation rate ν . The expansion is therefore expected to be valid for $\Delta/\nu < 1$. Since the n th term in Eq. (5.46) involves n integrations in time, its contribution is proportional to the volume of integration $(\nu t)^n$. It is therefore anticipated that the iterative approach accurately describes the muon spin relaxation for $\nu t < 1$. The second order iteration formula and the strong collision model with the numerically exact static function give the same result when the muon jumping rate is sufficiently large. However, it can be shown that these methods do not describe the depolarisation in detail given slow fluctuation or hopping rates. Celio discusses a full quantum mechanical description [123, 124] for this regime.

Chapter 6

$Y_2Mo_{2-x}Ti_xO_7$: a comparison with AuFe

Both randomness and frustration are thought to be essential criteria for the formation of a spin glass state [23]. However, bulk magnetic susceptibility measurements [152] on the pyrochlore $Y_2Mo_2O_7$ show strong irreversible behaviour below $T_F = 22$ K, characteristic of spin glass ordering, even though the level of chemical disorder is small. In this chapter our investigation of the low temperature magnetic properties of pyrochlores $Y_2Mo_{2-x}Ti_xO_7$ using μ SR is discussed.

Spin glasses display sharp ordering features in their magnetic response but no such anomalies in their thermal response. There is a transition from a state which has rapid dynamic moment fluctuations to one where the moments are static or at most slowly changing, but there is no long range order. Different techniques are sensitive to the dynamics on various time scales. Hence it is still a matter for debate as to whether spin glasses exhibit a true static phase transition or just a dynamical gradual freezing process of the spins, where the correlation length is large but finite. Since the pioneering work of Cannella and Mydosh on AuFe [142] many random spin systems have been found to exhibit a sharp cusp in their ac susceptibility at a temperature T_F . The spatial spin correlation in these systems is basically random at any temperature, without staggered magnetisation at any particular wave-vector, or equivalently, $\langle S_j \rangle \neq 0$ but

$$\frac{1}{N} \sum_j \langle S_j \rangle \exp(ik \cdot R_j) = 0 \quad (6.60)$$

for $N \rightarrow \infty$. However, some properties are history dependent below T_F . These characteristics are thought to arise from a ground state characterised not by a single potential well representing the uniform arrangement of perfectly ordered spins, as in a ferromagnet,

but rather by an energy landscape with many nearly degenerate ground state configurations separated by barriers of random height: a “many valley” picture. There are a number of locally stable magnetisation configurations. When the system finds itself in one of these valleys, it will exhibit properties specific to that valley, but not necessarily equilibrium properties, which involve averages over all valleys with appropriate relative thermal weights.

There are a number of theoretical models which attempt to describe the behaviour of spin glasses and cope with the complexities in thermal and configuration space averages. A discussion of these is beyond the scope of this thesis. However, the Edwards-Anderson order parameter has played a central role in the development of theoretical ideas about spin glasses. Edwards and Anderson [143] suggested an “ordering in time” based on the replica method, widely used in the statistical mechanics of random systems. It makes use of the identity

$$\ln Z = \lim_{n \rightarrow 0} \frac{Z^n - 1}{n} \quad (6.61)$$

as a way around the difficulty of averaging the partition function Z . They introduced an order parameter

$$Q_{EA} = \lim_{t \rightarrow \infty} \lim_{N \rightarrow \infty} [\langle S_j(t_0) S_j(t_0 + t) \rangle]_{av} \quad (6.62)$$

where $\langle \rangle$ denotes the thermal average for one impurity moment and $[]_{av}$ represents the spatial average over different spins. This is zero if the system is ergodic and non-zero if the system is trapped in a single phase. The order parameter Q_{EA} measures the mean square single-valley local spontaneous magnetisation, averaged over all possible valleys. In contrast, the mean square local *equilibrium* magnetisation is given by $[\langle S_j \rangle^2]_{av}$, which differs from Q_{EA} in having “intervalley” contributions. A picture emerges where each spin is oriented along a preferred direction, about which it fluctuates. This behaviour may be approximated by the autocorrelation function

$$[\langle S(t) S(0) \rangle] / [\langle S(0) \rangle^2]_{av} = (1 - Q) \exp(-\nu t) + Q. \quad (6.63)$$

Each spin is assumed to be a vector sum of a static component $\sqrt{Q}S$ and a dynamic

component $\sqrt{1-Q}S$ fluctuating randomly at a rate ν . It should be noted that the Edwards-Anderson model is a mean field theory. The solution has some unphysical properties and mean field theories sometimes predict phase transitions in cases where none are observed. It is based on the assumption that a spin glass may be described by spins connected by a random distribution of bonds and does not rely on the assumption of RKKY interactions; in the former case $[\]_{av}$ indicates an average over a distribution of exchange couplings. Hence it holds for a much larger class of systems.

6.1 AuFe : an archetypal spin glass

To serve as a comparison with $Y_2Mo_2O_7$, the conventional spin glass system AuFe (0.5%) was examined. This material has already been extensively studied [10]. Nevertheless, the region below $0.1T_F$ has not been well explored and since the μ SR measurements of Uemura *et al.* [25] there have been considerable improvements in spectrometers. In particular, the separate spectra apparatus described in Chapter 4 facilitates measurements nominally free of any background signal. The μ SR measurements were made at TRIUMF in a 4He gas flow cryostat for temperatures above 2 K and in an Oxford Instruments Model 400 top loading dilution refrigerator (DR) for lower temperatures. For the DR measurements the foil was greased onto the cold finger and covered by a thin (0.025 mm) Ag foil.

Above the spin glass transition at ~ 5 K, the data are well described by a phenomenological power exponential relaxation function $G_{zz}(t) = \exp[-(t/T_1)^\beta]$. The results of fits over the limited time range of $0.05 - 9.5 \mu s$ are shown in Figs. 6.26 and 6.27. Above 50 K the data have been fitted to a single exponential function to simplify the analysis. The values of T_1^{-1} remain unchanged compared to fits where β is allowed to vary. It should be noted that it is not possible to fit data to a stretched exponential function without holding the corrected asymmetry constant, as the fitting routine will merely force β to its lower bound and the corrected asymmetry to be unphysically large. As a result, the signal amplitude has been fixed at 0.208(1) from a precession measurement in a small

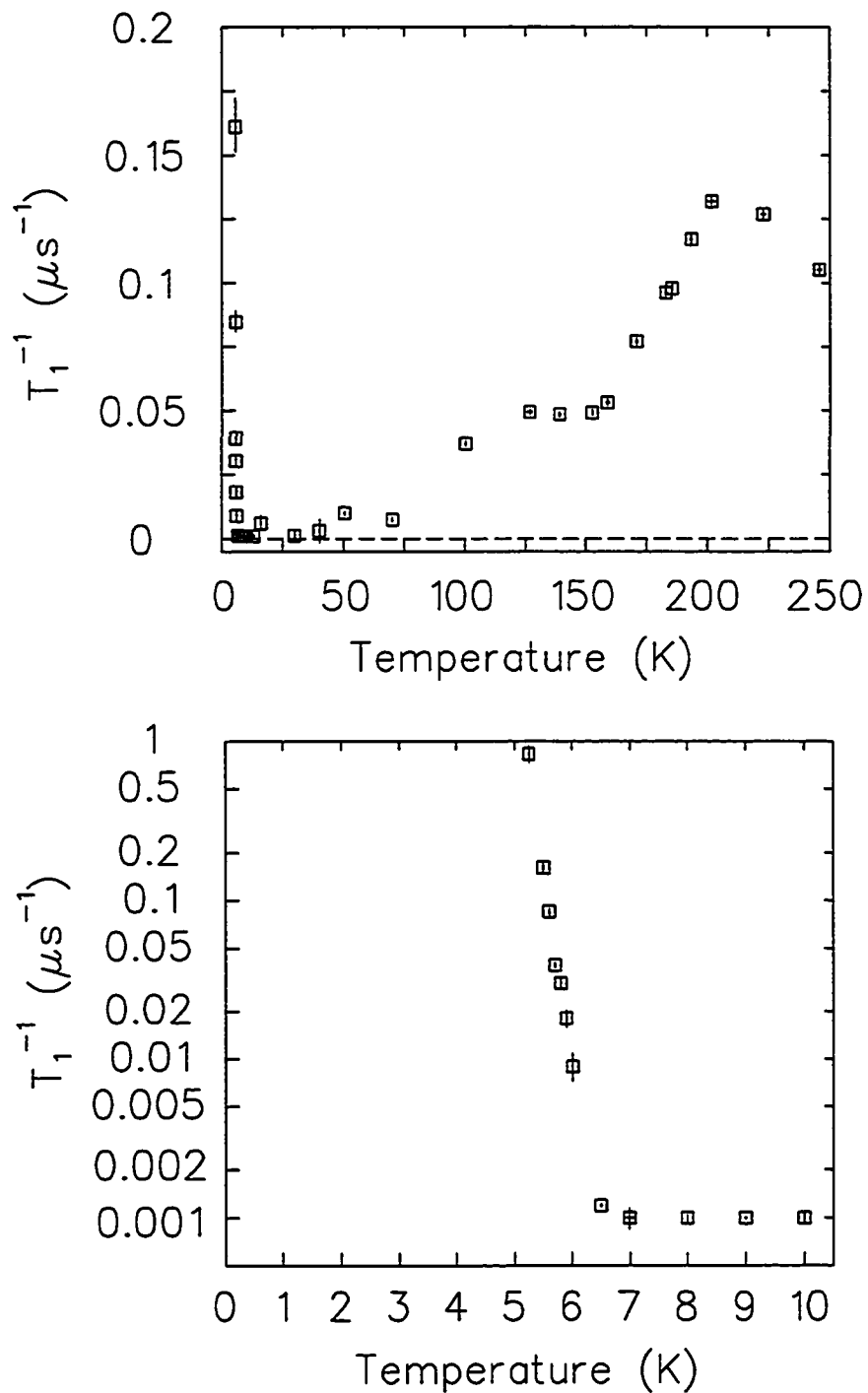


Figure 6.26: Muon spin relaxation rate T_1^{-1} above the spin glass transition temperature in AuFe (0.5%) measured in a longitudinal field of 0.005 T. The low temperature behaviour is shown on an expanded scale in the lower panel.

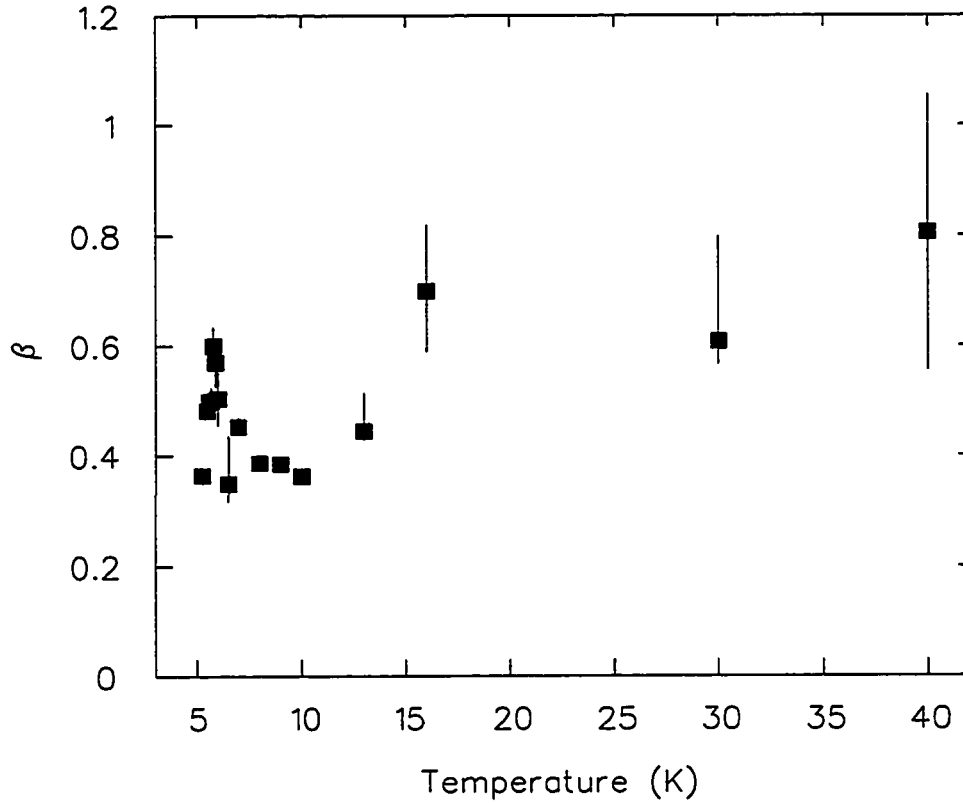


Figure 6.27: Parameter β above the spin glass transition temperature in $AuFe$ (0.5%) measured in a longitudinal field of 0.005 T. Above 50 K the data is fit to an exponential function $\exp(-t/T_1)$, while below the transition temperature Eq. (6.68) is used.

(0.001 T) transverse field at 275 K, a so called “indirect alpha calibration”.

The stretched exponential form is often used to analyse longitudinal field μ SR data. Note that this has no direct relation to stretched exponential relaxation of bulk magnetisation [29]. This behaviour indicates the presence of a distribution of relaxation times and may indicate a distribution of fluctuation rates. For example, in dilute alloys it is explained by the fact that the muon stops at different distances from the magnetic ion, which gives rise to different Gaussian field distributions. Uemura *et al.* encountered such a phenomenon in dilute alloys of magnetic ions in metals and modelled the observed *Lorentzian* internal field distribution with a distribution of *Gaussian* field distributions,

with second moments Δ^2/γ_μ^2 :

$$\rho(\Delta) = \sqrt{\frac{2}{\pi}} \frac{a}{\Delta^2} \exp\left(-\frac{a^2}{2\Delta^2}\right). \quad (6.64)$$

Assuming that the relaxation $G_{zz}^G(t)$ at each site is an exponential function $e^{-\lambda t}$ where λ_I is given by Eq. (5.59), the resultant relaxation function is found by averaging over the signals from different muon sites:

$$G_{zz}(t) = \int_0^\infty G_{zz}^G(t) \rho(\Delta) d\Delta \quad (6.65)$$

$$= \exp\left(-\left[\frac{4a^2\nu t}{\nu^2 + \omega_\mu^2}\right]^{1/2}\right). \quad (6.66)$$

In real systems the integral must have finite limits which avoid both unphysically large and small instantaneous internal fields. Computer simulations of muon spin relaxation in dilute spin glasses by Fiory [144] are consistent with this “root exponential” shape.

At high temperatures (> 50 K) the behaviour of T_1^{-1} shown in Fig. 6.26a is qualitatively similar to studies by Heffner [145] of muon diffusion in metallic hosts doped with dilute concentrations of magnetic impurities, in particular Au with Gd and Er ¹. The increase in T_1^{-1} above 50 K is attributed to muon diffusion. At temperatures of several hundred kelvin, the muon encounters many Fe ions without trapping. As the temperature is lowered the muon moves more slowly and eventually no longer diffuses close to a paramagnetic impurity within its lifetime. Between 50 and 7 K the muon appears to be static. In this region, since the iron spins are fluctuating rapidly, the observed muon spin depolarisation rate is at its lower resolution limit due to exchange narrowing, as described in Chapter 5.

As the temperature is reduced below 7 K, the muon spin relaxation rate increases rapidly to a maximum at 5.25 K. This is due to critical slowing down of the iron spin fluctuations associated with approaching a continuous phase transition. Below 5.25 K

¹There are constraints on such studies in pure non-magnetic metals: as the muon motion becomes too rapid the nuclear dipolar field inhomogeneities are averaged to zero and no depolarisation is produced. Furthermore, many host metals (like Ag and Au) have negligible nuclear moments and information on muon diffusion is very difficult to obtain in the pure host. Introducing the larger electronic moment of dilute impurities means larger diffusion rates can be studied independent of the host nuclear moments.

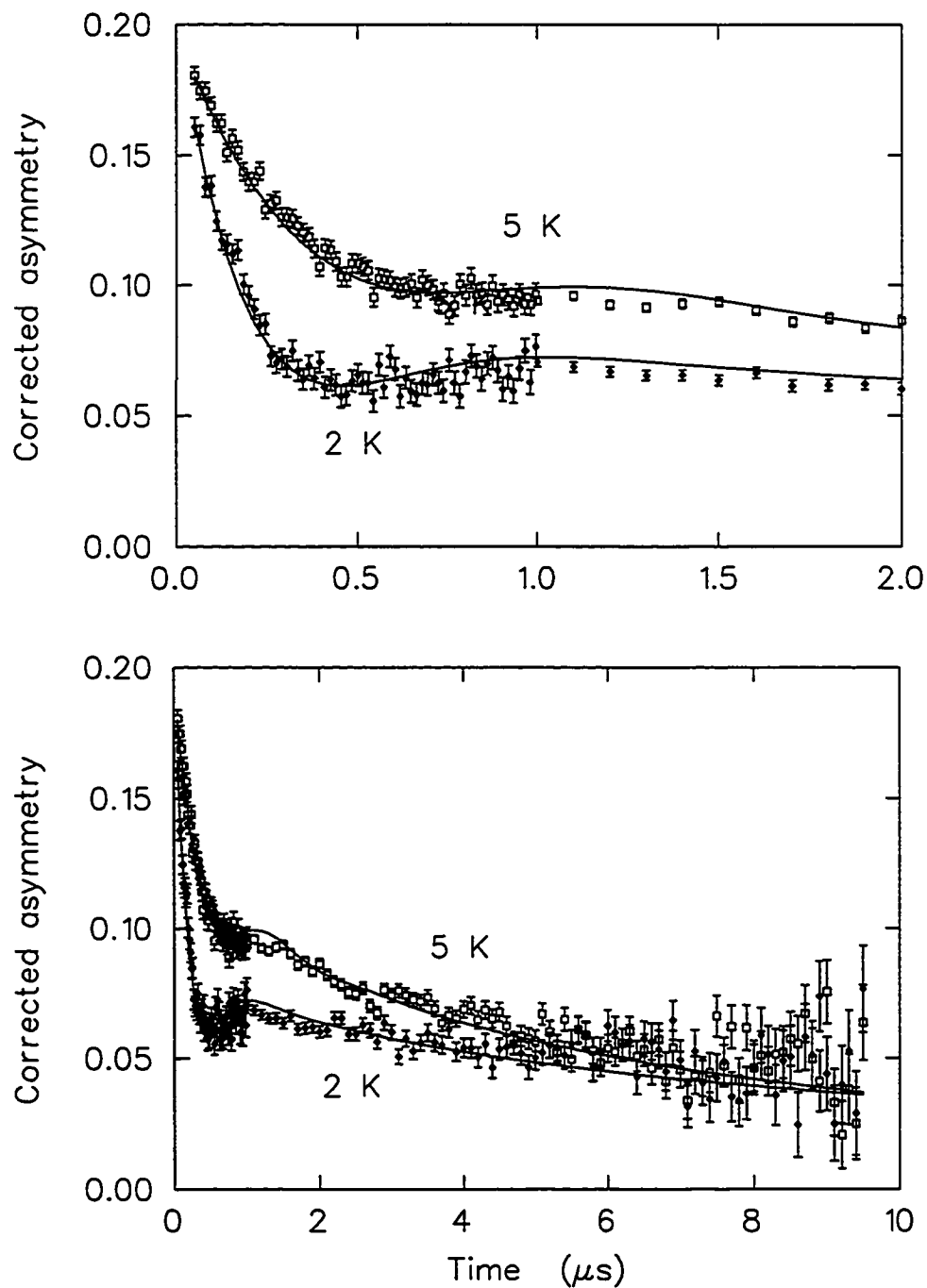


Figure 6.28: Typical μ SR spectra in $AuFe$ (0.5%) in 0.005 T longitudinal field. The solid lines are fits to Eq. (6.68).

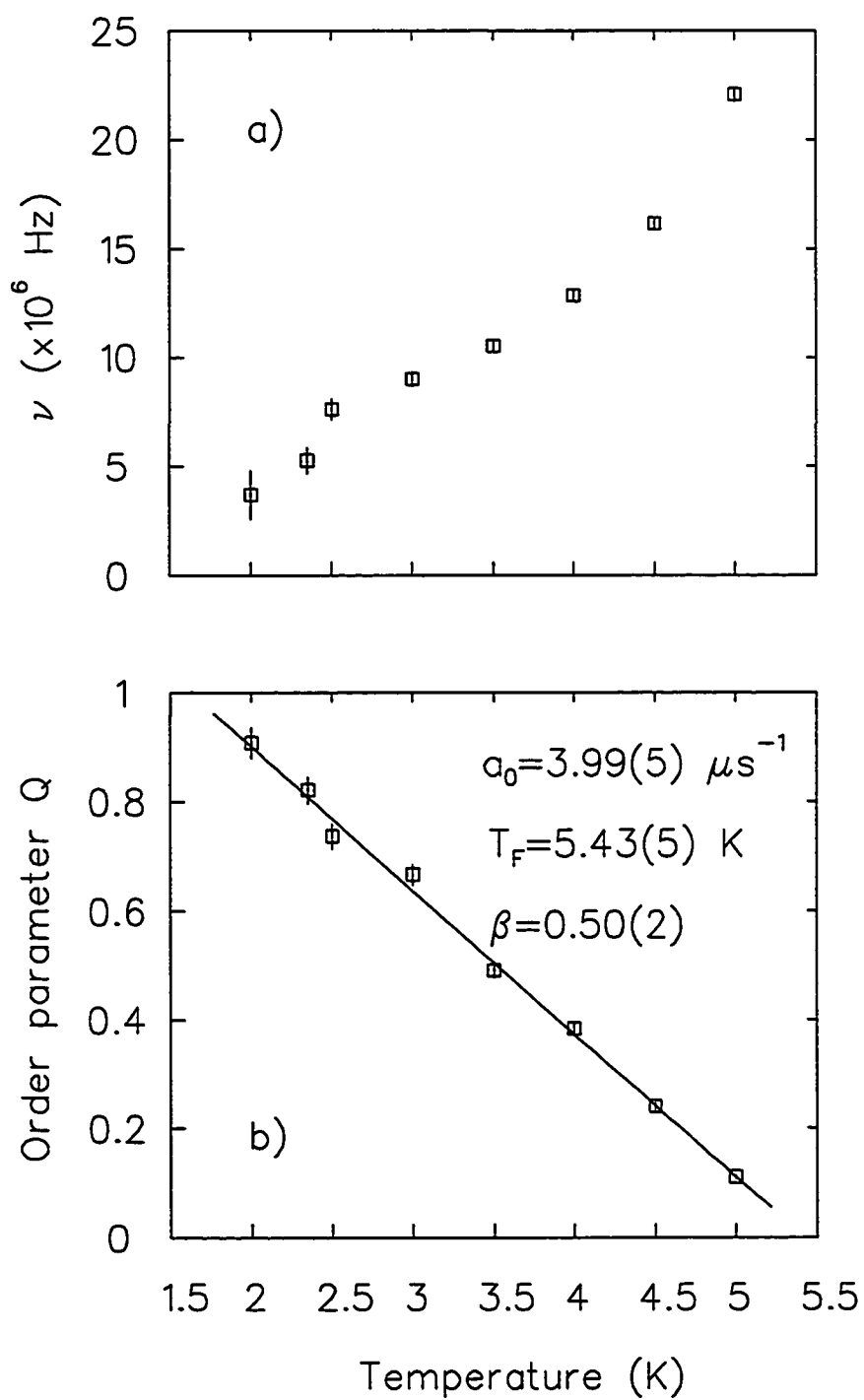


Figure 6.29: a) Fluctuation rate and b) spin glass order parameter in AuFe (0.5%) measured in a longitudinal field of 0.005 T.

several distinctive features develop in the μ SR spectra (see Fig. 6.28). There is a rapid initial muon spin depolarisation, followed by a minimum and partial recovery and subsequent decay of the so called “1/3 tail”. The spectra have many features in common with the Kubo Toyabe functions shown in Fig. 5.23 and are evidence of coexisting static and fluctuating internal fields below the spin glass transition, consistent with the Edwards Anderson model of spin glasses. As the temperature is reduced, the amplitude of the initial rapid depolarisation increases and the position of the minimum moves back earlier in time, indicating that the size of the static component increases at the expense of the dynamic one in the manner of an order parameter. For a particular muon site such behaviour may be described as the product of the Kubo Toyabe function [Eq. (5.40)] due to the static internal field $\Delta_s = \sqrt{Q}\Delta$ and Eqs. (5.58) and (5.59), where $\Delta_d = \sqrt{1-Q}\Delta$ is the instantaneous local field of the dynamic part. The stochastic behaviour of the dipolar fields at muon sites is essentially the same as that of the impurity spins themselves at all temperatures [146]. In zero applied field, Uemura *et al.* [25] have calculated the overall spin glass relaxation function by averaging over the muon sites to give

$$\begin{aligned}
G_{zz}^{SG}(t) &= \int_0^\infty \sqrt{\frac{2}{\pi}} \frac{a}{\Delta^2} \exp\left(-\frac{a^2}{2\Delta^2}\right) \left[\frac{1}{3} + \frac{2}{3}(1 - Q\Delta^2 t^2) \exp\left(-\frac{Q\Delta^2 t^2}{2}\right) \right] \\
&\quad \cdot \exp\left(-\frac{2(1-Q)\Delta^2 t}{\nu}\right) d\Delta \\
&= \frac{1}{3} \exp\left(-\left[\frac{4a_d^2 t}{\nu}\right]^{1/2}\right) + \\
&\quad \frac{2}{3} \exp\left(-\left[a_s^2 t^2 + \frac{4a_d^2 t}{\nu}\right]^{1/2}\right) \left[1 - a_s^2 t^2 \left(a_s^2 t^2 + \frac{4a_d^2 t}{\nu}\right)^{-1/2} \right], \quad (6.67)
\end{aligned}$$

where $a_s = \sqrt{Q}a$ and $a_d = \sqrt{1-Q}a$. A calculation for finite longitudinal fields has been performed by the author in a similar way to yield

$$\begin{aligned}
G_{zz}^{SG}(t) &= \int_0^\infty \sqrt{\frac{2}{\pi}} \frac{a}{\Delta^2} \exp\left(-\frac{a^2}{2\Delta^2}\right) \exp\left(-\frac{2(1-Q)\Delta^2 \nu t}{\nu^2 + \omega_\mu^2}\right) \\
&\quad \left(1 - \frac{2\Delta_s^2}{\omega_\mu^2} \left(1 - \exp\left(-\frac{\Delta_s^2 t^2}{2}\right) \cos \omega_\mu \tau \right) + \right. \\
&\quad \left. \frac{2\Delta_s^4}{\omega_\mu^3} \int_0^\infty \exp\left(-\frac{\Delta_s^2 \tau^2}{2}\right) \sin \omega_\mu \tau d\tau \right) d\Delta
\end{aligned}$$

$$\begin{aligned}
&= \exp\left(-\left[\frac{4a_d^2\nu t}{\nu^2 + \omega_\mu^2}\right]^{1/2}\right) - \frac{2a_s^2}{\omega_\mu^2} \left(\frac{\nu^2 + \omega_\mu^2}{4a_d^2\nu t}\right)^{1/2} \exp\left(-\left[\frac{4a_d^2\nu t}{\nu^2 + \omega_\mu^2}\right]^{1/2}\right) + \\
&\frac{2a_s^2}{\omega_\mu^2} \cos \omega_\mu t \left(\frac{\nu^2 + \omega_\mu^2}{4a_d^2\nu t + a_s^2 t^2(\nu^2 + \omega_\mu^2)}\right)^{1/2} \exp\left(-\left[\frac{4a_d^2\nu t}{\nu^2 + \omega_\mu^2} + a_s^2 t^2\right]^{1/2}\right) + \\
&\frac{2a_s^4}{\omega_\mu^3} \int_0^t d\tau \sin \omega_\mu \tau \left(\frac{\nu^2 + \omega_\mu^2}{4a_d^2\nu t + a_s^2 \tau^2(\nu^2 + \omega_\mu^2)}\right)^{3/2} \exp\left(-\left[\frac{4a_d^2\nu t}{\nu^2 + \omega_\mu^2} + a_s^2 \tau^2\right]^{1/2}\right) + \\
&\frac{2a_s^4}{\omega_\mu^3} \int_0^t d\tau \sin \omega_\mu \tau \left(\frac{\nu^2 + \omega_\mu^2}{4a_d^2\nu t + a_s^2 \tau^2(\nu^2 + \omega_\mu^2)}\right) \exp\left(-\left[\frac{4a_d^2\nu t}{\nu^2 + \omega_\mu^2} + a_s^2 \tau^2\right]^{1/2}\right).
\end{aligned} \tag{6.68}$$

This makes use of the generalisation of Eq. (5.40) to include finite longitudinal fields, as given by Hayano *et al.* [130]. Equations (6.67) and (6.68) are plotted in Fig. 6.30 for different values of ω_μ and Δ . Note that for $Q < 1$ the amplitude of the slowly relaxing tail is less than 1/3 in zero applied field. The reduction in the amplitude of the tail depends on the value of ν . This may be seen by considering the limit $\nu \rightarrow 0$, where the dynamic contribution to the depolarisation becomes a constant and Eq. (6.67) simplifies to the static Kubo-Toyabe function for a Lorentzian internal field distribution. The non-relaxing tail then has an amplitude of 1/3 of the total signal.

Fitting Eq. (6.68) to the data between 2 and 5 K, the fluctuation rate of the residual dynamic component and the order parameter Q may be extracted, as illustrated in Fig. 6.29. It is interesting to note that ν decreases monotonically as the order parameter increases. In conventional antiferromagnets such as MnF_2 , the magnon frequency increases as the temperature is lowered [147], while the magnon population factor rapidly decreases. Using Eq. (6.68) to analyse the spectra taken in the dilution refrigerator below 2 K, the χ^2 minimisation routine would not converge, as ν is close to zero. However, as may be seen in Fig. 6.31, the data are characterised by rapid depolarisation of 2/3 of the signal, followed by a slowly relaxing 1/3 component. The relaxation rate of the 1/3 tail decreases steadily to zero as the temperature is lowered, such that the data is well described by the generalisation of Eq. (5.42) (see Ref. [25]) at the base temperature of

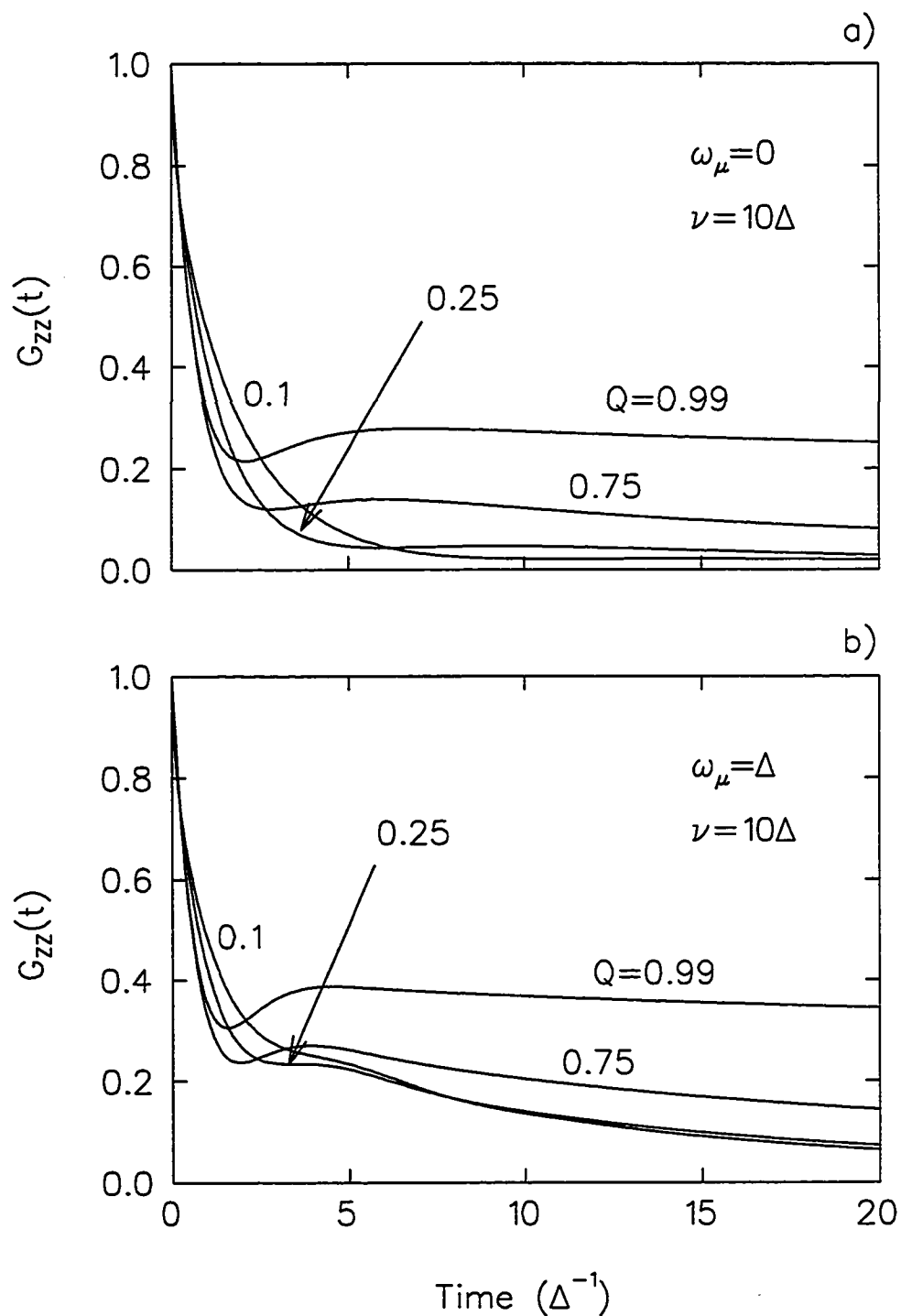


Figure 6.30: Muon spin depolarisation functions appropriate for dilute spin glasses in a) zero applied field [Eq. (6.67)] and b) longitudinal field $\omega_\mu = \Delta$ [Eq. (6.68)].

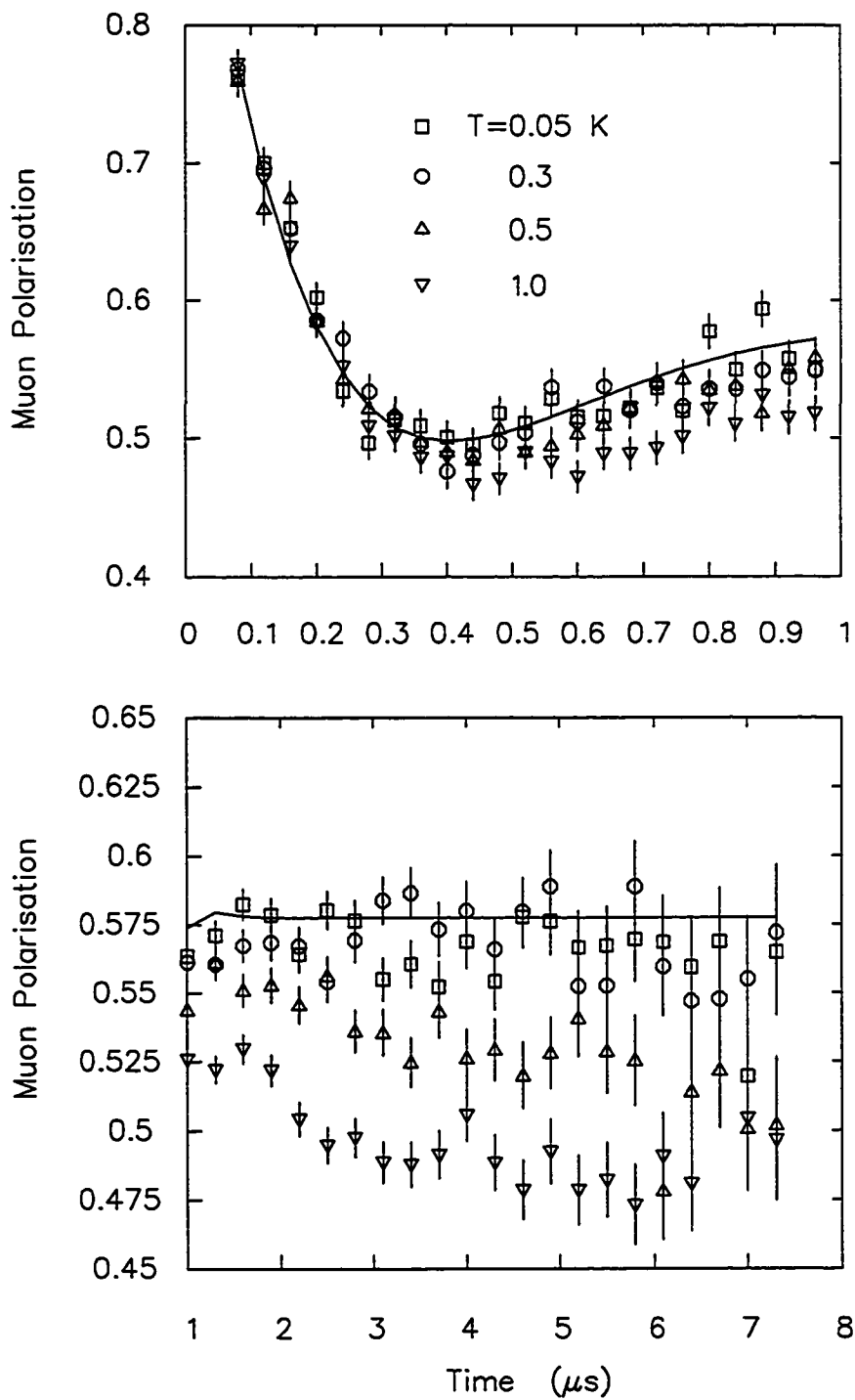


Figure 6.31: Typical μ SR spectra in AuFe (0.5%) in 0.005 T longitudinal field.

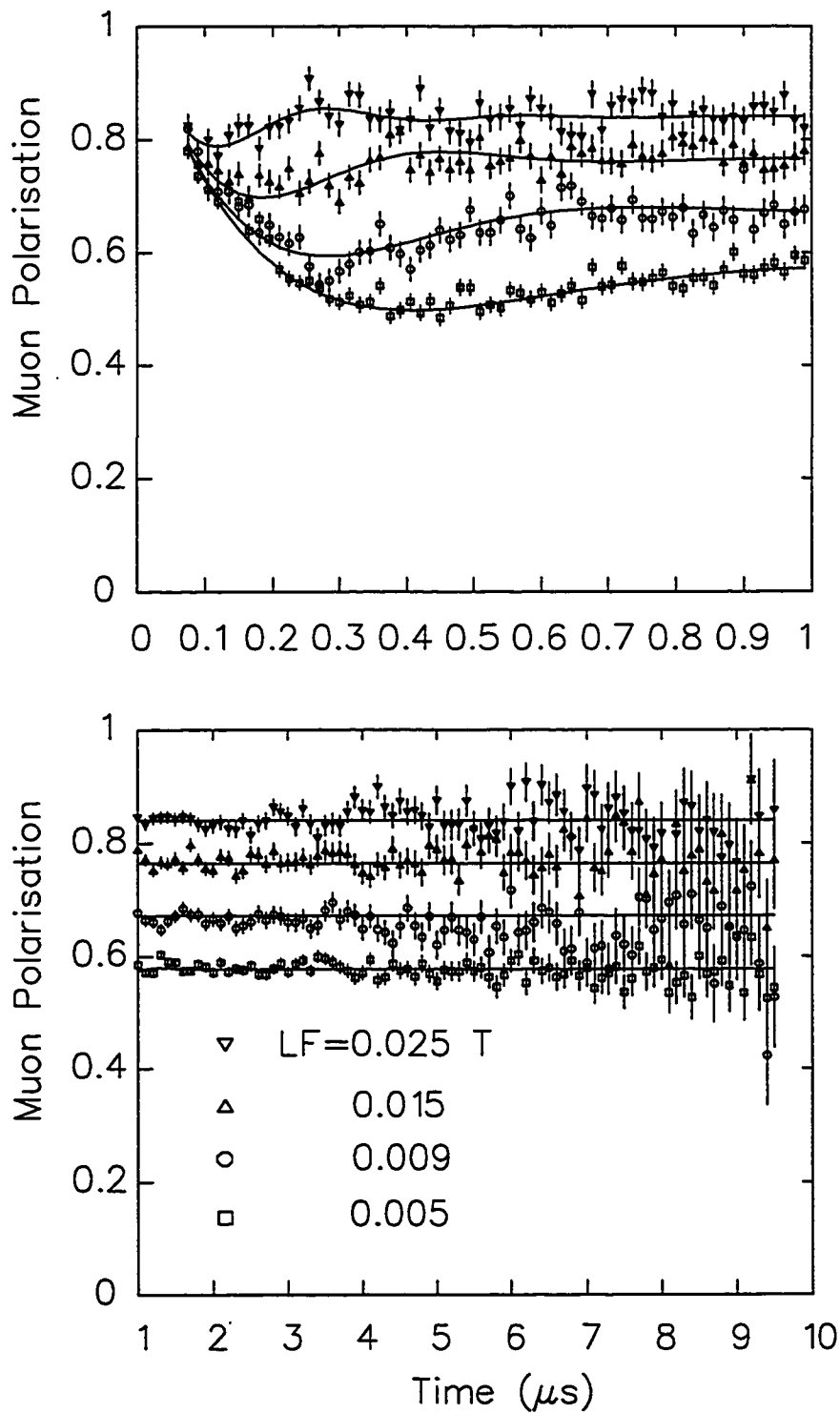


Figure 6.32: Typical μ SR spectra in AuFe (0.5%) at 0.025 K in various longitudinally applied magnetic fields.

25 mK (Fig. 6.32). This indicates that, on the timescales probed by μSR , the internal fields become completely “static” and characterised by a value of $a_s = 3.34(5) \mu\text{s}^{-1}$. The size of internal field, which scales linearly with impurity concentration, agrees reasonably well with an estimate of the theoretical dipolar width by Uemura *et al.* [25] of $\sim 5.6 \mu\text{s}^{-1}$ for a 1% sample of \underline{AuFe} . The muon Larmor frequency associated with the applied magnetic field of 0.005 T is thus a significant fraction of the internal field. The “tails” of the spectra thus have an amplitude larger than 1/3rd of the signal, as expected from the decoupling curves shown in Fig. 5.23. The main aim of the experiments was to study the relaxation due to the residual dynamic component and hence it proved advantageous to increase its amplitude.

It is appropriate to comment on the increase in Q with decreasing temperature. Attempting to extract critical exponents is prone to error, as the extent of the critical region depends on many things. For an isotropic Heisenberg system it is on the order of $\pm 1/z$, where z is the number of nearest neighbours and may thus range from 8 – 25% of the transition temperature. Nevertheless, it is interesting to note that the behaviour in the order parameter is well described by the function

$$a_s = a_0 \left(\frac{T_F - T}{T_F} \right)^\beta \quad (6.69)$$

over the whole range between 5 and 2 K, as shown in Fig. 6.29b. In this instance β is the zero field magnetisation critical exponent, not to be confused with the parameter used in fitting to a stretched exponential function. Interestingly, the value of β of 0.50(2) agrees well with Monte Carlo simulations by Ogielski [148] for a three dimensional Ising spin glass with a $\pm\mathcal{J}$ distribution of nearest neighbour bonds, as well as critical exponents based on finite size scaling calculated by Bhatt and Young [149]. Experimentally, values of β for various spin glasses are more scattered, ranging from 0.2 – 1.4 [10].

Surprisingly, after all these years the whole picture of dilute metallic spin glasses has recently been called into question. Neutron scattering measurements by Werner [150] show evidence for *sharp* magnetic peaks in some dilute spin glasses, indicating the presence of antiferromagnetic spin density waves, as well as small ferromagnetic clusters

arising from atomic short range order. Such spin density waves were first predicted by Overhauser [151]. These findings and their interpretation are currently subject to debate.

6.2 $Y_2Mo_2O_7$

Despite its low level of disorder, the magnetic behaviour in $Y_2Mo_2O_7$ is found to be close to that observed in conventional random spin glasses. Specifically, irreversible behaviour is observed in field cooled and zero field cooled bulk dc magnetic susceptibility measurements below $T_F \approx 22$ K [152]. A Curie-Weiss fit to high temperature (300-1000 K) susceptibility data [81] yields $\Theta_{CW} = -200$ K, indicating strong antiferromagnetic interactions. It should be pointed out that estimates of the exchange coupling based on Θ_{CW} may vary by orders of magnitude. Raju *et al.* [152] extract a value of $\Theta_{CW} = -28$ K using measurements below 300 K. High temperature measurements are thus clearly crucial.

A large static internal magnetic field with a very broad distribution develops below the spin glass transition temperature T_F , such that no coherent muon spin precession is observed. The data are not consistent with superparamagnetism, where no discontinuity in the dc susceptibility is anticipated [153]. Nor is a quantum spin liquid a possible explanation, where the ground state is a fluid of spin pairs correlated together into singlets [43]; in that case no large internal magnetic fields would be expected for $T \ll T_F$.

The μ SR measurements were made at TRIUMF in a 4He gas flow cryostat for temperatures above 2 K and in an Oxford Instruments Model 400 top loading dilution refrigerator (DR) for lower temperatures. For the DR measurements the pressed polycrystalline pellets were varnished onto an Ag plate and covered by 0.025 mm thick Ag foil; the Ag plate was then bolted to the cold finger. The present measurements were made in a small longitudinal field of 0.02 T to quench any effect from static nuclear dipolar fields in the sample holder, whose associated spin relaxation would have complicated the observed spectra, giving rise to an additional signal like the Kubo Toyabe function shown

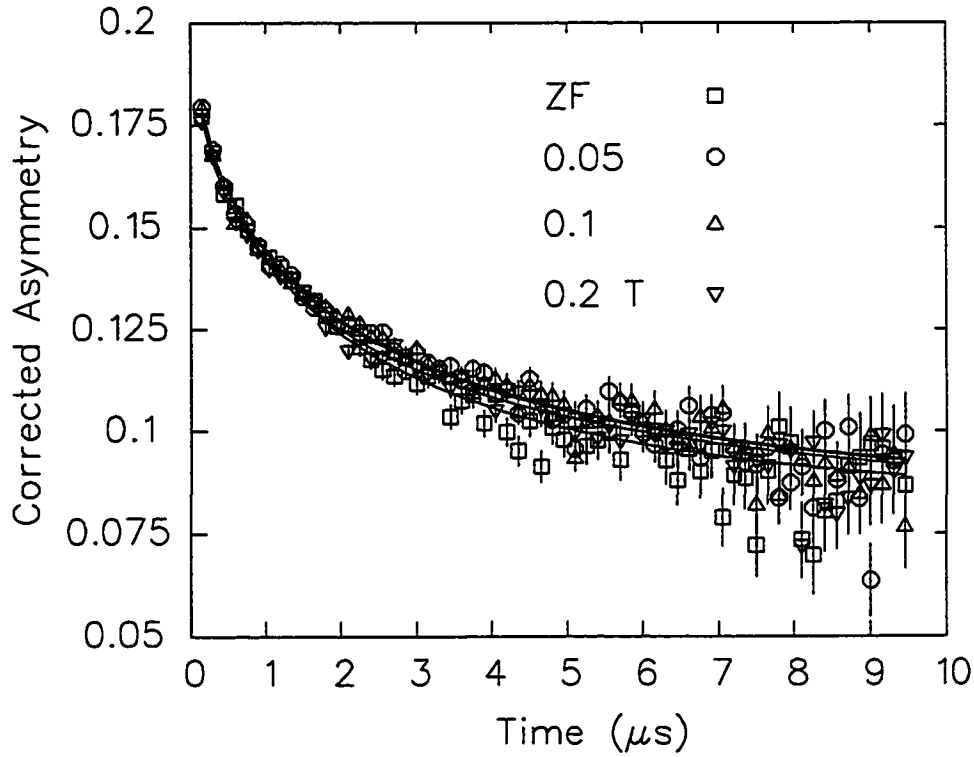


Figure 6.33: Typical longitudinal field μ SR spectra in $Y_2Mo_2O_7$ at 27.5 K.

in Fig. 5.23.

Figure 6.33 shows several typical μ SR spectra in $Y_2Mo_2O_7$. Above $T_F = 22$ K the observed spin relaxation is attributed to rapid fluctuations of the internal magnetic field due to Mo^{4+} moments in the paramagnetic phase. When the fluctuation rate ν is much greater than the internal field Δ , the relaxation function for each magnetically equivalent muon site I can be described by a single exponential $e^{-\lambda_I t}$ with a relaxation rate given by Eq. (5.59); the experimental $G_{zz}(t)$ is a convolution of such functions over the distribution of Δ . The theoretical relaxation rate is only weakly dependent on the applied field provided $\nu_I \gg \omega_\mu$; this is consistent with the absence of any observed field dependence in the spectra for temperatures well above T_F . Above the transition temperature Fig. 6.34a shows the average muon spin relaxation rate in $Y_2Mo_2O_7$ obtained from fits to a stretched exponential relaxation function

$$G_{zz}(t) \sim \exp[-(t/T_1)^\beta] \quad (6.70)$$

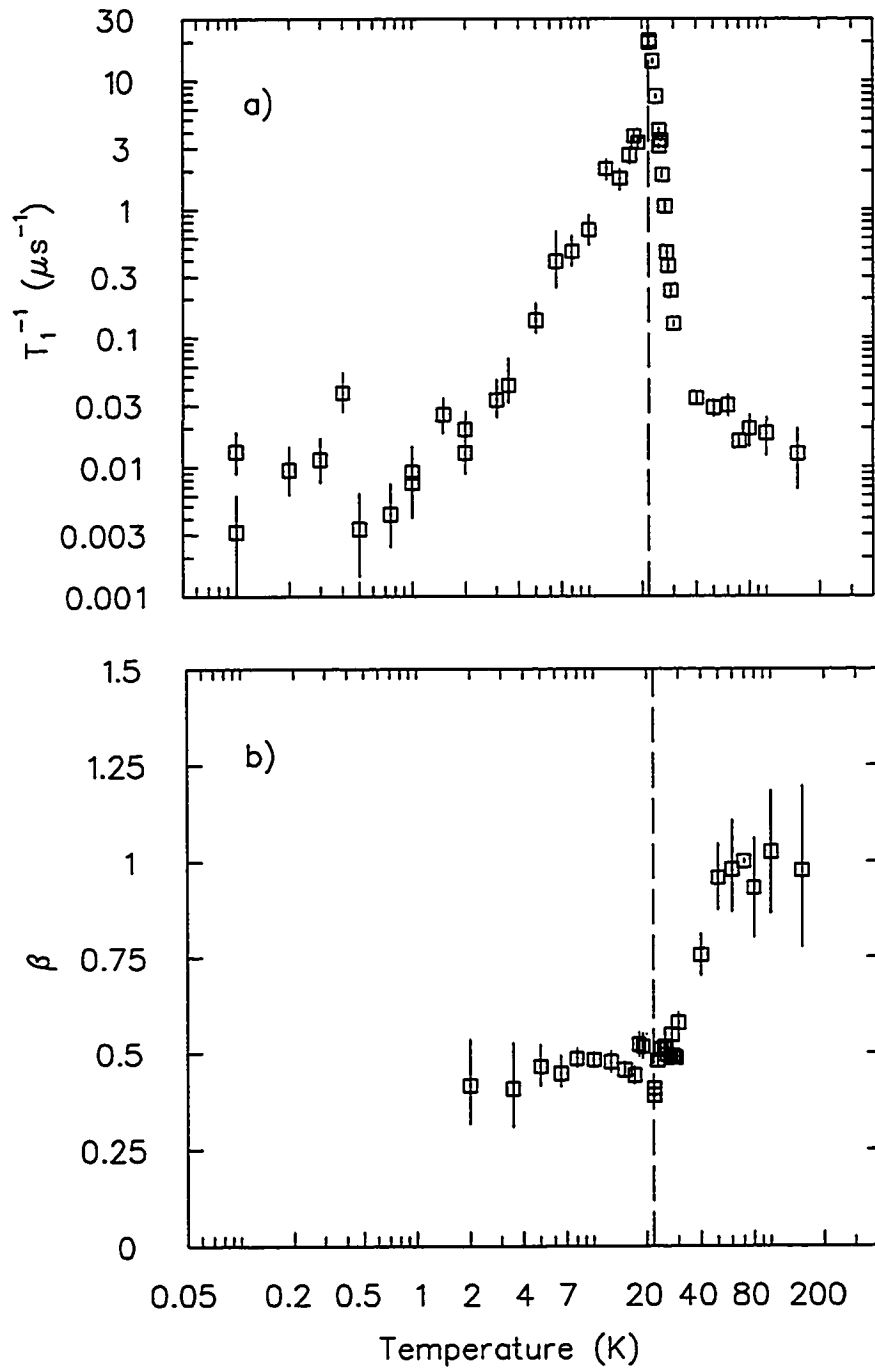


Figure 6.34: a) Muon spin relaxation rate and b) β as a function of temperature in $Y_2Mo_2O_7$ measured in a longitudinal field of 0.02 T. Below 2 K β is held constant at a value of 0.47.

over a time interval of 0.01 to 10 μs , where $\lambda = T_1^{-1}$. The full corrected asymmetry, which includes a contribution from a silver background signal, is held constant above 22 K at a value of 0.20(1) found from an “indirect alpha calibration” at 70 K. Below the spin glass transition temperature the asymmetry was held constant at a value of 0.20/3, fitting the data to a stretched exponential function between 0.1 and 10 μs .

Below ~ 50 K, $P_z(t)$ deviates somewhat from a single exponential (see Fig. 6.34b), the observed value of β decreasing with decreasing temperature. Similar behaviour has recently been observed in other dense spin glasses like AgMn and AuFe [29] and is discussed in greater detail in the next section. While non-exponential relaxation is anticipated in a dilute spin glass due to the distribution in Δ , β is expected to be temperature *independent* at a value of 1/2.

In the paramagnetic phase above 50 K one may use Eq. (5.59) to estimate the average fluctuation rate of the moments. For example with $\Delta/\gamma_\mu = 0.061$ T (see below) one obtains the fluctuation rates shown in Fig. 6.35. Note the sharp rise in the average T_1^{-1} and corresponding decrease in the Mo^{4+} fluctuation rate as one approaches $T_F = 22$ K. These values are within an order of magnitude of the relaxation rate of the thermal spin fluctuation spectrum measured by inelastic neutron scattering at $Q = 0.44 \text{ \AA}^{-1}$ [154]. Considering the statistical error of roughly 19% in the results from neutron scattering and the systematic errors in both measurements, the agreement is reasonable. From this it may be concluded that both techniques are sensitive to the same quantity in this material, *i.e.* the Mo^{4+} moment fluctuation rates. Note that the μSR results are averaged over all Q . Above 55 K the scattering function $S(Q, \omega)$ displays a rather broad frequency spectrum. In the temperature regime between 45 K and the spin glass transition, low energy spin fluctuations are enhanced and the frequency spectrum progressively sharpens as the temperature is reduced. There is no further development in spatial correlations below ~ 40 K. At lower temperatures it is the temporal correlations which evolve independently; in other words, the q and ω dependences become decoupled. This picture recurs in a number of geometrically frustrated systems. The downshift in the spectral

weight of fluctuations is another common theme. It is interesting to note that this temperature regime, *i.e.* below 40 K corresponds to the onset of non-exponential muon spin relaxation. Recent measurements of the dc magnetisation of $Y_2Mo_2O_7$ show a diver-

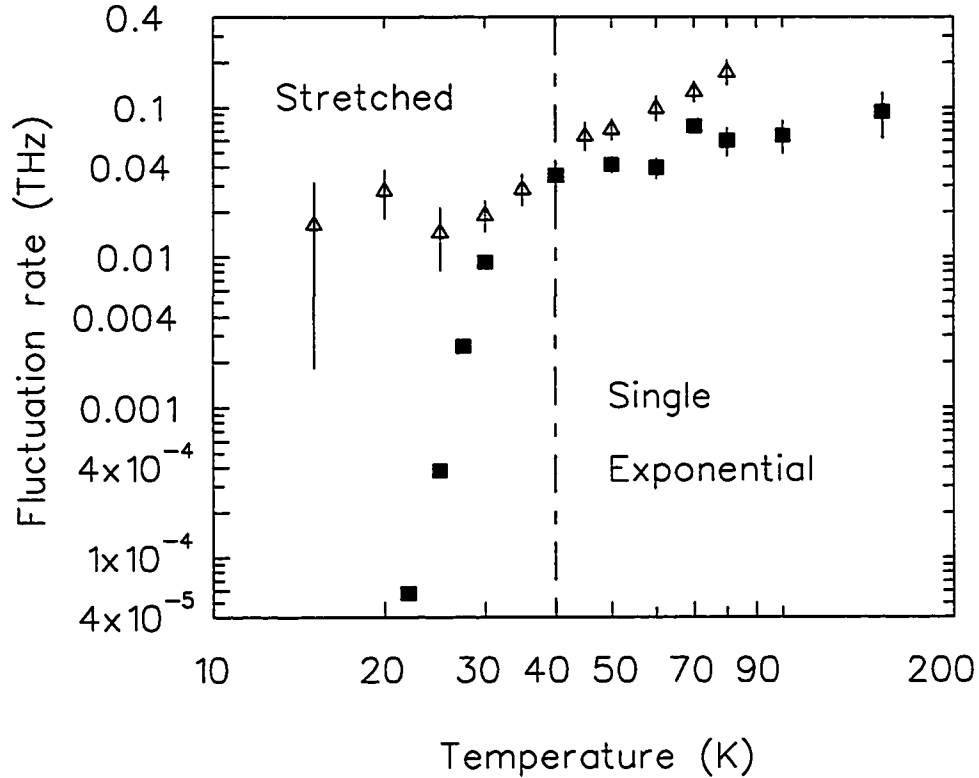


Figure 6.35: Fluctuation rate as a function of temperature in $Y_2Mo_2O_7$. The triangles indicate values from inelastic neutron scattering measurements by Gardner *et al.* (Ref. [154]). The values obtained by μ SR (square symbols) are extracted using Eq. (5.59) from measurements in a longitudinal field of 0.02 T. The area to the left of the dot-dashed line indicates where the concept of a single fluctuation rate is likely no longer appropriate.

gent non-linear susceptibility χ_3 at $T \approx 22$ K [155, 156], which is a signature of a true thermodynamic spin glass phase transition [157].

The muon spin relaxation function below T_F (see Fig. 6.36) is characterised by rapid damping of 2/3 of the initial polarisation, followed by slow relaxation of the remaining 1/3 component. This is a characteristic signature of a highly disordered magnetic state in which the moments are quasi-static on the timescale of the muon lifetime. The curves

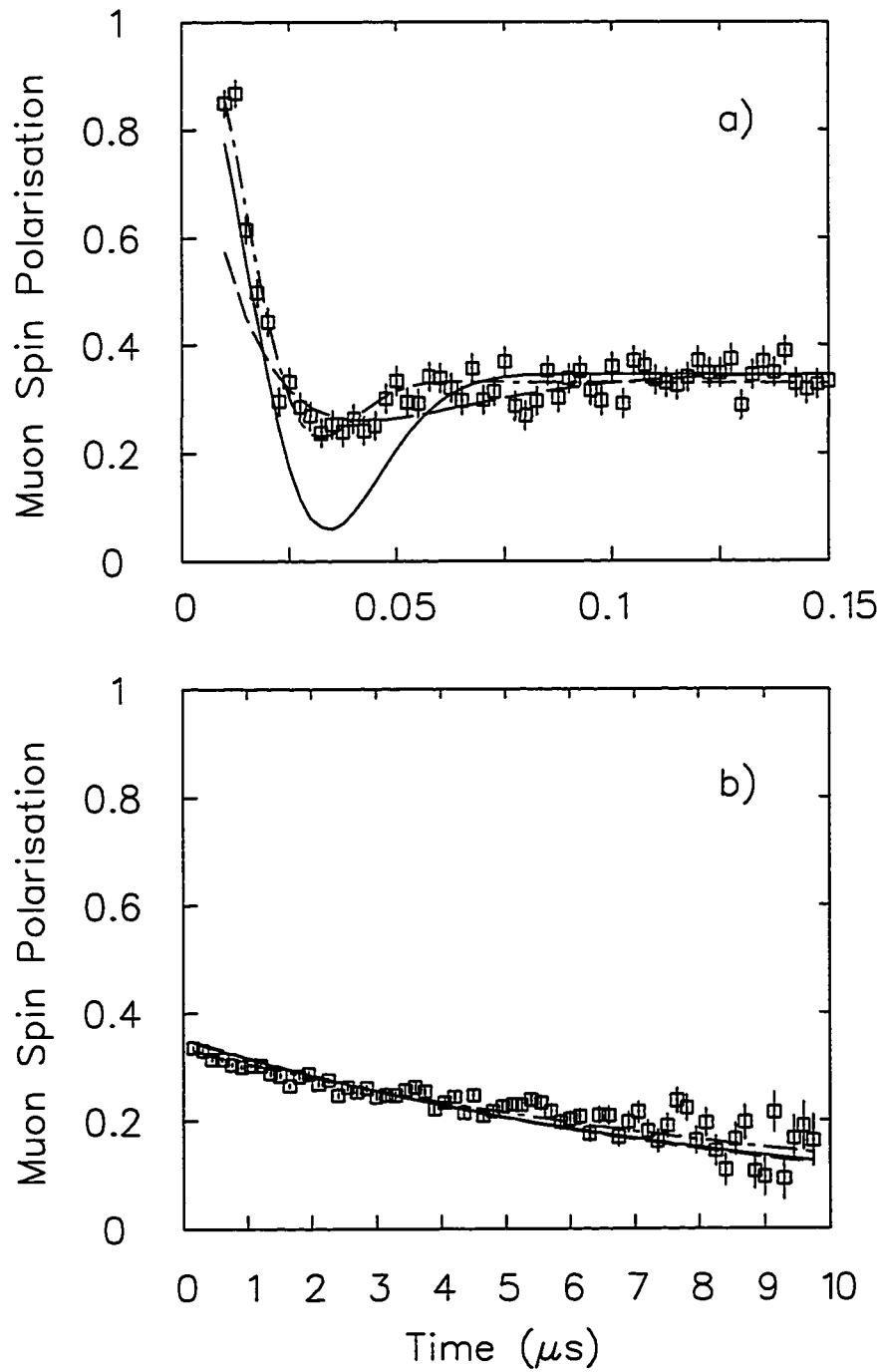


Figure 6.36: a) Short time behaviour of the muon polarisation in $Y_2Mo_2O_7$ at 2.32 K and b) the depolarisation of the 1/3 component. The solid, dashed and dot-dashed lines are fits which are described in the text.

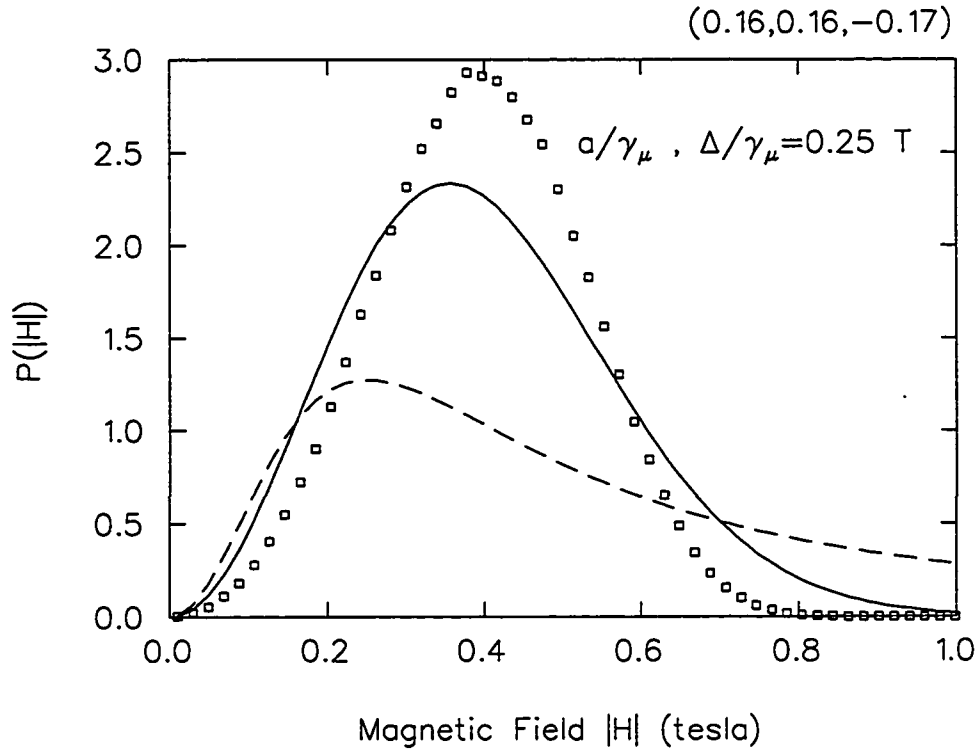


Figure 6.37: Simulation of the magnetic field at the muon site (0.16, 0.16, -0.17) assuming randomly oriented spins of magnitude $2.8 \mu_B$. For comparison, the solid and dashed lines indicate internal fields distributions with Gaussian and Lorentzian $\hat{x}, \hat{y}, \hat{z}$ components respectively.

show fits of the data at 2.32 K to Eqs. (5.40) (solid line) and (5.42) (dashed line), modified slightly to include the small external field of 0.02 T and multiplied by an exponential function. The dot-dashed line is the function

$$G_{zz}(t) = \frac{1}{3} \exp(-\lambda t) + \frac{2}{3} \exp(-\sigma^2 t^2) \cos(2\pi f t). \quad (6.71)$$

appropriate for modelling systems with long range order. The fit to Eq. (5.40) gives a value $\sqrt{\langle B_i^2 \rangle} = \Delta/\gamma_\mu = 0.061(2) \text{ T}$, which corresponds to an average field strength $\sqrt{\langle B^2 \rangle} = \sqrt{8/\pi} \Delta/\gamma_\mu = 0.097(3) \text{ T}$. Note however that the dip in $G_{zz}(t)$ at $0.036 \mu\text{s}$ is not as deep as predicted by the modified Eq. (5.40), indicating the distribution of internal fields is more complicated than a single Gaussian. Nor does a Lorentzian internal field accurately describe the data. The overall best fits were obtained using Eq. (6.71), where $\sigma = 38(2) \mu\text{s}^{-1}$ and $f = 13(1) \text{ MHz}$. This implies that the static internal fields within

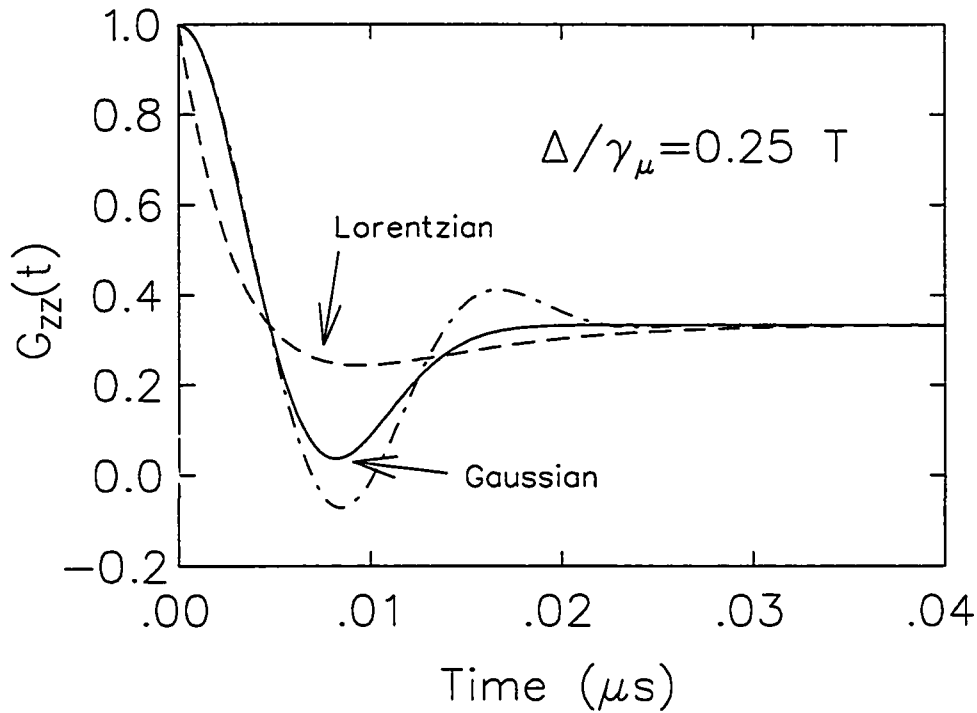


Figure 6.38: Resultant muon spin depolarisation function given the static internal field distribution shown in Fig. 6.37 (dot-dashed line). The solid and dashed lines are Eqs. 5.40 and 5.42 respectively using the values of Δ , a shown in Fig. 6.37.

$Y_2Mo_2O_7$ average at 0.096 T, but have a broad distribution around that value.

Figure 6.37 illustrates the results of attempting to model the internal field distribution. The magnetic field at the muon site (0.16, 0.16, -0.17) calculated in Chapter 3 due to surrounding dipoles is shown. The corresponding muon spin depolarisation functions are shown in Fig. 6.38. Including the contribution due to moments within a cube of 4 conventional unit cells on a side, point like dipoles with effective moments of $g\sqrt{S(S+1)}\mu_B = 2.8\mu_B$ expected for $S = 1$ Mo^{4+} ions were randomly oriented on Mo^{4+} sites. This field distribution is more sharply peaked than the Gaussian function shown in Fig. 6.37 and $\Delta/\gamma_\mu = 0.25$ T does not agree with the experimentally observed value. However, the discrepancy may be partially explained by noting that Raju *et al.* [152] determine the effective moment to be $1.7\mu_B$ below 300 K, a reduction ascribed to spin-orbit splitting effects of the 4d electrons [158]. In addition, a more involved model of the

static internal field distribution would have to include the effect of spin correlations in an analogous manner to the work of Walker and Walstedt. In their classic paper Walker and Walstedt [159] investigated dilute RKKY coupled spin systems using computer simulations and showed that the effect of short range correlations is to broaden the distribution of exchange fields by $\sim 50\%$ for equilibrium configurations and diminish the number of spins with very small fields.

The three relaxation functions described above have been generalised to include a fluctuating component to the internal field, which results in (among other things) relaxation of the $1/3$ tail. As may be seen in Fig. 6.36b, this component is again better described by a stretched exponential function. Below the spin glass transition temperature only this component has been analysed, fitting the data to a stretched exponential function between 0.1 and $10 \mu s$. As shown in Fig. 6.30, in a conventional dilute spin glass the amplitude of the “tail” is less than $1/3$ in zero field when the spin glass order parameter is significantly less than 1 . This of course depends on the value of ν . By holding the corrected asymmetry constant at $1/3$ of the full signal below T_F , it is therefore possible that a slight systematic error is being made. It would be most pronounced just below T_F , where the static internal fields are small and comparable with the applied field. However, at temperatures of $< 0.1T_F$ it is certainly a good approximation and the data was well fitted by using this model. A complete description of the muon spin depolarisation in $Y_2Mo_2O_7$ would involve the exact shape of the static internal field distribution and how it is decoupled in the applied field of 0.02 T, as well as the functional form of the spin glass autocorrelation function. It should be pointed out that the small residual relaxation rate [$\lambda_0 = 0.006(1) \mu s^{-1}$] at the lowest temperatures is at the resolution limit of the μSR technique.

The initial amplitude of the slowly relaxing tail increases as the ratio between the external magnetic field and internal static field, as shown in Fig. 6.39. This dependence was used to estimate the magnitude of the static component of the internal magnetic field at various temperatures below the spin glass transition, assuming both Gaussian and

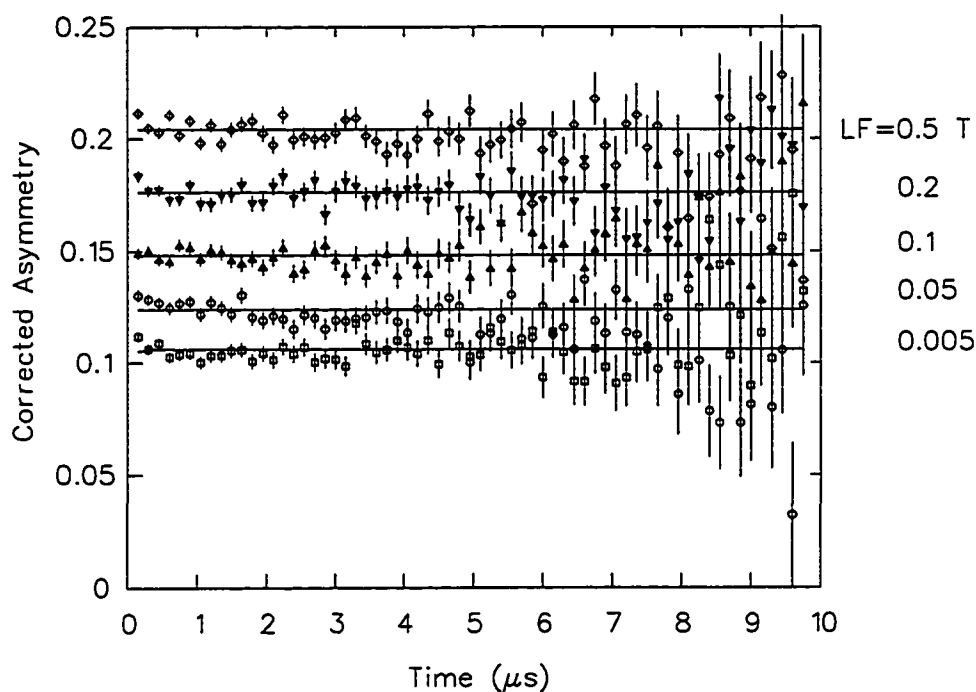


Figure 6.39: Characteristic spectra in $Y_2Mo_2O_7$ in various longitudinal magnetic fields at ~ 40 mK. The increase in the amplitude of the long time tail with field is evidence of a static internal field distribution.

Lorentzian field distributions (see Fig. 6.40). The static component becomes larger with decreasing temperature at the expense of the fluctuating component. Within the limits of the μ SR technique, the “1/3” tail is completely non-relaxing by 40 mK (Fig. 6.39). Hence the spin glass-like behaviour observed in $Y_2Mo_2O_7$ closely resembles that found in conventional random spin glass systems. It remains unclear whether this transition is intrinsic to the pure material, *i.e.* “topological” in nature, or driven by residual disorder. Very recent XAFS results described in Chapter 3 suggest that the spin glass phase is nucleated by 5% lattice disorder, which gives rise to a distribution of exchange interactions. However, the quantum mechanical mean field theory of Sherrington and Southern [160] for Ising spins would imply that disorder in the exchange coupling on the level of 20 – 25% is required to reproduce the observed transition temperature [83]. The point charge crystal electric field calculations described in Chapter 3 indicate that the lowest energy levels of the Mo^{4+} ion in its pyrochlore environment are a ground state

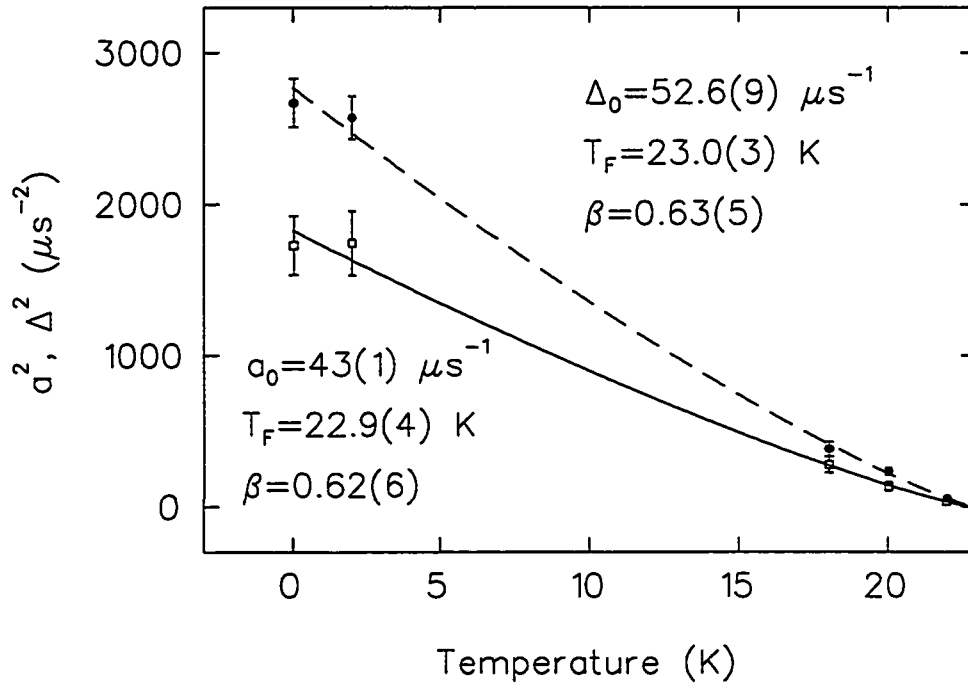


Figure 6.40: Static internal field as a function of temperature in $Y_2Mo_2O_7$ assuming Gaussian (dashed line) and Lorentzian (solid line) internal field distributions. The quoted values are from fits to Eq. (6.69).

singlet and then an excited state doublet, suggesting that the ion is slightly XY like. Given N spins in the system, of the order of Avogadro's number, the associated planar anisotropy means that only disorder at the level of $N^{2/3}$ would be required to drive the system into a spin glass state [2]. This also implies that the ratio of the exchange coupling to the energy level splitting is larger than the critical value necessary for a singlet ground state system to undergo a phase transition.

6.2.1 Spin glass autocorrelation functions

In simple models on non-random magnetic systems, the spin autocorrelation function typically exhibits decay with an exponential time dependence outside the critical region [161] above its transition temperature. There have been a number of studies both above and below the spin glass transition to determine the form of the autocorrelation function in random systems. The first using μ SR were done by MacLaughlin *et al.* [27]

at temperatures $< T_F$, where power law behaviour was observed. The muon spin depolarisation rate varied with field as $H^{-0.46 \pm 0.05}$ for AgMn spin glasses below the glass transition ($0.30 \leq T/T_F \leq 0.66$). The time dependent component of the autocorrelation function was found to decay as t^{-x} , where $x \sim 1/2$ below T_F . This behaviour is consistent with infinite range mean field theories of spin glass dynamics [165] and Monte Carlo simulations [166]. This latter theory, due to Kirkpatrick, predicts an exponential decay of correlations above T_F and an algebraic decay below with an exponent which decreases with temperature from the value of $x = 1/2$ at T_F . Subsequently, the classic measurements of Mezei and Murani [162] using neutron spin echo, which probes the autocorrelation function directly, have been successfully fitted to both power law [163, 146] and stretched exponential forms [164]. Ogielski [148] proposed the empirical formula

$$q(t) = c \frac{\exp[-(t/\tau)^\beta]}{t^x} \quad (6.72)$$

above T_F and a power law form $q(t) = ct^{-x}$ below to describe the results of his Monte Carlo simulations of three dimensional short range Ising spin glasses both above and below the transition temperature. All four parameters c , x , τ and β may depend on temperature. The Kohlrausch or stretched exponential component results from averaging over approximately uncorrelated contributions of localised fluctuations which are due to local variations of the density of frustration in an inhomogeneous lattice [148].

The seemingly inconsistent conclusions as to the form of the spin glass autocorrelations may in part be due to the non-trivial form of the muon spin depolarisation function below T_F . In the spin glass state both dynamic and static fields contribute to the relaxation, complicating the interpretation of the data. The local dipolar fields contribute to the total *static* field seen by the muon, in addition to the applied field. Campbell *et al.* [29] studied AgMn and AuFe alloys above the glass transition and found a stretched exponential form for the local spin autocorrelation function by Laplace transforming the observed stretched exponential muon spin relaxation functions. If there were a unique relaxation time τ for all spins at each temperature, because of the geometrical distribution of internal fields within a dilute system, β should be somewhat less than one and

temperature *independent*. In reality, β is often found to decrease as the temperature approaches T_F from above, reaching a value of 1/3 at the transition [30].

Extensive work has also been undertaken by Keren *et al.* [30] on dilute spin glasses. Zero and longitudinal field μ SR measurements on \underline{AgMn} (0.5%) above the spin glass transition showed that the muon polarisation obeys a time-field scaling relation $P(H, t) = P(t/H^\gamma)$ which depends on the form of the spin-spin autocorrelation function: if $\gamma \leq 1$ then $\gamma = 1 - x$, implying a power law or cut off power law (CPL). However, if $\gamma > 1$ then $\gamma = 1 + y$ and the autocorrelation function decays as a stretched exponential. The power law form is time scale invariant and dynamical modulations should be observed in any time window. The CPL is time scale invariant only at times much shorter than τ , where

$$q(t) \sim ct^{-x} f(t/\tau). \quad (6.73)$$

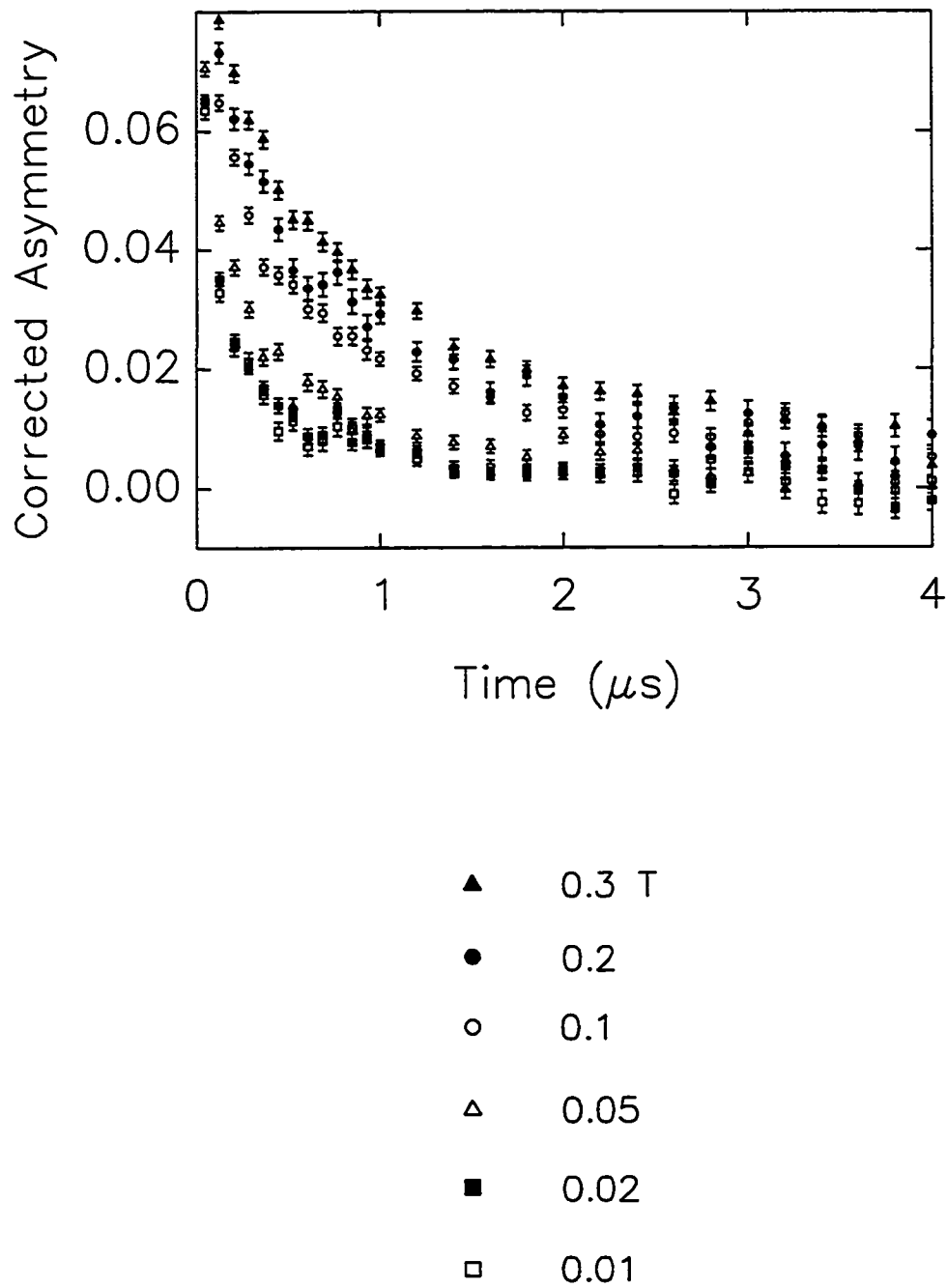
The μ SR spectra between 0.0125 and 0.4 T on \underline{AgMn} at 3.2 K are found to collapse onto each other for $\gamma = 0.75(5)$. The value of γ may change with temperature. Analogous measurements on $Y_2Mo_2O_7$ by the author are shown in Figs. 6.41 and 6.42, where scaling is observed for $\gamma = 0.63(0.19)$. In particular, it is possible to fold all the longitudinal field data into one universal plot, consistent with Keren's results. This indicates that the spin autocorrelation function in $Y_2Mo_2O_7$ has either a power law or CPL form and hence another aspect of the behaviour of this material is very similar to traditional random spin glasses. It is not possible to describe the field dependence in terms of Abragam's formula 5.59, where in the high field limit the relaxation rate would scale as H^{-2} .

Note that no specific form for the depolarisation function has been assumed thus far. Keren *et al.* have shown [167] that it is possible to relate power law autocorrelation functions with stretched exponential muon spin depolarisation. An expression of the form

$$P(H, t) = P_0 \exp[-\lambda(t)t] \quad (6.74)$$

is assumed, where

$$\lambda(t)t = \int_0^t (t - \tau) q(\tau) \cos(\omega_\mu \tau) d\tau. \quad (6.75)$$

Figure 6.41: Asymmetry in $Y_2Mo_2O_7$ at 22.5 K in various longitudinal magnetic fields.

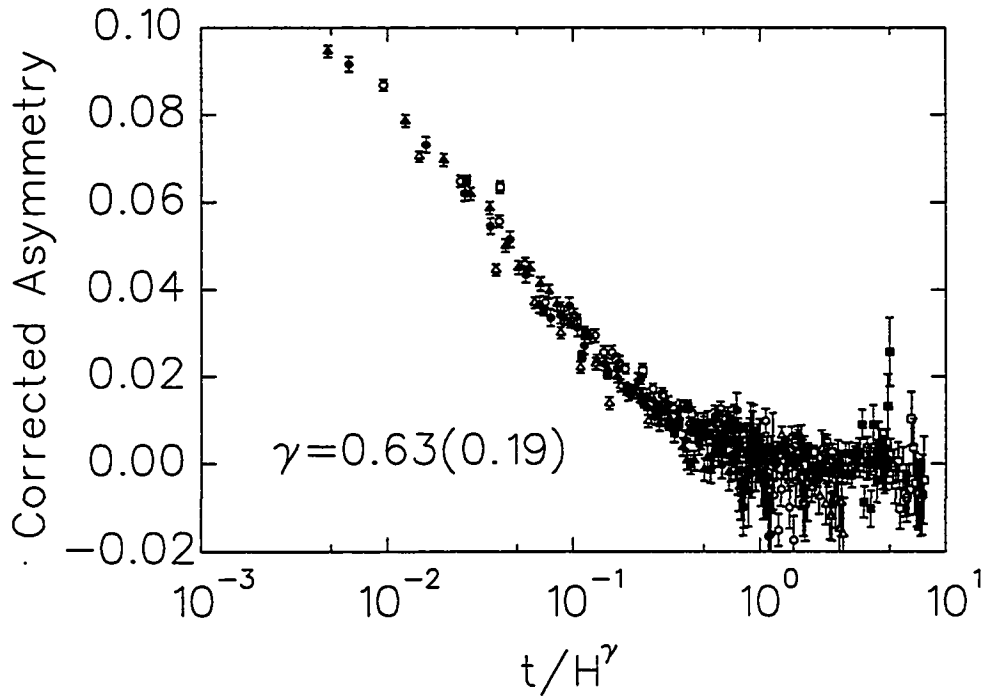


Figure 6.42: Asymmetry in $Y_2Mo_2O_7$ at 22.5 K in various longitudinal magnetic fields H , plotted as a function of t/H^γ .

Given the autocorrelation function

$$\langle \mathbf{S}_j(t) \cdot \mathbf{S}_j(0) \rangle - \langle \mathbf{S}_j(\infty) \cdot \mathbf{S}_j(0) \rangle = q(t) = 2\Delta^2 \frac{\tau_{co}^x}{(t + \tau_{co})^x} \exp[-(vt)^y], \quad (6.76)$$

y is set to 0 for simplicity and the crossover time τ_{co} is introduced so that $q(t)$ is properly normalised at $t = 0$. However, this quantity is expected to be of the order of $10^{-13} - 10^{-11}$ s. Eq. (6.75) must be solved numerically [167] but in zero field it may be integrated by dividing it into two parts: the first from 0 to τ_{co} , the second from τ_{co} to t . At the end of the calculation we set $\tau_{co} \rightarrow 0$ as only the behaviour at times much greater than τ_{co} are of interest in a μ SR experiment. In this case,

$$\lambda(t)t = \frac{2\Delta^2 \tau_c^x t^{2-x}}{(2-x)(1-x)} + O(t^{3-x}). \quad (6.77)$$

The second term comes from the integral over early times and is typically 10% of the first term for $x > 0.5$. The relaxation rate thus itself becomes a power law function of time. Therefore the onset of non-exponential muon spin relaxation in $Y_2Mo_2O_7$, as

shown in Fig. 6.34b, likely corresponds to the crossover of the autocorrelation function to an exotic form as the spin glass phase is approached. In the regime between ~ 45 K and the transition temperature, it is no longer appropriate to think in terms of a single spin fluctuation rate. Rather, spin dynamics begin to develop over a wide range of timescales.

6.3 Titanium substituted Yttrium compounds

The results of similar μ SR experiments done in a longitudinally applied field of 0.02 T on $Y_2Mo_{1.6}Ti_{0.4}O_7$, $Y_2Mo_{1.2}Ti_{0.8}O_7$ and Y_2MoTiO_7 are shown in Figs. 6.43, 6.44 and 6.45, where the diamagnetic Ti^{4+} ions are substitutional impurities on the B site, thereby introducing random disorder. In the paramagnetic phase the spectra are fitted to a stretched exponential function over a time range of 0.01 to 9.5 μs , holding the corrected asymmetry constant at a value found from high temperature alpha calibrations. In the ordered phase only the 1/3 component is analysed out from 0.1 μs . It proved necessary to hold the parameter β constant below 2 K in the $Y_2Mo_{1.6}Ti_{0.4}O_7$ and $Y_2Mo_{1.2}Ti_{0.8}O_7$ samples.

The most remarkable feature in the data is the presence of a sizeable residual spin relaxation rate at low temperatures, which is not evident from previous data on conventional metallic spin glasses like CuMn [25] or AuMn [163]. This is direct evidence for a larger density of magnetic excitations near zero energy than in conventional random spin glasses. The muon spin depolarisation rate is roughly temperature independent below 1 K, at values which increase with increasing impurity concentration (see Fig. 6.46b). The mechanism giving rise to this behaviour is possibly enhanced by the addition of random disorder. As shown in Fig. 6.47, the rapidly relaxing 2/3 component is also affected by the dilution as expected, since the internal field distribution narrows with decreasing molybdenum concentration. In particular, the dip observed at early times in undiluted $Y_2Mo_2O_7$ becomes increasingly “washed out”.

The spin freezing temperatures, as seen by a peak in T_1^{-1} , are in agreement with magnetic susceptibility measurements, summarised in Fig. 6.46a. As shown, there is a

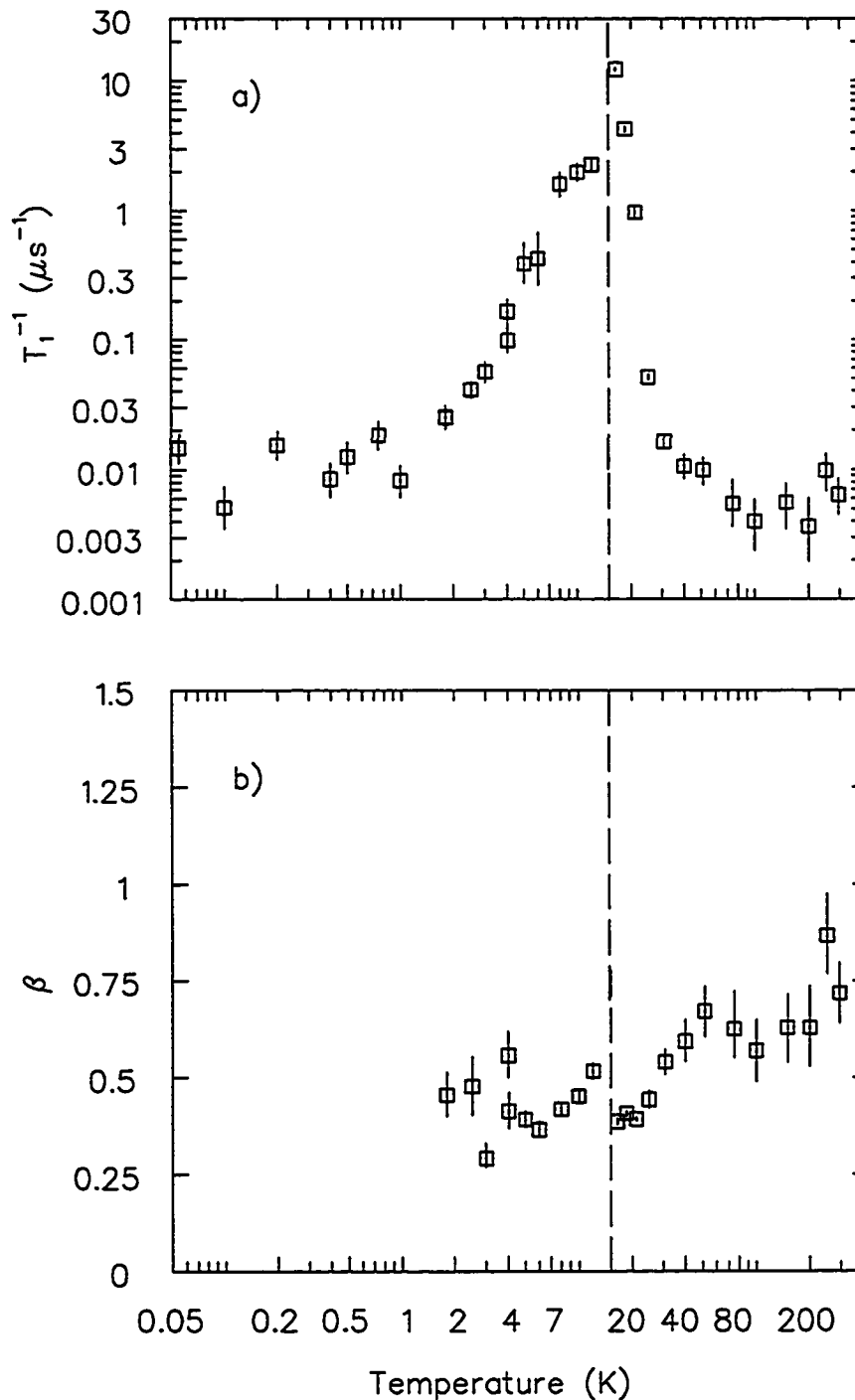


Figure 6.43: a) Muon spin relaxation rate and b) β as a function of temperature in $Y_2Mo_{1.6}Ti_{0.4}O_7$ measured in a longitudinal field of 0.02 T. The parameter β is defined by Eq. (6.70).

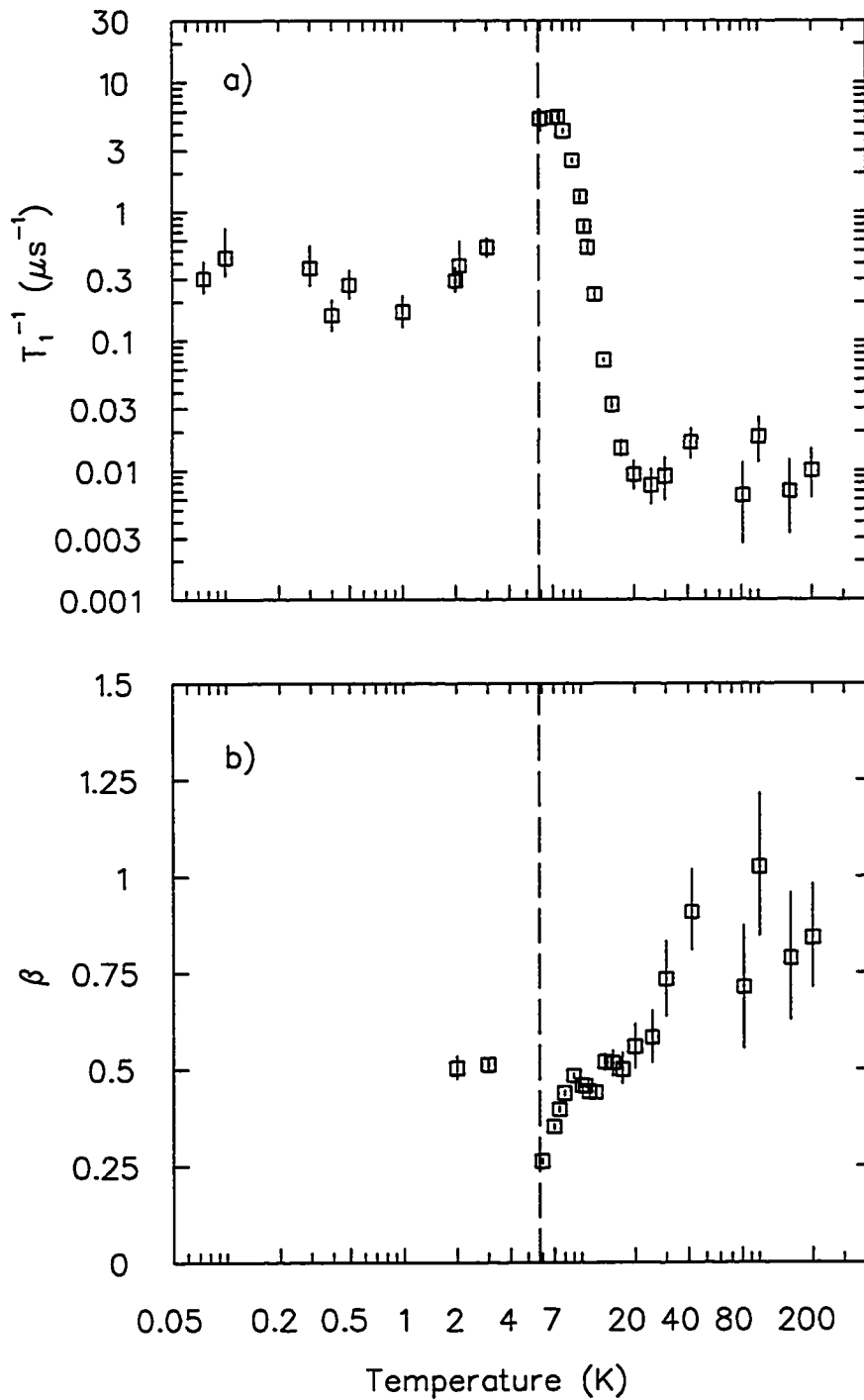


Figure 6.44: a) Muon spin relaxation rate and b) β as a function of temperature in $Y_2Mo_{1.2}Ti_{0.8}O_7$ measured in a longitudinal field of 0.02 T. The parameter β is defined by Eq. (6.70).

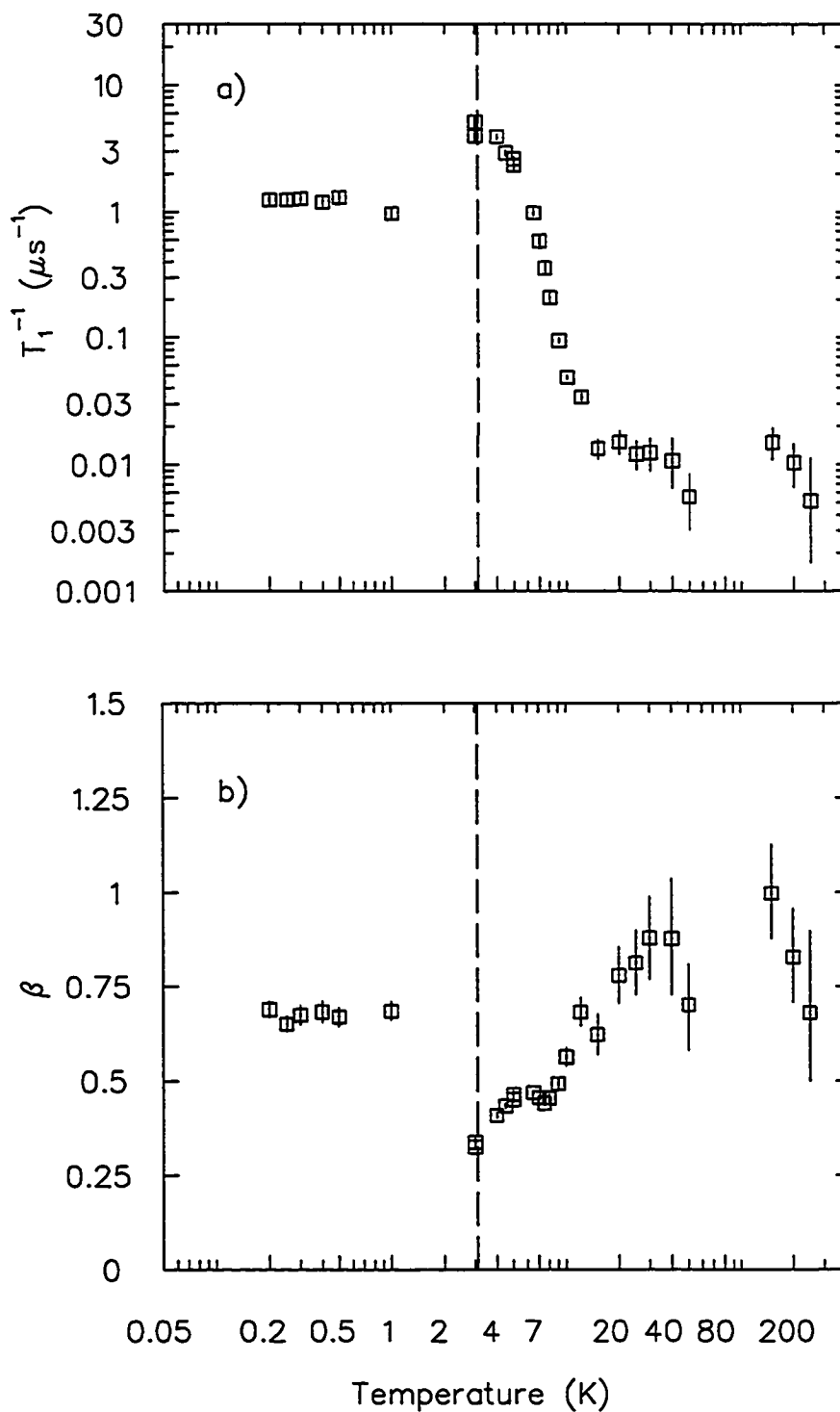


Figure 6.45: a) Muon spin relaxation rate and b) β as a function of temperature in Y_2MoTiO_7 measured in a longitudinal field of 0.02 T.

decrease in the transition temperature with increasing impurity concentration. While this is observed universally in conventional magnets [168], as T_c scales with the number of nearest neighbours, it is not clear that this approach is appropriate for describing spin glasses, where the order parameter is not a simple quantity. It is important to realise that the fact that the transition temperature decreases with increasing dilution has profound implications as to whether the spin glass transition in $Y_2Mo_2O_7$ is *due* to disorder and then is *robust* to disorder. Minimising the disorder does not make the transition disappear; it has now been observed in a variety of nominally pure samples. In addition, site dilution appears to have different effects compared to bond disorder.

Muon spin relaxation results from the exchange of energy with magnetic excitations. A first order process, in which the muon absorbs or creates an excitation with an energy equal to the muon Zeeman energy, is normally suppressed in conventional systems with LRO, where the density of states $\rho(E) \rightarrow 0$ as $E \rightarrow 0$, since it requires excitations near zero energy. In principle, both first and second order muon spin depolarisation processes are present in spin glasses, since $\rho(E)$ is thought to be only weakly dependent on energy. In a second order (Raman magnon scattering) process involving inelastic scattering of an excitation, application of Fermi's Golden rule gives:

$$T_1^{-1} \propto \int_0^\infty dE \left\langle n \left(\frac{E}{k_B T} \right) \right\rangle \left\langle n \left(\frac{E}{k_B T} \right) + 1 \right\rangle |M|^2(E) \rho^2(E) \quad (6.78)$$

where the muon Zeeman energy has been neglected and $M(E)$ is the matrix element for inelastic scattering of an excitation of energy E causing a muon spin flip. In a spin glass, $n(E/k_B T)$ is the probability distribution (assumed to be Bose-Einstein) for "intravalley" excitations, *i.e.* spin excitations within one of the macroscopic number of metastable states or valleys. Intervalley transitions, involving reorientations of finite sized spin clusters, are thought to be important only in the mK range [169], where T_1^{-1} is independent of temperature in these samples. From Eq. (6.78), the temperature dependent behaviour of T_1^{-1} is primarily determined by the energy dependence of $\rho(E)M(E)$. The low temperature linear specific heat observed in $Y_2Mo_2O_7$ [152] suggests $\rho(E)$ is flat or at least weakly dependent on energy for $E > T$. Note however that a peak in the density of

states is still possible near $T = 0$. If $\rho(E)$ and $M(E)$ have power law dependences with powers l and m respectively, then Eq. (6.78) implies that T_1^{-1} varies as $T^{2(l+m)+1}$ below T_F . In other words, below T_F , T_1^{-1} decreases gradually as magnetic excitations freeze out.

The large residual T_1^{-1} observed in the titanium substituted compounds establishes that there is a non-zero density of low energy excitations, which cause relaxation either by a first or second order process. Computer simulations by Ching *et al.* [170] on insulating Heisenberg spin glasses $Eu_xSr_{1-x}S$ ($x = 0.54$ and 0.40) have indicated that the density of states $\rho(E)$ may be peaked at low energies and $\rho(0)$ finite.

As described in Chapter 2, Villain has considered the effect of disorder on the pyrochlore lattice qualitatively [2]. More recently, Moessner and Berlinsky [171] have investigated the effect of magnetic dilution on the magnetic susceptibility of the pyrochlores, using Monte Carlo simulations for a system of classical Heisenberg spins with nearest neighbour interactions. The spin-spin correlations in this system are always short ranged and a small amount of dilution does not affect this property, inducing neither ordering nor glassiness. However, this ceases to be the case when 1/4 of the sites are vacant. At any non-zero dilution, the low temperature magnetic behaviour is dominated by the tetrahedra where only one magnetic ion is present (a $p = 1$ unit). The effect of a magnetic field on the total spin of a unit is the same for all $p \geq 2$. There is merely a difference in the magnetic susceptibility per spin, as the total magnetisation is shared between a total of $p < 4$ spins in a diluted unit and is proportional to the applied field. In striking contrast, an infinitesimal field suffices to align the single spin in a $p = 1$ unit and hence the susceptibility is infinite at $T = 0$. In the full system at low dilution, a unit with $p = 1$ in general corresponds not to an isolated spin as it also belongs to a second unit with $p \geq 0$. In this regime, there are sufficiently many undiluted tetrahedra to generate an extensive ground state [49] and a finite density of zero energy modes, *i.e.* the possibility of reorienting local spin clusters at no cost in energy. As a result, spins separated by a

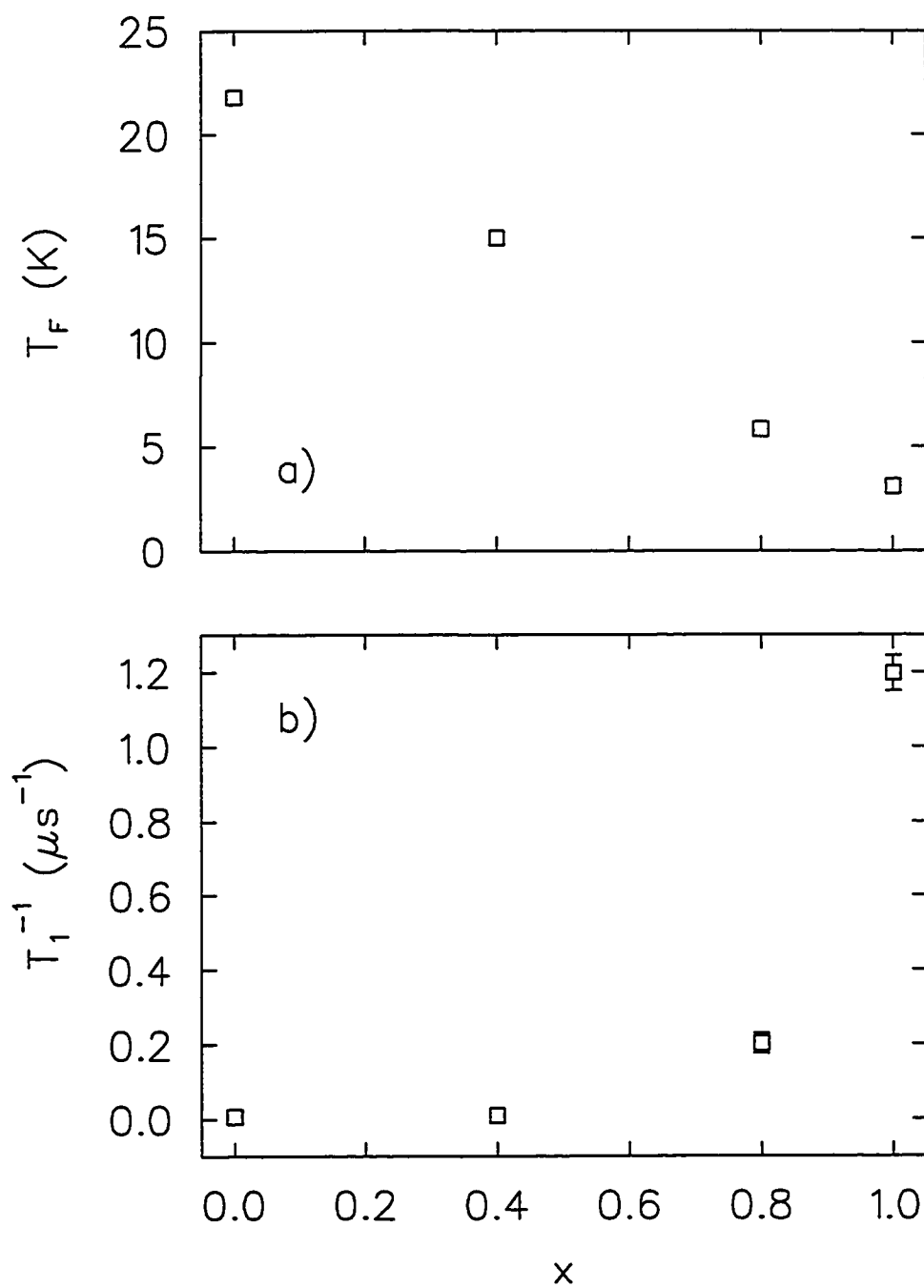


Figure 6.46: a) Transition temperature and b) residual relaxation rate as a function of Ti substitution in $Y_2Mo_{2-x}Ti_xO_7$.

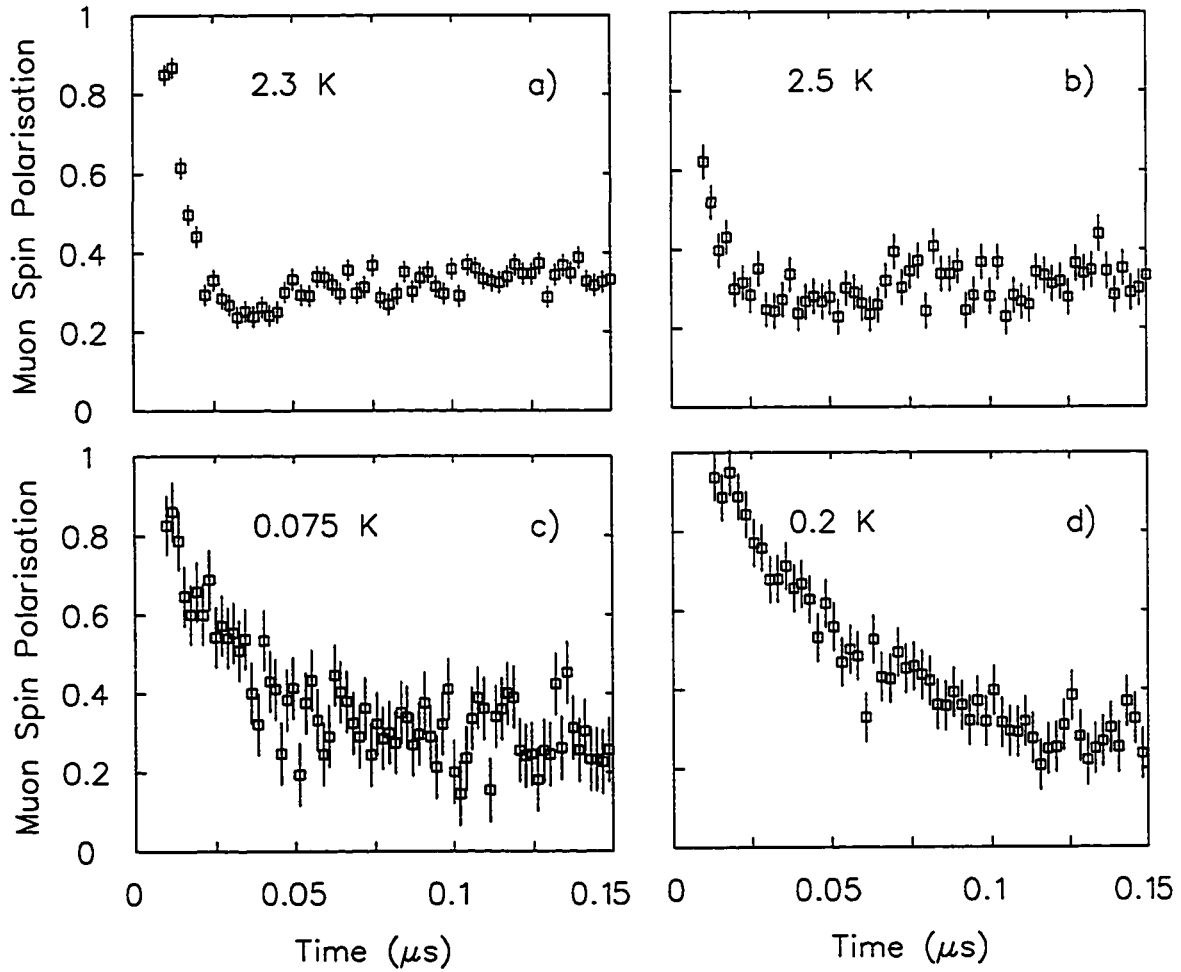


Figure 6.47: Behaviour at early times of the muon spin depolarisation in $Y_2Mo_{2-x}Ti_xO_7$: a) $x=0$; b) $x=0.4$; c) $x=0.8$; and d) $x=1$.

distance larger than the size of such clusters are essentially uncorrelated at all temperatures. Since the spins in the $p = 1$ units are well separated at low dilution, they behave like paramagnetic spins even though they are not isolated. This results in a Curie-like contribution to the susceptibility, with the most dramatic changes in χ^{-1} occurring below $T/J < 0.02$.

It is possible to compare the spin lattice relaxation rate T_1^{-1} with the dynamical susceptibility of a system through the fluctuation-dissipation theorem:

$$T_1^{-1} \propto k_B T \lim_{\omega \rightarrow 0} \sum_q \frac{\chi''}{\omega}, \quad (6.79)$$

where

$$\chi''(q, \omega, T) = \chi'(q, 0, T) f(q, \omega, T) \hbar \omega \pi \quad (6.80)$$

by the Kramers-Krönig relation and f is the spectral function. Since the frequencies probed by the muon, set by its gyromagnetic ratio, are on the order of MHz and the characteristic frequency scale of the electronic moments is in the THz range, taking the limit $\omega \rightarrow 0$ is justified. Note that there is a *quasi-elastic* contribution to χ' due to diffusive modes [172]. If it can be assumed that there is no temperature dependence to the spectral function, then a Curie-like susceptibility χ' may be associated with temperature independent spin relaxation. Even though a model with classical Heisenberg spins with nearest neighbour interactions does not predict a spin glass transition, given completely undiluted tetrahedra, the idea that the $p = 1$ units behave like paramagnetic spins may have some relevance to explaining the behaviour below 1 K in the substituted yttrium pyrochlores. Similarly, paramagnetic contributions to the dc susceptibility of the frustrated spinel $ZnCr_{1.6}Ca_{0.4}O_4$ below its spin glass ordering temperature [19] are attributed to unfrozen “entropic” clusters of spins. Susceptibility measurements at millikelvin temperatures might indicate whether a similar mechanism is present in the pyrochlores.

It should be emphasized that previous μ SR experiments on conventional spin glasses [25, 163] found a strong temperature dependence of T_1^{-1} in the temperature range $T/T_F \in$

[0.1 – 1.0], with no sign that T_1^{-1} was approaching a limiting and temperature independent value $\lim_{T \rightarrow 0}[T_1^{-1}(T)]$ above the experimental μ SR resolution limit. In any case, these experiments did not probe the temperature range $T/T_F < 0.1$. It is interesting to note that other spin glasses like $Cd_{1-x}Mn_xTe$ ($0.27 \leq x \leq 0.65$) [173] and $La_{1.94}Sr_{0.06}CuO_4$ [174] show indications of low temperature spin dynamics; but again, these insulating Heisenberg spin glasses have not been studied in the important region below $0.1T_F$. The geometrically frustrated kagomé lattice system $SrCr_8Ga_4O_{19}$ has also recently been studied using μ SR [34]. Dynamic spin fluctuations are observed without static freezing, even at 100 mK, well below $T_F = 3.5$ K. There is, however, some controversy over $SrCr_8Ga_4O_{19}$ [58, 175], as it has been suggested that this material does not show a thermodynamic freezing transition at T_F [175]. In this case, one would expect to find spin dynamics persisting down to zero temperature. This is not the case for $Y_2Mo_2O_7$, where there is strong evidence for a *collective freezing transition* at T_F as seen in the critical slowing down observed by μ SR and the divergent nonlinear susceptibility. In the $Y_2Mo_{2-x}Ti_xO_7$ ($x \neq 0$) compounds there is convincing evidence for a limiting temperature independent T_1^{-1} in the temperature range $T/T_F < 0.1$, $\lim_{T \rightarrow 0}[T_1^{-1}(T)]$ growing with increasing x . Interestingly, both the classic random spin glass $AuFe$ and $Y_2Mo_2O_7$, which has many spin glass-like features but only very low levels of chemical disorder, have internal field distributions which are completely static on the timescale of μ SR below $0.1T_F$. However, the systematic re-introduction of disorder into $Y_2Mo_2O_7$ through titanium substitution enhances the density of states of the low energy excitations responsible for low temperature relaxation. It is also important to note that minimising the site disorder does not make the phase transition disappear; rather the transition temperature increases as the disorder is removed. This suggests that while the effects of bond disorder may differ, the spin glass transition in $Y_2Mo_2O_7$ is not driven by site dilution.

6.3.1 $Y_2Ti_2O_7$

$Y_2Ti_2O_7$ was studied as a control, to isolate the effects due to magnetic ions. Both the Y^{3+} and Ti^{4+} ions have closed electronic shells and hence no permanent moments. The typical transverse field spectrum shown in Fig. 6.48b is very similar to that of silver. The silver reference has a corrected asymmetry of 0.2272(5) and a relaxation rate of 0.012(5) μs^{-1} , while the $Y_2Ti_2O_7$ has values of 0.2287(8) and 0.006(1) μs^{-1} respectively. In general, the muon may emerge from thermalisation as an apparently bare μ^+ in metals or sometimes in a muonium like state in semiconductors and insulators. The full amplitude of the signal in Fig. 6.48 is observed at the Larmor frequency of the muon: there is no evidence of any “missing fraction” due to prompt muonium formation, a process which occurs while the muon is still losing its initial kinetic energy (see the thesis of Morris [108] and references therein) ².

There is also the possibility of delayed muonium formation, which depends on the transport of radiolysis electrons to the muon under the influence of their mutual Coulomb attraction and any external fields after the muon has come to thermal equilibrium with its surroundings. The muon is thought to lose kinetic energy near the end of its track by the creation of free electrons, ions and radicals in a radiation spur. The thermal muon in the vicinity of the terminal spur could then form muonium by simply capturing a free electron from among the spur products. The associated time over which the electrons diffuse to the muon can be large enough to have an observable effect on timescales accessible by μSR if the initial separation is great enough and/or the electron mobility is low enough. The elapsed time between muons entering the sample and the arrival of electrons

²At high energies of several MeV the muon should behave like any fast charged particle and undergo energy loss by Bethe-Bloch ionisation of the medium. Charge exchange collisions become important when the kinetic energy has dropped to several tens of keV, comparable with the orbital velocity of electrons of the medium. In this regime, the muon undergoes a rapid series of several hundred electron pickup and stripping cycles, shedding energy with each ionisation process. At an energy of order 100 eV the fraction of muonium formed is a function of the relative electron affinities of the muon and atoms of the sample. In materials with ionisation potentials smaller than that of muonium (13.5 eV) most muons are expected to emerge from this stage as hot muonium atoms. Further thermalisation of both muons and muonium atoms will then continue by elastic and inelastic collisions. In such a process, muonium is formed within a few tens of picoseconds of entering a sample.

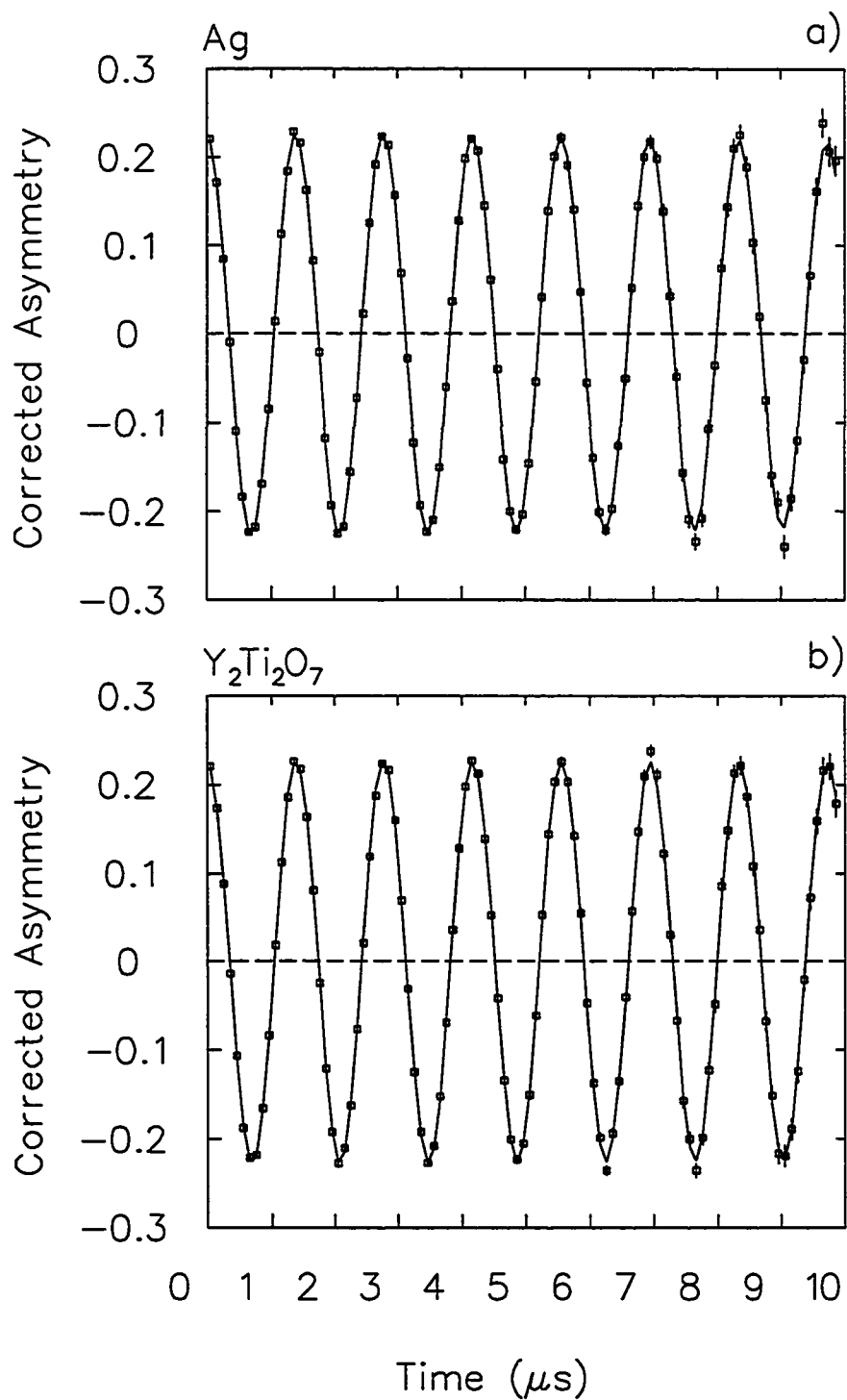


Figure 6.48: Muon polarisation decay asymmetries of silver and $Y_2Ti_2O_7$ measured in a transverse field of 0.005 T at $T=295$ K.

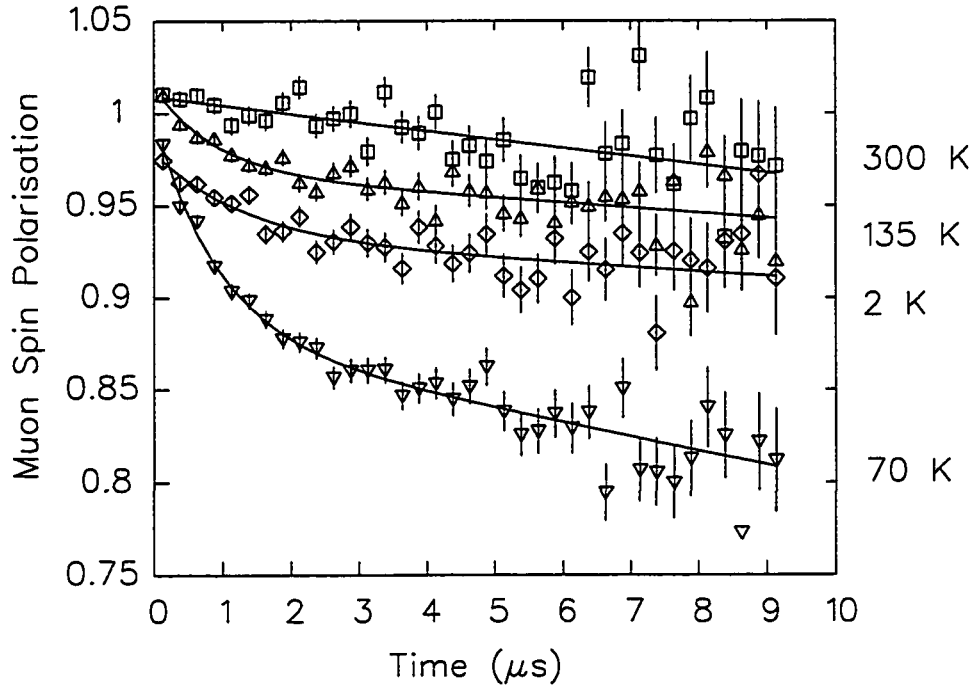


Figure 6.49: Typical μ SR spectra in $Y_2Ti_2O_7$ in a longitudinally applied field of 0.02 T. Note that the vertical scale starts at a muon spin polarisation of 0.75, *i.e.* the relaxing signal is small. This small effect is attributed to residual magnetic impurities (see text).

at the muons will have some distribution, so the bare muon spin polarisation will be converted to muonium polarisation over a range of times. In principle therefore, delayed muonium formation is experimentally observable in the shape of the muon spin relaxation function as a rapidly damped signal. Such two component spectra have been observed in $Y_2Ti_2O_7$ (see Fig. 6.49). The asymmetry of the fast relaxing signal is small, as may be seen in Fig. 6.50 and the corresponding relaxation rate has no obvious temperature dependence. While such behaviour could be interpreted as evidence of delayed muonium formation³, magnetisation measurements (see Fig. 6.51) in 0.02 T indicate a small Curie-like contribution at low temperatures, likely due to paramagnetic impurities. If it is

³In some materials it is possible to influence the muonium and muon fractions with an external electric field applied either parallel to or anti-parallel to the incoming muons' direction of motion [118, 176]. Such an effect suggests that, at least sometimes, the electrons which eventually become bound to muons originate far from the muons. Thus, it seems that electron transport properties of the solid play a role in muonium formation. No electric field dependence of T_1^{-1} was observed in $Y_2Ti_2O_7$ at 70 K and ± 13.8 kV cm⁻¹.

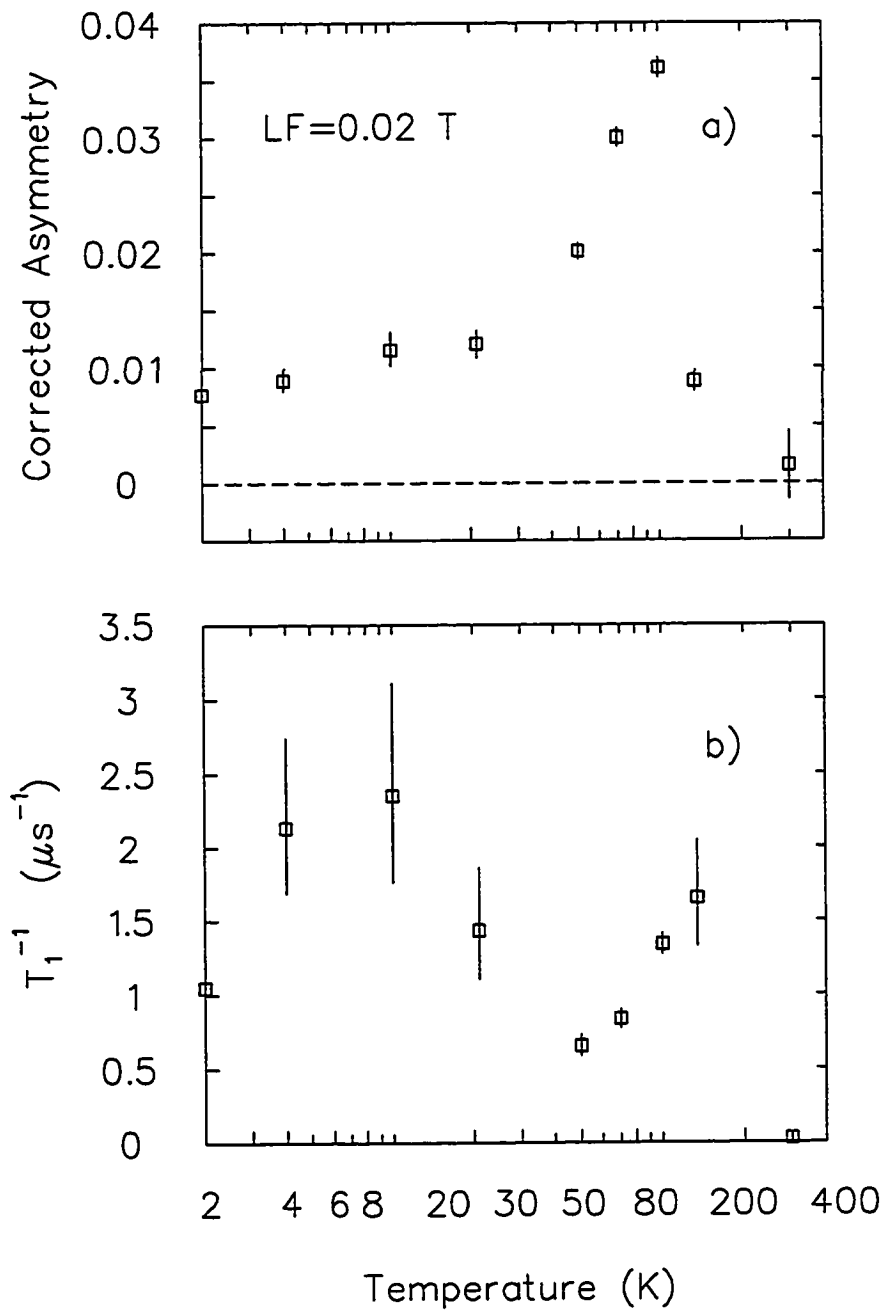


Figure 6.50: a) Asymmetry and b) T_1^{-1} of the fast relaxing component in $Y_2Ti_2O_7$ in a longitudinally applied field of 0.02 T.

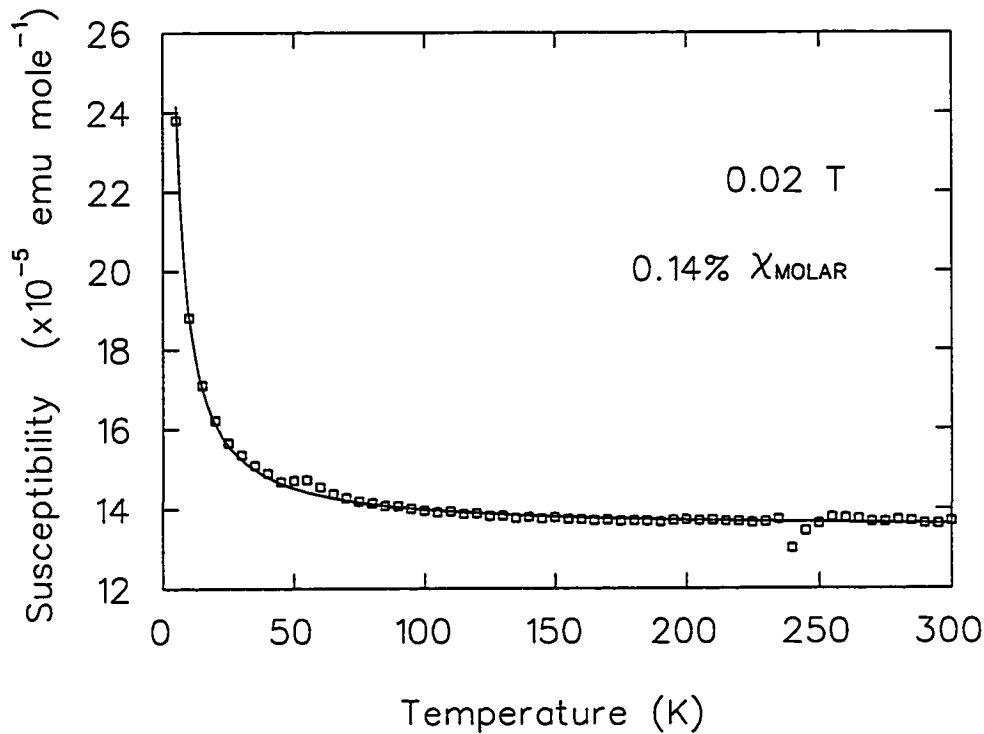


Figure 6.51: dc magnetisation measurements in $Y_2Ti_2O_7$ in a magnetic field of 0.02 T.

assumed that the most likely source of these impurities is due to oxygen deficiencies, then a small fraction of the titanium ions will be found in an altered oxidation state of 3+, rather than 4+. Fitting the dc susceptibility with diamagnetic and paramagnetic components, the sample has 0.14% of the molar susceptibility expected for this ion, indicating the low impurity concentration. In this case, the observed relaxation could be explained as follows: below ~ 90 K the muon is assumed to be static and seldom “sees” a Ti^{3+} ion. However, at higher temperatures the muon has a greater chance of diffusing⁴ near a paramagnetic ion and rapidly relaxing. Hence the asymmetry of this fast component increases. At still higher temperatures this effect becomes averaged out due to rapid diffusion.

The source of the muon spin depolarisation in $Y_2Ti_2O_7$ is unclear. In any event, whatever its origin, such a small rapidly damped signal would be swamped by the much

⁴Note however, it is unusual for the muon to start hopping below about 150 K in an oxide.

larger effects from the electronic moments in the paramagnetic materials studied.

Chapter 7

$\text{Gd}_2\text{Ti}_2\text{O}_7$: the paramagnetic phase

The Gd^{3+} ion ($4f^7$) has an ${}^8\text{S}_{7/2}$ ground state with no orbital contribution to its angular momentum. Thus crystal field splittings and anisotropy are expected to be relatively unimportant, at least as a first approximation. $\text{Gd}_2\text{Ti}_2\text{O}_7$ should be an excellent approximation to a classical Heisenberg antiferromagnetic system with dipole-dipole interactions as the leading perturbation. Muon spin relaxation is well suited to study gadolinium compounds. By contrast, neutron scattering measurements on any gadolinium compound require significant preparation. This is because the absorption cross section of the ${}^{157}\text{Gd}$ nucleus is enormous (254 000 barns at a neutron wavelength of 1.8 Å), making the observed scattering rate prohibitively small. Instead, samples of the material of interest must be fabricated using the isotope ${}^{160}\text{Gd}$, which has an absorption cross section of 0.77 barns. However, this in itself is a difficult and expensive process.

Our μSR measurements on $\text{Gd}_2\text{Ti}_2\text{O}_7$ have to date concentrated on the behaviour of the spin relaxation rate T_1^{-1} at higher temperatures, comparing this geometrically frustrated magnet with more conventional systems in the paramagnetic regime. Extensive use is made of the ideas developed in section 5.2. Using first order perturbation theory, a very similar general formula for T_1^{-1} , given either dipolar or hyperfine probe-electron interactions, has been derived by Moriya [32, 33] in terms of the autocorrelation function of the local field, which is the Fourier transform of the local field spectrum. His model applies to an *antiferromagnet* both above and below the Néel temperature. Van Kranendonk and Bloom also independently developed an equivalent theory [177]. Mitchell has calculated the form of T_1^{-1} in a *ferromagnet* given a hyperfine coupling [178]. In agreement with Moriya's calculations, the spin relaxation rate in $\text{Gd}_2\text{Ti}_2\text{O}_7$ is independent of temperature well above its transition temperature, where $J/k_B T \ll 1$. An extension of

his formulation is found to quantitatively describe the magnetic field dependence of T_1^{-1} in the paramagnetic regime at temperatures larger than the exchange coupling \mathcal{J} . Using this description, the magnitude of \mathcal{J} may be extracted independent of susceptibility measurements of the Curie-Weiss temperature.

Measurements were made on the M13 and M20 secondary channels at TRIUMF in a ^4He gas flow cryostat using pressed polycrystalline pellets. Typical spectra are shown in Fig. 7.52. Figure 7.53 shows the average muon spin relaxation rate in $Gd_2Ti_2O_7$ obtained from fits to a single exponential relaxation function $P_z(t) = A_{\text{corr}}e^{-t/T_1} = A_{\text{corr}}e^{-\lambda t}$ over the time interval of 0.05 to 10 μs after the muon's arrival. For each magnetic field, a global fit of all the spectra was used to assign a fixed corrected asymmetry.

Using the results from section 5.2, the muon spin depolarisation rate is given by Eq. (5.52)

$$\lambda(t) = \frac{1}{t} \frac{\gamma_\mu^2}{2} \int_0^t d\tau (t - \tau) [\exp(i\omega_\mu \tau) \Phi_{+-}(\tau) + \exp(-i\omega_\mu \tau) \Phi_{-+}(\tau)], \quad (7.81)$$

where $\Phi_{+-}(\tau)$ is the symmetrised local field autocorrelation function. In the fast fluctuation limit, the timescale set by the fluctuating fields is much shorter than that set by the muon Larmor frequency or equivalently $t \gg \tau$. In this case the first term in Eq. (7.81) dominates and the integral may be extended to infinity:

$$\lambda \approx \frac{\gamma_\mu^2}{2} \int_0^\infty d\tau [\exp(i\omega_\mu \tau) \Phi_{+-}(\tau) + \exp(-i\omega_\mu \tau) \Phi_{-+}(\tau)]. \quad (7.82)$$

Taking account of only nearest neighbour exchange interactions between electronic spins in the paramagnetic regime, the unperturbed hamiltonian of the sample may be written as

$$\mathcal{H}_s = g\mu_B H_0 \sum_j S_{zj} + \frac{1}{2} \sum_{j,k} J_{jk} \mathbf{S}_j \cdot \mathbf{S}_k. \quad (7.83)$$

The first term is the Zeeman interaction between the electronic spins and an externally applied magnetic field H_0 directed along the \hat{z} axis. The interaction between the muon spin and the fluctuations of the l^{th} electron spin $\delta \mathbf{S}_l = \mathbf{S}_l - \langle \mathbf{S}_l \rangle$, its position relative to the probe at the origin given by \mathbf{r}_l , is taken as a perturbation and in this case has the

form of a dipolar coupling:

$$\mathcal{H}_{dip} = -\frac{\gamma\mu\hbar}{2} \left[\sigma_z \delta B_z + \frac{1}{2}(\sigma_+ \delta B_- + \sigma_- \delta B_+) \right] \quad (7.84)$$

where

$$\begin{aligned} \delta B_z &= \sum_{j=1}^N \left[\frac{A_j}{2} \exp(-i\phi_j) S_{j,+} + \frac{A_j}{2} \exp(i\phi_j) S_{j,-} - 2C_j S_{j,z} \right] \\ \delta B_+ &= \sum_{j=1}^N [B_j \exp(2i\phi_j) S_{j,-} + A_j \exp(i\phi_j) S_{j,z} + C_j S_{j,+}] \\ \delta B_- &= (\delta B_+)^* \end{aligned} \quad (7.85)$$

and the geometrical factors are

$$\begin{aligned} A_j &= 3D_j \cos \theta_j \sin \theta_j \\ B_j &= \frac{3}{2} D_j \sin^2 \theta_j \\ C_j &= D_j \frac{1 - 3 \cos^2 \theta_j}{2} \\ D_j &= \frac{\mu_0 \gamma_j \hbar}{4\pi r_j^3}. \end{aligned} \quad (7.86)$$

The axes of quantisation of the muon and electronic spin system need not coincide. Although only transverse components of the local field autocorrelation function give rise to spin relaxation, this includes longitudinal components of the electronic spin autocorrelation function as well, as may be seen from Eq. (7.85). The symmetrised field correlation function involves terms of the form

$$\begin{aligned} \Phi_{+-}(\tau) &= \left\langle \sum_{j=1}^N \left(C_j S_{j,+}(\tau) + B_j e^{2i\phi_j} S_{j,-}(\tau) + A_j e^{i\phi_j} S_{j,z}(\tau) \right) \right. \\ &\quad \left. \sum_{k=1}^N \left(C_k S_{k,+} + B_k e^{-2i\phi_k} S_{k,-} + A_k e^{-i\phi_k} S_{k,z} \right) \right\rangle \\ &\quad + \left\langle \sum_{j=1}^N \left(C_j S_{j,+} + B_j e^{-2i\phi_j} S_{j,-} + A_j e^{-i\phi_j} S_{j,z} \right) \right. \\ &\quad \left. \sum_{k=1}^N \left(C_k S_{k,+}(\tau) + B_k e^{2i\phi_k} S_{k,-}(\tau) + A_k e^{i\phi_k} S_{k,z}(\tau) \right) \right\rangle. \end{aligned} \quad (7.87)$$

It is assumed that correlations between spins where $j \neq k$ are negligible and only on site spin autocorrelations are considered. Only terms involving $\langle S_{l_z}(\tau) S_{l_z} \rangle$, $\langle S_{l_+}(\tau) S_{l_-} \rangle$ and $\langle S_{l_-}(\tau) S_{l_+} \rangle$ are nonzero.

Moriya made use of Kubo and Tomita's theory for the quantum mechanical treatment of the correlation function. It is developed as a power series in time t , where the coefficient of $t^n/n!$ is the n^{th} moment of the local field spectra. The spin autocorrelation functions can then be calculated as

$$\begin{aligned}\langle S_l(t)S_l(0) \rangle &= \left\langle \exp\left(\frac{it\mathcal{H}_s}{\hbar}\right) S_l \exp\left(-\frac{it\mathcal{H}_s}{\hbar}\right) S_l(0) \right\rangle \\ &= \langle S_l S_l \rangle + \left(\frac{it}{\hbar}\right) \langle [\mathcal{H}_s, S_l] S_l \rangle + \frac{1}{2} \left(\frac{it}{\hbar}\right)^2 \langle [\mathcal{H}_s, [S_l, \mathcal{H}_s]] S_l \rangle + \dots \quad (7.88)\end{aligned}$$

using the Baker-Hausdorff lemma. Each coefficient is also evaluated as a series expansion in $1/k_B T$. The traces are given by van Vleck [179]. Above the transition temperature a Gaussian distribution of local field spectra is assumed. In other words, the series expansion used to describe the autocorrelation function is compared with the first few terms of an exponential function. The expansion need only be taken to second order in t to adequately describe the data. This is because, by definition, in the fast fluctuation limit the contribution to the integral in Eq. (7.82) at large t is negligible; the terms at small t (comparable with τ) dominate.

As an illustration,

$$\begin{aligned}& \langle \delta S_{zl}(t) \delta S_{zl} \rangle + \langle \delta S_{zl} \delta S_{zl}(t) \rangle \\ & \approx 2 \left(\text{Tr}\{S_{zl}^2\} - \frac{1}{k_B T} \text{Tr}\{\mathcal{H}_s S_{zl}^2\} - \frac{1}{2} \frac{t^2}{\hbar^2} \text{Tr}\{[\mathcal{H}_s, [\mathcal{H}_s, S_{zl}]] S_{zl}\} \right. \\ & \quad \left. + \frac{1}{2} \frac{t^2}{\hbar^2} \frac{1}{k_B T} \text{Tr}\{\mathcal{H}_s [\mathcal{H}_s, [\mathcal{H}_s, S_{zl}]] S_{zl}\} \right) \\ & = \frac{2}{3} S(S+1) \left(1 - \frac{t^2}{\hbar^2} z \mathcal{J}^2 \cdot \frac{1}{3} S(S+1) \right. \\ & \quad \left. + \frac{1}{2} \frac{t^2}{\hbar^2} \frac{1}{k_B T} \left(z z' \frac{\mathcal{J}^3}{2} \left[\frac{1}{3} S(S+1) \right]^2 - z \frac{\mathcal{J}^3}{4} \frac{1}{12} S(S+1) \right) \right) \\ & \approx \frac{2}{3} S(S+1) \exp\left(-\frac{z \mathcal{J}^2}{3} S(S+1)\right) \\ & \quad + \frac{\beta}{2} \left(z z' \frac{\mathcal{J}^3}{2} \left[\frac{1}{3} S(S+1) \right]^2 - z \frac{\mathcal{J}^3}{4} \frac{1}{12} S(S+1) \right) \frac{t^2}{\hbar^2} \quad (7.89)\end{aligned}$$

and

$$\langle \delta S_{+l}(t) \delta S_{-l} \rangle + \langle \delta S_{-l}(t) \delta S_{+l} \rangle + \langle \delta S_{+l} \delta S_{-l}(t) \rangle + \langle \delta S_{-l} \delta S_{+l}(t) \rangle$$

$$\begin{aligned} &\approx \frac{8}{3}S(S+1) \exp\left(-\frac{1}{2}(g\mu_B H_0)^2 - \frac{z\mathcal{J}^2}{3}S(S+1)\right) \\ &\quad + \frac{\beta}{2} \left(zz' \frac{\mathcal{J}^3}{2} \left[\frac{1}{3}S(S+1)\right]^2 - z \frac{\mathcal{J}^3}{4} \frac{1}{12}S(S+1)\right) \frac{t^2}{\hbar^2}, \end{aligned} \quad (7.90)$$

where z is the number of nearest neighbours and z' the number of neighbours common to two spins. Substituting into Eq. (7.82), the muon spin depolarisation rate is given by

$$\begin{aligned} T_1^{-1} = & C_1 \sqrt{\frac{2}{\nu_e^2[1 + O(\mathcal{J}\hbar/k_B T)]}} \exp\left(-\frac{\omega_\mu^2}{2\nu_e^2[1 + O(\mathcal{J}/k_B T)]}\right) \\ & + C_2 \sqrt{\frac{2}{\nu_e^2[1 + (g\mu_B H_0/\hbar\nu_e)^2 + O(\mathcal{J}/k_B T)]}} \\ & \exp\left(-\frac{\omega_\mu^2}{2\nu_e^2[1 + (g\mu_B H_0/\hbar\nu_e)^2 + O(\mathcal{J}/k_B T)]}\right) \end{aligned} \quad (7.91)$$

where $\nu_e = \sqrt{(2zJ^2S(S+1)/3\hbar^2)}$ is the spin fluctuation rate, ω_μ the muon Larmor frequency in the applied field and C_1, C_2 are coefficients which depend on the muon site and the instantaneous local dipolar field. Good fits to Eq. (7.91) were obtained for the magnetic field scan at 100 K, as shown in Fig. 7.54. The best fit values are $C_1 = 2.9(1) \times 10^{-5} \text{ K}\mu\text{s}^{-1}$, $C_2 = 3.2(2) \times 10^{-5} \text{ K}\mu\text{s}^{-1}$ and $|\mathcal{J}|/k_B = 0.22(1) \text{ K}$. As noted in Chapter 4, the corrected asymmetry is a function of magnetic field and so the spectra taken at 100 and 7.5 K were fitted with exponentially relaxing functions where A_{corr} was allowed to vary, as shown in Fig. 7.55. This effect is purely systematic, due to the changing radius of curvature of the positron orbits as the magnetic field is varied.

As can be seen from the data taken at 7.5 K, the field dependence is no longer well described by the theoretical curve at lower temperatures. This is thought to be due to the build up of short range correlations which can no longer be ignored as the temperature becomes comparable with the exchange coupling.

Moriya's calculations of the temperature dependence of $T_1(T)/T_1(T \rightarrow \infty)$ for a bcc lattice with $S = 5/2$ may be compared with ^{19}F NMR measurements on single crystals of MnF_2 , which undergoes a transition to a long range ordered antiferromagnet at a Néel temperature of $68 \pm 1 \text{ K}$. Shulman and Jacarino [180] measured the experimental line width above the transition temperature in this classic material as a measure of

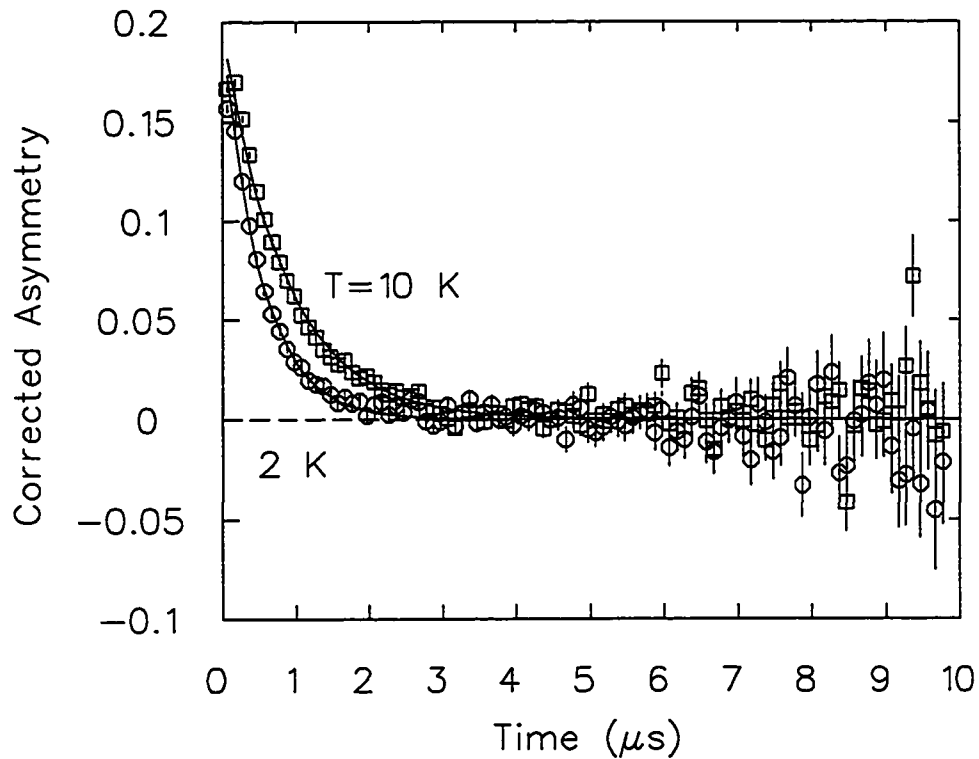


Figure 7.52: Typical μ SR spectra in $Gd_2Ti_2O_7$ in a longitudinally applied field of 0.005 T.

$T_2(T)/T_2(T \rightarrow \infty)$ and found a much more rapid temperature dependence. The hyperfine interaction is at least an order of magnitude more important than the dipolar contribution to the linewidths. However, in doing the comparison the authors assumed that the temperature dependence of the relaxation times are essentially identical for both dipolar and hyperfine broadening mechanisms, since in either case the broadening is linearly dependent on the electron spin correlation time. For $T > T_N$, $T_2 \sim T_1$ (this is only true for an isotropic hyperfine interaction, *i.e.* both the electron spin fluctuations and the electron nucleus interaction are isotropic). Since the observed temperature dependence was much more pronounced than that predicted by Moriya, it is clear that the theory is less than adequate to account for the effects of short range order on the local field spectra. Hence it is not surprising that the form of the field dependence of T_1^{-1} changes at low temperatures and the data at 7.5 K does not fit well to Eq. (7.91).

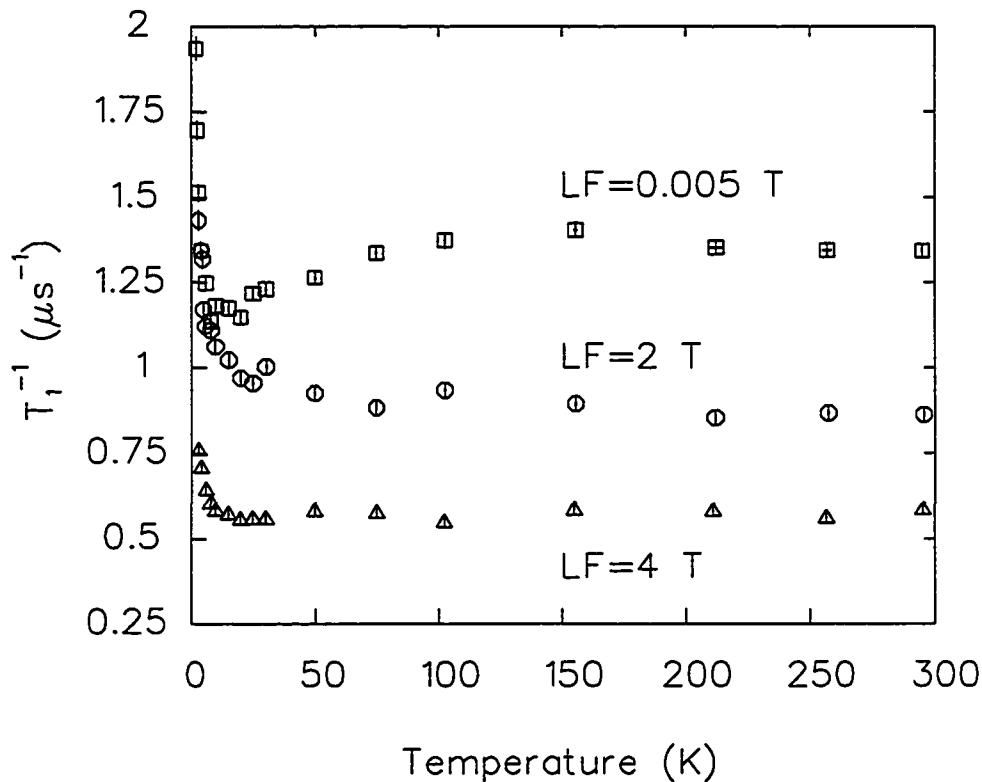


Figure 7.53: Spin relaxation rates T_1^{-1} in $Gd_2Ti_2O_7$ as a function of temperature in various applied longitudinal fields.

The magnitude of the exchange coupling \mathcal{J} extracted from the field dependence of T_1^{-1} is in good agreement with that obtained from measurements of the d.c. susceptibility by Raju *et al.* [44]. From mean field theory, the exchange coupling is related to the Curie-Weiss temperature through the relation $\Theta_{CW} = (1/3)z\mathcal{J}_1S(S+1)$. The Curie-Weiss temperature $\Theta_{CW} = -9.6(3)$ K, extracted from measurements between 10 and 300 K, is thought to be largely due to exchange interactions of the order of $\mathcal{J}_1 = -0.30(1)$ K. In the diluted compound $(Gd_{0.02}Y_{0.98})_2Ti_2O_7$, where the magnetic ions are isolated, Θ_{CW} drops to ~ -0.9 K. A non-zero value must therefore be due to single ion effects. The effective dipole moment of the Gd^{3+} ion in its $S = 7/2$ ground state is $g\mu_B\sqrt{S(S+1)} = 7.94\mu_B$. The magnitude of the dipole-dipole interaction $63\mu_B^2\mu_0/(4\pi r_{nn}^3)$ is hence estimated to be 0.84 K, calculating the nearest neighbour distance r_{nn} from Tables 3.3 and 3.4. The magnetic permeability is given by μ_0 . Comparing this with the classical nearest neighbour

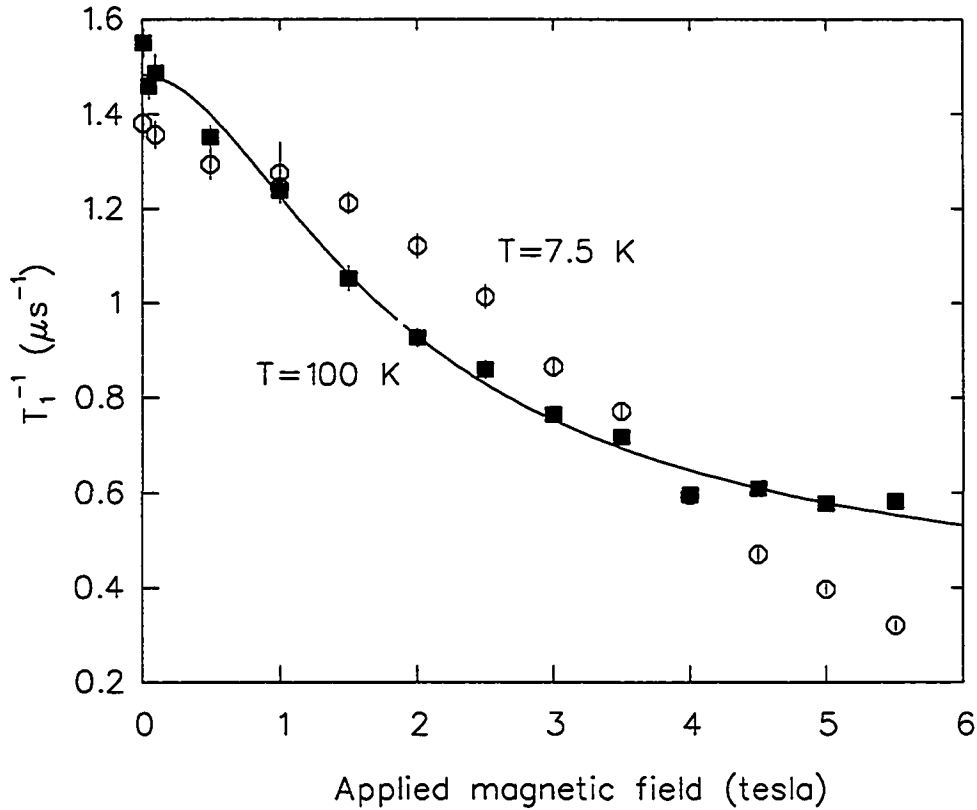


Figure 7.54: Spin relaxation rates T_1^{-1} in $Gd_2Ti_2O_7$ as a function of longitudinal magnetic field at 7.5 and 100 K. The fitted curve is described in the text [Eq. (7.91)].

exchange energy $\mathcal{J}_{classical} = \mathcal{J}_1 S(S+1)$ of -4.8 K, it can be seen that unlike systems containing transition metal ions, the dipolar interaction is not insignificant. Deviations from Curie-Weiss behaviour occur below ~ 10 K, while specific heat measurements by the same authors indicate that $Gd_2Ti_2O_7$ exhibits short range order which starts developing at 30 K.

Below ~ 4 K, T_1^{-1} increases rapidly due to critical slowing down of the Gd spin fluctuations. This is consistent with experimental evidence from measurements of the ac and dc susceptibility and heat capacity data, which show that $Gd_2Ti_2O_7$ exhibits long range order at 0.97 K. There is a broad peak in the specific heat centred around 2 K and a sharp decrease below 1 K. There is no frequency dependence to the ac susceptibility,

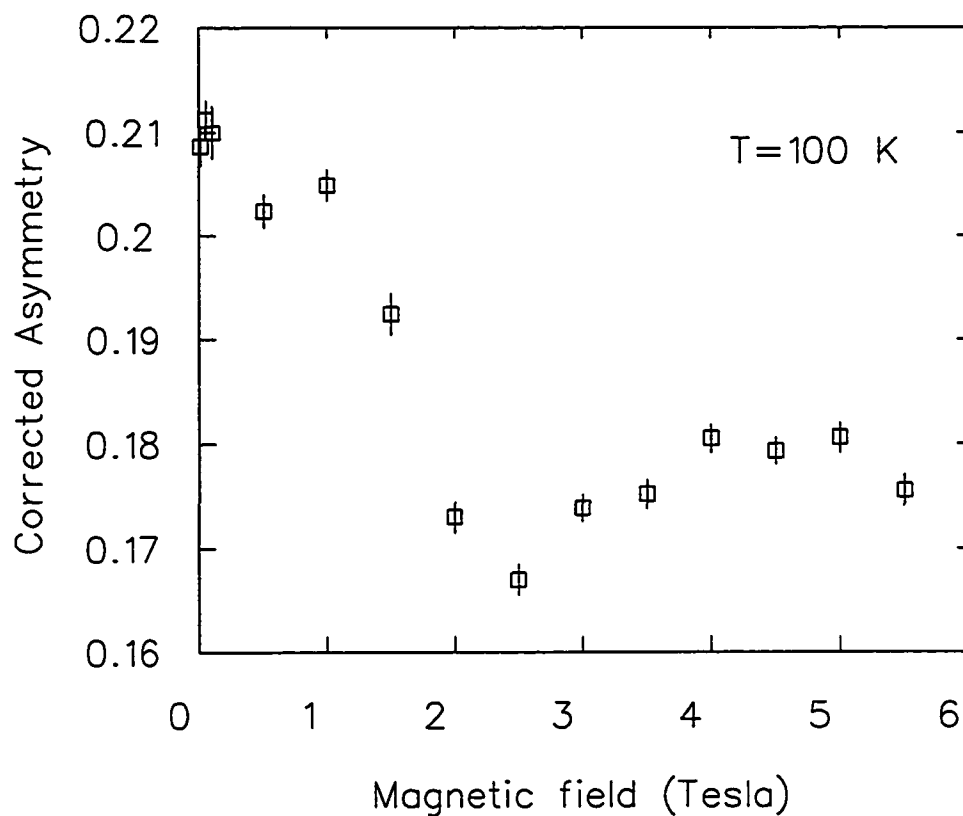


Figure 7.55: Corrected asymmetry in $Gd_2Ti_2O_7$ as a function of longitudinal magnetic field at $T=100$ K.

in either the short or long range ordered regimes, which would have suggested spin glass-like behaviour. Interestingly, unpublished specific heat measurements by Ramirez [181] indicate a complicated low temperature phase diagram with possibly as many as four phases as a function of temperature and applied magnetic field. Clearly further μ SR experiments are necessary below 2 K.

Chapter 8

$\text{Tb}_2\text{Ti}_2\text{O}_7$: an intriguing puzzle

Muon spin relaxation experiments indicate that unlike other geometrically frustrated systems, $\text{Tb}_2\text{Ti}_2\text{O}_7$ displays neither conventional Néel order nor a glass-like state down to temperatures as low as ~ 0.015 K, despite the fact that antiferromagnetic correlations (AFC) develop at ~ 50 K. No evidence for static order is seen in measurements of the spin-lattice relaxation rate even at temperatures of a few percent of the Curie-Weiss temperature. Rather, in terms of the spin fluctuations the system appears essentially to remain dynamic at low temperatures. In addition, inelastic neutron scattering shows incomplete soft mode behaviour in its magnetic excitation spectrum below about 30 K. The relatively flat magnetic excitation spectrum softens at the first antiferromagnetic wave vector, in a manner reminiscent of the roton minimum in superfluid liquid ^4He .

A fit of dc susceptibility measurements [95] taken in a magnetic field of 0.01 T in the high temperature regime (> 200 K) to a Curie-Weiss form $\chi^{-1} \sim T - \theta_{CW}$ yields an antiferromagnetic Curie-Weiss temperature of $\theta_{CW} = -18.9(3)$ K and a paramagnetic moment of $9.6\mu_B$, which compares favorably with the free ion value appropriate to Tb^{3+} in its 7F_6 ground state. While the observed susceptibility departs from the Curie-Weiss form below ~ 100 K, no anomalies or history dependences are observed at low temperatures, indicating the absence of a transition to a long range ordered or spin glass-like state above 2 K.

The behaviour of $\text{Tb}_2\text{Ti}_2\text{O}_7$ was studied by μSR measurements in a small longitudinal field of 0.005 T at TRIUMF using both powder and [111] single crystal samples. Large rapidly fluctuating internal magnetic fields, which characterise a paramagnet, are evidenced by the single exponential muon spin relaxation observed at all temperatures.

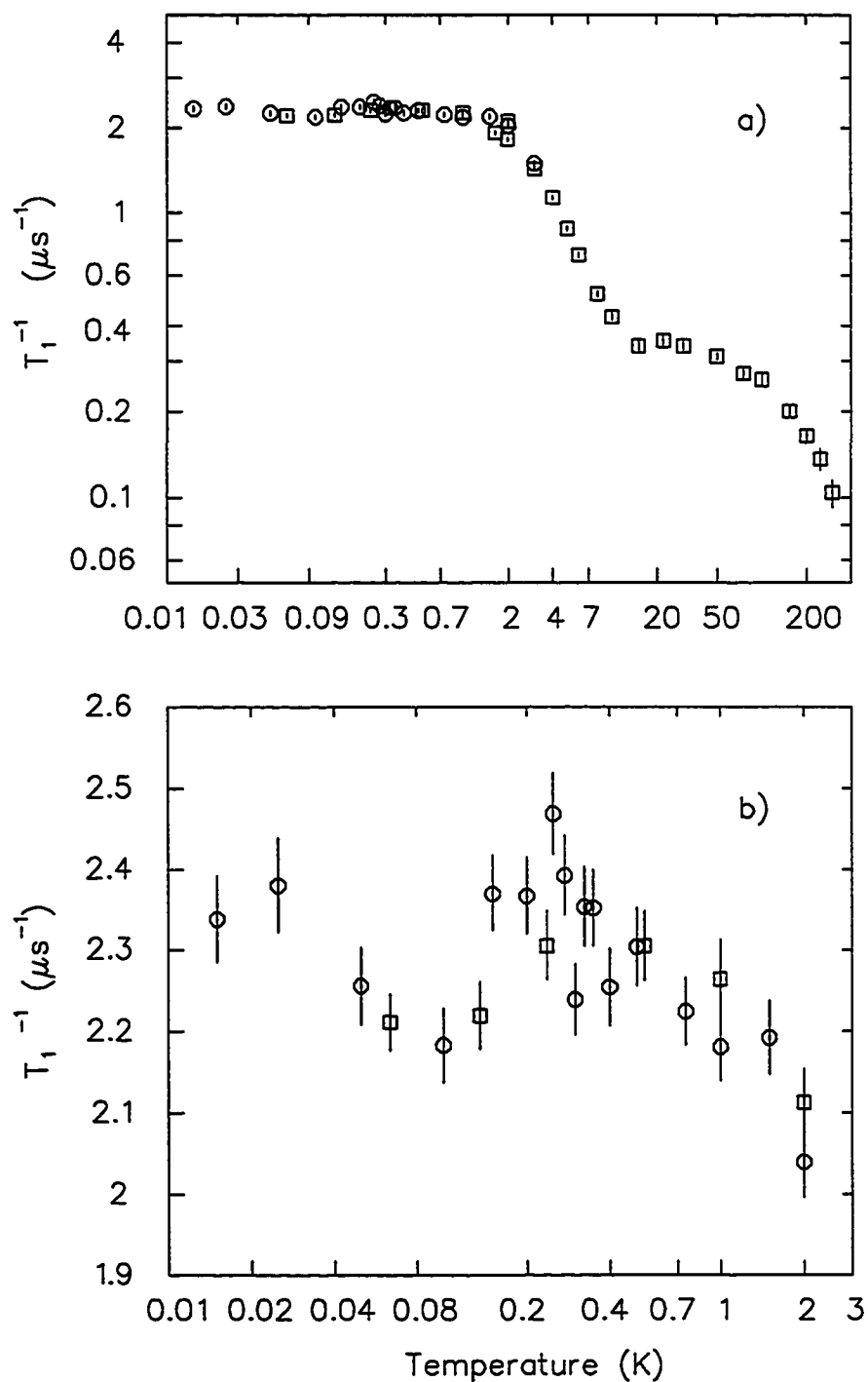


Figure 8.56: Muon spin depolarisation rate versus temperature for $Tb_2Ti_2O_7$ in a longitudinal field of 0.005 T. The squares indicate data taken on a powder sample, the circles a [111] single crystal.

The results of analysing ¹ the data between 0.05 and 10 μs are shown in Fig. 8.56. The smooth monotonic increase of T_1^{-1} down to 75 mK for the powder and 15 mK for the single crystal establishes that $Tb_2Ti_2O_7$ remains paramagnetic down to very low temperatures. There is no evidence of a peak in T_1^{-1} , which would indicate the critical slowing down of spin fluctuations associated with a continuous phase transition. In the fast fluctuation limit, which is appropriate here, the muon spin relaxation rate is given by Eq. (5.59). Taking $\Delta/\gamma_\mu = 0.70(6)$ T from studies of the isostructural compound $Tb_2Mo_2O_7$ [22], one can estimate the spin fluctuation rate. This is reasonable as the behaviour of the Tb^{3+} moments in the paramagnetic regime is measured to be roughly the same. In $Tb_2Mo_2O_7$ one can measure the magnitude of the internal field directly since spin freezing is observed. For example on the low temperature plateau below 2 K it is estimated that ν saturates at about 0.04 THz.

Powder neutron diffraction measurements were carried out on the C2 diffractometer at the NRU reactor at Chalk River Laboratories (CRL). Measurements were performed between 2.5 and 100 K employing a Si(1,1,3) monochromator and 3.52 THz neutrons, with a pyrolytic graphite (PG) filter in the incident beam to remove higher order contamination. Results at 2.5 K are shown in the top panel of Fig. 8.57. Sharp, resolution limited nuclear Bragg peaks are superimposed on diffuse magnetic scattering, reminiscent of that seen from $Tb_2Mo_2O_7$ [80]. The 2.5 K and 50 K data sets, from which the diffraction pattern taken at 100 K has been subtracted, are shown in the bottom panel of Fig. 8.57. This net intensity has been corrected for the Q -dependence due to the Tb^{3+} magnetic form factor [184], and can be directly compared with models of short range AF order. The diffuse scattering evolves with temperature, clearly showing that short range antiferromagnetic correlations develop below 50 K and the form of the structure factor is reminiscent of that observed in liquids. Ashcroft and Lekner [185] calculated a closed form for the structure factor $S(Q)$ for a system of hard spheres of diameter σ and

¹At early times ($< 0.05 \mu s$) the spectra are prone to distortions which often appear as a step in the data. Hence the first 0.05 μs have been omitted from the analysis.

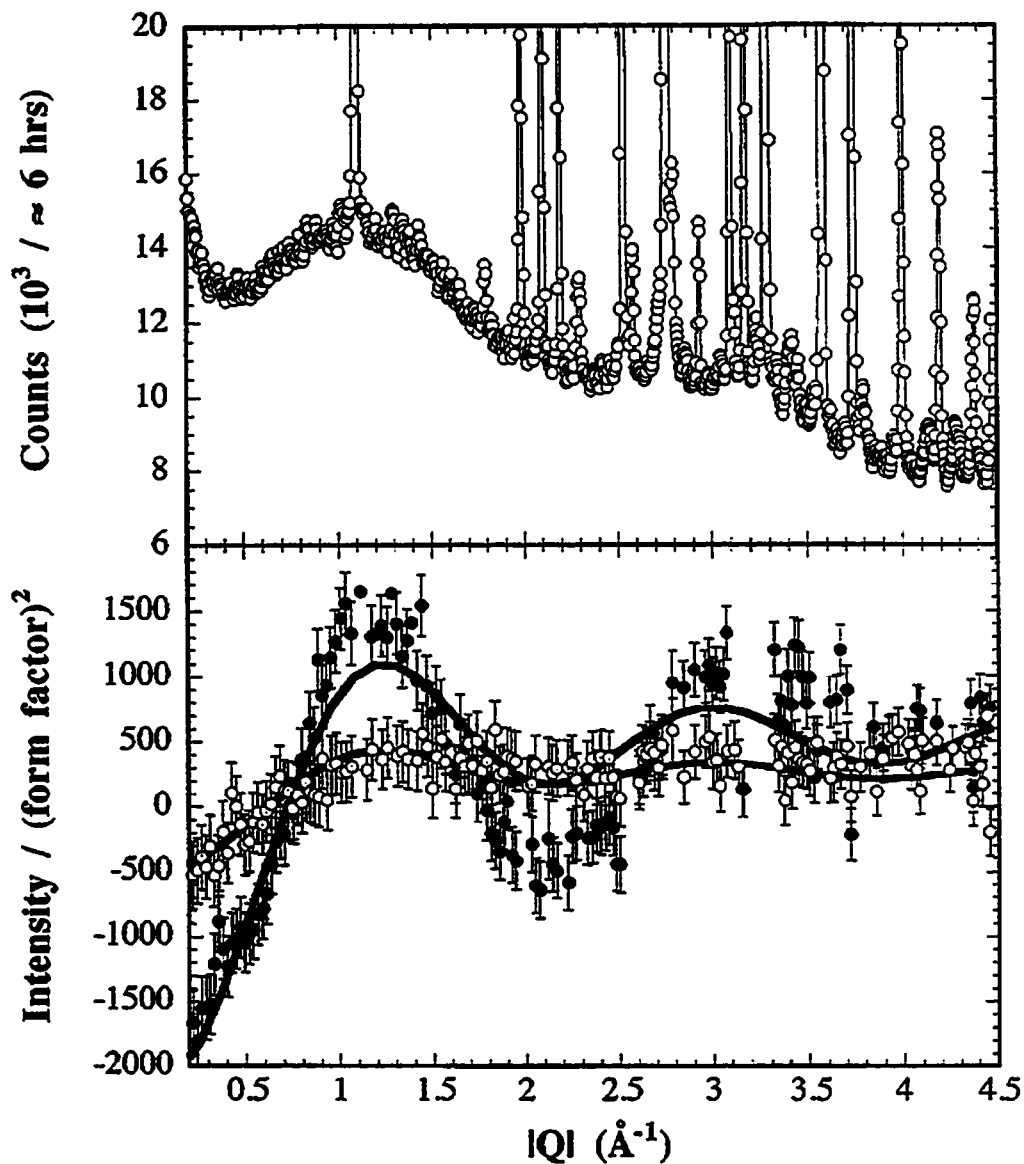


Figure 8.57: A neutron diffraction pattern in $Tb_2Ti_2O_7$ at 2.5 K is shown in the top panel. The difference between diffraction patterns taken at 2.5 K (filled circles) and 50 K (open circles) and that taken at 100 K is shown in the bottom panel. The solid lines are fits to Eq. (8.94).

number density n as

$$S(Q\sigma) = [1 - nC(Q\sigma)]^{-1} \quad (8.92)$$

where

$$C(Q\sigma) = -4\pi\sigma^3 \int_0^1 ds s^2 \frac{\sin sQ\sigma}{sQ\sigma} (\alpha + \beta s + \gamma s^3) \quad (8.93)$$

is the Fourier transform of the correlation function. The quantities α , β and γ depend only on the fraction of the total volume occupied by the hard spheres. The above equation is in good agreement with experimental data on liquid He, Ne, Ar, Kr and Xe [186]. An analogous equation for the scattering from a polycrystal displaying a local magnetic structure due to short range magnetic correlations is given by Bertaut *et al.* [187]:

$$S(Q) \sim \sum_{j,k} \langle S_j \cdot S_k \rangle \frac{\sin(Qr_{j,k})}{Qr_{j,k}} \propto \frac{\sin(Qr_{j,k})}{Qr_{j,k}}. \quad (8.94)$$

Using this model, involving spins correlated over nearest neighbours only, provides a good description of the diffuse scattering shown in Fig. 8.57, as shown by the solid lines. It correctly accounts for the positions of the peaks and valleys, at this and other temperatures up to 50 K. Interestingly, the inclusion of spin correlations beyond nearest neighbour and using, for example, the FeF_3 local structure, produces another broad peak in the calculated net intensity intermediate between those at ~ 1.2 and $\sim 3.1 \text{ \AA}^{-1}$. This is consistent with the peaks at 1 and 2 \AA observed in $Tb_2Mo_2O_7$ [80], where magnetic moments at the Mo^{4+} site can mediate longer-range spin correlations. The intermediate peak is not observed experimentally in this material and it is therefore concluded that spins in $Tb_2Ti_2O_7$ are correlated over a single tetrahedron only, down to at least 2.5 K.

Inelastic neutron scattering measurements were performed on the C5 triple axis spectrometer at CRL in constant scattered energy mode. Low energy-resolution measurements ($E'/h = 3.52 \text{ THz}$) with a PG filter in the scattered beam revealed the presence of dispersionless modes at frequencies of ~ 2.4 and 3.5 THz , which are crystalline electric field levels (see Fig. 8.58). The peak at $\sim 3.5 \text{ THz}$ is broadened due to mixing with phonons.

Lowering E'/h to 1.2 THz with a cooled Be filter in the scattered beam allowed for

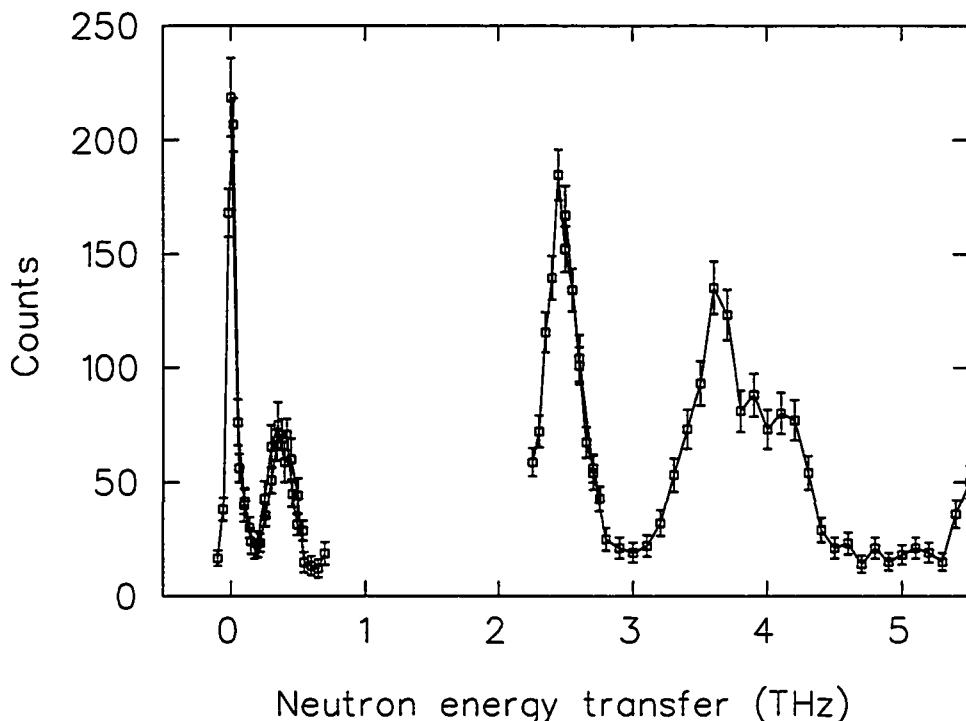


Figure 8.58: Inelastic neutron scattering data obtained at a temperature of 12 K and $Q=2.2 \text{ \AA}^{-1}$ in $Tb_2Ti_2O_7$.

higher energy resolution ($\sim 0.09 \text{ THz FWHM}$) measurements and typical constant $|Q|$ scans are shown in the top panel of Fig. 8.59. The energy of the modes at 0.7 and 2.2 \AA^{-1} are nearly identical, while there is a pronounced decrease in the integrated intensity of the mode at 2.2 \AA^{-1} compared with that at 0.7 \AA^{-1} , consistent with that expected due to the Tb^{3+} magnetic form factor. The energy of these modes clearly dips near 1.2 \AA^{-1} and Gaussian fits to these and similar data at a variety of $|Q|$'s bear this out, as is seen in the lower panel of Fig. 8.59. At 12 K the energy of this mode dips by roughly 10%, at the wavevector corresponding to the first maximum in the magnetic structure factor (see Fig. 8.57). Recently, similar measurements have been done on a single crystal by Kanada *et al.* [188].

This incomplete softening of a well defined excitation has not been previously observed in geometrically frustrated magnets, or in chemically disordered spin glasses. Similar magnetic behavior has been observed in the amorphous ferromagnet Co_4P [189]. The

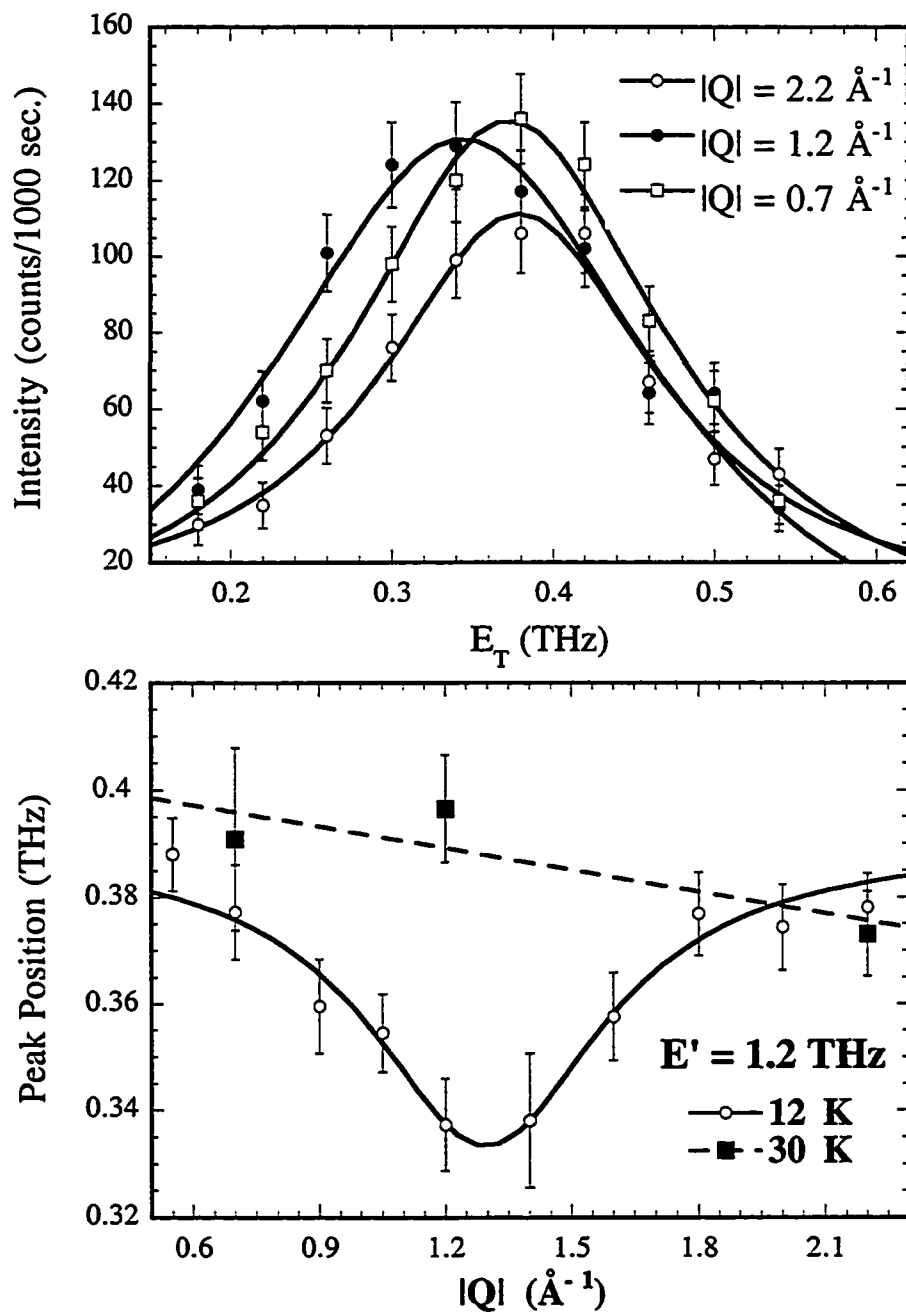


Figure 8.59: Top panel: constant $|Q|$ scans at 12 K in $Tb_2Ti_2O_7$. Lower panel: Dispersion of the magnetic excitation spectrum at 12 and 30 K.

minimum in the magnetic excitation spectrum goes away with increasing temperature roughly on the scale of θ_{CW} and by 30 K it is no longer evident as seen in the bottom panel of Fig. 8.59, even though the excitations themselves are still well defined. On further increasing the temperature the mode weakens in intensity and has merged into the background by 100 K.

A gapped magnetic excitation spectrum with weak dispersion is known to exist in a variety of singlet ground state systems such as Haldane[190] and spin-Peierls[191] materials and in a few praseodymium intermetallics[194], where the ground and first excited states are singlets. Haldane [192] predicted the existence of a gap between the many-body singlet ground state and triplet first excited state in an one-dimensional system with Heisenberg interactions between antiferromagnetically coupled integer spins. The spin-Peierls transition [193] is also due to collective behaviour in one-dimensional antiferromagnetic spin chains. The coupling between the electronic spins and three-dimensional lattice phonons leads to a magneto-elastic instability and hence a transition to a dimerised ground state. This again gives rise to a gap in the magnetic excitation spectrum, separating a singlet ground state from a triplet excited state. By contrast, the singlet ground state arises from single ion crystal electric field effects in the praseodymium compounds. Such a singlet ground state occurs in the Tm^{3+} based titanate, $Tm_2Ti_2O_7$ [96]. It is important to rule out such a possibility for Tb^{3+} in $Tb_2Ti_2O_7$ as such a system trivially fails to undergo transitions to either an ordered or a spin glass state on lowering the temperature, due to the non-magnetic nature of the rare earth ground state. However, $Tm_2Ti_2O_7$ displays the characteristic temperature-independent low temperature susceptibility and the absence of elastic magnetic neutron scattering, clearly distinguishing it from our present study of $Tb_2Ti_2O_7$. This, along with the μ SR results, lead us to conclude that the Tb^{3+} ground state is magnetic and that potential explanation for the absence of a transition can be eliminated.

Susceptibility measurements have also been carried out on the dilute system $(Tb_{0.02}Y_{0.98})_2Ti_2O_7$ to investigate the nature of the ground state of isolated Tb^{3+} ions in

their pyrochlore environment. Strongly temperature dependent behaviour was observed down to 2 K with a Curie-Weiss temperature of $-6.3(4)$ K, also indicating a magnetic ground state. This is borne out by the crystal electric field calculations described in Chapter 3, which predict doublets for both the ground and first excited states. Furthermore a large paramagnetic frequency shift is observed in a transverse magnetic field of 0.096 T at all temperatures. These measurements are discussed in greater detail in section 8.2. The muon precession frequency shift, which is a measure of the local susceptibility, tracks the bulk dc susceptibility down to 2 K, indicating that the muon is not perturbing the magnetic system in any significant way. There is thus every indication that the muon is simply probing the low frequency dynamics as a simple spectator in this system. It should be kept in mind that the few special cases where the muon is a significant perturbation such as $PrNi_5$ [195] and $PrIn_3$ [196] are singlet ground state systems. Their crystal field levels are dramatically altered because of the delicate magnetic balance in that state. That is certainly not the case in $Tb_2Ti_2O_7$.

The gapped magnetic excitation spectrum is then attributed to Ising-like anisotropy in the spin Hamiltonian, as would be expected from orbital contributions to the Tb^{3+} magnetic moment in its crystalline environment. The present measurements indicate an anisotropy gap of ~ 0.38 THz or 18 K. It is possible to think of the dip in the excitation spectrum as a collective tumbling of spin orientations on loosely correlated tetrahedra from one such local ground state to another. A magnetic excitation with such a characteristic has been discussed theoretically [197]. It is speculated that further softening of this mode, requiring larger exchange relative to the competing energy scales in the problem, including the anisotropy gap and perhaps dipolar energies, would precipitate a transition to either a non-collinear ordered magnetic state or a spin glass state. However, this does not occur in $Tb_2Ti_2O_7$, leaving it a cooperative paramagnet to low temperatures. In light of this, the low temperature plateau in the μ SR spin relaxation rate and the corresponding field fluctuation rate may be determined by some effective exchange coupling between the correlated tetrahedra of Tb^{3+} spins, as illustrated in Chapter 7.

8.1 Calculations of T_1^{-1}

An extensive series of μ SR measurements on the powder sample have also been carried out in higher longitudinally applied magnetic fields, the results of which may be seen in Fig. 8.60. All the spectra were analysed between 0.05 and 10 μ s. Most of the data is well described by a single exponential $A_{\text{corr}} \exp(-t/T_1)$, with the exception of that at 1 and 2 T, where non-exponential behaviour gradually develops below 4 K (see Fig. 8.61). The cause of this phenomenon is as yet unclear. The corrected asymmetry A_{corr} was held constant for the temperature scans at values found from global fits of the data at a particular field. This is no longer appropriate for field scans, as illustrated in Fig. 7.55. Hence the asymmetry was allowed to vary for the field scans shown in Fig. 8.62. All the data were well fitted by a single exponential function for fields below 0.15 T, even at 0.075 K.

The muon spin depolarisation rates observed as a function of temperature and field in $Tb_2Ti_2O_7$ are highly unusual and a detailed theoretical framework is needed to interpret the data. The calculation of T_1^{-1} in a system of electronic moments subject to crystal electric fields, dipolar and exchange interactions is by no means straightforward and to the author's knowledge a complete description is not as yet available.

The shift in the observed resonance frequency, a function of the local field, relative to an external applied field, depends on the dynamical spin susceptibility $\chi(\mathbf{r}, t)$. This is also related to the scattering function $S(\mathbf{Q}, \omega)$ in the neutron magnetic scattering differential cross section [198] and, via the fluctuation-dissipation theorem, to the spin lattice relaxation rate T_1^{-1} [199]. The fluctuation-dissipation theorem describes the relationship between the response of a system and its thermal fluctuation spectrum. It is quite general, but here only its application to a magnetic medium is considered. The magnetisation is given by $\langle \psi | \mathcal{M} | \psi \rangle$ where \mathcal{M}_α is the magnetic moment operator in the

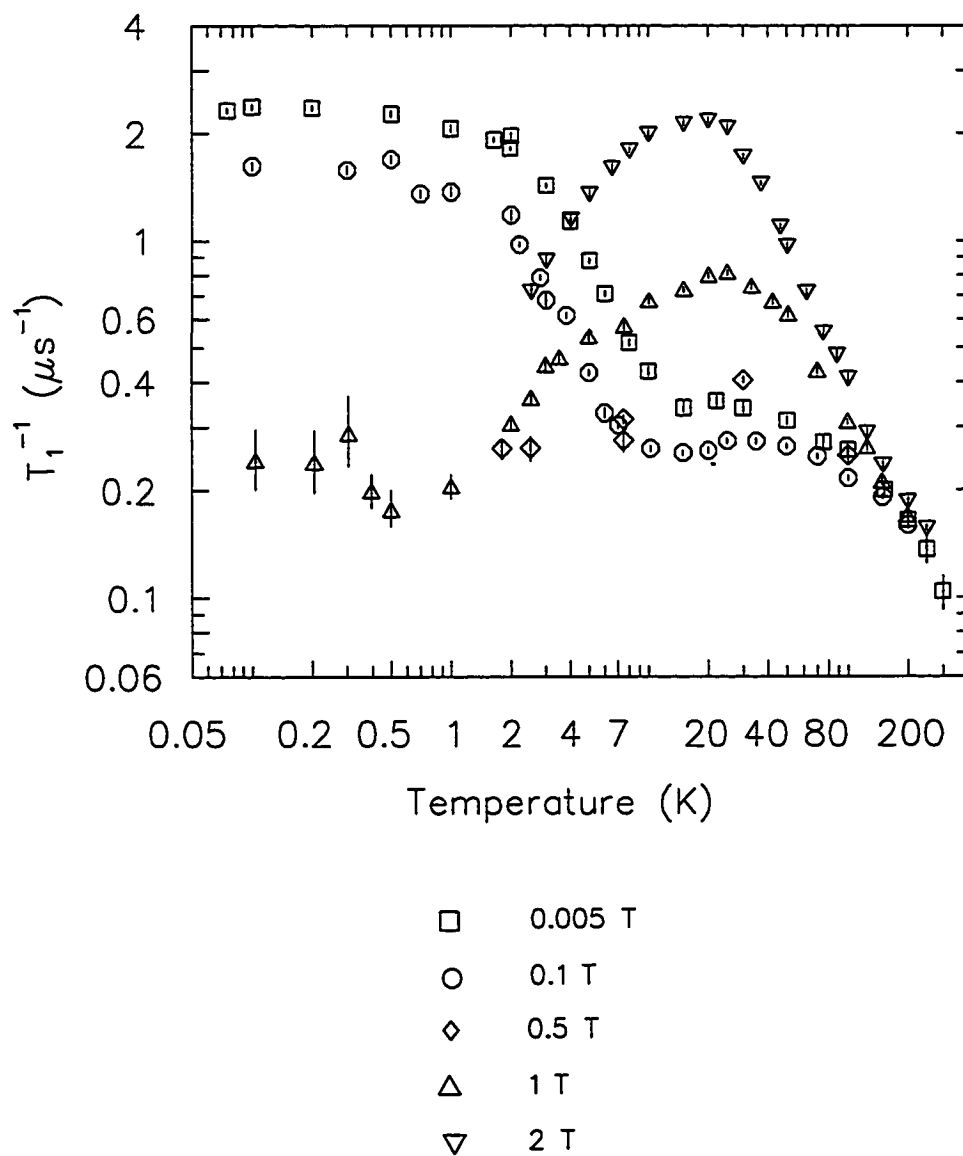


Figure 8.60: Muon spin depolarisation rate versus temperature for a powder sample of $Tb_2Ti_2O_7$ in a various longitudinally applied magnetic fields. The spectra at 0.005, 0.1 and 0.5 T were analysed using a single exponential function, those at 1 and 2 T with a stretched exponential.

α direction. As derived in White [200],

$$\int_{-\infty}^{\infty} \langle 1/2[\mathcal{M}_{\alpha'}(\mathbf{q}, t)\mathcal{M}_{\alpha}(-\mathbf{q}) + \mathcal{M}_{\alpha}(-\mathbf{q})\mathcal{M}_{\alpha'}(\mathbf{q}, t)] \rangle_s e^{i\omega t} dt = \hbar V \coth\left(\frac{\beta\hbar\omega}{2}\right) \chi''_{\alpha'\alpha}(\mathbf{q}, \omega)_s, \quad (8.95)$$

where s denotes the symmetric part of the tensor. In other words, the Fourier transform of the correlation function is proportional to the imaginary or absorptive part χ'' of the dynamic susceptibility. The reactive part of the response, which is in phase with the perturbation, is denoted by χ' , such that $\chi(\mathbf{q}, \omega) = \chi'(\mathbf{q}, \omega) + i\chi''(\mathbf{q}, \omega)$. In the limits $\omega \rightarrow 0$ and $\mathbf{q} \rightarrow 0$, the dynamic susceptibility becomes the ordinary static susceptibility. As a point probe, the spectrum obtained with the μ SR technique is an average over all wave vectors.

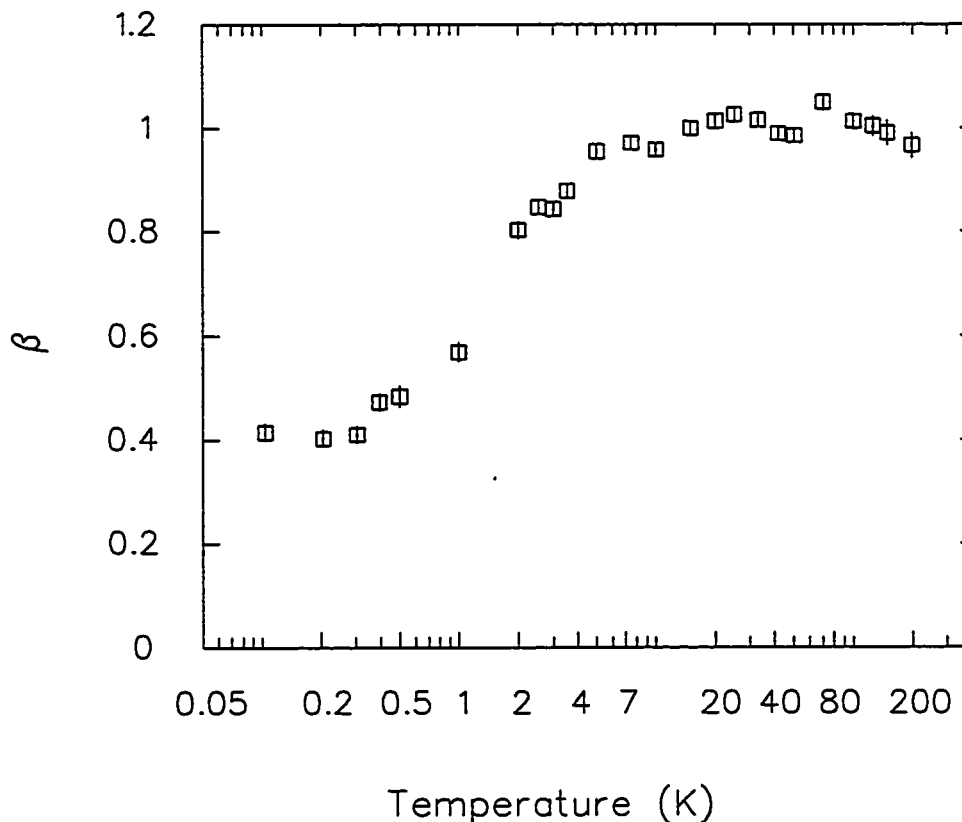


Figure 8.61: The parameter β versus temperature for $Tb_2Ti_2O_7$ in an applied field of 1 T. The spectra were fitted to a stretched exponential function $G_{zz}(t) = \exp[-(t/T_1)^\beta]$.

In principle, it should be possible to extract both the scattering function and spin

lattice relaxation rate from a calculation of $\chi''(\omega)$. In intermetallic compounds, where the dynamics of the rare earth ion are dominated by the coupling between the total momentum J and the conduction electron spin density, general methods have been developed to calculate $\chi''(\omega)$ in the presence of CEF splittings [201, 202, 203]. Following the notation of Dalmas de Réotier *et al.* [204], a description for the muon spin relaxation rate in a 4f paramagnet with strong crystal electric fields and weak intersite interactions is developed below. It is written in terms of the van Vleck formula [205] for the susceptibility, derived using linear response theory [172]. The exchange narrowing approximation has been assumed.

Making use of the approximate model of Holland-Moritz *et al.* [206] derived for the computation of inelastic neutron scattering spectra, the susceptibility is split into Curie and van Vleck terms. The diagonal elements of the susceptibility tensor, the only ones which are non-zero, are given by:

$$\frac{\chi''_{\alpha\alpha}(\omega)}{\pi\omega} = \sum_m \chi_C^m P_{mm}(\omega) + \frac{1}{2} \sum_{n \neq m} \chi_{VV}^{nm} [1 - \exp(-\beta\Delta_{nm})] P_{nm} \left(\omega - \frac{\Delta_{nm}}{\hbar} \right) \quad (8.96)$$

where the sums are over the CEF energy levels. The first term, the Curie susceptibility of the m^{th} level, is written as

$$\chi_C^m = \frac{\mu_0(gJ\mu_B)^2}{k_B T} \left(\rho_m |\langle m | J_\alpha | m \rangle|^2 - |\rho_m \langle m | J_\alpha | m \rangle|^2 \right) \quad (8.97)$$

while the second term

$$\chi_{VV}^{nm} = \mu_0(gJ\mu_B)^2 \rho_m \frac{|\langle n | J_\alpha | m \rangle|^2}{\Delta_{nm}} \quad (8.98)$$

is the van Vleck susceptibility for the transition from the state with energy E_m to the state with energy E_n , such that $\Delta_{nm} = E_n - E_m$. These terms describe the elastic and inelastic CEF transitions respectively. The probability of the m^{th} level being occupied is governed by Boltzmann statistics:

$$\rho_m = \exp(-\beta E_m) / Z \quad (8.99)$$

where $\beta = 1/k_B T$ and Z is the partition function.

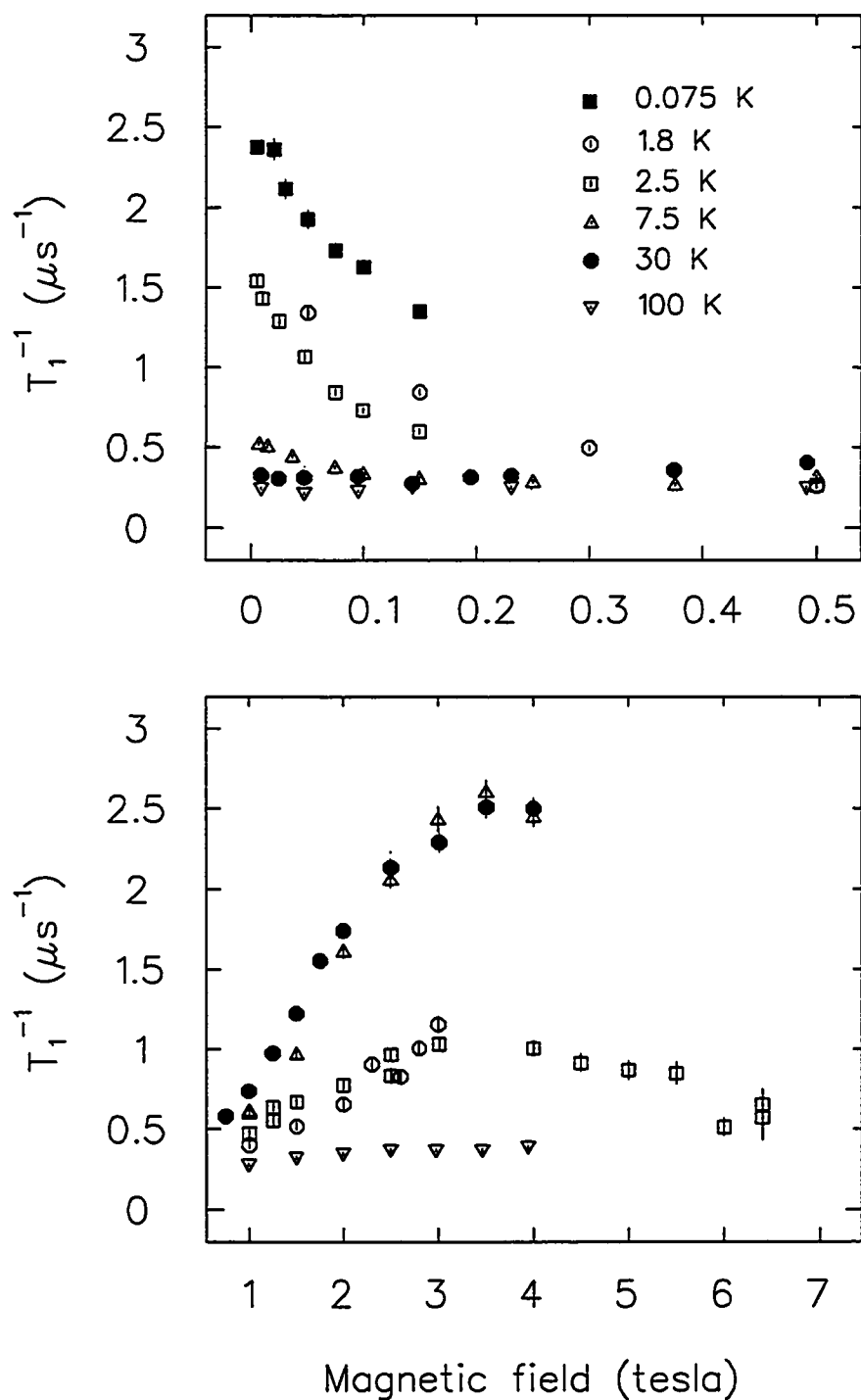


Figure 8.62: Muon spin depolarisation rate versus magnetic field for a powder sample of $Tb_2Ti_2O_7$ at various temperatures. All the spectra were fitted to a single exponential function $G_{zz}(t) = \exp(-t/T_1)$.

Introducing the Curie susceptibility for the free ion,

$$\chi_C = \frac{\mu_0(g_J\mu_B)^2 J(J+1)}{3k_B T}, \quad (8.100)$$

the relaxation rate can be written generally as

$$\lambda_Z = \left[\sum_{\alpha, \alpha'} L_{\alpha, \alpha'}(\theta, \phi) M_{\alpha, \alpha'} \right] \frac{1}{\chi_C} \lim_{\omega \rightarrow 0} \frac{\chi''(\omega)}{\omega} \quad (8.101)$$

or equivalently

$$\lambda_Z = \left[\sum_{\alpha, \alpha'} L_{\alpha, \alpha'}(\theta, \phi) M_{\alpha, \alpha'} \right] \frac{1}{\Gamma_{\mu SR}}, \quad (8.102)$$

where $M_{\alpha, \alpha'}$ is the coupling tensor between the magnetic ion and the muon spin and $L_{\alpha, \alpha'}$ is a tensor

$$\begin{pmatrix} \cos^2 \phi \cos^2 \theta + \sin^2 \phi & -\cos \phi \sin \phi \sin^2 \theta & -\cos \phi \cos \theta \sin \theta \\ -\cos \phi \sin \phi \sin^2 \theta & \sin^2 \phi \cos^2 \theta + \cos^2 \phi & -\sin \phi \cos \theta \sin \theta \\ -\cos \phi \cos \theta \sin \theta & -\sin \phi \cos \theta \sin \theta & \sin^2 \theta \end{pmatrix}. \quad (8.103)$$

The powder average of each diagonal element is $2/3$; off-diagonal elements vanish. If the crystalline axes and laboratory axes are coincident, for cubic symmetry $M_{xx} = M_{yy} = \Delta^2$ and so the well known formula valid in the motionally narrowed limit is recovered: $\lambda_Z(T) = 2\Delta^2/\Gamma_{\mu SR}(T)$. Note that the fluctuation rate $\Gamma_{\mu SR}$ is a now complex quantity with contributions from both quasielastic and inelastic excitations. If one neglects the possible effect of the inelastic excitations, as is usual in NMR, $\Gamma_{\mu SR}$ is determined by the quasi-elastic linewidth measured by inelastic neutron scattering. However, the two quantities are not in general equal.

Complications arise in attempting to evaluate $P_{nm}(\omega)$, the spectral function for the nm excitation. To compare neutron scattering and μ SR data a lorentzian shape is assumed:

$$P_{nm}(\omega - \Delta_{nm}/\hbar) = \frac{1}{\pi} \frac{\Gamma_{nm}}{\Gamma_{nm}^2 + (\hbar\omega - \Delta_{nm})^2} \quad (8.104)$$

where Γ_{nm} is the dynamical half width at half maximum. In the absence of a theoretical model, Γ_{nm} must be measured experimentally. The energy broadening of the magnetic

excitation at ~ 0.4 THz has been followed as a function of temperature by Kanada *et al.* [188]. It decreases linearly with temperature above roughly 40 K, below which it becomes almost temperature independent at ~ 1 meV, above the resolution limit of the spectrometer. However, in the limit of rapid spin fluctuations, μ SR is sensitive to the magnetic excitations at an energy associated with the muon Larmor frequency, which is typically in the MHz range. Hence, it is the broadening of the quasi-elastic peak which is the relevant quantity needed to evaluate T_1^{-1} . Unfortunately, the peak around zero energy transfer is thought to be mainly due to incoherent elastic scattering. In general, the coherent and incoherent contributions to neutron scattering arise in the following way [198]: a system has different scattering lengths b associated with the nuclear spin (in particular, different values of S_z for the combined nucleus and neutron system), or with the presence of isotopes. The coherent scattering is that which would arise if all the scattering lengths were set equal to \bar{b} . The incoherent scattering results from the random distribution of the deviations of the scattering lengths from their mean value.

To simplify the problem, $P_{nm}(\omega)$ has been set equal to 1 and T_1^{-1} calculated using Eqs. (8.96) and (8.101), substituting in the eigenvalues and eigenvectors of crystal electric field and Zeeman Hamiltonians. The energy levels associated with the former interaction alone are summarised in Table 3.7, where the charges on the terbium and oxygen ions, as well as the oxygen parameter x , have been adjusted to match the inelastic transitions shown in Fig. 8.58. The energy levels are therefore infinitely sharp, which is unphysical as it implies that the ions are completely isolated. In a real system dipolar and exchange interactions between electronic moments would give rise to energy levels with finite linewidths. Nevertheless, this naive calculation does reproduce some of the features seen in Fig. 8.62, as shown in Fig. 8.63. In contrast with $Gd_2Ti_2O_7$, at high temperatures T_1^{-1} increases smoothly with applied magnetic field, reaching a peak at roughly 3.5 T before decreasing again. The effect of a magnetic field applied along the local \hat{z} axis is to split any degeneracies in the CEF energy levels in Table 3.7. For example, fields of 0.1 and 2 T result in splittings in the ground state doublet of 0.7 and 17 K respectively.

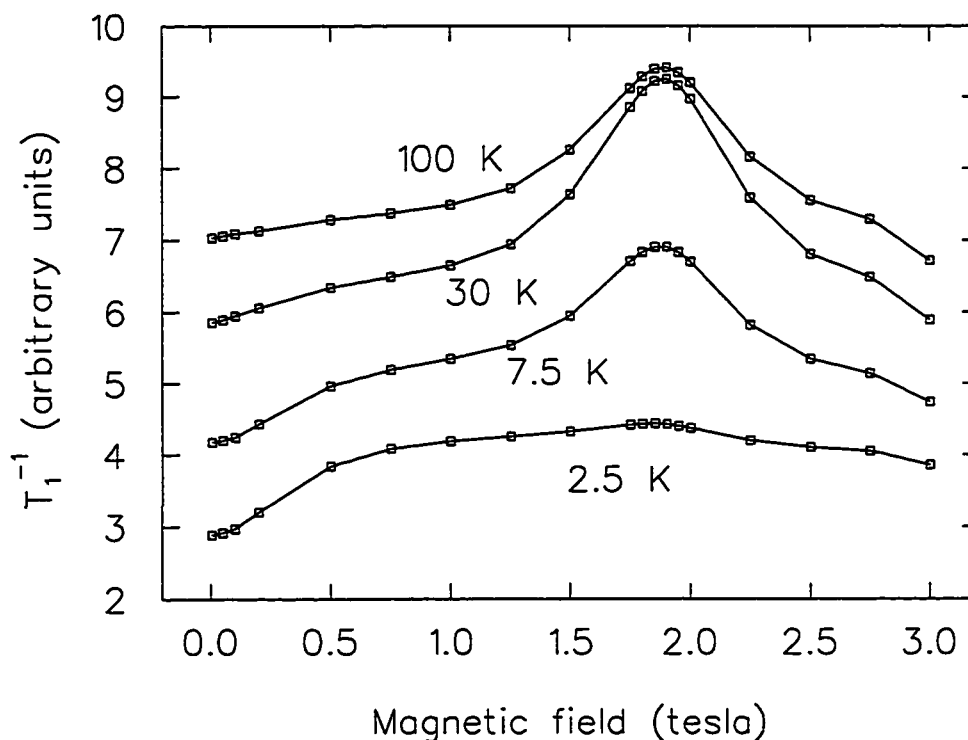


Figure 8.63: Calculation of the muon spin relaxation rate using Eqs. (8.96) and (8.101).

It is the splitting of the ground state and first excited doublets which are of the greatest interest. As shown in Table 3.7, the former is made up of predominately $|J_z = \pm 5\rangle$ and the former $|\pm 4\rangle$. The peak in the calculated value of T_1^{-1} at approximately 2 T corresponds to significant mixing of the $|J_z = +5\rangle$ and $|-4\rangle$ states and is associated with a level crossing resonance, while by 3 T the $|-4\rangle$ state has dropped lower than the $|+5\rangle$ state. By contrast, fields applied along the \hat{x} and \hat{y} directions cause transitions between energy levels, mixing different values of the z component of the total angular momentum J_z such that, for instance, the probability amplitude of $|J_z = +5\rangle$ for the lowest energy level drops from $\sim 96\%$ in zero field to $\sim 66\%$ at 2 T. As a result, the contribution from the van Vleck term in the susceptibility increases. The results shown in Fig. 8.63 are an average of contributions from magnetic fields in the \hat{x} , \hat{y} and \hat{z} directions. Interestingly, the more pronounced increase in T_1^{-1} observed at 30 K as compared with those at both 100 K and 2.5 K is also qualitatively reproduced. The peak is suppressed at low

temperatures since only the lowest state is occupied. There is a discrepancy in the field associated with the peak in T_1^{-1} between the data and calculation. This may be because of the crude nature of the point charge calculations of the crystal electric field levels.

The variation in the spin relaxation rate as a function of temperature is much less well modelled, likely because of the temperature dependence of the linewidth. In an applied field of 0.005 T, the Curie term in the susceptibility does increase by $\sim 50\%$ to a rounded peak at 25 K, due to the depopulation of higher CEF energy levels as the temperature is reduced, but this feature is washed out. In the absence of CEF effects, (as in the case of the Gd^{3+} ion) only the Curie term contributes to the susceptibility, the energy level splittings are governed by the Zeeman interactions and are hence much smaller. Since the populations of the various energy levels then do not change significantly over the temperature and field range explored, the spin relaxation rate is independent of temperature and *decreases* with magnetic field. The spectral functions act to alter the relative importance of the various elastic and inelastic transitions, changing the temperature and field dependence of T_1^{-1} .

The field dependence modelled by Eq. (8.96) is a single ion effect and does not reproduce the features observed below 0.5 T at low temperatures, which are as yet not fully explained. In this regime $\mu_B H/k_B T$ is large and the Tb spins are significantly magnetised, as can be seen in Fig. 8.64, which describes the magnetisation of Tb^{3+} ions in the absence of crystal electric field splittings. Hence, as the static component of the internal field increases, there is a corresponding decrease in the spin relaxation rate. The reported decrease in T_1^{-1} with magnetic field occurs at temperatures where transverse field measurements show a large shift in the muon Larmor frequency (see Fig. 8.68). Through the fluctuation dissipation theorem [Eq. (6.79)], T_1^{-1} may be related to χ''/ω . Assuming that the spectral function in Eq. (6.80) does not change rapidly over the frequencies probed, this is proportional to the fractional frequency shift, a measure of the local susceptibility χ' . Transverse field measurements were carried out at 3 and 285 K on the powder $Tb_2Ti_2O_7$ sample to extract the local susceptibility, as illustrated in

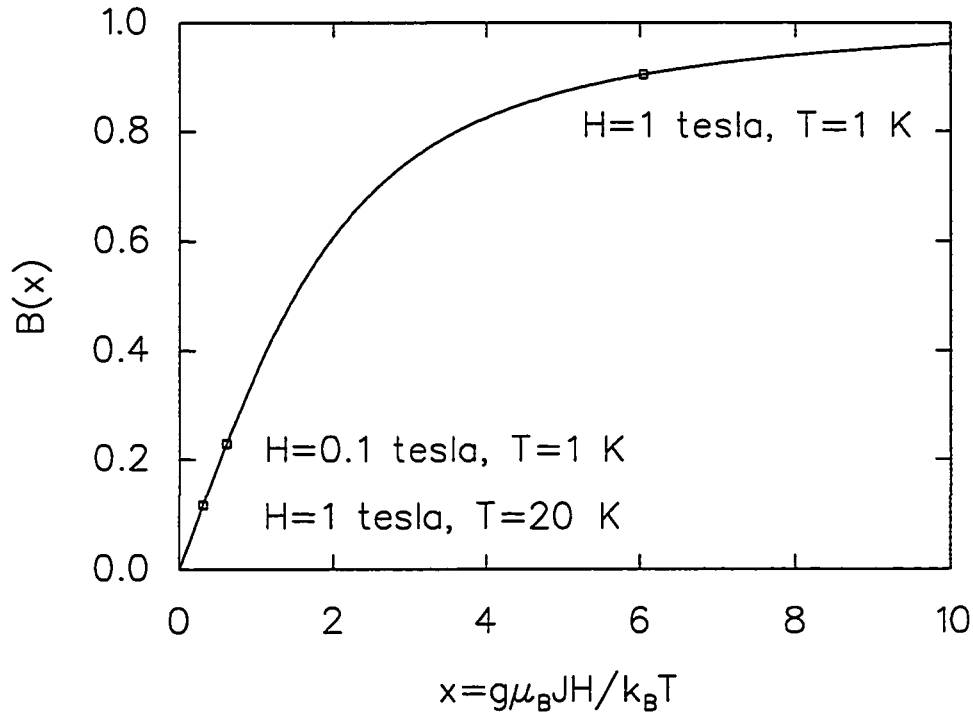


Figure 8.64: Plot of the Brillouin function describing the magnetisation of a set of identical free Tb^{3+} ions in their 7F_6 ground state.

Fig. 8.65. While the theoretical functional form of χ' is not understood in this highly magnetised regime where short range correlations predominate, Fig. 8.65 shows that the field dependence of the spin relaxation rate can be qualitatively reproduced.

It is clear that there are two relevant energy scales in this material: that associated with the crystal electric field energy splittings of tens of kelvin and the scale where the Zeeman splitting of the lowest doublet becomes comparable with $k_B T$ (at ~ 1 K and ~ 0.1 T).

8.2 Evidence for *partial* spin ordering

The spin-ice picture described in Chapter 2 cannot be *a priori* ruled out in $Tb_2Ti_2O_7$ and may help to explain the complicated temperature and field dependent behaviour in this material. Point charge crystal electric field calculations indicate that the ground state of the Tb^{3+} ion in its pyrochlore environment is a doublet with the next excited

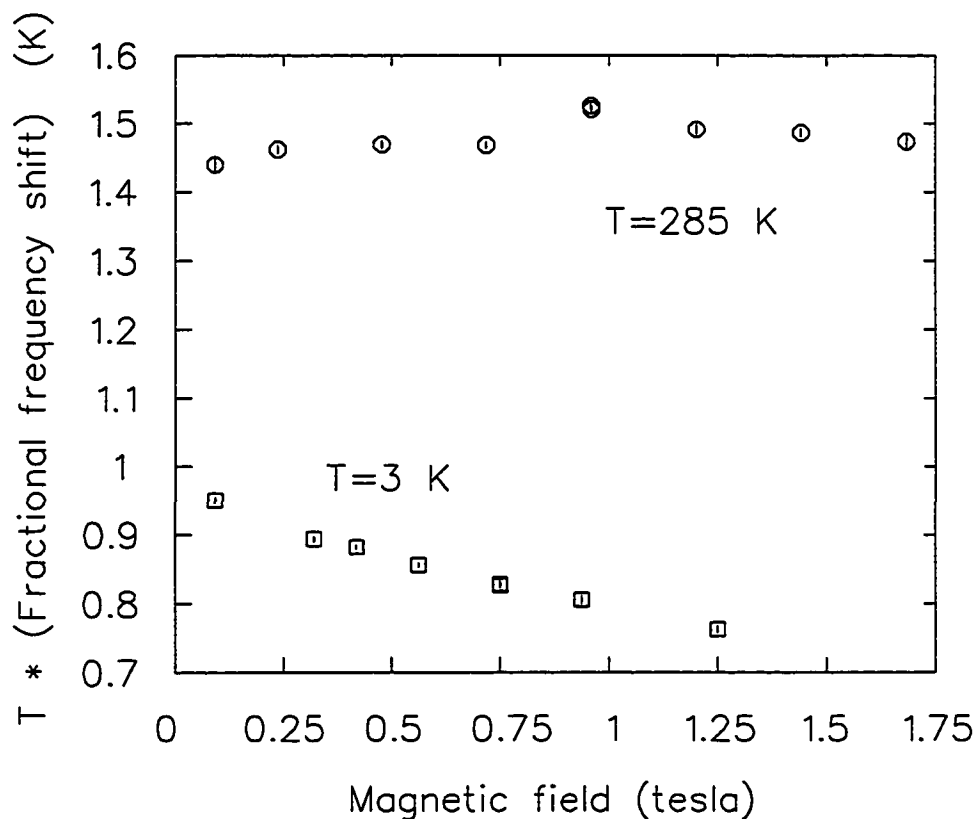


Figure 8.65: Temperature times fractional frequency shift versus applied magnetic field for $Tb_2Ti_2O_7$ at 285 and 3 K. The fractional frequency shift, a measure of the local susceptibility χ' , is proportional to χ''/ω and through the fluctuation dissipation theorem to T_1^{-1} [Eq. (6.79)].

state roughly 18 K higher. This is evidence that at low temperatures $Tb_2Ti_2O_7$ should behave as a quasi spin 1/2 system, where each spin is constrained to point along its local [111] axis. To a first approximation the contribution to θ_{CW} from magnetic interactions (as opposed to crystal electric field effects) may be estimated as $\theta_{CW}(Tb_2Ti_2O_7) - \theta_{CW}((Tb_{0.02}Y_{0.98})_2Ti_2O_7) = [-19 - (-6)] = -13$ K, comparable with $Gd_2Ti_2O_7$. Thus estimates of the ratio \mathcal{J}/\mathcal{D} yield a value of ~ -1 , close the phase boundary for spin-ice behaviour described in Ref. [72].

The T_1^{-1} results described in section 8 show no evidence of spin freezing but rather that $Tb_2Ti_2O_7$ remains in a cooperative paramagnetic state down to 15 mK. Theoretically however, it is very difficult at the classical level to prevent a transition below 100-200 mK

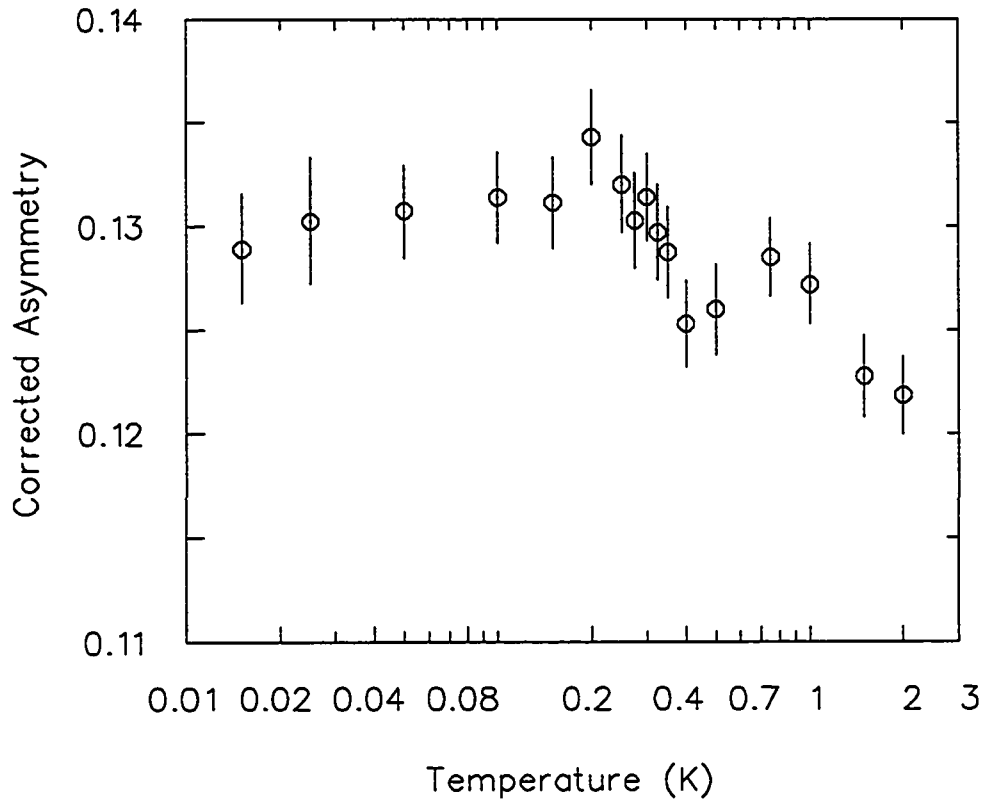


Figure 8.66: Corrected asymmetry versus temperature for $Tb_2Ti_2O_7$ [111] single crystal in a longitudinal field of 0.005 T.

or so. Azaria *et al.* conjectured that frustration in the pyrochlore Heisenberg antiferromagnet can easily induce a first order phase transition [207]. The calculations of Reimers *et al.* [208] based on Landau theory predict long range order with an ordering wave-vector of $Q = 0$ for models where the nearest neighbour exchange coupling $\mathcal{J}_1 < 0$ and $\mathcal{J}_3 > 0$. Analysis of Monte-Carlo simulations with these same combinations of interactions also suggest that the transition may be first order [209]. There is no critical slowing down of spin fluctuations. Consequently, one would not necessarily see a peaking of the dynamical relaxation rate upon approaching the transition. At best, a reduction in the corrected asymmetry below the transition temperature would be observed, corresponding to the $1/3$ component associated of a Kubo-Toyabe function. Figure 8.66 shows the corrected asymmetry measured below 3 K in a longitudinally applied field of 0.005 T for the single crystal sample of $Tb_2Ti_2O_7$. As can be seen, there is no obvious change.

A frequency dependent peak has been observed around 250 mK [210] in ac susceptibility measurements between 25.9 Hz and 793.4 Hz. Such frequency dependence is reminiscent of the behaviour of conventional spin glasses. On a cautionary note, superparamagnets may show similar frequency dependent behaviour, as well as history dependence. It should be remembered that spin glass behaviour is thought to be due to the collective response of many spins versus the reorientation of finite sized spin clusters, which becomes inhibited below a so called “blocking” temperature in a superparamagnet. In the latter system the temperature dependence of the peak in the a.c. susceptibility typically obeys an Arrhenius law due to an anisotropy gap, whereas in spin glasses the shift is generally much smaller.

With these results in mind, μ SR spectra were recorded at very fine temperature intervals for the single crystal sample. Nevertheless, as shown in Fig. 8.56b, there is only very slight if any evidence of a peak in T_1^{-1} at ~ 250 mK. No freezing of the spins is seen on the time scale of μ SR, as would be evidenced by the development of a 1/3 static component.

It cannot be claimed that no static ordering occurs. The μ SR results imply only that the dynamic part does not show any abrupt features which are typical of an ordinary phase transition. This suggests that only a small fraction of the moments or a small fraction of each moment is involved. One may only say that there remains a large dynamic part to the internal field through the region of the phase transition, if it exists. Even in zero field it is not straightforward to quote a “sensitivity limit” for detection of a partial static component. Coexisting static and dynamic internal magnetic fields have been discussed in Chapter 6 with respect to conventional spin glasses. The dip in the Kubo Toyabe function shown in Fig. 5.23 occurs at $\sim 1/\Delta$, where Δ is a measure of the static internal field. Hence the rapid depolarisation of 2/3 of the signal due to an internal field of greater than ~ 20 MHz would not be visible, as it occurs within the initial dead time of ~ 50 ns. Instead, the static component would appear as a loss of asymmetry, as only the 1/3 component would be detectable. Such a loss of asymmetry is *not* clearly observed

in the measurements. However, a smaller static internal field would give rise to rapid depolarisation of 2/3 of the signal. This is difficult to separate from rapid depolarisation due to dynamic spins. The dynamic signal acts to wash out any feature reminiscent of a Kubo Toyabe function. On the other hand, single exponential relaxation would not be expected given a sizeable static component. The single exponential behaviour observed in low fields implies that any static contribution must be small. In the longitudinal field geometry used in the field scans shown in Fig. 8.62 there is little or no sensitivity to the buildup of a small static internal field.

While the longitudinal field μ SR measurements give no indication of a phase transition, experiments in a transverse field geometry of ~ 0.09 T show history dependence below 1 K (see Fig. 8.68b). The data in a conventional cryostat (square symbols) were taken using the separate spectra apparatus described in Chapter 4, recording the shift in the muon Larmor frequency in the $Tb_2Ti_2O_7$ sample relative to a silver reference. The shift is a measure of the local contact hyperfine field at the muon site, since the dipolar field contributes nothing ² in a powder material [121]. This is because the orientation of the grains is random and so the angle between the external field direction and the vector between a particular spin and the muon is also random. The field associated with a magnetic dipole averaged over all directions with respect to the point of observation is thus zero. A typical spectrum is shown in Fig. 8.67. The spectra taken in the dilution refrigerator were analysed by fitting them to two oscillating signals between 0.01 and 1.5 μ s with gaussian and exponential envelopes. The former was used to model the silver background, the latter the sample. As shown, there is a difference of $\sim 5 - 10\%$ in the inverse fractional frequency shift

$$\nu_{\text{Silver}} / (\nu_{\text{Silver}} - \nu_{\text{Sample}}) \quad (8.105)$$

between spectra taken on cooling or warming. The frequency shift of $\sim 50\%$ observed at 0.5 K corresponds with a magnetic field of 0.5 T and hence the history dependence implies there is a static component to the internal field of $\sim 0.0025 - 0.005$ T. It is speculated

²However, it does contribute to the linewidth.

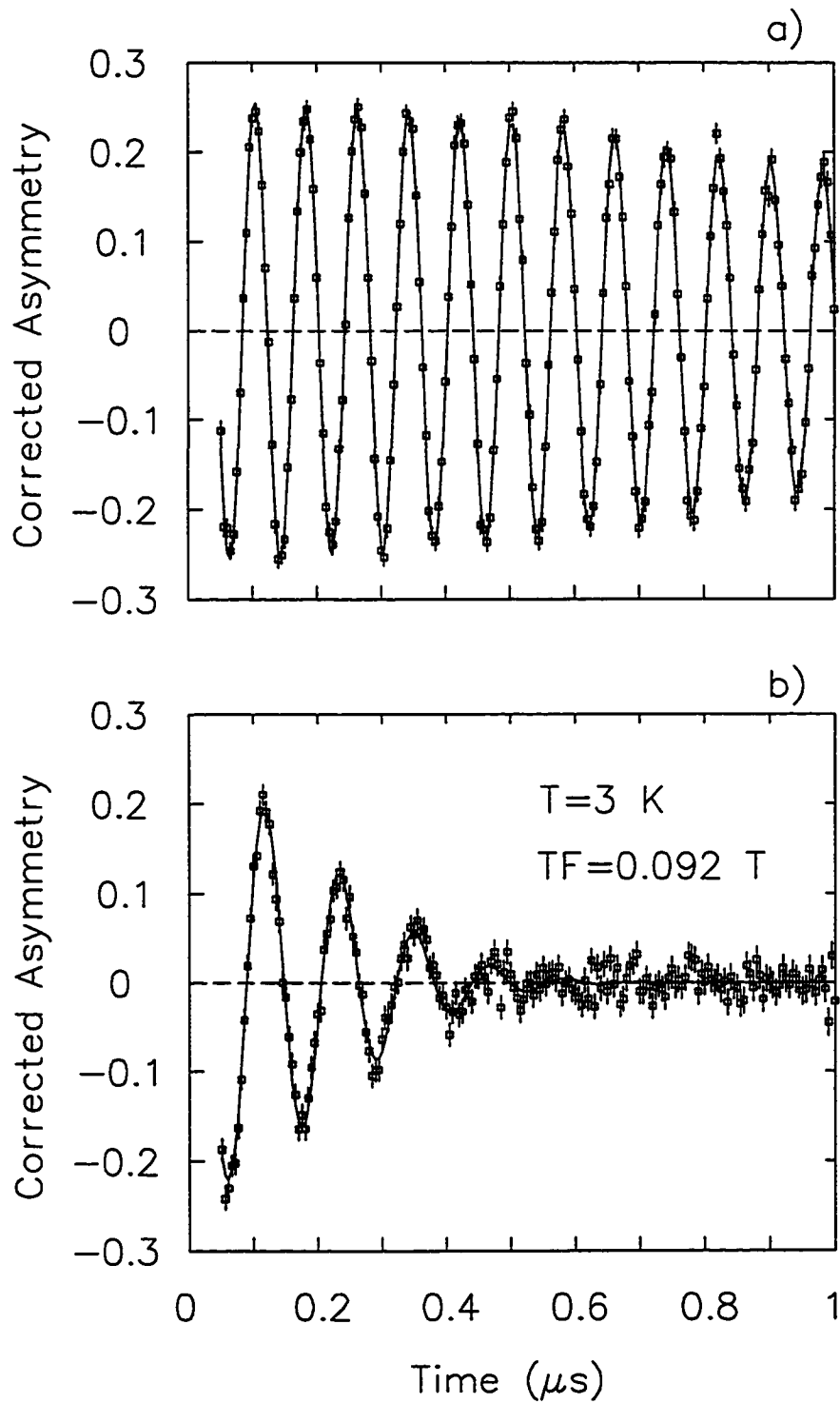


Figure 8.67: Muon precession signals observed in a) Ag and b) $Tb_2Ti_2O_7$ in a transverse field of 0.092 T at 3 K. The data were recorded using the separate spectra apparatus described in Chapter 4.

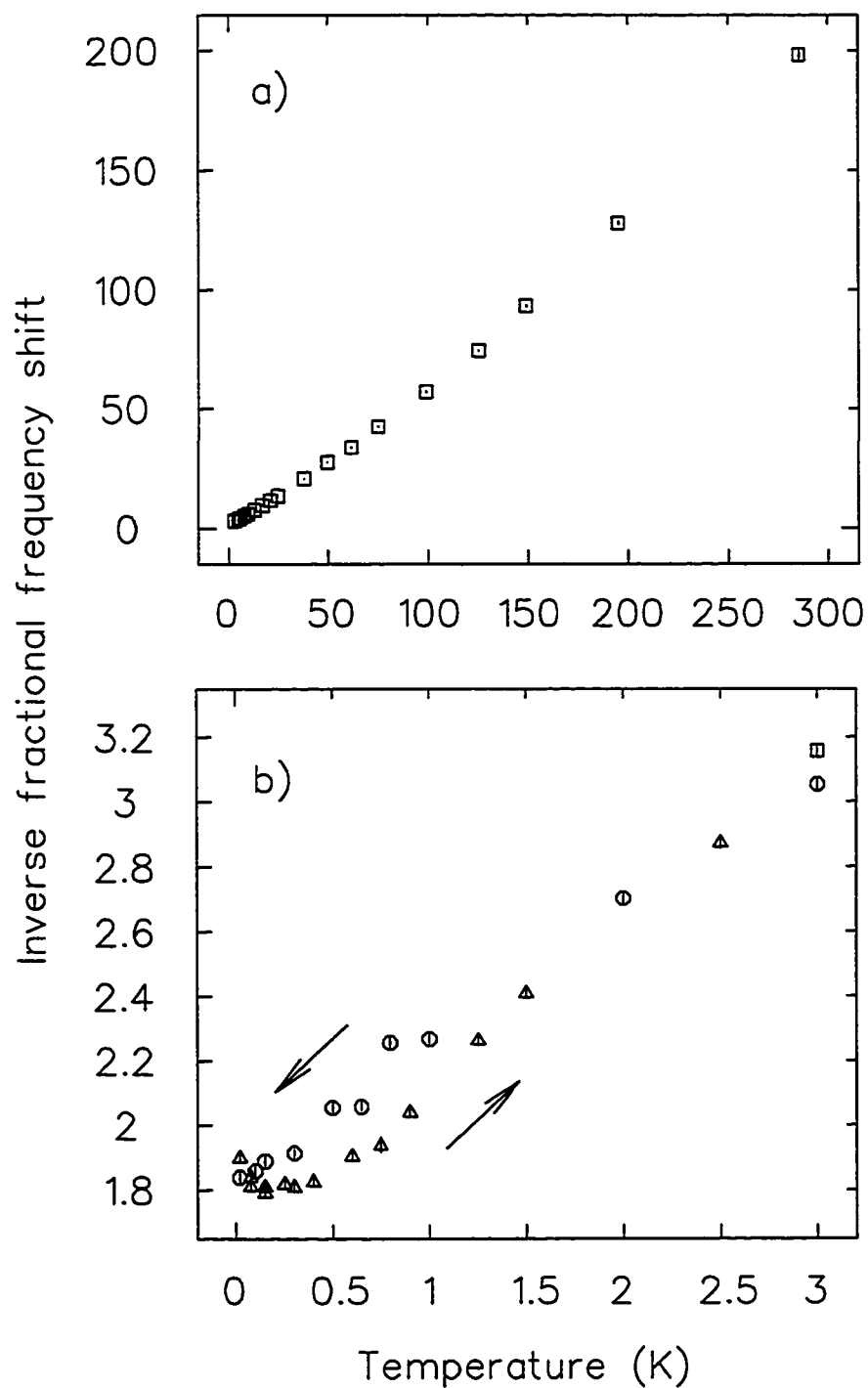


Figure 8.68: Inverse fractional shift in the muon precession frequency relative to a silver reference versus temperature for $Tb_2Ti_2O_7$ in a transverse field of 0.09 T. The squares indicate data taken on a powder sample, the circles and triangles a [111] single crystal.

that the sample is magnetised on cooling, inducing a small ferromagnetic component which persists on warming to 1 K. However, the signal from such a small static internal field could easily be swamped by that from the dynamic internal fields, which are of the order of 1 T.

Similar hysteretic behaviour has been observed in preliminary unpublished neutron diffraction experiments carried out by J. S. Gardner *et al.*. The intensity of the (002) reflection builds up as a magnetic field is increased above 3 T at 2.1 K. The intensity of this signal then persists as the field is reduced below 3 T. This magnetic Bragg peak is resolution limited and has been observed with the applied magnetic field along all three major symmetry directions. It suggests that a fraction of the spins are correlated over a range of ~ 400 Å, forming ferromagnetic clusters. It should be noted that these diffraction measurements are energy integrated and therefore completely insensitive to the spin dynamics.

In a number of the rare earth titanates, it has been shown that applying a magnetic field causes the system to enter one or more stable phases which at present are not well characterised. Monte-Carlo simulations of spin-ice systems have been able to describe the magnetic susceptibility and diffuse magnetic neutron scattering results well, but the nature of the spin dynamics has not been fully studied to date. Muon spin relaxation is providing a window into the dynamic behaviour of the Tb spins which is difficult to access with other methods.

Chapter 9

Conclusions

Pyrochlores exhibit a rich variety of novel magnetic behaviour which is most likely caused by geometric frustration but controlled by second order effects, such as the range of the spin-spin interactions, disorder, anisotropy, thermal and quantum fluctuations. Muon spin relaxation is one of the principal methods which has been used to characterise this diverse behaviour since it is uniquely sensitive to the low frequency magnetic fluctuations which are often present in these systems in the interesting low temperature regime. It has also proved to be a natural complement to neutron scattering.

Despite the high degree of crystalline order, the freezing process in $Y_2Mo_2O_7$ appears similar to that expected for a dilute spin glass. In particular, non-exponential muon spin relaxation and critical slowing down of the spin fluctuations is observed near T_F , indicative of an exotic spin autocorrelation function which obeys a power law function in time. Below T_F there is evidence for a highly disordered magnetic structure. The transition temperature is suppressed with increasing substitution of Mo by Ti. The most striking feature in the diluted systems $Y_2Mo_{2-x}Ti_xO_7$ is the presence of a residual, temperature independent spin relaxation which persists down to very low temperatures. This shows there is an appreciable density of states for low energy magnetic excitations which is much larger in these systems than in conventional randomly frustrated spin glasses. It is possible that the residual low temperature dynamics in these systems are “remnants” of the zero-modes predicted theoretically for nearest-neighbour Heisenberg spins on a pyrochlore lattice [3, 51, 52, 211].

A clear field dependence of the spin relaxation rate T_1^{-1} in $Gd_2Ti_2O_7$ in the paramagnetic state is reported. This effect, which is expected theoretically but has not been previously observed, is believed to be due to contributions to the transverse component

of the spin auto-correlation function arising from the Zeeman interaction. The reduction in T_1^{-1} occurs when the Zeeman interaction exceeds the exchange interaction and is thus a direct measure of the near neighbour exchange constant. This could be a sensitive new way to obtain \mathcal{J} when it is small and difficult to measure *via* other means such as susceptibility.

The combined μ SR and neutron scattering results on $\text{Tb}_2\text{Ti}_2\text{O}_7$ point to the persistence of a paramagnetic state down to 0.015 K, even though antiferromagnetic correlations develop as high as 50 K. This is thought to be the result of competition between the near neighbour exchange and anisotropy energy scales on the pyrochlore lattice. Thus, correlated tetrahedra are only weakly coupled and continue to fluctuate, as demonstrated directly by the non-zero low temperature T_1^{-1} values measured by μ SR. The low lying magnetic excitation spectrum displays an anisotropy gap of ~ 18 K, which undergoes incomplete softening at the wave vector characterising the antiferromagnetic short range order. Significant spin fluctuations remain even in an applied field, where preliminary measurements with techniques other than μ SR suggest partial ordering. Clearly a more sophisticated theoretical model is called for to explain the complicated temperature and magnetic field dependence of the spin dynamics which has been observed.

Obviously frustrated systems form a vast field of study within the rich subject of magnetism. Spin ice materials such as $\text{Ho}_2\text{Ti}_2\text{O}_7$ and $\text{Dy}_2\text{Ti}_2\text{O}_7$ have become particularly topical within the last two years. In the immediate future there are plans to examine these compounds using μ SR. The variety of ordered phases reported in $\text{Gd}_2\text{Ti}_2\text{O}_7$ below 1 K also have yet to be explored with μ SR and will without doubt exhibit interesting spin dynamics. Further neutron scattering experiments on $\text{Tb}_2\text{Ti}_2\text{O}_7$ in a applied magnetic field should also shed new light on the behaviour of this perplexing material.

There is an almost limitless number of combinations of rare earth and transition metals ions from which different compounds with a pyrochlore structure may be synthesised. In this thesis no mention has been made of those which contain 2 magnetic species or are metallic. In the former the interplay between the two species introduces an extra

complication, while in the latter the interaction with the conduction electrons similarly makes theoretical modelling of the data more involved. Nonetheless, a variety of compounds have been studied [212, 213, 214, 215, 22] and (perhaps not surprisingly) have been shown to exhibit anything from long range order to spin glass or re-entrant spin glass behaviour.

In conclusion, geometrically frustrated systems are “fragile”. The low temperature behaviour depends sensitively on *all* the interactions in the system and a prediction can not be made on the basis of the interaction with the largest energy scale alone. This is perhaps the most exciting aspect of these systems, since the only certainty is that one will find new and unexpected magnetic behaviour.

Bibliography

- [1] A. P. Ramirez, *Annu. Rev. Mater. Sci.* **24**, 453 (1994). P. Schiffer, A. P. Ramirez, *Comments Cond. Mat. Phys.* **18**, 21 (1996).
- [2] J. Villain, *Z. Physik B* **33**, 31 (1979).
- [3] J. N. Reimers, A. J. Berlinsky, A. -C. Shi, *Phys. Rev. B* **43**, 865 (1991).
- [4] J. N. Reimers, *Phys. Rev. B* **45**, 7287 (1992).
- [5] S. T. Bramwell, M. J. P. Gingras, J. N. Reimers, *J. Appl. Phys.* **75**, 5523 (1994).
- [6] A. B. Harris, A. J. Berlinsky, C. Bruder, *J. Appl. Phys.* **69**, 5200 (1991).
- [7] B. Canals and C. Lacroix, *Phys. Rev. Lett.* **80**, 2933 (1998).
- [8] B. Canals and C. Lacroix, *Phys. Rev. B* **61**, 1149 (2000).
- [9] K. Binder, A. P. Young, *Rev. Mod. Phys.* **58**, 801 (1986).
- [10] K. H. Fischer, J. A. Hertz, *Spin Glasses*, (Cambridge University Press 1991).
- [11] M. Mekata, *J. Magn. Magn. Mat.* **90 & 91**, 247 (1990).
- [12] M. Shiga, *J. Magn. Magn. Mater.* **129**, 17 (1994).
- [13] M. Shiga, *Physica B* **149**, 293 (1988).
- [14] A. S. Wills, N. P. Raju and J. E. Greedan, *Chem. Mater.* **11**, 1510 (1999).
- [15] J. E. Greedan, N. P. Raju, A. S. Wills, C. Morin and S. M. Shaw, *Chem. Mater.* **10**, 3058 (1998).
- [16] N. Fujiwara, H. Yasuoka and Y. Ueda, *Phys. Rev. B* **57**, 3539 (1998).
- [17] W. Schiessl, W. Potzel, H. Karzel, M. Steiner, G. M. Kalvius, A. Martin, M. K. Krause, I. Halevy, J. Gal, W. Schäfer, G. Will, M. Hillberg, R. Wäppling, *Phys. Rev. B* **53**, 9143 (1996).
- [18] P. K. Baltzer, P. J. Wojtowicz, M. Robbins, E. Lopatin, *Phys. Rev.* **151**, 367 (1966).
- [19] D. Fiorani, S. Viticoli, J. L. Dormann, J. L. Tholence, A. P. Murani, *Phys. Rev. B* **30**, 2776 (1984).
- [20] M. J. Harris, M. P. Zinkin, M. J. Harris and T. Zeiske, *Phys. Rev. B* **56**, 11786 (1997).

- [21] M. J. Harris, M. P. Zinkin, Z. Tun, B. M. Wanklyn and I. P. Swaison, *Phys. Rev. Lett.* **73**, 189 (1994).
- [22] S.R. Dunsiger, R. F. Kiefl, K. H. Chow, B. D. Gaulin, M. J. P. Gingras, J. E. Greedan, A. Keren, K. Kojima, G. M. Luke, W. A. MacFarlane, N. P. Raju, J. E. Sonier, Y. J. Uemura and W. D. Wu, *Phys. Rev. B* **54**, 9019 (1996).
- [23] G. Toulouse, *Commun. Phys* **2**, 115 (1977).
- [24] D. E. Murnick, A. T. Fiory, W. J. Kossler, *Phys. Rev. Lett.* **36**, 100 (1976).
- [25] Y. J. Uemura, T. Yamazaki, D. R. Harshman, M. Senba, E. J. Ansaldo, *Phys. Rev. B* **31**, 546 (1985).
- [26] F. Mezei, A. P. Murani, *J. Magn. Magn. Mater.* **14**, 211 (1979).
- [27] D. E. MacLaughlin, L. C. Gupta, D. W. Cooke, R. H. Heffner, M. Leon and M. E. Schillaci, *Phys. Rev. Lett.* **51**, 927 (1983).
- [28] R. H. Heffner, D. E. MacLaughlin, *Phys. Rev. B* **29**, 6048 (1984).
- [29] I. A. Campbell, A. Amato, F. N. Gygax, D. Herlach, A. Schenck, R. Cywinski, S. H. Kilcoyne, *Phys. Rev. Lett.* **72**, 1291 (1994).
- [30] A. Keren, P. Mendels, I. A. Campbell and J. Lord, *Phys. Rev. B* **77** 1386 (1996).
- [31] S. W. Lovesey, *Theory of neutron scattering from condensed matter* Vol. 2, Clarendon Press (1984).
- [32] T. Moriya, *Prog. Theor. Phys.* **16**, 23 (1956).
- [33] T. Moriya, *Prog. Theor. Phys.* **16**, 641 (1956).
- [34] Y. J. Uemura, A. Keren, K. Kojima, L. P. Le, G. M. Luke, W. D. Wu, Y. Ajiro, T. Asano, Y. Kuriyama, M. Mekata, H. Kikuchi, K. Kakurai, *Phys. Rev. Lett.* **73**, 3306 (1994).
- [35] S. -H. Lee, C. Broholm, G. Aeppli, A. P. Ramirez, T. G. Perring, C. J. Carlile, M. A. Adams, T. J. L. Jones, B. Hessen, *Europhys. Lett.* **35**, 127 (1996).
- [36] A. Keren, K. Kojima, L. P. Le, G. M. Luke, W. D. Wu, Y. J. Uemura, M. Takano, H. Dabkowska, M. J. P. Gingras, *Phys. Rev. B* **53**, 6451 (1996).
- [37] J. A. Ripmeester, C. I. Ratcliffe, J. E. Dutrizac, J. L. Jambor, *Can. Mineral.* **24**, 435 (1986).
- [38] W. P. Wolf *et al.*, *J. Phys. Soc. Jpn. Suppl.* **B1 17**, 443 (1962).
- [39] P. Schiffer, A. P. Ramirez, D. A. Huse, and A. J. Valentino, *Phys. Rev. Lett.* **73**, 2500 (1994).

- [40] O. A. Petrenko, C. Ritter, M. Yethiraj, D. M. Paul, *Phys. Rev. Lett.* **80**, 4570 (1998).
- [41] S. R. Dunsiger, J. S. Gardner, J. A. Chakhalian, A. L. Cornelius, M. Jaime, R. F. Kiefl, R. Movshovich, W. A. McFarlane, R. I. Miller, J. E. Sonier, B. D. Gaulin, *Phys. Rev. Lett.* **85**, 3504 (2000).
- [42] P. W. Anderson, *Phys. Rev.* **102**, 1008 (1956).
- [43] P. W. Anderson, *Mater. Res. Bull.* **8**, 153 (1973).
- [44] N. P. Raju, M. Dion, M. J. P. Gingras, T. E. Mason and J. E. Greedan, *Phys. Rev. B* **59**, 14 489 (1999).
- [45] J. N. Reimers, J. E. Greedan, C. V. Stager and M. Bjorgvinnsen, *Phys Rev B* **43**, 5692 (1991).
- [46] G. Ferey, R. de Pape, M. Leblanc and J. Pannetier, *Revue de Chimie minérale* **23**, 474 (1986).
- [47] N. Metropolis, A. Rosenbluth, M. Rosenbluth, A. Teller, E. Teller, *Journal of Chemical Physics* **21**, 1087 (1953).
- [48] M. P. Zinkin and M. J. Harris, *J. Magn. Magn. Mater.* **140-144**, 1803 (1995).
- [49] R. Moessner and J. T. Chalker, *Phys. Rev. B* **58**, 12 049 (1998).
- [50] J. Goldstone, *Nuovo Cimento* **19**, 154 (1961).
- [51] A.B. Harris, C. Kallin and A.J. Berlinsky, *Phys. Rev. B* **45**, 7536 (1992).
- [52] J. T. Chalker, P. C. W. Holdsworth and E. F. Shender, *Phys. Rev. Lett.* **68**, 855 (1992).
- [53] J. N. Reimers and A. J. Berlinsky, *Phys. Rev. B* **48**, 9539 (1993).
- [54] A. J. Berlinsky and C. Kallin, *Hyp. Int.* **85**, 173 (1994).
- [55] R. Moessner and J. T. Chalker, *Phys. Rev. Lett.* **80**, 2929 (1998).
- [56] R. R. Sobral and C. Lacroix, *Solid State Commun.* **103**, 407 (1997).
- [57] C. Battistoni, J. L. Dormann, D. Fiorani, E. Paparazzo and S. Viticoli, *Solid State Commun.* **39**, 581 (1981).
- [58] A. P. Ramirez, G. P. Espinosa, A. S. Cooper, *Phys. Rev Lett.* **17**, 2070 (1990).
- [59] J. Villain, R. Bidaux, J. P. Carton and R. Conie, *J. Phys* **41**, 1263 (1980).
- [60] J. D. Bernal and R. H. Fowler, *J. Chem. Phys.* **1**, 515 (1933).
- [61] J. F. Nagle, *Commun. Math. Phys.* **13**, 62 (1969).

- [62] R. J. Baxter *Exactly Solved Models in Statistical Mechanics*, Academic Press (1982).
- [63] R. Moessner, *Phys. Rev. B* **57**, R5587 (1998).
- [64] S. T. Bramwell and M. J. Harris, *J. Phys. Condens. Matter* **10**, L215 (1998).
- [65] A. P. Ramirez, A. Hayashi, R. J. Cava, R. Siddharthan and B. S. Shastry, *Nature* **399**, 333 (1999).
- [66] L. Pauling *The Nature of the Chemical Bond*, Cornell University Press (1960), p 465-468.
- [67] H. W. J. Blöte, R. F. Wierlinga and W. J. Huiskamp, *Physica* **43**, 549 (1969).
- [68] Mark Harris, *Nature* **399**, 311 (1999).
- [69] M. J. Harris, S. T. Bramwell, T. Zeiske, D. F. McMorrow and P. J. C. King, *J. Magn. Magn. Mater.* **177-181**, 757 (1998).
- [70] M. J. Harris, S. T. Bramwell, P. C. W. Holdsworth and J. D. M. Champion, *Phys. Rev. Lett.* **81**, 4496 (1998).
- [71] R. Siddharthan, B. S. Shastry, A. P. Ramirez, A. Hayashi, R. J. Cava and S. Rosenkranz, *Phys. Rev. Lett.* **83**, 1854 (1999).
- [72] B. C. den Hertog and M. J. P. Gingras, *Phys. Rev. Lett.* **84**, 3430 (2000).
- [73] M. A. Subramanian, G. Aravamudan, G. V. Subba Rao, *Mat. Res. Bull.* **15**, 1401 (1980).
- [74] M. A. Subramanian, G. Aravamudan, G. V. Subba Rao, *Progr. Solid St. Chem.* **15**, 55-143 (1983).
- [75] J. E. Greedan, *Oxides with Trirutile and Pyrochlore Structures*, in Landolt-Bornstein, New Series III, Vol. 27G, Springer-Verlag, Ed. H. P. J. Wijn, (1992).
- [76] J. Pannetier and J. Lucas, *Mater. Res. Bull.* **5**, 797 (1970).
- [77] M. Faucher and P. Caro, *J. Solid State Chem.* **12**, 1 (1975).
- [78] J. E. Greedan, M. Sato, Xu Yan, F. S. Razavi, *Solid State Commun.* **59**, 895 (1986).
- [79] J. N. Reimers and J. E. Greedan, *J. Solid State Chem.* **72**, 390 (1988).
- [80] B. D. Gaulin, J. N. Reimers, T. E. Mason, J. E. Greedan, Z. Tun, *Phys. Rev. Lett.* **69**, 3244 (1992).
- [81] P. H. Hubert, *Bull. Soc. Chim. Fr.*, 2385 (1974); 2463 (1975).
- [82] T. van Dijk, R. B. Helmholdt, A. J. Burggraaf, *Phys. Status Solidi B* **101**, 765 (1980).

- [83] C. H. Booth, J. S. Gardner, G. H. Kwei, R. H. Heffner, F. Bridges and M. A. Subramanian, *Phys. Rev. B* **62**, R755 (2000).
- [84] A. P. Murani, *Solid State Commun.* **34**, 705 (1980).
- [85] D. L. Martin, *Phys. Rev. B* **21**, 1906 (1980).
- [86] A. F. J. Morgownik and J. A. Mydosh, *Solid State Commun.* **47**, 321 (1983).
- [87] A. F. J. Morgownik and J. A. Mydosh, *Solid State Commun.* **47**, 325 (1983).
- [88] M. T. Hutchings, *Solid State Physics* **16**, 227 (1965).
- [89] M. Blume, A. J. Freeman and R. E. Watson, *Phys. Rev.* **134**, A320 (1964).
- [90] A. J. Freeman and R. E. Watson, *Magnetism Vol 2A*, G. T. Rado and H. Suhl eds., p 137 (Academic Press 1965).
- [91] A. Abragam and B. Bleaney, *Electron Paramagnetic Resonance of Transition Ions*, Clarendon Press (1970), p.377.
- [92] MATHEMATICA (Wolfram Research Inc., Cambridge (1988)).
- [93] A. Abragam and B. Bleaney, *Electron Paramagnetic Resonance of Transition Ions*, Clarendon Press (1970), p.426.
- [94] K. R. Lea, M. J. M. Leask and W. P. Wolf, *J. Phys. Chem. Solids* **23**, 1381 (1962).
- [95] M. J. P. Gingras, B. C. den Hertog, M. Faucher, J. S. Gardner, S. R. Dunsiger, L. J. Chang, B. D. Gaulin, N. P. Raju and J. E. Greedan, *Phys. Rev. B* **62**, 6496 (2000).
- [96] M. P. Zinkin, M. J. Harris, Z. Tun, R. A. Cowley and B. M. Wanklyn, *J. Phys. Condens. Matter* **8**, 193 (1996).
- [97] J. H. Brewer, S. R. Kreitzman, D. R. Noakes, E. J. Ansaldo, D. R. Harshman and R. Keitel, *Phys. Rev. B* **33**, 7813 (1986).
- [98] D. R. Noakes, E. J. Ansaldo, S. R. Kreitzman and G. M. Luke, *J. Phys. Chem. Solids* **54**, 785 (1993).
- [99] D. R. Noakes, E. J. Ansaldo and G. M. Luke, *J. Appl. Phys.* **73**, 5666 (1993).
- [100] E. Holzschuh, A. B. Dension, W. Kündig, P. F. Meier and B. D. Patterson, *Phys. Rev B* **27**, 5294 (1983).
- [101] C. Boekema, R. L. Lichti and K. J. Ruegg, *Phys. Rev. B* **30**, 6766 (1984).
- [102] J. H. Brewer, R. F. Kiefl, J. F. Carolan, P. Dosanjh, W. N. Hardy, S. R. Kreitzman, Q. Li, T. M. Riseman, P. Schleger, H. Zhou, E. J. Ansaldo, D. R. Noakes, L. P. Le, G. M. Luke, Y. J. Uemura, K. Hepburn-Wiley and C. E. Stronach, *Hyp. Int.* **63**, 177 (1990).

- [103] S. K. Estreicher, *Materials Science and Engineering* **R14**, 319 (1995).
- [104] P. P. Ewald, *Ann. Physik* **64**, 253 (1921).
- [105] J. C. Slater, *Quantum Theory of Molecules and Solids Vol 3: Insulators, Semiconductors and Metals*, McGraw-Hill Book Company (1967), p. 206.
- [106] M. Born and J. E. Mayer, *Z. Physik* **75**, 1 (1932).
- [107] M. Catti, C. M. Mari and V. Valerio, *Journal of Solid State Chemistry* **98**, 269 (1992).
- [108] G. D. Morris, Ph.D. Thesis, University of British Columbia, 1997, (unpublished).
- [109] *Introductory Nuclear Physics*, K. S. Krane, John Wiley and Sons (1988).
- [110] A. E. Pifer, T. Bowen, K. R. Kendall, *Nucl. Instrum. Methods* **135**, 39 (1976).
- [111] M. Goldhaber, L. Grodzins, A. W. Sunyar, *Phys. Rev.* **106**, 826 (1957).
- [112] R. L. Garwin, L. M. Lederman and M. Weinrich, *Phys. Rev.* **105**, 1415 (1957).
- [113] A. Schenck, *Muon Spin Rotation Spectroscopy*, Bristol: Adam Hilger Ltd., (1985).
- [114] J. H. Brewer, *Encycl. of Appl. Phys.* **11**, 23 (1994).
- [115] D. M. Garner, Ph.D. Thesis, University of British Columbia, 1979, (unpublished).
- [116] T. M. Riseman, Ph.D. Thesis, University of British Columbia, 1993, (unpublished).
- [117] R. A. Swanson, *Phys. Rev.* **112**, 580 (1958).
- [118] J. D. Brewer, J. H. Brewer, G. D. Morris, D. Eshchenko and V. G. Storchak, *Physica B* **289-290**, 428 (2000).
- [119] E. V. Minaichev, G. G. Myasishcheva, Yu. V. Obukhov, V. S. Roganov, G. I. Savel'ev and V. G. Firsov, *Sov. Phys. JETP* **30**, 849 (1970).
- [120] A. Abragam, *Principles of Nuclear Magnetism*, Clarendon Press, Oxford, (1961).
- [121] C. P. Slichter *Principles of Magnetic Resonance* 3rd ed., Springer-Verlag (1990).
- [122] T. M. Riseman and J. H. Brewer, *Hyp. Int.* **87**, 1141 (1994).
- [123] M. Celio and P. F. Meier, *Phys. Rev. B* **27**, 1908 (1983).
- [124] M. Celio, *Phys. Rev. Lett.* **56**, 2720 (1986).
- [125] R. Kubo and T. Toyabe in *Magnetic Resonance and Relaxation*, R. Blinc Ed., North-Holland, Amsterdam (1967).
- [126] K. Y. Szeto, *Phys. Rev. B* **35**, 5209 (1987).

- [127] C. Kittel and A. Abrahams, *Phys. rev.* **90**, 238 (1953).
- [128] P. W. Anderson, *C. R. Acad. Sci.* **82**, 342 (1951).
- [129] R. E. Walstedt and L. R. Walker, *Phys. Rev. B* **9**, 4857 (1974).
- [130] R. S. Hayano, Y. J. Uemura, J. Imazato, N. Nishida, T. Yamazaki, R. Kubo, *Phys. Rev. B* **20**, 850 (1979).
- [131] J. H. Van Vleck, *J. Chem. Phys* **5**, 320 (1937).
- [132] *Fluctuation, Relaxation and Resonance in Magnetic Systems*, Scottish Universities' Summer School, D. Ter Haar Ed., Oliver and Boyd, Edinburgh and London (1962), p.27.
- [133] N. Bloembergen, E. M. Purcell, R. V. Pound, *Phys. Rev.* **73**, 679 (1948).
- [134] P. W. Anderson and P. R. Weiss, *Rev. Mod. Phys.* **25**, 269 (1953).
- [135] M. Weber, A. Kratzer, G. M. Kalvius, *Hyp. Int* **87**, 1117 (1994).
- [136] T. McMullen and E. Zaremba, *Phys. Rev. B* **18**, 3026 (1978).
- [137] P. Dalmas de Réotier and A. Yaouanc, *J. Phys. Condens. Matter* **4**, 4533 (1992).
- [138] R. E. Watson, A. J. Freeman, *Phys. Rev.* **123**, 2027 (1961). A. J. Freeman, R. E. Watson, *Magnetism, Vol IIA*, G. T. Rado, H. Suhl Eds., Academic Press, New York - London (1965).
- [139] N. Bloembergen and T. J. Rowland, *Phys. Rev.* **97**, 1679 (1955).
- [140] R. M. White *Quantum Theory of Magnetism*, Springer-Verlag (1983), p.158.
- [141] A. Keren, *Phys. Rev. B* **50**, 10 039 (1994).
- [142] V. Cannella and J. A. Mydosh, *Phys. Rev. B* **6**, 4220 (1972).
- [143] S. F. Edwards and P. W. Anderson, *J. Phys. F* **5**, 965 (1975), **6**, 1927 (1976).
- [144] A. T. Fiory, *Hyp. Int.* **8**, 777 (1981).
- [145] R. H. Heffner, *Hyp. Int.* **8**, 655 (1981).
- [146] R. H. Heffner and D. E. MacLaughlin, *Phys. Rev. B* **29**, 6048 (1984).
- [147] M. P. Schulhof, R. Nathans, P. Heller and A. Linz, *Phys. Rev. B* **4**, 2254 (1971).
- [148] A. T. Ogielski, *Phys. Rev. B* **32**, 7384 (1985).
- [149] R. N. Bhatt and A. P. Young in *Heidelberg Colloquium on Glassy Dynamics*, Lecture Notes in Physics **275**, J. L. van Hemmen and I. Morgenstern eds., Springer, Berlin (1986).

- [150] S. A. Werner, *Comments Cond. Mat. Phys.* **15**, 55 (1990).
- [151] A. W. Overhauser, *J. Chem. Solids* **13**, 71 (1960).
- [152] N. P. Raju, E. Gmelin, R. K. Kremer, *Phys. Rev. B* **46**, 5405 (1992).
- [153] G. Eiselt *et al.*, *Phys. Rev. B* **19**, 2664 (1979).
- [154] J. S. Gardner, B. D. Gaulin, S. H. Lee, C. Broholm, N. P. Raju and J. E. Greedan, *Phys. Rev. Lett.* **83**, 211 (1999).
- [155] M. J. P. Gingras, C. V. Stager, B. D. Gaulin, N. P. Raju, J. E. Greedan, *J. Appl. Phys.* **79**, 6170 (1996).
- [156] M. J. P. Gingras, C. V. Stager, N. P. Raju, B. D. Gaulin and J. E. Greedan, *Phys. Rev. Lett.* **78**, 947 (1997).
- [157] M. Suzuki, *Prog. Theor. Phys.* **58**, 1151 (1977).
- [158] H. Kamimura, S. Koide, H. Sekiyama and S. Sugano, *J. Phys. soc. Jpn.* **15**, 1264 (1960).
- [159] L. R. Walker and R. E. Walstedt, *Phys. Rev. B* **22**, 3816 (1980).
- [160] D. Sherrington and B. W. Southern, *J. Phys. F: Metals Phys.* **5**, L49 (1975).
- [161] S. -K. Ma, *Modern Theory of critical Phenomena* (Benjamin, Reading, Mass., 1976).
- [162] F. Mezei, A. P. Murani, *J. Magn. Magn. Mater.* **14**, 211 (1979).
- [163] H. Pinkvos, A. Kalk and Ch. Schwink, *Phys. Rev. B* **41**, 590 (1990).
- [164] I. A. Campbell, J. -M. Flesselles, R. Jullien and R. Botet, *Phys. Rev. B* **37**, 3825 (1988).
- [165] H. Sompolinsky and A. Zippelius, *Phys. Rev. B* **25**, 6860 (1982).
- [166] S. Kirkpatrick and D. Sherrington, *Phys. Rev. B* **17**, 4304 (1978).
- [167] A. Keren and G. Bazalitsky, *Physica B* **289-290**, 205 (2000).
- [168] R. B. Stinchcombe, *Phase Transitions and Critical Phenomena Vol 7*, C. Domb, J. L. Lebowitz eds., Academic Press Inc. (London) Ltd. (1983).
- [169] W. Y. Ching, D. L. Huber, *Phys. Rev. B* **34**, 1960 (1986).
- [170] W. Y. Ching, D. L. Huber, K. M. Leung, *Phys. Rev. B* **21**, 3708 (1980).
- [171] R. Moessner and A. J. Berlinsky, *Phys. Rev. Lett.* **83**, 3293 (1999).

- [172] Jens Jensen and Allan R. Mackintosh, *Rare Earth Magnetism: Structures and Excitations*, Clarendon Press Oxford (1991).
- [173] E. J. Ansaldo, D. R. Noakes, J. H. Brewer, S. R. Kreitzman, J. K. Furdyna, *Phys. Rev. B* **38**, 1183 (1988).
- [174] B. J. Sternlieb, G. M. Luke, Y. J. Uemura, T. M. Riseman, J. H. Brewer, P. M. Gehring, K. Yamada, Y. Hidaka, T. Murakami, T. R. Thurston, R. J. Birgeneau, *Phys. Rev. B* **41**, 8866 (1990).
- [175] B. Martínez, A. Labarta, R. Rodríguez-Solá, X. Obradors, *Phys. Rev. B* **50**, 15779 (1994).
- [176] J. H. Brewer, G. D. Morris, D. J. Arseneau, D. J. Eschenko, V. G. Storchak and J. Bermejo, *Physica B* **289-290**, 425 (2000).
- [177] J. van Kranendonk and M. Bloom, *Physica* **22**, 545 (1956).
- [178] A. H. Mitchell, *J. Chem. Phys.* **27**, 17 (1957).
- [179] J. H. van Vleck, *Phys. Rev.* **74**, 1168 (1948).
- [180] R. G. Shulman and V. Jacarino, *Phys. Rev.* **108**, 1219 (1957).
- [181] A. P. Ramirez, (unpublished).
- [182] M. J. Harris, S. T. Bramwell and J. D. M. Champion, ISIS Experimental Report #10394 (1999).
- [183] J. S. Gardner, S. R. Dunsiger, B.D. Gaulin, M. J. P. Gingras, J.E. Greedan, R.F. Kiefl, M.D. Lumsden, W. A. MacFarlane, N.P. Raju, J. E. Sonier, I. Swainson, Z. Tun, *Phys. Rev. Lett.* **82**, 1012 (1999).
- [184] G. H. Lander *et al.*, *Phys. Rev. B* **8**, 3237 (1973).
- [185] N. W. Ashcroft and J. Lekner, *Phys. Rev.* **145**, 83 (1966).
- [186] N. W. Ashcroft, *Physica* **35**, 148 (1967).
- [187] E.F. Bertaut and P. Burlet, *Solid State Commun.* **5**, 279 (1967).
- [188] M. Kanada, Y. Yasui, M. Ito, H. Harashina, M. sato, H. Okumura and K. Kakurai, *J. Phys. Soc. Japan* **68**, 3802 (1999).
- [189] H. A. Mook, N. Wakabayashi, D. Pan, *Phys. Rev. Lett.* **34**, 1029 (1975).
- [190] R.M. Morra *et al.*, *Phys. Rev. B* **38**, 543 (1988).
- [191] O. Fujita *et al.*, *Phys. Rev. Lett.* **74**, 1677 (1995) and references contained therein.
- [192] F. D. M. Haldane, *Phys. Lett.* **93A**, 464 (1983); *Phys. Rev. Lett.* **50**, 1153 (1983).

- [193] G. Beni, P. Pincus, J. Chem. Phys. **57**, 3531 (1972).
- [194] J. A. Blanco, R. M. Nicklow and D. Schmitt, Phys. Rev. B **56**, 11666 (1997).
- [195] R. Feyerherm, A. Amato, A. Grayevsky, F. N. Gygax, N. Kaplan and A. Schenck, Z. Phys. B **99**, 3 (1995).
- [196] T. Tashma, A. Amato, A. Grayevsky, F. N. Gygax, M. Pinkpank, A. Schenck and N. Kaplan, Phys. Rev. B **56**, 9397 (1997).
- [197] P. Chandra and P. Coleman, Inter. Journal of Mod. Phys. B, **3**, 1729 (1989).
- [198] G. L. Squires, *Introduction to the theory of Thermal Neutron Scattering*, Cambridge University Press, (1978).
- [199] T. Moriya, J. Phys. Soc. Jpn. **18**, 516 (1963).
- [200] Robert M. White *Quantum Theory of Magnetism* 2nd ed., Springer-Verlag (1983), p.15.
- [201] K. W. Becker, P. Fulde and J. Keller, A. Phys **28**, 9 (1977).
- [202] P. M. Richards, *Magnetic Excitations and Fluctuations*, S. W. Lovesey, U. Balucani, F. Borsa and V. Tognetti eds., Springer, (1984).
- [203] S. V. Maleyev, Phys. Rev. B **50**, 302 (1994).
- [204] P. Dalmas de Réotier and A. Yaouanc and P. Bonville, J. Phys. Condens. Matter **8**, 5113 (1996).
- [205] J. H. van Vleck, *Electric and Magnetic Susceptibilities*, Oxford University Press (1932).
- [206] E. Holland-Moritz, D. Wohlleben and M. Loewenhaupt, Phys. Rev. B **25**, 7482 (1982).
- [207] P. Azaria, B. Delamotte and T. Jolicoeur, Phys. Rev. Lett. **64**, 3175 (1990).
- [208] J. N. Reimers, J. E. Greedan and M. Björgvinsson, Phys. Rev. B **45**, 7295 (1992).
- [209] A. Mailhot and M. L. Plumer, Phys. Rev. B **48**, 9881 (1993).
- [210] D. Reich, (unpublished).
- [211] J. N. Reimers and A. J. Berlinsky, Phys. Rev. B **48**, 9539 (1991).
- [212] M. a. Subramanian, G. Aravamudan and G. V. Subba Rao, Mat. Res. Bull. **15**, 1401 (1980).
- [213] J. E. Greedan, J. N. Reimers, C. V. Stager and S. L. Penny, Phys. Rev. B **43**, 5682 (1991).

- [214] J. E. Greedan, M. Sato, Naushad Ali and W. R. Datars, *Journal of Solid State Chemistry* **68**, 300 (1987).
- [215] J. E. Greedan, N. P. Raju, A. Maignan, Ch. Simon, J. S. Pedersen, A. M. Niraimathi, E. Gmelin and M. A. Subramanian, *Phys. Rev. B* **54**, 7189 (1996).
- [216] R. C. Zeller and R. O. Pohl, *Phys. Rev. B* **4**, 2029 (1971).
- [217] N. W. Ashcroft and N. D. Mermin *Solid State Physics*, Saunders College, Philadelphia (1976).
- [218] O. V. Lounasmaa, *Experimental Principles and Methods below 1 K*, Academic Press (1974).
- [219] G. K. White, *Experimental Techniques in Low Temperature Physics* 3rd ed., Clarendon Press Oxford (1979).

Appendix A

Crystal electric field and spin-orbit hamiltonians for $Y_2Mo_2O_7$

```

Clear["Global`*"]
Off[General::spell1]
L = 3; S = 1;
J = L - S;
lsize = 2 + L + 1;
ssize = 2 S + 1;
(*Calculations are in units of THz*)
kb = 8.617*10^(-5)*2.41796*10^2; (*Boltzmann's constant*)
bohr = 5.7884*10^(-5)*2.41796*10^2; (*Bohr magneton*)
elec = 4.80324*10^(-10); (*Electronic charge*)
Bohrradius = 0.529177; (*Bohr radius*)
Angstrom = 1*10^(-8);
VunitTHz = elec^2/(6.6262*10^(-27)*10^(12)*Angstrom);
a = 10.23; (*Conventional unit cell of Y2Mo2O7 in angstroms*)
xparam = 0.3382; charge = 4;
λ =  $\frac{950}{33.333*2S}$ ; (* Spin-orbit coupling parameter *)

repec = {0, 2.9052*Bohrradius^2, 0, 14.3861*Bohrradius^4, 0, 0};
θ = {0, -2/105, 0, -2/315, 0, 0};

Opos = {{1/4 - xparam, 1/8, 1/8}, (*Oxygen ion positions *)
        {1/8, 1/4 - xparam, 1/8},
        {1/8, 1/8, 1/4 - xparam},
        {-1/4 + xparam, -1/8, -1/8},
        {-1/8, -1/4 + xparam, -1/8},
        {-1/8, -1/8, -1/4 + xparam}};

U = Opos;

R = Table[Sqrt[(U[[i, 1]]*a)^2 + (U[[i, 2]]*a)^2 + (U[[i, 3]]*a)^2], {i, 6}];
MatrixForm[N[R]];
Cvar = U*a;
(*Rotation of z axis to <111> direction *)
θ = ArcTan[1/√2];
φ = 0;
ψ = -ArcTan[1];

A = {{Sin[θ]*Sin[ψ], -Sin[θ]*Cos[ψ], Cos[θ]},
     {Cos[φ]*Cos[ψ] - Sin[φ]*Cos[θ]*Sin[ψ], Cos[φ]*Sin[ψ] + Sin[φ]*Cos[θ]*Cos[ψ], Sin[φ]*Sin[θ]},
     {-Sin[φ]*Cos[ψ] - Cos[φ]*Cos[θ]*Sin[ψ], -Sin[φ]*Sin[ψ] + Cos[φ]*Cos[θ]*Cos[ψ], Cos[φ]*Sin[θ]}};

Ctrns = A.Transpose[Cvar];
Cp = Transpose[Ctrns];
MatrixForm[Ctrns];

xp = Table[Cp[[i, 1]], {i, 6}];
yp = Table[Cp[[i, 2]], {i, 6}];
zp = Table[Cp[[i, 3]], {i, 6}];
rp = Table[Sqrt[xp[[i]]^2 + yp[[i]]^2 + zp[[i]]^2], {i, 6}];

```

y2mo2o7.nb

2

(*Tesseral Harmonics expressed in cartesian coordinates*)

$$Z_{20} [x_-, y_-, z_-, r_-] = \frac{1}{4} \sqrt{\frac{5}{\pi}} + \frac{(3z^2 - r^2)}{r^2};$$

$$Z_{22} [x_-, y_-, z_-, r_-] = \frac{1}{4} \sqrt{\frac{15}{\pi}} + \frac{(x^2 - y^2)}{r^2};$$

$$Z_{40} [x_-, y_-, z_-, r_-] = \frac{3}{16} \sqrt{\frac{1}{\pi}} + \frac{(35z^4 - 30z^2r^2 + 3r^4)}{r^4};$$

$$Z_{42} [x_-, y_-, z_-, r_-] = \frac{3}{8} \sqrt{\frac{5}{\pi}} + \frac{(7z^2 - r^2)(x^2 - y^2)}{r^4};$$

$$Z_{43} [x_-, y_-, z_-, r_-] = \frac{3}{8} \sqrt{\frac{70}{\pi}} + \frac{z(x^3 - 3xy^2 + x)}{r^4};$$

$$Z_{44} [x_-, y_-, z_-, r_-] = \frac{3}{16} \sqrt{\frac{35}{\pi}} + \frac{(x^4 - 6x^2y^2 + y^4)}{r^4};$$

$$Z_{60} [x_-, y_-, z_-, r_-] = \frac{1}{32} \sqrt{\frac{13}{\pi}} + \frac{(231z^6 - 315z^4r^2 + r^2 + 105z^4 + z^2 - 5z^6)}{r^6};$$

$$Z_{62} [x_-, y_-, z_-, r_-] = \frac{1}{64} \sqrt{\frac{2730}{\pi}} + \frac{(16z^4 - 16z(x^2 + y^2) + z^2 + (x^2 + y^2)^2)(x^2 - y^2)}{r^6};$$

$$Z_{63} [x_-, y_-, z_-, r_-] = \frac{1}{32} \sqrt{\frac{2730}{\pi}} + \frac{(11z^3 - 3zr^2)(x^3 - 3xy^2)}{r^6};$$

$$Z_{64} [x_-, y_-, z_-, r_-] = \frac{21}{32} \sqrt{\frac{13}{7\pi}} + \frac{(11z^2 - r^2)(x^4 - 6x^2y^2 + y^4)}{r^6};$$

$$Z_{66} [x_-, y_-, z_-, r_-] = \frac{231}{64} \sqrt{\frac{26}{231\pi}} + \frac{(x^6 - 15x^4y^2 + 15x^2y^4 - y^6)}{r^6};$$

y2mo2o7.nb

3

$$Y_{nm}[n_-, z_-, q_-] = \sum_{j=1}^6 \frac{4 * \pi^j}{2 * n + 1} * Q * \frac{Z[xp[[j]], yp[[j]], zp[[j]], xp[[j]]]}{xp[[j]]^{(n+1)}}$$

```

y = Chop[{{0, 0, 0, 0, 0, 0},
  {Ynm[2, Z20, -2], 0, Ynm[2, Z220, -2], 0, 0, 0, 0},
  {0, 0, 0, 0, 0, 0},
  {Ynm[4, Z40, -2], 0,
  Ynm[4, Z420, -2], Ynm[4, Z430, -2], Ynm[4, Z440, -2], 0, 0},
  {0, 0, 0, 0, 0, 0},
  {Ynm[6, Z60, -2], 0, Ynm[6, Z620, -2],
  Ynm[6, Z630, -2], Ynm[6, Z640, -2], 0, Ynm[6, Z650, -2]}}];

```

```
MatrixForm[y]
```

$$\begin{pmatrix} 0 & 0 & 0 & 0 & 0 & 0 \\ 0.379378 & 0 & 0 & 0 & 0 & 0 \\ 0 & 0 & 0 & 0 & 0 & 0 \\ 0.102924 & 0 & 0 & 0.284553 & 0 & 0 \\ 0 & 0 & 0 & 0 & 0 & 0 \\ -0.0284386 & 0 & 0 & -0.0135677 & 0 & 0 & -0.0269321 \end{pmatrix}$$

```
Zcoeff = {{0, 0, 0, 0, 0, 0},
```

$$\left\{ \frac{1}{4} * \sqrt{\frac{5}{\pi}}, 0, \frac{1}{4} * \sqrt{\frac{15}{\pi}}, 0, 0, 0, 0 \right\},$$

```
{0, 0, 0, 0, 0, 0},
```

$$\left\{ \frac{3}{16} * \frac{1}{\sqrt{\pi}}, 0, \frac{3}{8} * \sqrt{\frac{5}{\pi}}, \frac{3}{8} * \sqrt{\frac{70}{\pi}}, \frac{3}{16} * \sqrt{\frac{35}{\pi}}, 0, 0 \right\},$$

```
{0, 0, 0, 0, 0, 0},
```

$$\left\{ \frac{1}{32} * \sqrt{\frac{13}{\pi}}, 0, \frac{1}{64} * \sqrt{\frac{2730}{\pi}},$$

$$\frac{1}{32} * \sqrt{\frac{2730}{\pi}}, \frac{21}{32} * \sqrt{\frac{13}{7 * \pi}}, 0, \frac{231}{64} * \sqrt{\frac{26}{231 * \pi}} \right\};$$

```
(* Stevens' operator multiplicative factors *)
```

```
FO = {{0, 0, 0, 0, 0, 0},
  {3, 0, 6, 0, 0, 0},
  {0, 0, 0, 0, 0, 0},
  {60, 0, 3, 3, 12, 0},
  {0, 0, 0, 0, 0, 0},
  {180, 0, 24, 18, 60, 0, 360}};
```

```
cefc = Chop[Array[cefcelement, {6, 7}]];
```

```
Do[cefcelement[n, m] = \gamma[[n, m]] * (-charge) * Zcoeff[[n, m]] *
  respec[[n]] * \theta[[n]] * FO[[n, m]] * \VunitHz,
  {n, 1, 6}, {m, 7}];
```

y2mo2o7.nb

4

```
(***Stevens' operator equivalent matrices***)
```

```
o20 = DiagonalMatrix[{5, 0, -3, -4, -3, 0, 5}];
MatrixForm[o20]
```

$$\begin{pmatrix} 5 & 0 & 0 & 0 & 0 & 0 & 0 \\ 0 & 0 & 0 & 0 & 0 & 0 & 0 \\ 0 & 0 & -3 & 0 & 0 & 0 & 0 \\ 0 & 0 & 0 & -4 & 0 & 0 & 0 \\ 0 & 0 & 0 & 0 & -3 & 0 & 0 \\ 0 & 0 & 0 & 0 & 0 & 0 & 0 \\ 0 & 0 & 0 & 0 & 0 & 0 & 5 \end{pmatrix}$$

```
o40 = DiagonalMatrix[{3, -7, 1, 6, 1, -7, 3}];
MatrixForm[o40]
```

$$\begin{pmatrix} 3 & 0 & 0 & 0 & 0 & 0 & 0 \\ 0 & -7 & 0 & 0 & 0 & 0 & 0 \\ 0 & 0 & 1 & 0 & 0 & 0 & 0 \\ 0 & 0 & 0 & 6 & 0 & 0 & 0 \\ 0 & 0 & 0 & 0 & 1 & 0 & 0 \\ 0 & 0 & 0 & 0 & 0 & -7 & 0 \\ 0 & 0 & 0 & 0 & 0 & 0 & 3 \end{pmatrix}$$

```
o43 = {{0, 0, 0, 3\sqrt{5}, 0, 0, 0},
       {0, 0, 0, 0, \sqrt{10}, 0, 0},
       {0, 0, 0, 0, 0, -\sqrt{10}, 0},
       {3\sqrt{5}, 0, 0, 0, 0, 0, -3\sqrt{5}},
       {0, \sqrt{10}, 0, 0, 0, 0, 0},
       {0, 0, -\sqrt{10}, 0, 0, 0, 0},
       {0, 0, 0, -3\sqrt{5}, 0, 0, 0}};
```

```
MatrixForm[o43]
```

$$\begin{pmatrix} 0 & 0 & 0 & 6.7082 & 0 & 0 & 0 \\ 0 & 0 & 0 & 0 & 3.16228 & 0 & 0 \\ 0 & 0 & 0 & 0 & 0 & -3.16228 & 0 \\ 3\sqrt{5} & 0 & 0 & 0 & 0 & 0 & -3\sqrt{5} \\ 0 & \sqrt{10} & 0 & 0 & 0 & 0 & 0 \\ 0 & 0 & -\sqrt{10} & 0 & 0 & 0 & 0 \\ 0 & 0 & 0 & -3\sqrt{5} & 0 & 0 & 0 \end{pmatrix}$$

y2mo2o7.nb

5

```

(**Full hamiltonian**)
mrx = (cefc[[2, 1]]*o20) + (cefc[[4, 1]]*o40) + (cefc[[4, 4]]*o43);

MatrixForm[mrx]

$$\begin{pmatrix} 582.842 & 0 & 0 & 1011.17 & 0 & 0 & 0 \\ 0 & -456.164 & 0 & 0 & 476.672 & 0 & 0 \\ 0 & 0 & -167.24 & 0 & 0 & -476.672 & 0 \\ 1011.17 & 0 & 0 & 81.123 & 0 & 0 & -1011.17 \\ 0 & 476.672 & 0 & 0 & -167.24 & 0 & 0 \\ 0 & 0 & -476.672 & 0 & 0 & -456.164 & 0 \\ 0 & 0 & 0 & -1011.17 & 0 & 0 & 582.842 \end{pmatrix}$$


{val, vec} = Chop[Eigensystem[mrx]];

MatrixForm[val]

$$\begin{pmatrix} 1783.84 \\ -1119.87 \\ -809.784 \\ -809.784 \\ 582.842 \\ 186.38 \\ 186.38 \end{pmatrix}$$


MatrixForm[vec]

$$\begin{pmatrix} -0.541476 & 0 & 0 & -0.643123 & 0 & 0 & 0.541476 \\ -0.454757 & 0 & 0 & 0.765763 & 0 & 0 & 0.454757 \\ 0 & 0.80313 & 0 & 0 & -0.595803 & 0 & 0 \\ 0 & 0 & -0.595803 & 0 & 0 & -0.80313 & 0 \\ -0.707107 & 0 & 0 & 0 & 0 & 0 & -0.707107 \\ 0 & 0.595803 & 0 & 0 & 0.80313 & 0 & 0 \\ 0 & 0 & 0.80313 & 0 & 0 & -0.595803 & 0 \end{pmatrix}$$


(* Lowest 3 eigenvalues and corresponding eigenvectors *)
ecef = {Abs[val[[3]] - val[[2]], 0, Abs[val[[4]] - val[[2]]]};
MatrixForm[ecef]

$$\begin{pmatrix} 310.087 \\ 0 \\ 310.087 \end{pmatrix}$$


ug = Transpose[{vec[[3]], vec[[2]], vec[[4]]}];
MatrixForm[ug]

$$\begin{pmatrix} 0 & -0.454757 & 0 \\ 0.80313 & 0 & 0 \\ 0 & 0 & -0.595803 \\ 0 & 0.765763 & 0 \\ -0.595803 & 0 & 0 \\ 0 & 0 & -0.80313 \\ 0 & 0.454757 & 0 \end{pmatrix}$$


```

y2mo2o7.nb

6

```

(* Angular momentum operators *)
Lx = DiagonalMatrix[{3, 2, 1, 0, -1, -2, -3}];
MatrixForm[Lx]


$$\begin{pmatrix} 3 & 0 & 0 & 0 & 0 & 0 & 0 \\ 0 & 2 & 0 & 0 & 0 & 0 & 0 \\ 0 & 0 & 1 & 0 & 0 & 0 & 0 \\ 0 & 0 & 0 & 0 & 0 & 0 & 0 \\ 0 & 0 & 0 & 0 & -1 & 0 & 0 \\ 0 & 0 & 0 & 0 & 0 & -2 & 0 \\ 0 & 0 & 0 & 0 & 0 & 0 & -3 \end{pmatrix}$$


Lp = Array[Lpelement, {lsize, lsize}];
Do[If[n == nprime - 1, Lpelement[n, nprime] =  $\sqrt{L(L+1) - (L-nprime+1)(L-nprime+2)}$ ,
  Lpelement[n, nprime] = 0], {n, lsize}, {nprime, lsize}];
MatrixForm[
  Lp]


$$\begin{pmatrix} 0 & \sqrt{6} & 0 & 0 & 0 & 0 & 0 \\ 0 & 0 & \sqrt{10} & 0 & 0 & 0 & 0 \\ 0 & 0 & 0 & 2\sqrt{3} & 0 & 0 & 0 \\ 0 & 0 & 0 & 0 & 2\sqrt{3} & 0 & 0 \\ 0 & 0 & 0 & 0 & 0 & \sqrt{10} & 0 \\ 0 & 0 & 0 & 0 & 0 & 0 & \sqrt{6} \\ 0 & 0 & 0 & 0 & 0 & 0 & 0 \end{pmatrix}$$


Lm = Transpose[Lp];
MatrixForm[Lm]


$$\begin{pmatrix} 0 & 0 & 0 & 0 & 0 & 0 & 0 \\ \sqrt{6} & 0 & 0 & 0 & 0 & 0 & 0 \\ 0 & \sqrt{10} & 0 & 0 & 0 & 0 & 0 \\ 0 & 0 & 2\sqrt{3} & 0 & 0 & 0 & 0 \\ 0 & 0 & 0 & 2\sqrt{3} & 0 & 0 & 0 \\ 0 & 0 & 0 & 0 & \sqrt{10} & 0 & 0 \\ 0 & 0 & 0 & 0 & 0 & \sqrt{6} & 0 \end{pmatrix}$$


Lx = 0.5 (Lp + Lm);
Ly = I (-0.5 (Lp - Lm));

(** Add in effect of spin orbit coupling **)

lsg = Transpose[ug].Lx.ug;
MatrixForm[lsg]


$$\begin{pmatrix} 0.935055 & 0. & 0. \\ 0. & -4.60352 \times 10^{-16} & 0. \\ 0. & 0. & -0.935055 \end{pmatrix}$$


```

y2mo2o7.nb

7

```

lpg = Chop[Transpose[ug].Lp.ug];
MatrixForm[lpg]


$$\begin{pmatrix} 0 & 0 & 0 \\ -2.4751 & 0 & 0 \\ 0 & -2.4751 & 0 \end{pmatrix}$$


lmg = Transpose[lpg];
MatrixForm[lmg]


$$\begin{pmatrix} 0 & -2.4751 & 0 \\ 0 & 0 & -2.4751 \\ 0 & 0 & 0 \end{pmatrix}$$


Sz = DiagonalMatrix[{1.0, 0, -1.0}];

Sp = Array[spelement, {ssize, ssize}];
Do[If[n == nprime - 1, spelement[n, nprime] =  $\sqrt{S(S+1) - (S-nprime+1)(S-nprime+2)}$ ,
spelement[n, nprime] = 0.0], {n, ssize}, {nprime, ssize}];

Sm = Transpose[Sp];

LLz = Array[LLzelem, {3 ssize, 3 ssize}];
Do[LLzelem[n, m] = 0, {n, 3 ssize}, {m, 3 ssize}];
Do[LLzelem[ssize (n-1) + m, ssize (n-1) + m] = lsg[[n, n]], {n, ssize}, {m, ssize}];
MatrixForm[Chop[LLz]]


$$\begin{pmatrix} 0.935055 & 0 & 0 & 0 & 0 & 0 & 0 & 0 \\ 0 & 0.935055 & 0 & 0 & 0 & 0 & 0 & 0 \\ 0 & 0 & 0.935055 & 0 & 0 & 0 & 0 & 0 \\ 0 & 0 & 0 & 0 & 0 & 0 & 0 & 0 \\ 0 & 0 & 0 & 0 & 0 & 0 & 0 & 0 \\ 0 & 0 & 0 & 0 & 0 & 0 & 0 & 0 \\ 0 & 0 & 0 & 0 & 0 & -0.935055 & 0 & 0 \\ 0 & 0 & 0 & 0 & 0 & 0 & -0.935055 & 0 \\ 0 & 0 & 0 & 0 & 0 & 0 & 0 & -0.935055 \end{pmatrix}$$


LLp = Array[LLpelem, {3 ssize, 3 ssize}];
Do[LLpelem[n, m] = 0, {n, 3 ssize}, {m, 3 ssize}];
Do[If[m1 == m, LLpelem[ssize (n1-1) + m1, ssize (n-1) + m] = lpg[[n1, n], 0],
{n, ssize}, {n1, ssize}, {m, ssize}, {m1, ssize}];
MatrixForm[
LLp]


$$\begin{pmatrix} 0 & 0 & 0 & 0 & 0 & 0 & 0 & 0 & 0 \\ 0 & 0 & 0 & 0 & 0 & 0 & 0 & 0 & 0 \\ 0 & 0 & 0 & 0 & 0 & 0 & 0 & 0 & 0 \\ -2.4751 & 0 & 0 & 0 & 0 & 0 & 0 & 0 & 0 \\ 0 & -2.4751 & 0 & 0 & 0 & 0 & 0 & 0 & 0 \\ 0 & 0 & -2.4751 & 0 & 0 & 0 & 0 & 0 & 0 \\ 0 & 0 & 0 & -2.4751 & 0 & 0 & 0 & 0 & 0 \\ 0 & 0 & 0 & 0 & -2.4751 & 0 & 0 & 0 & 0 \\ 0 & 0 & 0 & 0 & 0 & -2.4751 & 0 & 0 & 0 \\ 0 & 0 & 0 & 0 & 0 & 0 & -2.4751 & 0 & 0 \end{pmatrix}$$


```


y2mo2o7.nb

8

```

LLm = Transpose[LLp];
MatrixForm[LLm]

```

$$\begin{pmatrix} 0 & 0 & 0 & -2.4751 & 0 & 0 & 0 & 0 & 0 \\ 0 & 0 & 0 & 0 & -2.4751 & 0 & 0 & 0 & 0 \\ 0 & 0 & 0 & 0 & 0 & -2.4751 & 0 & 0 & 0 \\ 0 & 0 & 0 & 0 & 0 & 0 & -2.4751 & 0 & 0 \\ 0 & 0 & 0 & 0 & 0 & 0 & 0 & -2.4751 & 0 \\ 0 & 0 & 0 & 0 & 0 & 0 & 0 & 0 & -2.4751 \\ 0 & 0 & 0 & 0 & 0 & 0 & 0 & 0 & 0 \\ 0 & 0 & 0 & 0 & 0 & 0 & 0 & 0 & 0 \\ 0 & 0 & 0 & 0 & 0 & 0 & 0 & 0 & 0 \end{pmatrix}$$

```

SSz = Array[SSzelem, {3 ssize, 3 ssize}];
Do[SSzelem[n, m] = 0, {n, 3 ssize}, {m, 3 ssize}];
Do[SSzelem[ssize (n-1) + m, ssize (n-1) + m] = Sz[m, m], {n, ssize}, {m, ssize}];
MatrixForm[SSz]

```

$$\begin{pmatrix} 1. & 0 & 0 & 0 & 0 & 0 & 0 & 0 & 0 \\ 0 & 0 & 0 & 0 & 0 & 0 & 0 & 0 & 0 \\ 0 & 0 & -1. & 0 & 0 & 0 & 0 & 0 & 0 \\ 0 & 0 & 0 & 1. & 0 & 0 & 0 & 0 & 0 \\ 0 & 0 & 0 & 0 & 0 & 0 & 0 & 0 & 0 \\ 0 & 0 & 0 & 0 & 0 & -1. & 0 & 0 & 0 \\ 0 & 0 & 0 & 0 & 0 & 0 & 1. & 0 & 0 \\ 0 & 0 & 0 & 0 & 0 & 0 & 0 & 0 & 0 \\ 0 & 0 & 0 & 0 & 0 & 0 & 0 & 0 & -1. \end{pmatrix}$$

```

SSp = Array[SSpelem, {3 ssize, 3 ssize}];
Do[SSpelem[n, m] = 0, {n, 3 ssize}, {m, 3 ssize}];
Do[If[nl == n, SSpelem[ssize (nl-1) + ml, ssize (n-1) + m] = Sp[ml, m], 0],
  {n, ssize}, {nl, ssize}, {m, ssize}, {ml, ssize}];

SSm = Transpose[SSp];

ls = Array[lselement, {3 ssize, 3 ssize}];
Do[lselement[ssize (nl-1) + ml, ssize (n-1) + m] =
  lrg[nl, n] Sz[ml, m] +  $\frac{1}{2}$  lpg[nl, n] Sa[ml, m] +  $\frac{1}{2}$  lmg[nl, n] Sp[ml, m],
  {n, ssize}, {nl, ssize}, {m, ssize}, {ml, ssize}];

hso =  $\lambda$  ls;
MatrixForm[Chop[hso]]

```

$$\begin{pmatrix} 13.3247 & 0 & 0 & 0 & -24.94 & 0 & 0 & 0 & 0 \\ 0 & 0 & 0 & 0 & 0 & -24.94 & 0 & 0 & 0 \\ 0 & 0 & -13.3247 & 0 & 0 & 0 & 0 & 0 & 0 \\ 0 & 0 & 0 & 0 & 0 & 0 & 0 & -24.94 & 0 \\ -24.94 & 0 & 0 & 0 & 0 & 0 & 0 & 0 & -24.94 \\ 0 & -24.94 & 0 & 0 & 0 & 0 & 0 & 0 & 0 \\ 0 & 0 & 0 & 0 & 0 & 0 & -13.3247 & 0 & 0 \\ 0 & 0 & 0 & -24.94 & 0 & 0 & 0 & 0 & 0 \\ 0 & 0 & 0 & 0 & -24.94 & 0 & 0 & 0 & 13.3247 \end{pmatrix}$$

y2mo2o7.nb

9

```

ecef = Array[ecefelem, {3 ssize, 3 ssize}];
Do[ecefelem[ssize (n-1)+m, ssize (n-1)+m] =
  ecef[n], {n, ssize}, {m, ssize}];
Do[If[n != nprime, ecefelem[n, nprime] = 0], {n, 3 ssize}, {nprime, 3 ssize}];
MatrixForm[ecef]

( 310.087  0  0  0  0  0  0  0  0 )
( 0  310.087  0  0  0  0  0  0  0 )
( 0  0  310.087  0  0  0  0  0  0 )
( 0  0  0  0  0  0  0  0  0 )
( 0  0  0  0  0  0  0  0  0 )
( 0  0  0  0  0  0  310.087  0  0 )
( 0  0  0  0  0  0  0  310.087  0 )
( 0  0  0  0  0  0  0  0  310.087 )

MatrixForm[Chop[hso + ecef]]

( 323.412  0  0  0  -24.94  0  0  0  0 )
( 0  310.087  0  0  0  -24.94  0  0  0 )
( 0  0  296.762  0  0  0  0  0  0 )
( 0  0  0  0  0  0  0  -24.94  0 )
( -24.94  0  0  0  0  0  0  0  -24.94 )
( 0  -24.94  0  0  0  0  0  0  0 )
( 0  0  0  0  0  0  296.762  0  0 )
( 0  0  0  -24.94  0  0  0  310.087  0 )
( 0  0  0  0  -24.94  0  0  0  323.412 )

{valso, vecso} = Chop[Eigensystem[hso + ecef]];

(* Eigenvalues and corresponding eigenvectors of CEF + spin-orbit hamiltonians *)
MatrixForm[valso]

( 327.214 )
( 323.412 )
( 312.08 )
( 312.08 )
( 296.762 )
( 296.762 )
( -3.80183 )
( -1.99309 )
( -1.99309 )

MatrixForm[vecso]

( 0.703034  0  0  0  -0.10717  0  0  0  0.703034 )
( 0.707107  0  0  0  0  0  0  0  -0.707107 )
( 0  0  0  0.0796615  0  0  0  -0.996822  0 )
( 0  -0.996822  0  0  0  0.0796615  0  0  0 )
( 0  0  1.  0  0  0  0  0  0 )
( 0  0  0  0  0  0  0  1.  0 )
( -0.0757805  0  0  0  -0.994241  0  0  0  -0.0757805 )
( 0  0  0  -0.996822  0  0  0  -0.0796615  0 )
( 0  -0.0796615  0  0  0  -0.996822  0  0  0 )

```

Appendix B

Magnetic field map of HELIOS solenoid

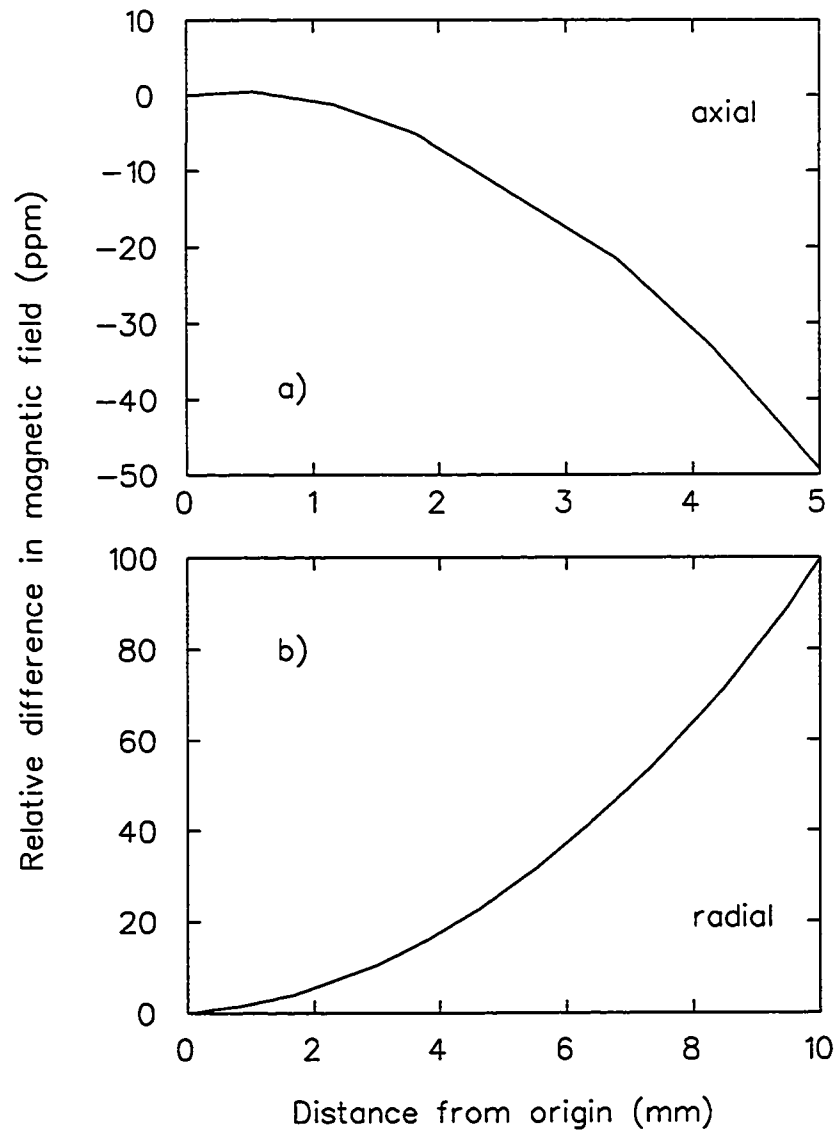


Figure B.69: Magnetic field map of HELIOS solenoid in the a) axial and b) radial directions.

Appendix C

Cooling polycrystalline samples in a dilution refrigerator

The issues of thermometry and adequate thermal contact with the sample under investigation are always of concern during experiments at millikelvin temperatures. In an insulating material well below its debye temperature the phonon mean free path is eventually limited by the spatial distribution of imperfections, impurities or the size of the specimen. The temperature dependence of the thermal conductivity is thus that of the specific heat, proportional T^3 . However, this result is dependent on the crystallinity, as indicated by experiments on glasses and amorphous materials [216] below 1 K. In these cases the thermal conductivity goes as T^2 .

To check the actual *sample* temperature of the semiconducting or insulating powder samples described in this thesis, a RuO_2 ceramic thermometer was calibrated using nuclear orientation. ^{60}Co nuclei are unstable, undergoing β decay and subsequently emitting 2 γ rays, which are detected with a NaI crystal. The emission probability is spatially anisotropic and depends on the initial nuclear spin direction. The nuclei must however be preferentially oriented in a particular direction. Cobalt orders ferromagnetically below 1388 K [217] and hence in a single crystal which has predominately aligned domains the electronic spins are also preferentially aligned. The nuclear spins are thus also polarised through the hyperfine interaction. The decay becomes increasingly anisotropic as the temperature drops below ~ 50 mK, or equivalently when the temperature becomes comparable with the splitting between nuclear hyperfine energy levels.

To calibrate the RuO_2 resistance thermometer, it was mounted next to two ^{60}Co single crystals on a sample holder like that shown in Fig. C.70 and loaded into the dilution refrigerator. The results of that calibration are summarised in the first half of Table C, which lists the resistances of RuO_2 thermometers in various positions when

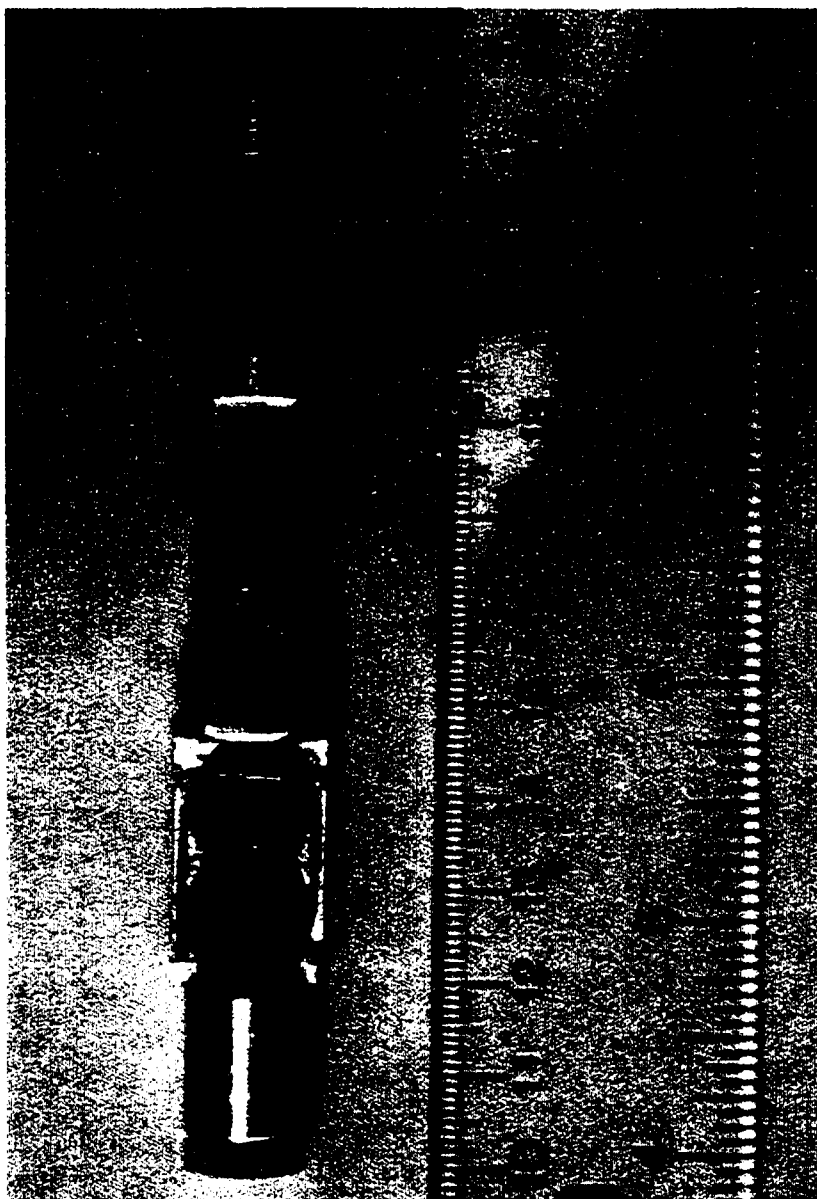


Figure C.70: Sample holder for a top loading dilution refrigerator with the sample of $\text{Y}_2\text{Mo}_2\text{O}_7$. The electrical connections for the thermometer are imbedded in teflon, shown at the bottom of the photograph. (S. R. Dunsiger)



Figure C.71: $Y_2Mo_2O_7$ prepared for a temperature calibration. The two pellets are wrapped with the copper wire leads attached to a RuO_2 thermometer. The silver plate behind is ~ 2.5 cm long. (S. R. Dunsiger)

the temperature at the sample position is either 38 or 53 mK, as measured by the ^{60}Co signal. The anisotropy as a function of temperature had been calibrated by Oxford Instruments for the particular geometry used. Since their thermal conductivity is much greater, the RuO_2 resistance thermometer is actually cooled through its two copper leads. However, to thermally isolate the sample thermometer from room temperature and prevent it from being warmed through the external leads, ~ 3 cm of niobium wire was soldered between the copper leads and external 4 wire electrical connection. Niobium becomes superconducting at 9.26 K [217]. As the temperature is reduced below its critical temperature, the number of superconducting electrons which are in a zero entropy state and hence cannot transport heat increases. A single crystal of niobium thus has a thermal conductivity of $\sim 3 \times 10^{-3} \text{ W K}^{-1}\text{m}^{-1}$ at 50 mK, approximately 3 orders of magnitude lower than commercial copper wire [218].

The calibrated RuO_2 thermometer was then mounted on a sample of $\text{Y}_2\text{Mo}_2\text{O}_7$, as shown in Fig. C.71. The copper leads were wrapped around the sample several times and GE varnished in place. A piece of cigarette paper was placed over the leads to ensure there was no electrical connection to the 0.025 mm thick silver foil folded over the top. The results of these measurements are summarised in Table C, where the resistance of various thermometers in different positions has been monitored over the course of ~ 1.5 hours. Increasing thermometer resistance corresponds to *decreasing* temperature.

The temperature at the base of the mixing chamber is monitored by two thermometers, a carbon resistor calibrated against germanium by Oxford Instruments and an uncalibrated RuO_2 resistor. The resistance of the carbon thermometer is quoted in Table C. It is well known that carbon thermometers show hysteresis effects when warmed up to room temperature and cooled again [219] but the changes are typically less than 1% over long periods of time [218]. This has been confirmed between 2 K and 50 mK by noting the variation in the resistance of the RuO_2 thermometer over a timescale of a number of years at the same nominal temperature given by the carbon resistor. The calibration has also been checked below 50 mK using nuclear orientation.

Temperature (mK) (Nuclear orientation)	Sample Resistance (k Ω) (RuO ₂)	Sample cup Resistance (k Ω) (RuO ₂)	Mixing chamber Resistance (k Ω) (Carbon)
⁶⁰ Co in sample position			
53	8.65 (1)	9.10 (1)	2.197 (8)
38	11.56 (2)	12.40 (2)	39.9 (1)
Y ₂ Mo ₂ O ₇ in sample position			
	9.93 (1)	16.15 (1)	38.5 (5)
	10.53 (1)	16.82 (2)	42 (1)
	11.00 (1)	17.97 (1)	44 (1)
	11.22 (1)	18.04 (1)	45 (1)

Table C.12: Characteristic resistances on cooling a powder sample in a dilution refrigerator.

A second RuO₂ resistor is positioned on the copper “sample cup” at nominally the same distance below the mixing chamber as the sample. This thermometer provides the best indication of the temperature closest to the sample for those measurements where there was no actual sample thermometer.

As may be seen from Table C, while the mixing chamber and sample holder temperatures steadily drop below 38 mK over the course of roughly 1.5 hours, that of the Y₂Mo₂O₇ pressed powder plateaus at ~ 40 mK. It should be noted that the base temperature of a dilution refrigerator may be affected by heat leaks from radiation shining through the thin windows over the sample position, wiring, vibration or residual exchange gas. While the cooling power of the dilution refrigerator is 400 μ W at 116 mK, it drops to 30 μ W at 45 mK and only 15 at 24 mK. After the majority of the experiments described in this thesis had already been completed, the base temperature was reduced by tightening the cold finger to the mixing chamber, improving thermal contact. Hence no data has been reported below 50 mK for the powder samples, where uncertainties about the real sample temperature become more pronounced.